Influence of cation substitution on the structure and dissolution of nuclear fuel analogues

Max Rhys Cole

A thesis submitted in partial fulfilment of the requirements for the degree of Doctor of Philosophy.

The University of Sheffield

Faculty of Engineering

Department of Materials Science and Engineering

January 2023

Abstract

Cation substitution in UO_2 may result from fission and transmutation of uranium during reactor operation, or from additions made in the fabrication of mixed oxide (MOX) and doped nuclear fuels. Replacement of U^{4+} cations in fluorite UO_2 can fundamentally alter its crystal chemistry and microstructure, which are both known to influence long-term aqueous durability.

Simulant disposal-MOX wasteforms, in which U^{4+} cations are substituted with Th^{4+} and Gd^{3+}, were fabricated *via* wet co-precipitation, and solid state synthesis routes, to compare the effects of composition and fabrication method on the phase formation and microstructure. X-ray diffraction (XRD) confirmed sintered materials formed a single cubic fluorite (Fm-3m) phase for all compositions tested, regardless of fabrication route. Greater homogenisation of Th^{4+} and Gd^{3+} within UO_2 was achieved in co-precipitated samples, as confirmed by EPMA. Charge compensation for trivalent Gd^{3+} was facilitated by oxygen vacancy generation, rather than oxidation to U^{5+}. These results demonstrate successful fabrication of disposal-MOX materials expected to retain the aqueous durability and radiation tolerance of UO_2.

CeO_2 – Gd_2O_3 mixed oxides, following the general formula $Ce_{1-x}Gd_xO_{2-x/2}$, were studied to investigate the potential influence of Gd^{3+} incorporation on the structure and dissolution behaviour of spent, or doped fuels. Sintered pellets were characterised through XRD, SEM-EDS, Raman spectroscopy, EBSD, EPMA and TEM to investigate the effects of Gd incorporation on crystal structure, secondary phase formation, microdomain formation, compositional homogeneity of the matrix, grain texture, grain size and density. Gd^{3+} incorporation was charge compensated *via* oxygen vacancy generation, confirmed by Raman spectroscopy. For compositions where $x \geq 0.40$, extensive oxygen vacancy ordering yielded a transition from a cubic fluorite (Fm-3m) to cubic C-type (Ia-3) phase, evidenced by XRD. Substitution of Ce^{4+} with Gd^{3+} significantly reduced grain size, as grain boundary migration was inhibited by segregated Gd^{3+}. A novel VSI-based dissolution study revealed preferential dissolution of grain boundaries, resulting in incongruent release of Gd relative to Ce. Incongruent dissolution was observed for all compositions, as confirmed by ICP-MS analysis of solutions obtained in C1308 dissolution tests. These results show that Gd^{3+} additions to nuclear fuel analogues strongly influence crystal structure, microstructure, and aqueous durability.

Acknowledgements

The existence of this thesis is testament to the incredible support I've received from the many wonderful people I've had the privilege to work with in the past few years. I have been so fortunate to be surrounded with the most remarkable colleagues. To my supervisor Prof. Claire Corkhill, I wish to express my upmost gratitude for offering me the opportunity to pursue this degree. Thank you for all the doors you have opened since we first applied for that SURE scheme, thank you for your patience and guidance throughout the years. My sincere thanks go also to Dr Laura Gardner, Dr Amber Mason, and Dr Sarah Pepper for your unmatched dissolution expertise. To Dr Martin Stennett, for your prudent advice and meticulous management of our labs. Dr Dan Bailey, for your breadth of expertise, and all your technical support. Dr Ritesh Mohun and Dr Josh Radford, for your sage Raman wisdom. Dr Malin Dixon Wilkins, for the eclectic M08 playlists, and your boundless obscure knowledge. Dr Hannah Smith, thank you for always radiating positivity, and your expert support in the lab. Dr Seb Lawson, it was a privilege to learn the tricks of the ceramicist trade as your Padawan. And lastly a sincere thanks to Dr Colleen Mann for settling me into what was once an intimidating environment all those years ago and helping me realise I could belong in a place like this. Beyond the realms of lab work, I couldn't ask for more excellent company on our group walks and at our (many) pub sessions from all of you wonderful people in the ISL.

I owe a great deal to a few friends whose company has helped me through some turbulent times. Lewis, your dedication to your work is matched only by that shown to your friends. I cannot overstate how the importance of your generosity and perseverance when I needed it most, thank you. I'm forever grateful for your invitations into coffee club, the inaugural vegan scran night, and that first Johnny Marr gig. Lucas, thank you for all your thoughtful gifts, enthusiasm, and unfailing confidence. Thank you for badders Thursdays and Rocket League Sundays; these little routines were islands of calm to cling to when I needed it most. John, my longest suffering friend, I can always rely on your kindness, warmth, and humour at the end of a long day. Thank you.

Finally, Thea. You are the bedrock of everything good in my life, the most beautiful and loving person I know. Thank you for enduring endless hours of waffling and woe. Thank you helping me celebrate every little win; thank you for your optimism, energy, and faith in me when I couldn't find it in myself. Scout, thank you for dragging me out of bed each morning, filling each day of writing with little bursts of joy, and keeping me company during those lonely all-nighters. Lastly, to my amazing family, thank you for all your counsel, support, and love.

Publications

During this research period, the author has contributed to the following publications:

Blackburn, L. R., Cole, M. R., Gardner, L. J., Bailey, D. J., Kuman, M., Mason, A. R., . . . Hyatt, N. C. (2021). Synthesis and characterisation of HIP $Ca_{0.80}Ce_{0.20}ZrTi_{1.60}Cr_{0.40}O_7$ zirconolite and observations of the ceramic–canister interface. *MRS Advances*, *6*(4-5), 112-118.

Austin, D. A., Cole, M., Stennett, M. C., Corkhill, C. L., & Hyatt, N. C. (2021). A preliminary investigation of the molten salt mediated synthesis of Gd_2TiO_5 'stuffed' pyrochlore. *MRS Advances*, *6*(4-5), 149-153.

Blackburn, L., Crawford, R., Walling, S., Gardner, L., Cole, M., Sun, S., . . . Corkhill, C. (2021). Influence of accessory phases and surrogate type on accelerated leaching of zirconolite wasteforms. *npj Materials Degradation*, *5*.

Corkhill, C. L., Mann, C., Eskelsen, J. R., Leonard, D. N., Mottram, L. M., Stennett, M. C., Ayling, J. M. S., Thorpe, C. L., Cole, M. R.; … Pierce, E. M. (2022). Surface interfacial analysis of simulant high level nuclear waste glass dissolved in synthetic cement solutions. *npj Materials Degradation*, *6*(1).

Mason, A. R., Blackburn, L. R., Thorpe, C. L., Aldean, I., Cole, M. R.; …Corkhill, C. L. (2022). The durability of ceramic plutonium wasteforms: A critical review. *Journal of Nuclear Materials* (IN REVIEW)

Cole, M. R. *et al.*, (2022). Demonstration of the Disposal-MOX Concept for Immobilisation of Plutonium. (IN DRAFT)

Cole, M. R. *et al.*, (2022). (Micro)structure-dissolution relationships in the $Ce_{1-x}Gd_xO_{2-x/2}$ System. (IN DRAFT)

Oral Presentations

Work presented in this thesis has been presented in part at the Universities' Nuclear Technology Forum (UNTF) 2022, 20 – 22nd June 2022, Bangor, Wales.

Contents

1. Introduction

Spent nuclear fuel remains extremely radioactive and highly dangerous following its removal from a reactor. The preferred route for high-level radioactive waste disposal in the UK is burial within a geological disposal facility (GDF), a highly engineered facility designed to isolate radionuclides from the biosphere for at least 100,000 years, after which activity falls to safer levels. Transport in groundwater represents the most likely mechanism by which radionuclides might resurface into the biosphere[1]. Spent fuel stored within a GDF will be isolated from groundwater by a series of barriers inhibiting the movement of groundwaters towards the waste, the most significant of these barriers being the rock formation itself. However, despite these measures, water ingress within 100,000 years is inevitable. Upon contact with water, spent fuel will begin to dissolve, releasing radionuclides. Once dissolved, radionuclides become far more mobile, posing a risk of re-emergence into the water table. Therefore, understanding the kinetics and mechanisms controlling spent fuel dissolution is essential in developing the safety case for its permanent disposal within a GDF.

Nuclear fuel in the UK is comprised of UO_2; a black ceramic material with a cubic fluorite (Fm-3m) crystal structure. UO_2, the most commonly used nuclear fuel worldwide[2], holds several advantages over uranium metal. Firstly, strong ionic bonds give UO_2 a melting temperature of 2,865 °C, well beyond double the melting temperature of uranium metal (1,132 °C). Furthermore, unlike uranium metal, UO_2 will not undergo phase changes below its melting point, allowing reactors to run at higher, more efficient, temperatures[3]. The fluorite structure of UO_2 also provides strong resistance to radiation and chemical attack, preventing amorphisation and rapid dissolution respectively.

Prior to its use in a reactor, nuclear fuel is comprised entirely of UO_2, but during reactor operation U transmutes into an array of chemically distinct fission products, which are incorporated into the fuel in several different ways. Some fission products are insoluble in the fluorite matrix of UO_2, resulting in the formation of gas bubbles or secondary phases. Soluble fission products such as actinides (An) and lanthanides (Ln) will instead replace U^{4+} cations within the fluorite structure to form a homogenous solid solution with UO_2. These substituted cations typically deviate from the ionic radius or valency of the U^{4+} within the host matrix. Incorporation of larger or smaller cations will expand or contract the fluorite lattice, whilst trivalent additions can induce oxygen vacancy defects. These additions are also known to influence the microstructure of spent fuel, alter the stoichiometry of UO_2, and affect the oxidation kinetics of UO_2, influencing dissolution rates[4].

Cation substitution in nuclear fuel may also result from deliberate additions made during fabrication. In advanced ‘doped’ UO_2 fuels, quantities of dopant cations are incorporated into

UO_2 to improve in-reactor performance. For example, U^{4+} can be substituted with Cr to promote large grain growth, or Gd^{3+} may be incorporated as a burnable neutron poison used to control burn-up[5]. In the example of mixed oxide (MOX) fuels, U^{4+} cations are substituted with Pu^{4+}, separated from reprocessed spent fuel, to form a $(U,Pu)O_2$ solid solution. In the case of disposal-MOX materials, a solid solution of $(U,Pu,Gd)O_2$ may be fabricated as a potential wasteform for the disposal of separated Pu. Here, U^{4+} is replaced with both Pu^{4+} and Gd^{3+}, which acts as a neutron poison to mitigate risk of criticality in a disposal environment. In all of these examples, cation substitution may cause changes in crystal structure, phase formation and microstructure, which are amongst the most significant material factors controlling the dissolution behaviour of nuclear ceramics.

This thesis explores the influence of cation substitution on the structure and dissolution of nuclear fuel analogues. Whilst it is widely acknowledged these compositional changes fundamentally alter crystal chemistry and microstructure, relatively few studies have investigated the subsequent consequences for dissolution behaviour. This thesis is presented in an alternative format. Chapters 4 and 5 are draft manuscripts prepared for submission to scientific journals, whereas Chapters 2, 3 and 6 are presented in the conventional monograph style.

Chapter 2 is a review of existing literature examining the effects of cation substitution within UO_2 and its fluorite analogue, CeO_2. Studies into the effects of Pu, Th, and Gd incorporation on the crystal structure, microstructure, and secondary phase formation in UO_2 and CeO_2 are summarised. Dissolution studies on $(Ce,Ln)O_2$ and $(U,Ln)O_2$ materials are also discussed. This review highlighted a lack of clarity surrounding the contribution of dopant segregation and high-energy surface features towards incongruent dissolution behaviour in $(Ce,Ln)O_2$ and $(U,Ln)O_2$ materials. The review also revealed no existing studies investigating the combined effects of Pu^{4+} and Gd^{3+} substitution on the crystal structure and microstructure of UO_2-based disposal-MOX materials. Lastly, key findings from studies into wasteform dissolution using surface profiling methods are summarised. This final section (2.5), titled *Determination of dissolution of nuclear ceramics using surface profiling*, was originally written for a review article titled: *The durability of ceramic plutonium wasteforms: A critical review.* The author was the sole contributor towards section 5 of the review article: *Determination of dissolution of wasteforms using surface profiling*.

Chapter 3 details the experimental methodology used to gather the data presented in this work. Whilst some of this information is repeated within the relevant manuscript drafts, Chapter 3 provides a more comprehensive summary of the experimental parameters, as well as a proof of concept for a novel *ex-situ* vertical scanning interferometry (VSI)-based surface dissolution

method developed as part of this work. Details of sample synthesis are not outlined in Chapter 3, as they are discussed within relevant papers (Chapters 4 and 5). Similarly, certain specific experimental and instrumental parameters are only detailed within these results chapters, so as to avoid repetition.

Chapter 4 presents an investigation into the feasibility of synthesising simulant disposal mixed oxide (disposal-MOX) materials in the form $(U,Th,Gd)O_2$ *via* different fabrication routes. This study characterised the influence both of Th/Gd incorporation and fabrication route on the crystal structure, phase formation, and microstructure of disposal-MOX materials. This chapter has been drafted for publication under the title:

"Demonstration of the Disposal-MOX Concept for Plutonium Immobilisation"

Max R. Cole, Lewis R. Blackburn, Latham T. Haigh, Luke T. Townsend, Sarah E. Pepper, Stuart Creasey-Gray, Daniel J. Bailey, Kristina O. Kvashnina, Neil C. Hyatt and Claire L. Corkhill.

Author contributions: **MRC** – Lead writing of manuscript, analysis, materials synthesis, collection of all data barring HERFD-XANES, ICP-OES, EPMA, and TGA. **LRB** – Materials synthesis, support with analysis, assistance with editing. **LTH** – Support with analysis. **LTT** – Fitting of HERFD-XANES. **SEP** – Collection of ICP-OES. **SCG** – Collection of EPMA. **DJB** – Materials synthesis, collection of TGA. **KOK** – Collection of HERFD-XANES by operation of BM20 beamline. **NCH** – Support with analysis. **CLC** – Acquisition of funding, supervision and support with analysis and editing.

Chapter 5 presents a detailed study of the CeO_2 – Gd_2O_3 solid solution, with CeO_2 providing an analogue for UO_2, characterising the influence of Gd incorporation on microstructure, crystal structure, as well as microdomain and secondary phase formation. Structural changes induced in $(Ce,Gd)O_2$ were linked to drastic changes in its dissolution behaviour in experiments underpinned by 3D profilometric measurements. This chapter has been drafted for publication under the title:

"(Micro)structure-dissolution relationships in the $Ce_{1-x}Gd_xO_{2-x/2}$ System"

Max R. Cole, Laura J. Gardner, Sarah E. Pepper, Stuart Creasey-Gray, Le Ma, Colm O' Regan and Claire L. Corkhill.

Author contributions: **MRC** – Lead writing of manuscript, analysis, materials synthesis, collection of all data barring EBSD, EPMA, ICP-MS, and TEM. **LJG** – Assistance with ASTM C1308 tests. **SEP** – Collection of ICP-MS. **SCG** – Collection of EPMA. **LM** – Collection of

EBSD. **COR** – Collection of TEM. **CLC** – Acquisition of funding, supervision and support with analysis and editing.

References

1. Bates, E. A., Driscoll, M. J., Lester, R. K. & Arnold, B. W. Can deep boreholes solve America's nuclear waste problem? *Energy Policy* **72**, 186–189 (2014).

2. Ganguly, C. Nuclear Fuels and Nuclear Fuel Cycle. in (International Atomic Energy Agency, 2009).

3. Sundaram, C. V. & Mannan, S. L. Nuclear fuels and development of nuclear fuel elements. *Sadhana* **14**, 21–57 (1989).

4. Liu, N. *et al.* Influence of Gd Doping on the Structure and Electrochemical Behavior of UO_2. *Electrochimica Acta* **247**, 496–504 (2017).

5. Iwasaki, K. *et al.* Effect of Gd_2O_3 Dispersion on the Thermal Conductivity of UO_2. *Journal of Nuclear Science and Technology* **46**, 673–676 (2009).

2. Literature review

2.1 Crystal chemistry of nuclear fuels

2.1.1 Crystal structure of UO_2

Uranium dioxide (UO_2) is a black, crystalline solid with a cubic fluorite (space group Fm-3m) crystal structure. The U^{4+} cations occupy a face-centred-cubic (FCC) sub-lattice, whilst the O^{2-} anions are arranged in a smaller simple cubic sub-lattice, positioned inside the FFC sub-lattice (Figure 1). The composite effect of these two sub-lattices yields a highly flexible and resilient crystal structure.

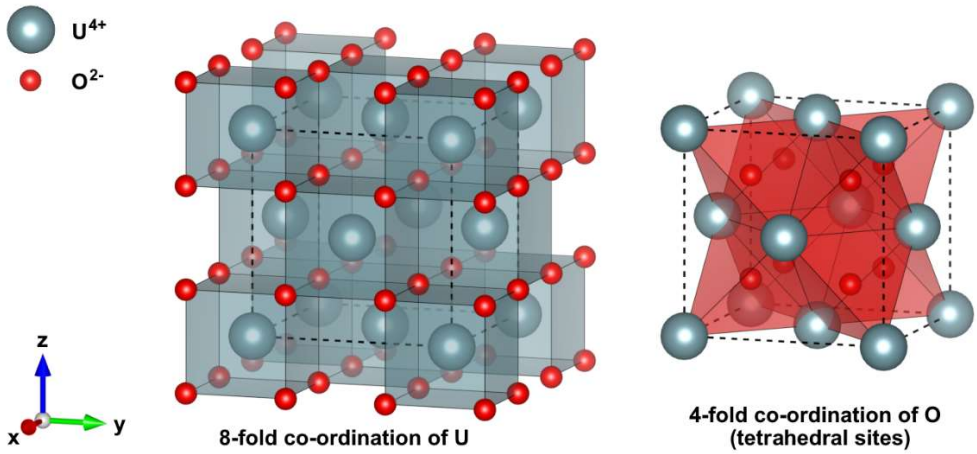

Figure 1: Illustration of 8-fold and 4-fold co-ordination environments of U^{4+} and O^{2-} ions in cubic fluorite (Fm-3m) UO_2.

UO_2 may deviate in its stoichiometry to form either hyper-stoichiometric UO_{2+x} or hypo-stoichiometric UO_{2-x}. UO_{2+x} is far more likely form compared to UO_{2-x}, as excess O is readily accommodated due to the negative formation energy of neutral oxygen interstitials (I_O) [1]. Hypo-stoichiometric UO_{2-x} will only form at very high (> 1400 °C) temperatures, as U^{4+} ions do not favour reduction to U^{3+} [2]. In both cases the cubic O^{2-} sub-lattice will become more disordered as defects are introduced in the form of oxygen interstitials (I_O) and vacancies (V_O), which in turn can affect the FFC sub-lattice of U cations, altering the entire fluorite structure. As the degree of hyper-stoichiometry increases in UO_{2+x}, I_O are known to associate, eventually forming cuboctahedral clusters associated with the U_4O_9 phase when $x > 0.23$[3,4]. U_4O_9 phases subtly alter the fluorite structure, giving rise to a superstructure consisting of I_O clusters embedded within a distorted UO_2 lattice[4]. I_O have been shown to cause a slight contraction in lattice parameter[5,6], permitted by the spatially optimised dense packing of cuboctahedral clusters[1]. Lattice contraction is similarly observed in hypo-stoichiometric UO_{2-x}, as reduced

O^{2-} - O^{2-} repulsion results in a slight reduction of the lattice parameter. Kapshukov *et al.* measured lattice contraction varied linearly with increasing hypo-stoichiometry in UO_{2-x}[7].

2.1.2 Crystal structure of (U,Pu)O_2

Mixed oxide (MOX) fuels are nuclear fuels manufactured for use in fast or thermal reactors[8], they are comprised of a UO_2 – PuO_2 solid solution described by (U,Pu)O_2. Fast reactors require fuels rich in fissile material to negate the need for a neutron moderator, hence highly fissile Pu is incorporated into UO_2 to produce MOX fuels. Both UO_2 and PuO_2 crystallise in the cubic fluorite (Fm-3m) crystal structure, adopt an M^{4+} oxidation state, and have similar lattice parameters (Figure 2). For these reasons, PuO_2 is completely soluble in UO_2, meaning a perfect solid solution exists between the two[9,10]. Substitution of U^{4+} with Pu^{4+} results in lattice contraction in accordance with Vegard's law[9,10], resulting from the smaller Shannon crystal radius of Pu^{4+} (Figure 2). Similarly to UO_2, (U,Pu)O_2 maintains its fluorite structure in both hyper- and hypo-stoichiometric compositions[11]. Markin *et al.* found incorporation of I_O in hyper-stoichiometric (U,Pu)O_{2+x} was associated with slight contraction of the fluorite lattice[12], as described previously for UO_{2+x}. The same study also showed hypo-stoichiometric (U,Pu)O_{2-x} exhibited lattice expansion due to the larger crystal radius of Pu^{3+}, induced by the reduction of Pu^{4+} in the absence of O^{2-} [12].

2.1.3 Microstructure of UO_2 and (U,Pu)O_2

UO_2-based nuclear fuels are polycrystalline ceramics, typically comprised of randomly oriented grains, between 5-15 μm in diameter[13]; relative densities are generally > 95%[14]. Several factors can influence obtained microstructures in UO_2. Hyper-stoichiometric UO_2 is known to promote faster grain growth during sintering is due to increased diffusivity permitted by I_O[15]. Higher sintering temperatures can yield larger grains and greater densities by providing more energy to promote greater rates of cation diffusion[16].

(U,Pu)O_2 materials exhibit similar microstructures to UO_2, however, obtained grain sizes and densities and more dependent on fabrication route, as heterogenous Pu distribution within the UO_2 matrix can influence sintering behaviour in (U,Pu)O_2. Haas *et al.* obtained average grain sizes of 10 – 15 μm in pellets of $(U_{0.55}Pu_{0.45})O_2$ produced using SOL GEL wet synthesis[17]; relative densities were measured to be ~95%. (U,Pu)O_2 MOX fuels produced using the MIMAS (MIcronized MASter blend) process, in which a primary 'master' blend of UO_2 and PuO_2 is diluted with UO_2 typically exhibit a highly heterogenous distribution of Pu[18]. Whilst a perfect solid solution exists between UO_2 and PuO_2, MOX fuels produced using the MIMAS process typically contain two or three phases, these being (U,Pu)O_2, pure PuO_2, and UO_2[19]. Despite this multi-phase microstructure, grain size and porosity between each phase are very similar[19].

2.2 CeO_2 and ThO_2 analogues for UO_2 and PuO_2

The fluorite structure of UO_2 is integral to much of its behaviour, for this reason, alternative fluorite oxides such as ceria (CeO_2) can be employed as non-radioactive analogues in experimental work. CeO_2 is a well-established surrogate for UO_2; previous studies have demonstrated its ability to replicate the typical microstructure of UO_2-based nuclear fuels[13], this being a dense sintered ceramic comprised of randomly orientated grains between 8 – 15 µm in diameter[14]. The crystal radius of Ce^{4+} is also comparable to U^{4+} (Figure 2).

Experiments involving PuO_2 can prove especially challenging, as no low activity isotopes of Pu exist. Surrogates used in place of PuO_2 in existing studies include UO_2, CeO_2, and ThO_2[8,20]. Whilst UO_2 and ThO_2 are still radioactive, isotopes U-238 and Th-232 emit very low energy alpha radiation. Typically, Ce is used as a convenient, inactive Pu surrogate, however, the tendency for Ce^{4+} to reduce to Ce^{3+} under the highly reducing conditions necessary for sintering of UO_2 compositions can render Ce an impractical surrogate[21,22]. Furthermore, Ce^{3+} is known to readily form at exposed surfaces, even under relatively oxidising conditions[23,24]. The comparatively stable redox behaviour of Th can simplify investigations into analogue materials, by avoiding the complications associated with reduction, such as charge compensation and changes to ionic radii. However, the ionic radius of Ce^{4+} is closer to that of Pu^{4+}, whereas Th^{4+} is notably larger (Figure 2). Employing a Ce^{4+} surrogate in disposal-MOX analogues will induce a lattice contraction representative of Pu^{4+} when substituted into UO_2 compared to Th^{4+}, which will induce lattice expansion as its ionic radius is larger than U^{4+}.

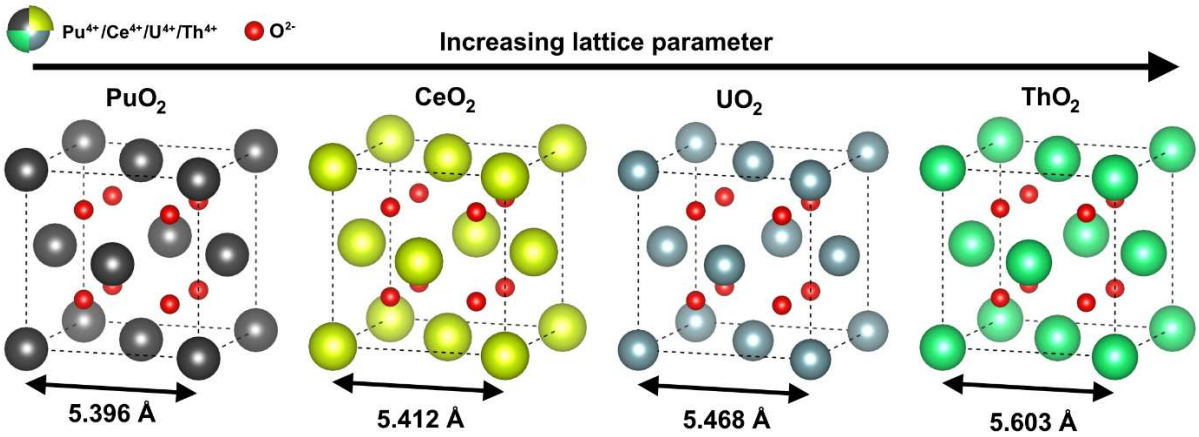

Figure 2: Illustration of fluorite structures in PuO_2, CeO_2, UO_2, and ThO_2. Quoted crystal radii taken from Shannon[25].

2.3 Cation substitution UO_2 and CeO_2

During reactor operation, U transmutes into an array of chemically distinct fission products. Some fission products are insoluble in the fluorite matrix of UO_2, resulting in the formation of

gas bubbles or secondary phases. Other fission products, such as actinides (An) and lanthanides (Ln), form a homogenous solid state solution in UO_2. Hiezl *et al.* used computational modelling to predict the composition of spent fuel after 100 years of cooling; they concluded the concentration of lanthanides such as Nd, Ce and La will continue to increase long after removal from the reactor as their isotopes are relatively stable[16]. Gd is amongst the major fission products capable of forming a solid solution with UO_2, the $U_{1-x}Gd_xO_{2-\delta}$ system has previously been employed as a simplified spent fuel surrogate to investigate the effects of lanthanide incorporation in UO_2 [25]. MOX fuels in the form $(U,Pu)O_2$ are another example of cation substitution in UO_2. The $Ce_{1-x}Gd_xO_{2-\delta}$ system has previously been investigated as an inactive analogue for Ln-doped UO_2. $Ce_{1-x}Gd_xO_{2-\delta}$ materials are also regarded as promising electrolyte material for use in intermediate temperature solid oxide fuel cells[26,27].

2.3.1 Influence of cation substitution on fluorite structure

The incorporation of substituted cations on the FCC sub-lattice of fluorite oxides such as UO_2 and CeO_2 alters the crystal structure. The nature and extent of these structural changes is dependent both on the radius and valency of the substituted cation[28]. Typically, substitution of a host cation with a cation of larger crystal radius will result and lattice expansion, and substitution with smaller cations causes lattice contraction. For example, the replacing U^{4+} cations (crystal radius 1.14 Å in 8-fold co-ordination[29]) with smaller Pu^{4+} cations (crystal radius 1.10 Å in 8-fold co-ordination[29]) reduces the lattice parameter in $(U,Pu)O_2$ [12], as discussed in Section 2.1.2. When U^{4+} is replaced with larger Th^{4+} cations (crystal radius 1.19 Å in 8-fold co-ordination[29]), the fluorite lattice undergoes volume expansion. Rao *et al.* measured a linear increase in the lattice parameter of $(U,Th)O_2$ with Th substitution, in accordance with Vegard's law[30]. Linear variation of lattice parameter with rate of cation substitution typically suggests successful incorporation within a single phase. Cation substitution does not always induce a linear change in lattice volume corresponding to the average crystal radius. In $U_{1-x}Gd_xO_{2-\delta}$, Gd additions yield a slight reduction in lattice parameter[31], despite the larger crystal radius of Gd^{3+} (1.193 Å in 8-fold co-ordination[29]). This lattice contraction has been attributed to reduced O^{2-} - O^{2-} repulsion, and oxidation to U^{5+} [32], which both result from charge compensation mechanisms necessary to charge balance trivalent Gd^{3+}. Charge compensation mechanisms are discussed in greater detail in Section 2.3.2. In CeO_2, Gd^{3+} additions cause lattice expansion[33], as the crystal radius of Gd^{3+} is significantly larger compared to Ce^{4+} (1.193 Å and 1.11 Å respectively in 8-fold co-ordination[29]), negating the reduced O^{2-} - O^{2-} repulsion caused by V_O generation. The lattice parameter variation with Gd^{3+} additions is compared in Figure 3.

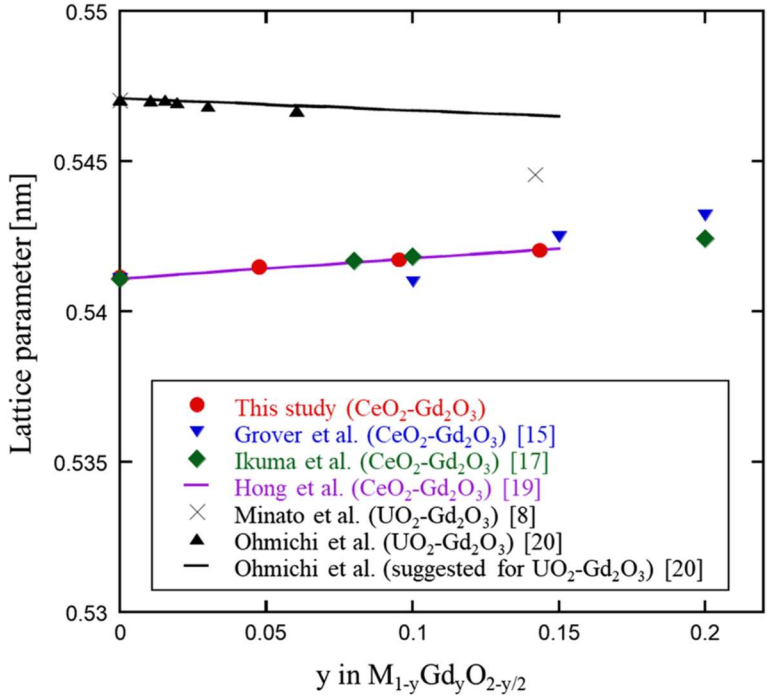

Figure 3: Experimentally obtained lattice parameters in various studies of $Ce_{1-x}Gd_xO_{2-\delta}$ and $U_{1-x}Gd_xO_{2-\delta}$. Vao Mao *et al.* (2020)[33]

2.3.2 Charge compensation mechanisms

In UO_2, incorporation of trivalent cations can be charge balanced by either the oxidation of U^{4+} to U^{5+}, or the generation of V_O[25]. The incorporation of two trivalent cations (M^{3+}) is charge balanced with the release of a single O^{2-} anion the cubic sub-lattice. In their study of fission product doped SIMFUELs, He *et al.* revealed evidence of both increased U^{5+} content, and Ln^{3+} - V_O clustering[34], suggesting both mechanisms may have compensated for trivalent additions. Prieur *et al.* found U^{5+} to form in equimolar proportion with La^{3+} substitution in UO_2, and concluded that V_O were not induced in the structure[35]. Bès *et al.* compared charge compensation mechanisms in $U_{1-x}Gd_xO_{2-\delta}$ and $Th_{1-x}Gd_xO_{2-\delta}$, their study found Gd^{3+} incorporation in UO_2 was associated with U^{5+} formation, whereas in ThO_2 the deficit was compensated *via* V_O generation[31], due to the inability of Th^{4+} to oxidise further. The same behaviour is observed for CeO_2, as Ce cannot be oxidised beyond +4, trivalent substitution must be compensated *via* V_O generation[36].

2.3.3 Phase formation in $Ce_{1-x}Ln_xO_{2-\delta}$

Extensive substitution of host cations in fluorite oxides can induce transitions to different crystal structures. In their study of $Ce_{1-x}Ln_xO_{2-x/2}$ systems, Horlait *et al.* found for $x \leq 0.40$, the fluorite structure was maintained, however compositions where $x \geq 0.60$ adopted the C-type superstructure[28]. As previously established, the incorporation of two trivalent cations is charge

balanced by the generation of a single V_O. In fluorite structures, V_O are randomly positioned within the cubic O^{2-} sublattice, but as the concentration of V_O increases due to extensive cationic substitution, it becomes energetically favourable for clusters of V_O to become ordered and occupy specific sites within the sublattice. The C-type structure is formed when a widespread V_O ordering displaces cations to new crystallographic sites; these displacements break the symmetry of the fluorite unit cell, doubling the lattice parameter through creation of a new cubic superlattice, known as the C-type structure[37,38]. The C-type structure remains very similar to fluorite, so distinguishing between the two structures can prove challenging.

The precise fluorite solubility limit was found to vary depending on the crystal radius of the incorporated Ln^{3+}. In the case of $Ce_{1-x}Nd_xO_{2-x/2}$, Horlait *et al.* noted a transition from fluorite to C-type for x = 0.42, similar studies by Ikuma *et al.*[39] and Hagiwara *et al.*[40] also reported this transition for x = 0.40 – 0.45. Further cation substitution beyond the C-type solubility limit may result in transitions to hexagonal structures in the case of the largest Ln^{3+} cations, such as La^{3+} and Nd^{3+}, or monoclinic structures in the case of Gd^{3+} or Sm^{3+} [41].

Cation heterogeneity can also influence phase formation in $Ce_{1-x}Ln_xO_{2-x/2}$, with localised deviations in composition yielding bi-phasic microstructures. Nitani *et al.* observed the formation of both fluorite and C-type phases for x = 0.40[42]; the lower solubility of Nd in CeO_2 achieved in this study may be attributed to the solid state route by which the samples were fabricated, compared to the wet precipitation routes employed in the aforementioned studies, which are known to yield greater compositional homogeneity.

Phase transitions in $Ce_{1-x}Ln_xO_{2-\delta}$ materials are also dependent on thermal treatment. Horlait *et al.* found elevated calcination temperatures of over 800 °C resulted in the formation of A-type (hexagonal) $Ce_{0.27}Nd_{0.73}O_{2-\delta}$ oxide powders[28], whereas below this the C-type phase was stable.

2.3.4 Phase formation in $U_{1-x}Ln_xO_{2-\delta}$

Durazzo *et al.* determined the solubility limit of Gd^{3+} in $U_{1-x}Gd_xO_{2-\delta}$ to be x = 0.50[43] (Figure 4), which is greater than that observed in $Ce_{1-x}Gd_xO_{2-\delta}$ (typically around x = 0.30 - 0.40[28,37]). This increased solubility limit may be attributed to the ability of U^{4+} to oxidise to U^{5+} when charge balancing for aliovalent Gd^{3+}. In fluorite systems where cations are unable to oxidise beyond +4, such as CeO_2 and ThO_2, Gd^{3+} must be solely charge balanced by the generation of V_O in the structure. Extensive V_O generation causes widespread V_O ordering and significant cation displacement, inducing an earlier phase change to C-type[44]. Beyond the fluorite solubility limit in UO_2[45], Ln^{3+} additions typically form rhombohedral phases, as with CeO_2 the solubility limit is dependent on crystal radius mismatch, thermal treatment, and spatial heterogeneity of substituted cations.

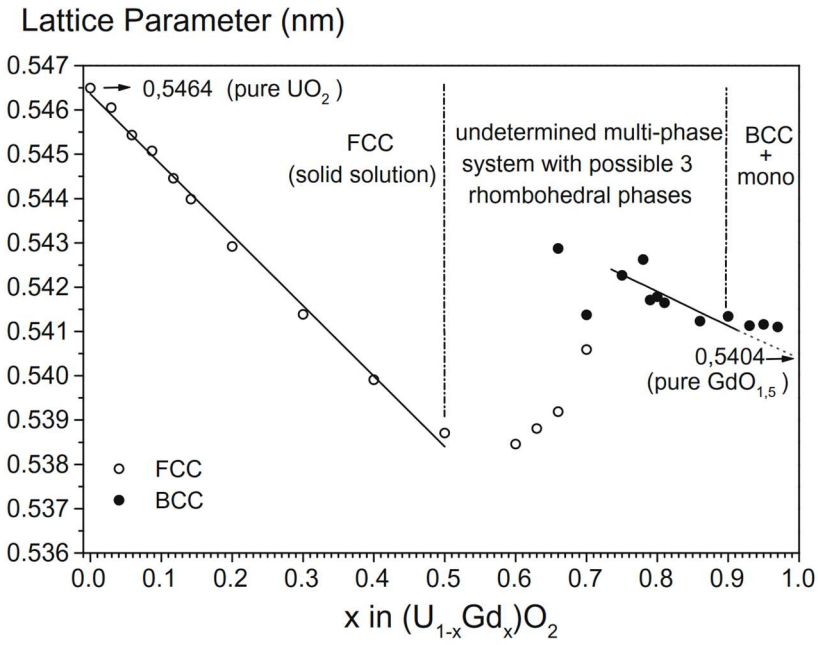

Figure 4: Lattice parameter against Gd molar fraction in $U_{1-x}Gd_xO_{2-\delta}$. Beyond x = 0.50, a linear relationship is no longer observed, indicating the formation of additional rhombohedral phases. Durazzo (2010)[43]

Formation of monoclinic phases in $U_{1-x}Gd_xO_{2-\delta}$ can occur for x > 0.90. Iwasaki *et al.* observed monoclinic particles in poorly homogenised Gd_2O_3-dispersed UO_2 with composition $U_{0.86}Gd_{0.14}O_{2-\delta}$. Whilst this global Gd content is well below the fluorite solubility limit in UO_2, spatial variations in composition caused by poor homogenisation permitted the formation of Gd-rich secondary monoclinic phases, shown in Figure 5[46].

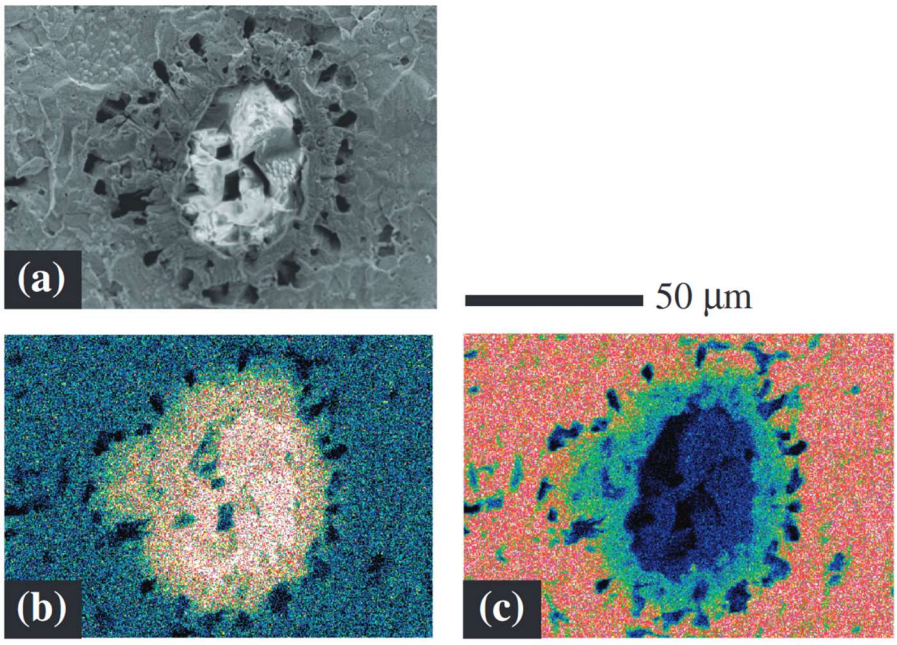

Figure 5: (a) SE image of monoclinic Gd-rich particle in poorly homogenised Gd_2O_3-dispersed UO_2. (b) EDS image of Gd distribution and (c) EDS image of U distribution. White indicates the highest concentration, followed by red, yellow, green, and finally blue. Iwasaki (2009)[46]

2.3.5 Grain boundary segregation and nanodomain formation

Even in single phase fluorite systems, substituted cations are never perfectly distributed within the material. As the concentration of substituted cations increases, they are more readily segregated to regions that can most readily accommodate them, most commonly being grain boundaries. Hong *et al.* used density functional theory to calculate the segregation energies of several fission products to a Σ5 grain boundary UO_2 [47]. Two prominent segregation sites found in the atomic structure of the Σ5 grain boundary were chosen to demonstrate compare the segregation energies of different dopants. Site 'a' featured lower oxygen coordination and larger free volume, site 'b' offered less free volume and a far higher oxygen coordination. By substituting the uranium ion in each site with an array of fission products, the segregation energy of was calculated. Segregation energy of a dopant is defined by Equation 1 [48].

$$E_{Seg} = E_B - E_{GB} \quad (1)$$

Equation 1 shows that where the system energy when the dopant is placed in the bulk, E_B, is greater than the system energy when the dopant is placed within the grain boundary, E_{GB}, the segregation energy E_{Seg} will be positive, meaning the dopant will preferentially segregate towards the grain boundary. The study found that the large free volume offered by site 'a' was generally preferred by low valence fission products, whereas higher valence fission products capable of forming strong bonds with oxygen ions segregated towards site 'b' due to its high O coordination. Similar studies into dopant segregation energy have also been conducted using CeO_2. Arora *et al.* also found that the ionic radius of the dopant strongly influenced segregation behaviour. The closer the ionic radius of the dopant was to the radius of the host cation, the lower the segregation energy[48]. The same study also found, in accordance with the Hong *et al.* study, that specific sites within grain boundaries play a key role in segregation. The segregation behaviour of each grain boundary will therefore differ depending on the local atomic environment of its segregation sites. Characterising the atomic structure of different grain boundaries is necessary for identifying these sites, and thus will allow for a greater understanding of segregation behaviour in fluorite grain boundaries. Bellière *et al.* La-doped CeO_2 was studied using STEM-EELS to reveal differences in stoichiometry on the nanoscale. The study found La rich phases formed near the grain edge; these phases were supported by La deficient phases in the bulk.

Segregation of substituted cations in fluorite materials may also be driven by strong binding energies that exist between aliovalent Ln^{3+} species, and oxygen vacancy (V_O) point defects. As just a single V_O is generated for each pair of Ln^{3+} cations introduced into the structure, Ln^{3+} cations have a strong affinity to migrate towards V_O, effectively competing for to 'scavenge' a finite resource[49]. Strong binding energies between V_O - V_O and V_O – Ln^{3+} result in segregation[48]

and eventually ordering[50]. As discussed in Section 2.3.3, widespread V_O ordering yields transition to a cubic C-type phase in $Ce_{1-x}Gd_xO_{2-x/2}$, however, V_O ordering over far smaller length scales (> 100 nm) can result in temporary discontinuities within fluorite crystallites, known as nanodomains. The structure of C-type nanodomains can be distinguished from true C-type phases by their differing degrees of ionic displacement, as illustrated in Figure 6.

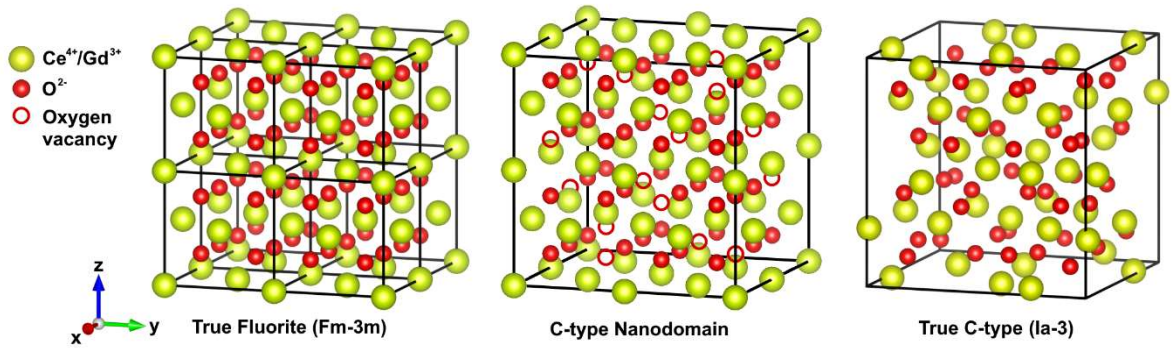

Figure 6: Illustration of cation positions in fluorite, C-type nanodomains, and true C-type structures. Note the lack of significant cation displacement in C-type nanodomains, which is readily observed in true C-type. Black borders indicate the unit cell, which is doubled in length for both forms of C-type structure.

C-type nanodomains may form in Gd-doped CeO_2 well below the fluorite solubility limit, typically stated to be ~40 mol%[50]. Ye *et al.* observed C-type nanodomain formation in compositions of $Ce_{1-x}Gd_xO_{2-x/2}$ where $x \geq 0.10$[51], whereas Li *et al.* reported nanodomain formation in samples where $x = 0.25$[52]. Nanodomains are known to increase in size and frequency as greater quantities of trivalent dopants are incorporated[37,53], and the concentration of V_O increases. Beyond a critical concentration, nanodomains can coalesce to build long-range structure that ultimately form true C-type phases.

As previously established, grain boundaries provide a large free volume that accommodates defects and impurities more readily than the bulk, thus encouraging segregation of both Ln^{3+} dopants and V_O. For this this reason, nanodomain formation is expected to be more prevalent in the regions towards the grain edge, and secondary phases often precipitate within grain boundaries.

2.3.6 Effect of cation substitution on microstructure

Cation substitution can strongly influence the rate of diffusion during sintering, affecting the obtained grain size and porosity. Grain growth during sintering is controlled by grain boundary mobility, which itself is dependent on a mechanism of cation diffusion *via* interstitial sites[54]. Dopants with far smaller crystal radius relative to the matrix cation can, in small quantities (< 1 mol%), enhance grain boundary motion by inducing a lattice distortion that enables

greater rates of cation diffusion. Similarly, small quantities of aliovalent Ln^{3+} can encourage greater cation diffusion, facilitated by V_O sites generated in the structure. However, significant (> 1 mol%) Ln^{3+} additions to CeO_2 are known to suppress grain growth due to the solute drag effect, which describes the pinning of grain boundary motion by segregated Ln^{3+}. Grain boundaries heavily enriched with Ln^{3+} cations are less mobile due to strong Ln^{3+} - V_O binding energies inhibiting cation diffusion[55]. Oversized dopants, with ionic radii greater than that of the host cation, are also known to restrict grain boundary motion, as solute drag increases with ionic radius.

Van Mao *et al.* noted a decrease in average grain size in CeO_2 from 30 μm to 6 μm with the addition of 5 wt% Gd_2O_3 to CeO_2, further additions of 10 and 15 wt% yielded no further significant decrease[33]. In their study of $Th_{1-x}Y_xO_{2-x/2}$ Cherkaski *et al.* found grain size and density were greatest when x = 0.01 (1 mol% Y), whereas grain sizes were similar for x = 0.08, 0.15 and 0.22[56].

2.4 Dissolution of nuclear fuel and its analogues

2.4.1 Spent fuel dissolution

To contextualise the investigation of nuclear fuel analogue dissolution, it is firstly important to summarise existing models of dissolution in real spent fuel. Following a breach of the fuel assembly cannister, fission gases such as Xe and Kr, as well as highly mobile volatile radionuclides such as I and Cs, will be rapidly released. The fraction of inventory lost upon the failure of the container is termed the instant release fraction (IRF). These volatile elements are leached so readily in part because they have migrated to grain boundaries and the pellet-cladding gap during reactor operation and cooling[57]. The contribution of the IRF increases towards the pellet edge, where grain size is smallest (< 1 μm). Sub-micron grains around the pellet edge are characteristic of the high burnup structure (HBS), which is caused by increased local fission density in peripheral regions. Extensive radiation damage in these areas results in recrystallisation within grain boundaries or pores, and precipitation of fission gases into bubbles[58]. The resulting increase in grain boundary area facilitates movement of volatile radionuclides towards the pellet-cladding gap. Figure 7 illustrates these areas and gives some indication of the typical distribution of fission products in spent fuel.

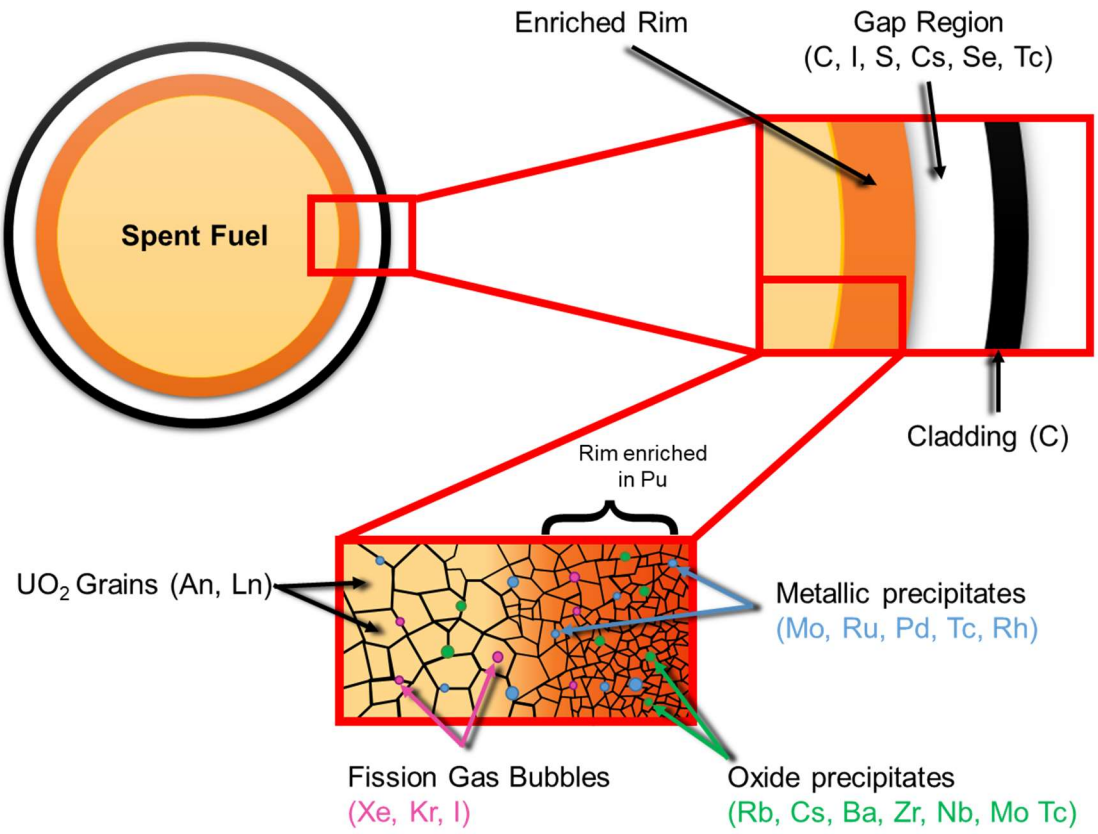

Figure 7: Schematic illustration of SNF microstructure and distribution of fission products. Adapted from Bruno (2006)[57]

Following the IRF, immiscible metallic and ionic precipitates that formed along the grain boundaries will begin to dissolve. Eventually, the UO_2 matrix itself will begin dissolving; this stage results in much slower release of radionuclides. The most important processes during UO_2 dissolution generally occur in the following order[57]: (1) Oxidation of U^{4+} to U^{6+} and formation of higher oxide structures on the fuel surface and at grain boundaries. (2) Bulk dissolution of the UO_2 and release of radionuclides that substitute for U (Pu and Np). (3) Dissolution of segregated oxides and immiscible metallic alloys (ε-particles) in the fuel grains 4 (4) Formation of secondary alterations products, such as coffinite ($USiO_4$) under reducing (U^{4+}) conditions, or becquerelite or uranophane under oxidising conditions (U^{6+}).

The complex mechanisms involved in spent fuel dissolution are also affected by burn-up, which changes composition and microstructure of spent fuel[14], and can be accelerated by the presence of H_2O_2 produced *via* radiolysis of groundwaters[59]. Deconvoluting these complex interlinked processes and controlling factors can prove very challenging. Spent fuel dissolution is however ultimately dominated by behaviour of UO_2 matrix, so typically this far simpler system is used in experiments to predict spent fuel dissolution behaviour.

2.4.2 Influence of cation substitution on dissolution of UO_2 and CeO_2

Razdan *et al.* showed that the electrochemical reactivity of Gd-doped UO_2 is diminished compared to SIMFUEL, though the dissolution mechanism is similar[3]. This decreased reactivity was attributed Gd^{3+} - V_O clusters limiting the incorporation of I_O that initiate accelerated, oxidative dissolution. Significant concentrations of I_O result in clustering, yielding U_4O_9 and U_3O_8 phases through extensive hyper-stoichiometry, resulting from encourage faster dissolution of UO_2[60]. Disposal-MOX wasteforms are expected to retain the high aqueous durability of pure UO_2. For example, the $U_{0.73}Pu_{0.27}O_2$ phase, readily produced by direct milling of constituent oxides, was found to demonstrate a long term U dissolution rate of 7.6 mol m^{-2} d^{-1} [61].

CeO_2 is limited in its ability to replicate the redox behaviour of UO_2, as Ce cannot oxidise beyond +4 to +5 and +6 oxidation as U cations do readily. This is renders CeO_2 incapable of mimicking oxidative UO_2 dissolution, which is significant as the enhanced dissolution rate of U^{6+} is integral to UO_2 dissolution mechanisms in a disposal context[57,62]. Conversely, the stable +4 oxidation state of Ce permits investigation into factors unrelated to redox behaviour that are known to influence UO_2 dissolution. Removing contributions from cation oxidation allows the more subtle effects of microstructure and crystalline defects on dissolution rate to be measured[63,64]. In their investigation of $Ce_{1-x}Ln_xO_{2-x/2}$ Horlait *et al.* noted the incorporation of Ln^{3+} significantly influenced dissolution behaviour due to weakening of the crystal lattice, resulting from V_O generation. They found the dissolution rate of $Ce_{1-x}Ln_xO_{2-x/2}$ oxide powders increased by approximately 1 order of magnitude with each 10 mol% of Ln^{3+} addition[65]. Phase transitions to cubic C-type were found to have no discernible impact on dissolution rates. In their study of $Th_{1-x}Ln_xO_{2-x/2}$, Horlait *et al.* again concluded that Ln^{3+} incorporation rate was the dominant factor controlling dissolution rates, with each 9 mol% of Ln^{3+} addition yielding an order of magnitude increase[63]. Again, phase transitions from fluorite to C-type appeared to exert no control on dissolution rates.

2.4.3 Influence of microstructure on UO_2 and CeO_2 dissolution

The presence of certain microstructural features such as grain boundaries can result in accelerated dissolution, due to their greater interfacial surface energies. Grain boundaries are the most common microstructural defect in UO_2; they provide routes for rapid diffusion, nucleation sites for secondary phases and the free volume to promote segregation of dopants and point defects. As a result, they play a decisive role in the dissolution of spent fuel. Crystallographic orientation is also known to exert strong control over dissolution rate in fluorite oxides such as CaF_2 and CeO_2[66,67]. Corkhill *et al.* found high-angle grain boundaries dissolved faster when compared to their low-angle equivalents, which was attributed to high

concentrations of defects incorporated into highly disordered structure of high-angle (~60°) grain boundaries[64]. Substituted cations preferentially segregate to grain boundaries, increasing localised elemental concentration and, in the case of aliovalent cations, forming nanodomains. As previously discussed, above a critical concentration, C-type nanodomains in fluorite $Ce_{1-x}Ln_xO_{2-x/2}$ combine to form true cubic C-type phases with accompanying cation displacements. Whilst Horlait *et al.* concluded these cubic superstructures had little influence on dissolution rates, they observed that further phase transitions induced by Ln^{3+} additions beyond the C-type solubility exhibited enhanced dissolution rates. Their *in-situ* dissolution study of $Ce_{0.24}Nd_{0.76}O_{1.62}$ observed rapid preferential dissolution of hexagonal A-type secondary phases, that precipitated within grain boundaries, through the use of an environmental scanning electron microscope (ESEM)[68].

It is unclear whether the Ln^{3+} enrichment of grain boundaries influences their preferential dissolution prior to the formation of secondary phases, although it might be expected that an increase in Ln^{3+} incorporation would exacerbate the accelerated dissolution rates observed within grain boundaries. As previously established, cation substitution exerts strong control over grain growth during sintering; smaller grain sizes may increase the reactivity of a surface due to the increased grain boundary area. It is not known whether Ln^{3+} incorporation within UO_2 might exert a grain texture, by encouraging preferential crystallographic alignment of adjacent grains.

2.5 Determination of dissolution of nuclear ceramics using surface profiling

Surface profiling techniques such as vertical scanning interferometry (VSI) and atomic force microscopy (AFM) offer unique insight into the heterogeneous nature of ceramic dissolution. Microstructural features such as grain boundaries, pores and secondary phases are known to exert control over the rate of dissolution (e.g. Corkhill *et al.*[64,69]), however, the relative significance of these individual rate contributions cannot easily be ascertained in conventional dissolution studies. Profiling techniques can quantify material loss in specific regions of a microstructure, allowing rate contributions from high energy surface features to be deconvoluted from the overall dissolution rate. This nuanced approach can elucidate dissolution behaviours otherwise homogenised within a single rate constant (e.g. Godinho *et al.*[67]).

AFM and VSI represent two of the most commonly used profilometry methods. Profilometers reveal the topography of a surface by measuring its height at a finite number of points within a selected area. Height values are then compiled into a 2D matrix and plotted as pseudo-colour figures. Pseudo-colour plots intuitively display the topography by assigning a specific range of hue or luminance to a corresponding range of heights; the same data can also be

presented in 3D plots. Measuring the same region prior to and following contact with a solution can reveal surface retreat where material has been dissolved. Subtracting two matrices from subsequent time points will generate a 'material flux' map, which reveals rates of retreat across the surface; regions of accelerated or inhibited dissolution are distinguished by high and low rates of retreat, respectively. The following equation (Equation 2) developed by Lüttge *et al.*[70], allows these varied retreat rates across the surface to be converted into localised rate constants k (mol m^{-2} s^{-1}):

$$k = v_n \bar{v}_m^{-1}$$

Equation 2: Calculation of rate constant k, where v_n is the surface normal retreat rate and V_m is the molar volume of the material.

Alternatively, the average retreat across the whole measured area can be used to calculate the overall rate of dissolution, providing a useful comparison with bulk dissolution data.

Surface profiling dissolution experiments can be broadly divided into *in-situ* and *ex-situ* studies. *In-situ* studies involve taking measurements whilst the sample remains submerged in solution, whilst *ex-situ* measurements involve removing the sample from solution prior to each individual measurement. *In-situ* studies require specialised equipment; in the case of VSI, a through-transmissive media (TTM) module is required, whilst AFM uses a fluid cell. *Ex-situ* studies are simpler to conduct as they avoid the complexities arising from measuring through a liquid medium, however they are generally more time consuming. No standardised method currently exists for either VSI or AFM based dissolution methods. Some studies use series of pumps to control the rate of solution renewal, akin to single-pass flow-through (SPFT) experiments, whereas others involve submerging a monolith in a static solution, and removing it for measurements at regular intervals, not unlike MCC-1 tests. For this reason, results can be difficult to compare between different laboratories and research groups.

As previously outlined, surface profilometry techniques such as VSI and AFM measure the height of a specimen across a surface plane. VSI achieves this by splitting a beam of white light in two; one of these beams travels a known distance to a reference mirror whilst the other is directed towards the sample surface, as illustrated in Figure 8. Both beams are then reflected back towards the beamsplitter, where they are superposed, generating a pattern of bright and dark fringes as the beams interfere constructively and destructively. The light source is raised and lowered to adjust the path length until the beams are in phase and the central peak of the interferogram has the greatest contrast with its neighbouring troughs[71]. At this point, the path lengths to the surface and reference mirror are equal; thus, the surface height is measured.

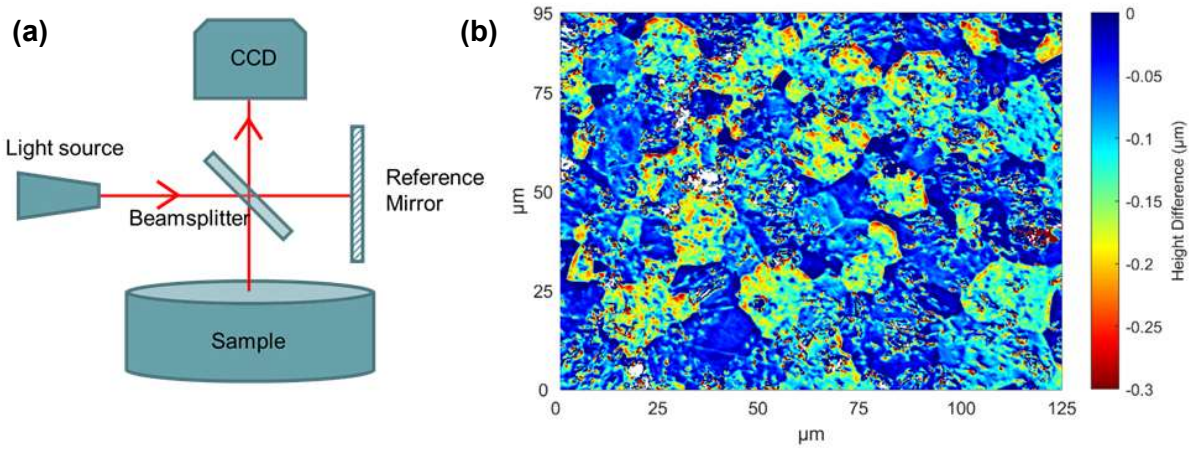

Figure 8: (a) Schematic diagram of an interferometer. (b) Material flux map of Cr-doped UO_2 pellet measured using VSI, showing accelerated dissolution of certain crystallographic orientations, pores, scratches, grain boundaries and polishing induced artefacts.

AFM operates by rastering a sharp-tipped cantilever over a surface; the interaction between tip and sample generates forces which, in turn, displace the cantilever in accordance with Hooke's law. When analysing ceramic surfaces, AFM is typically used in either contact or tapping mode. In contact mode, the cantilever tip remains in mechanical contact with the surface throughout the measurement. In tapping mode, the tip oscillates very near the surface in response to van der Waals forces. In both modes, the extent of the cantilever's deflection is measured using piezo electronics or photodiodes, this deflection is used to calculate the surface height at each point (see Figure 9).

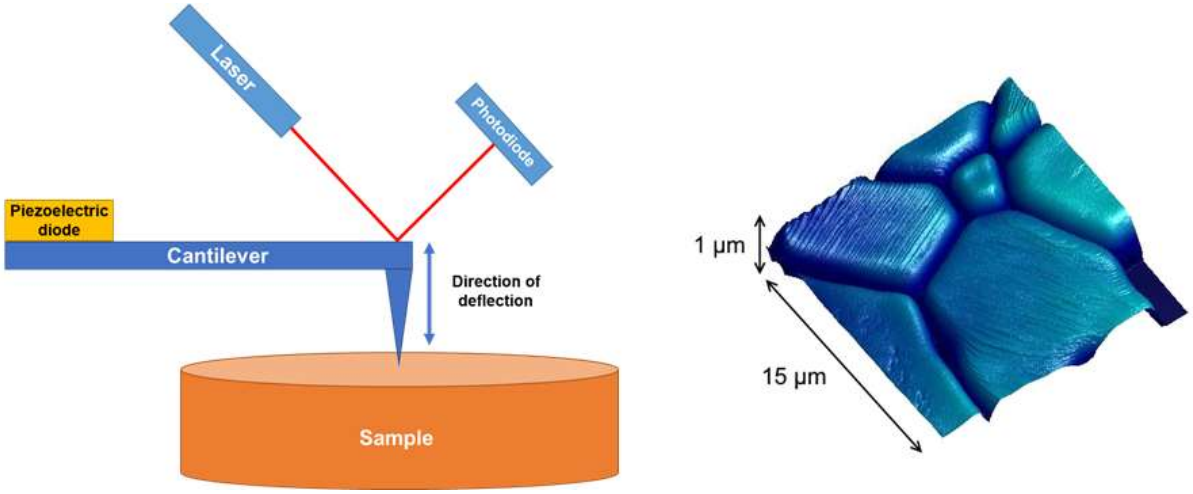

Figure 9: Left, schematic diagram of AFM operation. Right, 3-D AFM image of a sintered pellet of CeO_2, showing grains, grain boundaries, pores, and facets.

Whilst VSI and AFM provide similar data, there exist key differences that determine their suitability to certain applications. VSI boasts a far greater range of field of view (FOV) compared to AFM, making it better suited to characterising materials at varied length scales. Adjusting the FOV is easily achieved by switching between objective lenses with different magnifications. In addition, the vertical resolution of VSI (typically around 2 nm) is independent of any change to magnification[72] whereas lateral resolution will be diminished at lower magnifications. AFM offers superior lateral (~30 nm) and vertical (~0.1 nm) resolution, meaning it is more suited to analysing smaller regions of a sample with high precision. This precision, however, limits its speed; measurements take anywhere between a few minutes and several hours as the tip is rastered slowly over the surface. This, again, lends AFM more towards measuring smaller areas. VSI measurements by comparison are very fast, taking as little as one second per scan. This speed is particularly useful when conducting 'stitched' measurements (Figure 10), in which several scans are compiled to form a single dataset covering a very large region of the surface.

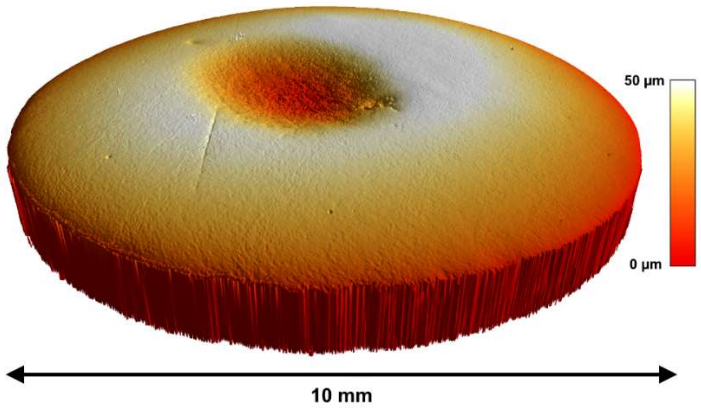

Figure 10: Stitched VSI measurement of $(Ce,Gd)O_2$ pellet, comprised of ~100 individual scans.

An approach utilising both VSI and AFM in conjunction would overcome these limitations and provide a comprehensive analysis across several length scales. The application of VSI and AFM are well established to ascertain the dissolution rates of various minerals, with many papers published on rapidly dissolving specimens, such as CaF_2, For example, Cama *et al*. combined VSI and AFM data with geochemical modelling to elucidate the dissolution mechanisms of CaF_2 in acidic solutions[73]. The study found dissolution in undersaturated solutions, with large Gibbs free energies, was dominated by the growth and deepening of trigonal etch pits. Conversely, in oversaturated solutions, with lower Gibbs free energies, dissolution predominantly proceeded through step-wave emanation from the pit walls, resulting in overall surface retreat.

The application of profilometry to examine candidate nuclear fuels and wasteforms for radioactive waste is less common, however, there do exist a collection of several studies that

deploy the unique ability of profiling techniques to elucidate dissolution behaviour and reveal the reactivity of specific microstructural features in nuclear ceramics. *In-situ* VSI measurements were obtained by Fischer *et al*., in their quantification of the surface dissolution of pyrochlore ($Nd_2Zr_2O_7$) in 4 M HCl at 90 °C[74]. The study concluded that pyrochlores, like any polycrystalline material, show heterogeneous surface dissolution. Material flux maps, shown in Figure 11, revealed that the morphology of pores exhibited a strong control over localised dissolution rates. The high FOV provided by VSI allowed a large number of pores to be studied, ensuring a representative area of the sample was observed.

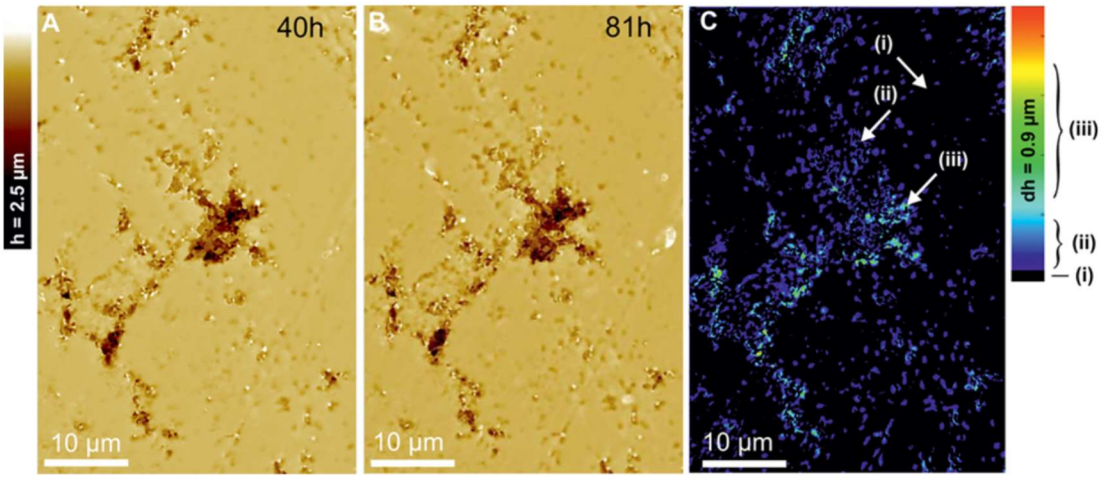

Figure 11: Material flux map illustrating heterogeneous dissolution of pores on the surface of a pyrochlore ($Nd_2Zr_2O_7$) pellet during dissolution in HCl – Fischer *et al.* (2015) [74].

Corkhill *et al.* utilised the high resolution of AFM to precisely quantify the retreat rates of CeO_2 grain boundaries with high and low misorientation angles[64]. Pellets were submerged in 0.01 M HNO_3 at 90 °C for 7 days; *in-situ* AFM measurements were carried out after 0, 1 and 7 days. The study found a positive correlation between the misorientation angle and dissolution rate of grain boundaries; this behaviour was attributed to the increased concentration of crystalline defects within these disordered interfaces.

Surface profilometry techniques are powerful and versatile tools capable of providing uniquely nuanced insight into spatially heterogenous dissolution behaviour, such as the preferential grain boundary dissolution of Synroc observed by Lumpkin *et al.*[75]. The material flux maps yielded from these methods are also especially useful for analysing multiphase materials, where distinct dissolution rate contributions from each phase would otherwise be convoluted in a single bulk rate using conventional techniques. Quantifying the evolving roles of specific phases and microstructural features during dissolution could prove pivotal in understanding the long-term degradation of a material.

References

1. He, H. & Shoesmith, D. Raman spectroscopic studies of defect structures and phase transition in hyper-stoichiometric UO_{2+x}. *Phys. Chem. Chem. Phys.* **12**, 8108 (2010).
2. Cooper, M. W. D., Murphy, S. T. & Andersson, D. A. The defect chemistry of $UO_{2\pm x}$ from atomistic simulations. *Journal of Nuclear Materials* **504**, 251–260 (2018).
3. Razdan, M. & Shoesmith, D. W. Influence of Trivalent-Dopants on the Structural and Electrochemical Properties of Uranium Dioxide (UO_2). *J. Electrochem. Soc.* **161**, H105–H113 (2014).
4. Elorrieta, J. M., Bonales, L. J., Rodríguez-Villagra, N., Baonza, V. G. & Cobos, J. A detailed Raman and X-ray study of UO_{2+x} oxides and related structure transitions. *Phys. Chem. Chem. Phys.* **18**, 28209–28216 (2016).
5. Grønvold, F. High-temperature X-ray study of uranium oxides in the UO_2 - U_3O_8 region. *Journal of Inorganic and Nuclear Chemistry* **1**, 357–370 (1955).
6. Teske, K., Ullmann, H. & Rettig, D. Investigation of the oxygen activity of oxide fuels and fuel-fission product systems by solid electrolyte techniques. Part I: Qualification and limitations of the method. *Journal of Nuclear Materials* **116**, 260–266 (1983).
7. Kapshukov, I. I., Lyalyushkin, N. V., Sudakov, V., Bevz, A. S. & Skiba, V. PREPARATION OF HYPOSTOICHIOMETRIC UO_{2-x} AT LOW TEMPERATURES AND STUDY OF SOME PROPERTIES.
8. Harrison, R. W. *et al.* Spark plasma sintering of $(U,Ce)O_2$ as a MOx nuclear fuel surrogate. *Journal of Nuclear Materials* **557**, 153302 (2021).
9. Böhler, R. *et al.* Recent advances in the study of the UO_2 – PuO_2 phase diagram at high temperatures. *Journal of Nuclear Materials* **448**, 330–339 (2014).
10. Lyon, W. L. & Baily, W. E. The solid-liquid phase diagram for the UO_2 - PuO_2 system. *Journal of Nuclear Materials* **22**, 332–339 (1967).
11. Kato, M. *et al.* Oxygen chemical diffusion in hypo-stoichiometric MOX. *Journal of Nuclear Materials* **389**, 416–419 (2009).

12. Markin, T. L. & Street, R. S. The uranium-plutonium-oxygen ternary phase diagram. *Journal of Inorganic and Nuclear Chemistry* **29**, 2265–2280 (1967).
13. Stennett, M. C., Corkhill, C. L., Marshall, L. A. & Hyatt, N. C. Preparation, characterisation and dissolution of a CeO_2 analogue for UO_2 nuclear fuel. *Journal of Nuclear Materials* **432**, 182–188 (2013).
14. Lucuta, P. G., Verrall, R. A., Matzke, Hj. & Palmer, B. J. Microstructural features of SIMFUEL — Simulated high-burnup UO_2-based nuclear fuel. *Journal of Nuclear Materials* **178**, 48–60 (1991).
15. Chevrel, H., Dehaudt, P., Francois, B. & Baumard, J. F. Influence of surface phenomena during sintering of overstoichiometric uranium dioxide UO_{2+x}. *Journal of Nuclear Materials* **189**, 175–182 (1992).
16. Hiezl, Z., Hambley, D. I., Padovani, C. & Lee, W. E. Processing and microstructural characterisation of a UO2-based ceramic for disposal studies on spent AGR fuel. *Journal of Nuclear Materials* **456**, 74–84 (2015).
17. Haas, D., Somers, J., Charollais, F., Fuchs, C. & Fourcaudot, S. FABRICATION AND CHARACTERIZATION OF MOX FUELS WITH HIGH PLUTONIUM CONTENT USING ALTERNATIVE PROCESSES. 8.
18. Oudinet, G. *et al.* Characterization of plutonium distribution in MIMAS MOX by image analysis. *Journal of Nuclear Materials* **375**, 86–94 (2008).
19. Portelette, L., Vincent, P.-G., Moulinec, H. & Gărăjeu, M. Viscoplastic behavior of a porous polycrystal with similar pore and grain sizes: Application to nuclear MOX fuel materials. *International Journal of Solids and Structures* **236–237**, 111316 (2022).
20. Blackburn, L. R. *et al.* Hot Isostatically Pressed Zirconolite Wasteforms for Actinide Immobilisation. *IOP Conf. Ser.: Mater. Sci. Eng.* **818**, 012010 (2020).
21. Schmitt, R. *et al.* A review of defect structure and chemistry in ceria and its solid solutions. *Chem. Soc. Rev.* **49**, 554–592 (2020).

22. Dixon Wilkins, M. C., Maddrell, E. R., Stennett, M. C. & Hyatt, N. C. The Effect of Temperature on the Stability and Cerium Oxidation State of $CeTi_2O_6$ in Inert and Oxidizing Atmospheres. *Inorg. Chem.* **59**, 17364–17373 (2020).
23. Chueh, W. C. *et al.* Highly Enhanced Concentration and Stability of Reactive Ce^{3+} on Doped CeO_2 Surface Revealed In Operando. *Chem. Mater.* **24**, 1876–1882 (2012).
24. Loche, D. *et al.* Determining the maximum lanthanum incorporation in the fluorite structure of La-doped ceria nanocubes for enhanced redox ability. *RSC Adv.* **9**, 6745–6751 (2019).
25. Lee, J. *et al.* Raman study on structure of $U_{1-y}Gd_yO_{2-x}$ (y=0.005, 0.01, 0.03, 0.05 and 0.1) solid solutions. *Journal of Nuclear Materials* **486**, 216–221 (2017).
26. Jadhav, L. D., Pawar, S. H. & Chourashiya, M. G. Effect of sintering temperature on structural and electrical properties of gadolinium doped ceria ($Ce_{0.9}Gd_{0.1}O_{1.95}$). *Bull Mater Sci* **30**, 97–100 (2007).
27. M., B. S. & Roy, J. The effect of strontium doping on densification and electrical properties of $Ce_{0.8}Gd_{0.2}O_{2-\delta}$ electrolyte for IT-SOFC application. *Ionics* **18**, 291–297 (2012).
28. Horlait, D. *et al.* Stability and Structural Evolution of $Ce^{IV}_{1-x}Ln^{III}_xO_{2-x/2}$ Solid Solutions: A Coupled μ-Raman/XRD Approach. *Inorg. Chem.* **50**, 7150–7161 (2011).
29. Shannon, R. D. Revised effective ionic radii and systematic studies of interatomic distances in halides and chalcogenides. *Acta Cryst A* **32**, 751–767 (1976).
30. Rao, R., Bhagat, R. K., Salke, N. P. & Kumar, A. Raman Spectroscopic Investigation of Thorium Dioxide–Uranium Dioxide (ThO_2 – UO_2) Fuel Materials. *Appl Spectrosc* **68**, 44–48 (2014).
31. Bès, R. *et al.* Charge compensation mechanisms in $U_{1-x}Gd_xO_2$ and $Th_{1-x}Gd_xO_{2-x/2}$ studied by X-ray Absorption Spectroscopy. *Journal of Nuclear Materials* **489**, 9–21 (2017).
32. Liu, N. *et al.* Influence of Gd Doping on the Structure and Electrochemical Behavior of UO_2. *Electrochimica Acta* **247**, 496–504 (2017).
33. Van Mao, P., Arima, T., Inagaki, Y. & Idemitsu, K. Evaluation of Structural and Thermal Properties of $Ce_{1-y}Gd_yO_{2-x}$ Solid Solution. *Int J Thermophys* **41**, 111 (2020).

34. He, H., Keech, P. G., Broczkowski, M. E., Noël, J. J. & Shoesmith, D. W. Characterization of the influence of fission product doping on the anodic reactivity of uranium dioxide. *Can. J. Chem.* **85**, 702–713 (2007).

35. Prieur, D. *et al.* Aliovalent Cation Substitution in UO_2 : Electronic and Local Structures of $U_{1-y}La_yO_{2\pm x}$ Solid Solutions. *Inorg. Chem.* **57**, 1535–1544 (2018).

36. Artini, C., Pani, M., Lausi, A., Masini, R. & Costa, G. A. High Temperature Structural Study of Gd-Doped Ceria by Synchrotron X-ray Diffraction (673 K ≤ *T* ≤ 1073 K). *Inorg. Chem.* **53**, 10140–10149 (2014).

37. Ye, F., Ou, D. R. & Mori, T. Microstructural Evolution in a CeO_2 -Gd_2O_3 System. *Microsc Microanal* **18**, 162–170 (2012).

38. Wang, B., Lewis, R. J. & Cormack, A. N. Computer simulations of large-scale defect clustering and nanodomain structure in gadolinia-doped ceria. *Acta Materialia* **59**, 2035–2045 (2011).

39. Ikuma, Y., Shimada, E. & Okamura, N. Effect of Nd_2O_3 Concentration on the Defect Structure of CeO_2-Nd_2O_3 Solid Solution. *J American Ceramic Society* **88**, 419–423 (2005).

40. Hagiwara, T., Kyo, Z., Manabe, A., Yamamura, H. & Nomura, K. Formation of C-type rare earth structures in the $Ce_{1-x}Nd_xO_{2-\delta}$ system: a factor in the decrease in oxide-ion conductivity. *Journal of the Ceramic Society of Japan* (2009).

41. Jiang, S. *et al.* Anomalous compression behaviour in Nd_2O_3 studied by x-ray diffraction and Raman spectroscopy. *AIP Advances* **8**, 025019 (2018).

42. Nitani, H. *et al.* XAFS and XRD study of ceria doped with Pr, Nd or Sm. *Materials Letters* **58**, 2076–2081 (2004).

43. Durazzo, M., Oliveira, F. B. V., Urano de Carvalho, E. F. & Riella, H. G. Phase studies in the UO_2 – Gd_2O_3 system. *Journal of Nuclear Materials* **400**, 183–188 (2010).

44. Nandi, C. *et al.* Structural and thermal expansion studies in ternary $ThO_2 - CeO_2 - NdO_{1.5}$ system: Mimicking actinide substituted ThO_2. *Journal of Nuclear Materials* **520**, 226–234 (2019).

45. Bartram, S. F., Juenke, E. F. & Aitken, E. A. Phase Relations in the System UO_2 - UO_3 - Y_2O_3. *J American Ceramic Society* **47**, 171–175 (1964).

46. Iwasaki, K. *et al.* Effect of Gd_2O_3 Dispersion on the Thermal Conductivity of UO_2. *Journal of Nuclear Science and Technology* **46**, 673–676 (2009).

47. Hong, M. *et al.* The role of charge and ionic radius on fission product segregation to a model UO_2 grain boundary. *Journal of Applied Physics* **113**, 134902 (2013).

48. Arora, G. & Aidhy, D. S. Segregation and binding energetics at grain boundaries in fluorite oxides. *J. Mater. Chem. A* **5**, 4026–4035 (2017).

49. Gerhardt-Anderson, R. & Nowick, A. S. Ionic conductivity of CeO_2 with trivalent dopants of different ionic radii. *Solid State Ionics* **5**, 547–550 (1981).

50. Scavini, M. *et al.* Percolating hierarchical defect structures drive phase transformation in $Ce_{1-x}Gd_xO_{2-x/2}$: a total scattering study. *IUCrJ* **2**, 511–522 (2015).

51. Ye, F. *et al.* Compositional and structural characteristics of nano-sized domains in gadolinium-doped ceria. *Solid State Ionics* **179**, 827–831 (2008).

52. Li, Z.-P., Mori, T., Auchterlonie, G. J., Zou, J. & Drennan, J. Direct evidence of dopant segregation in Gd-doped ceria. *Appl. Phys. Lett.* **98**, 093104 (2011).

53. Yan, P. *et al.* Microstructural and Chemical Characterization of Ordered Structure in Yttrium Doped Ceria. *Microsc Microanal* **19**, 102–110 (2013).

54. Chen, P.-L. & Chen, I.-W. Role of Defect Interaction in Boundary Mobility and Cation Diffusivity of CeO_2. *J American Ceramic Society* **77**, 2289–2297 (1994).

55. Chen, P.-L. & Chen, I.-W. Grain Growth in CeO_2: Dopant Effects, Defect Mechanism, and Solute Drag. *J American Ceramic Society* **79**, 1793–1800 (1996).

56. Cherkaski, Y., Clavier, N., Brissonneau, L., Podor, R. & Dacheux, N. Densification behavior and microstructure evolution of yttrium-doped ThO_2 ceramics. *Journal of the European Ceramic Society* **37**, 3381–3391 (2017).

57. Bruno, J. & Ewing, R. C. Spent Nuclear Fuel. *Elements* **2**, 343–349 (2006).

58. Barker, M. A. *et al.* Observations of high burnup structure in AGR fuel. *Progress in Nuclear Energy* **153**, 104433 (2022).

59. Wu, L., Qin, Z. & Shoesmith, D. W. An improved model for the corrosion of used nuclear fuel inside a failed waste container under permanent disposal conditions. *Corrosion Science* **84**, 85–95 (2014).

60. H. He, M. Broczkowski, K. O'Neil, D. Ofori, O. Semenikhin & D. W. Shoesmith. NWMO TR-2012-09 Toronto. *Nuclear Waste Management Organization* (2012).

61. Kerleguer, V. *et al.* The mechanisms of alteration of a homogeneous $U_{0.73}Pu_{0.27}O_2$ MOx fuel under alpha radiolysis of water. *Journal of Nuclear Materials* **529**, 151920 (2020).

62. Inoue, A. Mechanism of the oxidative dissolution of UO_2 in HNO_3 solution. *Journal of Nuclear Materials* **138**, 152–154 (1986).

63. Horlait, D., Tocino, F., Clavier, N., Dacheux, N. & Szenknect, S. Multiparametric study of $Th_{1-x}Ln_xO_{2-x/2}$ mixed oxides dissolution in nitric acid media. *Journal of Nuclear Materials* **429**, 237–244 (2012).

64. Corkhill, C. L. *et al.* Contribution of Energetically Reactive Surface Features to the Dissolution of CeO_2 and ThO_2 Analogues for Spent Nuclear Fuel Microstructures. *ACS Appl. Mater. Interfaces* **6**, 12279–12289 (2014).

65. Horlait, D., Clavier, N., Szenknect, S., Dacheux, N. & Dubois, V. Dissolution of Cerium(IV)–Lanthanide(III) Oxides: Comparative Effect of Chemical Composition, Temperature, and Acidity. *Inorg. Chem.* **51**, 3868–3878 (2012).

66. Godinho, J. R. A., Piazolo, S. & Evins, L. Z. Effect of surface orientation on dissolution rates and topography of CaF_2. *Geochimica et Cosmochimica Acta* **86**, 392–403 (2012).

67. Godinho, J. R. A., Putnis, C. V. & Piazolo, S. Direct Observations of the Dissolution of Fluorite Surfaces with Different Orientations. *Crystal Growth & Design* **14**, 69–77 (2014).

68. Horlait, D. *et al.* Environmental SEM monitoring of $Ce_{1-x}Ln_xO_{2-x/2}$ mixed-oxide microstructural evolution during dissolution. *J. Mater. Chem. A* **2**, 5193–5203 (2014).

69. Corkhill, C. L. *et al.* Role of Microstructure and Surface Defects on the Dissolution Kinetics of CeO_2 , a UO_2 Fuel Analogue. *ACS Appl. Mater. Interfaces* **8**, 10562–10571 (2016).

70. Luttge, A., Arvidson, R. S. & Fischer, C. A Stochastic Treatment of Crystal Dissolution Kinetics. *Elements* **9**, 183–188 (2013).

71. Kumar, A., Reed, J. & Sant, G. Vertical Scanning Interferometry: A New Method to Measure the Dissolution Dynamics of Cementitious Minerals. *J. Am. Ceram. Soc.* **96**, 2766–2778 (2013).
72. Luettge, A. An interferometric study of the dissolution kinetics of anorthite; the role of reactive surface area. *American Journal of Science* **299**, 652–678 (1999).
73. Cama, J. *et al.* Fluorite dissolution at acidic pH: In situ AFM and ex situ VSI experiments and Monte Carlo simulations. *Geochimica et Cosmochimica Acta* **74**, 4298–4311 (2010).
74. Fischer, C., Finkeldei, S., Brandt, F., Bosbach, D. & Luttge, A. Direct Measurement of Surface Dissolution Rates in Potential Nuclear Waste Forms: The Example of Pyrochlore. *ACS Appl. Mater. Interfaces* **7**, 17857–17865 (2015).
75. Lumpkin, G. R., Smith, K. L. & Blackford, M. G. Development of Secondary Phases on Synroc Leached at 150˚C. *MRS Proc.* **353**, 855 (1994).

3. Experimental methodology

3.1 Materials synthesis

3.1.1 Wet synthesis

Metal oxide precursors used to produce pellets of sintered ceramic were synthesised through two main routes. The first of these routes, wet synthesis, was used to produce the majority of samples presented in this work through the process of oxalic co-precipitation. Salt solutions corresponding to the desired composition of the sample were mixed in the presence of oxalic acid, resulting in spontaneous co-precipitation of a mixed oxalate powder[1]. Oxalate precipitates were vacuum filtered from the excess oxalic acid and dried. Oxalate powders were decomposed into oxides via calcination in a furnace. Comprehensive methodologies for the synthesis of specific compositions are detailed in relevant papers contained within Chapters 5 and 6.

3.1.2 Solid state synthesis

Oxide precursors were also prepared using conventional solid state synthesis. Solid state synthesis involved drying, batching, and milling appropriate masses of oxide reagents for a target composition, as determined by batch calculations. Milling was performed with a Retsch PM100 planetary mill using yttria-stabilised zirconia mill pots filled with zirconia milling media and IPA, which acted as a carrier fluid. Specific details on solid state synthesis parameters are detailed in the paper featured in Chapter 6.

3.1.3 Cold pressing and sintering

Oxide powders were compacted into a die under a uniaxial load, consolidating them into green bodies in a process known as cold pressing. Compaction during cold pressing occurs through rearrangement, fragmentation, and deformation of the oxide powders. Consolidated green bodies were then sintered to encourage grain grown, phase formation and improved mechanical integrity. Sintering of ceramics is achieved though heating to high temperatures below the melting point of the material. At elevated temperatures, necks are formed between adjacent particles of oxide through atomic diffusion; this diffusion is driven by the difference in energy between two exposed grain surfaces and a grain boundary[2]. As more of these necks form, the spaces between the grains grow smaller and more spherical, eventually forming pores. The sintering process is illustrated in Figure 1.

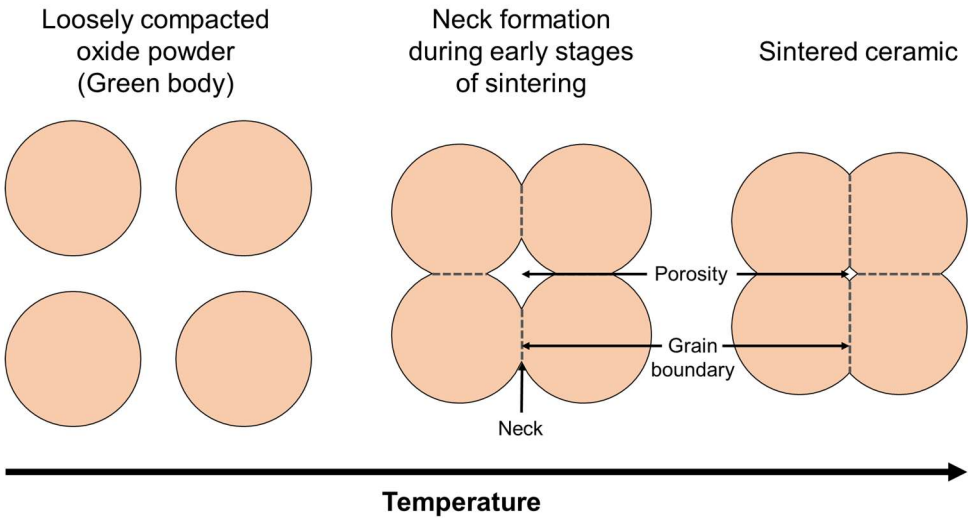

Figure 1: Schematic illustration of processes involved in ceramic sintering.

Pellets produced for this work were sintered at 1700 °C in air or under the constant flow of reducing 5% H_2/N_2 gas, depending on the oxidation behaviour of the sample. An Elite 1800 °C Elevator Hearth Furnace was used for sintering in air, whilst an Elite 1800 °C alumina tube furnace was used for sintering under H_2/N_2. Samples were positioned in the centre of the tube, which was purged for several hours to remove air prior to heating. Pellets were sintered within zirconia crucibles; these were fitted with lids to avoid contamination from within the furnace. Further details on sintering heat treatments can be found in the papers featured in Chapters 4 and 5.

3.1.4 Polishing procedure for sintered pellets

Grinding and polishing is an essential step in the preparation of sintered pellets for various forms of microscopy and dissolution testing. The following general procedure was followed for the polishing of samples to 1 µm. Deviations from this procedure necessary for specific techniques are detailed where relevant. Sintered pellets were ground and polished using a Buehler EcoMet 250 Grinder-Polisher. This process involved firstly mounting pellets individually to 32 mm Al stubs using CrystalBond adhesive. The first side of each pellet was ground using P2500 (~8.4 µm) SiC grinding papers for 30 seconds at complimentary head and platen speeds of 30 and 51 rpm respectively. A force of 5 N was applied to each pellet during grinding, and a constant stream of water acted as a coolant and lubricant[3]. The same grinding step was then repeated for the reverse of the pellet, resulting in a flat parallel sample. After careful rinsing to remove residual SiC polishing media, the pellets were then polished to 6 µm using diamond suspension dispersed on a Buehler TexMet C pressed cloth pad for ~45 minutes, or until scratches were no longer visible under a visible light microscope. During polishing, the applied force was increased to 10 N, whilst platen speed was increased to

111 rpm. The subsequent 3 and 1 μm polishing steps employed the same parameters. Thirty minutes was spent polishing to 3 μm, whilst 60 minutes was used on the final polishing step to 1 μm. Care was taken to clean samples, mounts, and the platen before each additional polishing step, thus avoiding issues with contamination of residual polishing media.

3.2 Materials characterisation

3.2.1 X-ray diffraction

X-ray diffraction (XRD) is a fundamental technique for characterisation of crystalline materials capable of investigating crystal structure, lattice parameter, crystallite size, secondary phase formation and even elastic strain. X-ray diffraction reveals structural information by utilising Bragg's law, shown in Equation 1:

$$n\lambda = 2d\ \sin\theta$$

Equation 1: Bragg's law, where n is an integer, λ is the X-ray wavelength, d_{hkl} is the interatomic spacing between crystal layers and θ is the incident angle.

This expression relates the X-ray wavelength to the interatomic spacing using the angle of the diffracted X-ray beam. X-rays, with a wavelength similar to atomic spacings in solids, are fired at a polycrystalline specimen. The X-ray beam interacts with a periodic array of atoms, causing it to diffract. At a certain angle of incidence, two diffracted X-rays will constructively interfere, this occurs when the incident angle θ is such that the path difference between the X-rays is equal to the interatomic, or lattice, spacing. The value of the angle θ allows the lattice spacing d to be calculated, provided the wavelength of the X-ray beam is known. This principle is demonstrated in Figure 2.

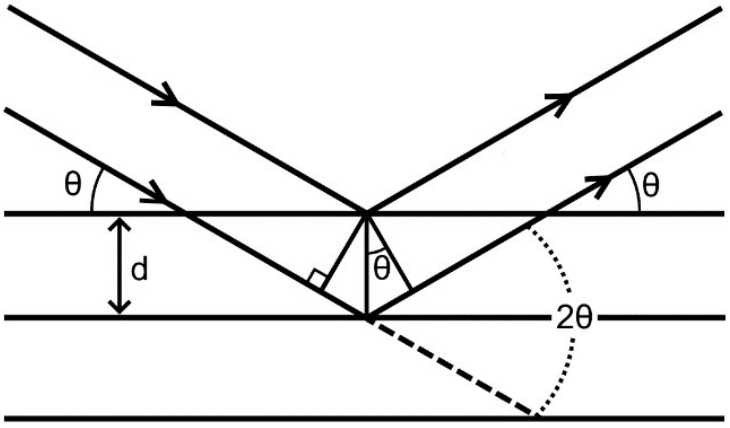

Figure 2: Schematic illustrating the Bragg condition for X-ray diffraction in crystalline solids.

XRD traces feature sharp peaks in measured intensity of diffracted X-rays at angles satisfying the Bragg condition; these diffraction peaks are often referred to as reflections. At angles that fail to satisfy the Bragg condition, destructive interference prevents the detection of diffracted X-rays. The interatomic spacing within the crystal lattice varies depending on its orientation, meaning that plots of diffracted X-ray intensity against twice the incident angle (*2θ*) reveal a series of reflections characteristic of the crystal lattice of a specimen. Each of these reflections represents an individual crystallographic plane that exists within that particular crystal structure. These planes, which are described using Miller indices (e.g. (1 1 1)), represent directions of regular atomic stacking that exist within a crystal lattice. The greater the density of atoms aligned on a single plane, the more strongly it will diffract the X-ray beam, resulting in greater measured intensity on the XRD trace. Example XRD traces collected on samples of cubic fluorite (Fm-3m) La-doped CeO_2 are presented in Figure 3. Note the (1 1 1) plane is responsible for the most intense peak, as Ce^{4+} cations are stacked most densely in this direction.

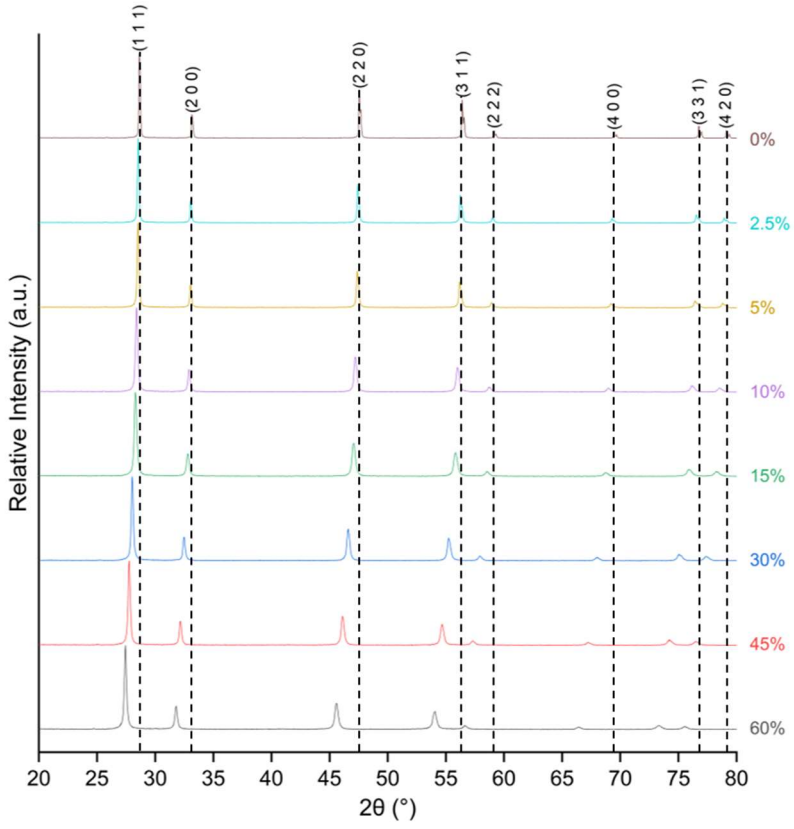

Figure 3: Stacked plot of XRD traces collected on samples of fluorite $Ce_{1-x}La_xO_{2-\delta}$, where $0.00 \leq x \leq 0.60$.

In Figure 3, dotted lines indicate the position of each fluorite peak in pure CeO_2. Reflections are shifted to lower values of *2θ* in more highly doped samples, indicating plane expansion due to the incorporation of the larger La^{3+} dopant ion. Resources such as the Crystallographic Open Database (COD) and Powder Diffraction File (PDF-4$^+$) database provide information

about expected position and intensity of peaks across a vast collection of crystalline materials. Peak markers accessed from these databases were used to aid with phase identification and measurement of peak shift.

XRD analysis presented in this work was collected using a Bruker D2 diffractometer with CuKα (λ = 1.5418 Å) X-rays, generated using 30 mA and 10 mV. The step size used was 0.02° and the *2θ* range was 20 – 80°. XRD sample preparation for analysis precursor powders such as oxalates and calcined oxides involved placing powders into a 3 or 10 mm zero-background PMMA holder and using a glass slide to level off surface roughness. Sintered pellets were mounted into a 10 mm deep PPMA holder using adhesive putty. Sintered powder XRD samples were prepared by crushing pellets into fine powders using a pestle and mortar. In select samples, 10 wt% LaB_6 was added as an internal standard to improve the quality of Rietveld refinements.

3.2.2 Rietveld refinements

Powder XRD data can be analysed through refinement using the Rietveld method. The Rietveld method involves fitting a least squares crystallographic model to experimental XRD traces. This model uses the relative positions, heights and widths of reflections to calculate structural parameters of the material, such as the lattice parameter[4]. The quality of Rietveld fits is most commonly described by the weight profile residual (R_{wp}), shown in Equation 2.

$$R_{wp} = \sum_{i}^{n} \sqrt{\frac{w_i\left(Y_i^{obs} - Y_i^{calc}\right)^2}{\sum_i^n w_i\left(Y_i^{obs}\right)^2}} \times 100$$

Equation 2: Calculation of weight profile residual (R_{wp}).

The least mean squares approach is used to minimise the weighted sum, *w*, of the computed diffraction pattern, $y_{i,}calc$, and the observed diffraction pattern, $y_{i,}obs$. Smaller values of R_{wp} therefore indicate more accurate fits of the computed crystallographic model to the experimental data.

Rietveld refinements of sintered materials were performed using Bruker's Topas software package. Structural information used to generate computed diffraction patterns was provided by the appropriate Crystallographic Information File (CIF). CIF files were produced and edited using the CrystalMaker software.

3.2.3 Geometric density measurements

The density of a material is a measure of its mass per unit volume. Geometric density measurements are obtained by measuring the mass of a sample with a balance, before

measuring its physical dimensions using digital callipers. In the case on sintered pellets, the geometry can be assumed to be cylindrical, allowing volume to be easily estimated.

3.2.4 Archimedes density measurements

Archimedes density measurements can determine the density of monolithic samples by exploiting the Archimedes principle, outlined in Equation 3.

$$\frac{\rho_{object}}{\rho_{fluid}} = \frac{Weight}{Weight\ of\ displaced\ fluid}$$

Equation 3: Calculation of density *via* the Archimedes principle, where ρ_{object} is the density of the sample and ρ_{fluid} is the density of ethanol at the measured ambient temperature.

Archimedes measurements involve firstly weighing a sample in air before immersing the sample in a fluid of known density, such as ethanol or water, and weighing a second time. All Archimedes density measurements presented in this work were made using a METTLER TOLEDO ME204 Archimedes balance. A minimum of 10 measurements were used to calculate average densities for sintered pellets. Quoted errors are the standard deviations of these measurements.

3.2.5 Gas pycnometry

Gas pycnometry is another technique used to determine the density of a material. Gas pycnometry operates by filling two chambers of known volume with helium gas. One chamber is loaded with the sample, whilst the other remains empty as a reference. Measuring the deviation in pressures as both chambers are filled with helium allows for determination of the sample volume contained within the first chamber. The density of the material can then be calculated simply by dividing its mass, as measured with a balance, by this determined volume. Gas pycnometry has the advantage over Archimedes density measurements of being capable of measuring both monolithic and powder samples. A Micromeritics AccuPyc II gas pycnometer was used collect all the gas pycnometry presented in this work. A 1 cm^3 chamber was purged and filled for a minimum of 10 cycles, using an equilibration rate of 101.4 kPa min^{-1} at 21 °C. Presented densities and their corresponding errors were calculated using the mean and standard deviation of these measured volumes.

3.2.6 Relative density calculations

The relative density of a specimen can be calculated by dividing its experimentally measured density by its theoretical density. Relative densities are typically expressed as percentages, with 100% representing a sample that achieved maximum theoretical density. Relative density provides a convenient metric for comparing the sintering behaviour of samples without

consideration of theoretical densities. Theoretical densities in this work were calculated using measurements of sample composition and lattice parameter.

3.2.7 Thermo-gravimetric analysis

Thermo-gravimetric analysis (TGA) measures the change in the mass of a powder sample as it is heated. Mass losses generally occur as gases, such as H_2O and CO_2, are released[5]. TGA is capable of accurately measuring these mass losses, and the temperatures at which they occur. Coupling TGA analysis with differential thermal analysis (DTA) allows exothermic and endothermic thermal events to be distinguished. TGA is also complimented by concurrent mass spectrometry (MS) measurement, which enables the identification of the gases released through their mass to charge ratio. TGA presented in this work was collected using a Netzch TG 449 F3 Jupiter simultaneous thermal analyser. Samples were heated from ambient temperatures to 1000 °C at a rate of 10 °C min^{-1} under an Ar atmosphere. Further experimental parameters are listed in the paper featured in Chapter 6.

3.2.8 Raman spectroscopy

Raman spectroscopy is a powerful technique in the analysis of crystalline materials, capable of investigating bonding, defects, and lattice distortion. This is achieved through measurement of the frequency and intensity of characteristic Raman scattering modes[6]. Raman spectroscopy involves firstly directing monochromatic light, typically a laser, towards a specimen. The interaction between the laser and specimen surface scatters photons within the beam in various ways. Elastic scattering results in the emission of photons with wavelength equal to the incident light ($\hbar\omega_0 = \hbar\omega_0$; where $\hbar$ is the reduced Planck's constant and ω is the angular frequency). This elastic response is known as Rayleigh scattering. Raman scattering, however, arises from inelastic scattering of a photon by the oscillation of a crystal lattice, or phonon. This inelastic response causes a shift in the frequency of the emitted photon which is equal to the phonon frequency. Raman scattering results in either the emission of photons with lower frequency, known as Stokes scattering ($\hbar\omega_0 > \hbar\omega_0 - \hbar\omega_{vib}$; where $\hbar\omega_{vib}$ is the phonon energy), or emission of photons with greater frequency, known as anti-Stokes scattering ($\hbar\omega_0 < \hbar\omega_0 + \hbar\omega_{vib}$)[7], as illustrated in Figure 4.

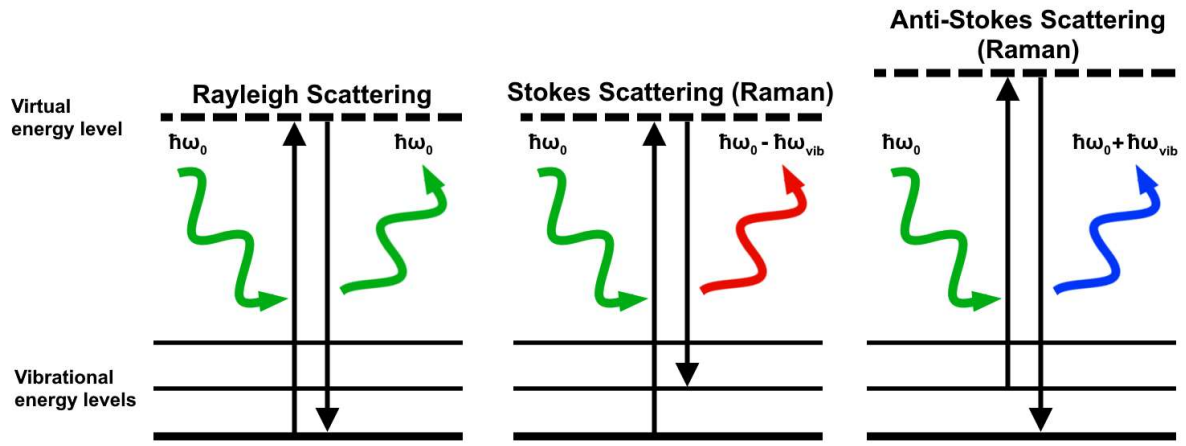

Figure 4: Schematic illustration of energy levels associated with Rayleigh, Stokes, and anti-Stokes scattering. Adapted from Schmitt (2020)[8].

As the vast majority of scattering resulting from the interaction between monochromatic light and the material is elastic (Rayleigh scattering), filtering out photons with equal wavelength to the laser is essential for examination of the comparatively weak Raman response. Measurement of the relative intensity of inelastic Raman scattering at different frequencies permits investigation into bonding, lattice distortion, and crystalline point defects in ceramic materials. Raman is an especially useful technique for probing defect chemistry and oxygen stoichiometry in these ceramics due to its sensitivity to non-periodic features[8], presenting a considerable advantage over techniques such as XRD.

Raman spectroscopy performed in this thesis was conducted on polished and annealed pellets of sintered ceramics using a Renishaw inVia microscope equipped with a 514 nm laser. Deconvolution of the spectra was performed using the Igor Pro software. Further details on observation conditions and convolutions are listed in relevant papers found in Chapters 5 and 6.

3.2.9 Scanning electron microscopy — energy dispersive X-ray spectroscopy

Scanning electron microscopy (SEM) is a fundamental technique in materials characterisation. SEM produces images, or micrographs, of a specimen by rastering a focussed electron beam across its surface. The various interactions of the electron beam with the specimen provide signals revealing information about its topography and composition. The region of the specimen surface in contact with the electron beam at one time is known as the interaction volume. Interaction volumes are dependent on the accelerating voltage of the beam, spot size (aperture selection), and specimen composition. Different types of SEM detectors are sensitive to electrons emitted from different regions of the interaction volume, as outlined in Figure 5.

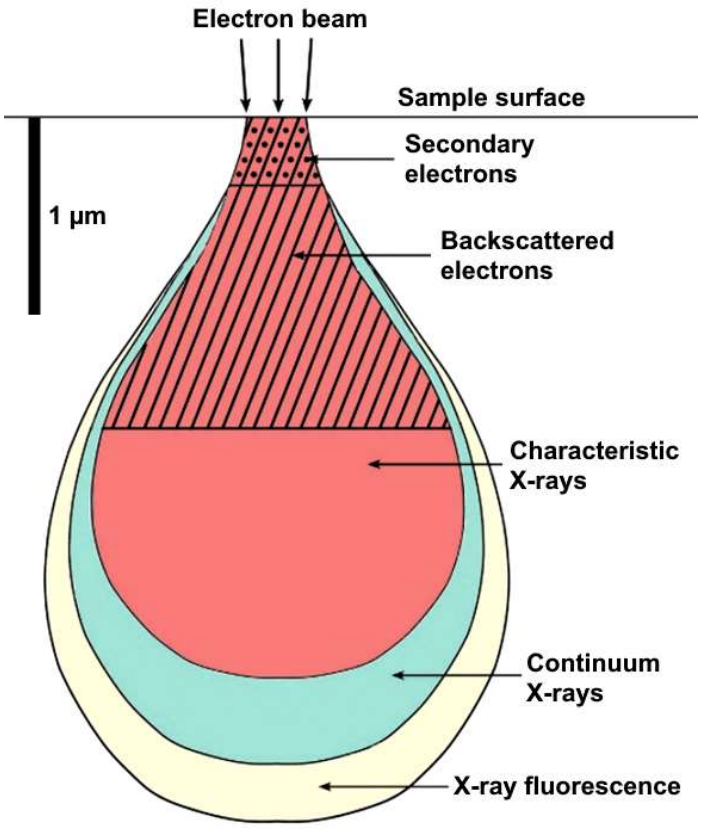

Figure 5: Schematic illustrating various zones of electron and X-ray emission within interaction volume between electron beam and specimen surface. Adapted from Heath (2016)[9].

The two most common forms of SEM detectors are secondary electron (SE) and back-scattered electron (BSE) detectors. SE detectors are sensitive to low-energy (< 50 eV) electrons ejected from the conduction or valence bands of atoms though inelastic scattering interactions with the electron beam. Secondary electrons are generated throughout the entire interaction volume however, those emitted at depths > 10 nm are generally reintegrated into the material. This reintegration means the vast majority of measured SEs are ejected from the top 10 nm of the surface. The surface sensitivity of SE imaging results in high-resolution images that reveal the surface topography of a specimen. Contrast in SE images is determined by the measured intensity of ejected electrons. As previously established, secondary electrons are readily absorbed and reintegrated within the material; meaning surface features with greater exposed areas will appear brighter on SE micrographs. High surface area regions, such as pore edges, provide more paths for secondary electron release and fewer paths leading to reintegration; this phenomenon, termed the edge effect, is illustrated in Figure 6.

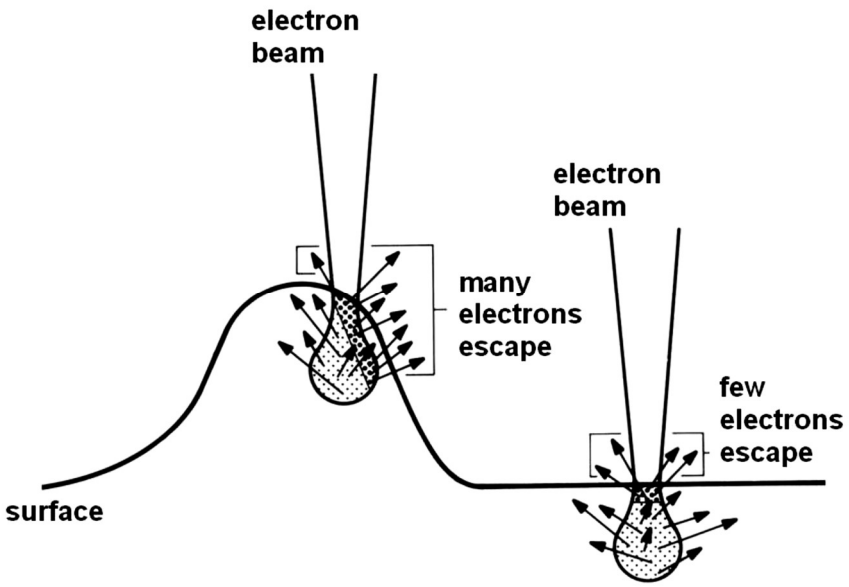

Figure 6: Schematic diagram illustrating the origin of the edge effect in SE images, whereby increased surface area facilitates the release of greater number of secondary electrons, resulting in increased brightness within regions with sharper, exposed features. Krumeich (2022)[10].

Backscattered electron (BSE) detectors are instead sensitive to electrons that have been backscattered by the columbic repulsion of the positively charged nuclei within the specimen surface. Contrast in BSE images typically corresponds to compositional differences between different phases arising from the variation of atom mass, Z. Heavier elements with large nuclei and high Z exert greater columbic repulsion on the electron beam, resulting in a more intense backscattered response, manifested as brighter contrast. Dark contrast by extension indicates the presence of lighter elements with smaller nuclei, which scatter fewer electrons for detection. Contrast in BSE images of crystalline materials can also be influenced by grain orientation, as the intensity of Bragg scattering varies between different exposed crystallographic planes. Backscattered electrons can be detected from a much larger probing depth compared to secondary electrons, as shown previously in Figure 5. In BSE imaging, electrons scattered several μm beneath the specimen surface can be detected; this larger interaction volume renders BSE less useful for examining surface topography, as its spatial resolution is far lower compared to SE.

Energy dispersive X-ray spectroscopy (EDS) is a powerful technique often coupled with SEM for elemental analysis of materials. EDS exploits the principle that each element has a unique atomic structure which gives rise to a unique electromagnetic emission spectrum. The electron beam incident on a specimen excites and ejects an electron, leaving an electron hole on the inner shell. In response to this, an electron from a higher energy shell will drop to the inner shell to fill the hole. As it does so, this electron releases energy in the form of an X-ray. The

energy of this X-ray is characteristic of the difference in energy between the two shells, and therefore characteristic of the atomic structure of the emitting element within the specimen. EDS can spatially resolve the elemental composition of a specimen by measuring changes in X-ray intensity as the electron beam is rastered across its surface. Whilst a useful technique for rapid compositional measurements, EDS provides purely qualitative data. Without comparing measured spectra to those from standards of known composition, EDS cannot provide a quantitative measure of a sample's composition, only approximations of the relative abundance of elements (this is discussed further in Section 3.2.15).

In this work, ceramic pellet surfaces were observed using an Inspect F50 scanning electron microscope (SEM) in secondary electron (SE) mode, whilst a Hitachi TM3030 was used to conduct energy dispersive X-ray spectroscopy (EDS) analysis of the samples. The SE imaging was carried out with accelerating voltages of 15 and 20 kV, with spot sizes of 3.5 and 5 respectively. EDS was conducted with an accelerating voltage of 15 kV. Bruker's Quantax 70 software was used to map and quantify the composition of the samples. Three areas of the pellet were EDS mapped for 5-minutes each; the average of these measurements provided an estimate for the overall composition. In cases where a suspected secondary phase had formed, spot analysis was conducted on relevant areas within the map. In preparation for SEM-EDS analysis, sintered pellets were firstly ground and polished to a 1 μm as per the procedure described in Section 3.1.4. Pellets were adhered to aluminium SEM specimen stubs using silver dag and carbon coated using a Quorum Q150T Sputter Coater.

3.2.10 Grain size analysis of SEM micrographs

Grain size in sintered ceramics is known to influence various properties, including mechanical properties, ionic conductivity, radiation tolerance and corrosion behaviour[11–13]. Grain size is strongly dependent on ceramic composition and can also indicate the sinterability of powder. The average grain size in samples was measured using image analysis of SEM micrographs. This firstly required thermal etching of polished pellets to reveal grain boundaries on their surface. Thermal etching, or annealing, involves heating a sample to 90% of its sintering temperature, which allows the grains to recrystallise and form grooves at the intersections between them[14]. A total of around 1000 grains spanning the whole surface of the pellet were imaged a using SEM; these images were processed using morphological segmentation[15]. Morphological segmentation divides an image into several catchment basins by measuring the rate of change in greyscale intensity across the image. Grain boundaries appear as clearly defined black lines in the micrograph, allowing morphological segmentation to distinguish between adjacent grains by the rapid rate of change in grayscale value. Once the image is segmented, each grain is outlined, and their areas can be calculated using the 'Analyse

Particles' function in the Fiji software suite[16]. The process of morphological segmentation is demonstrated in Figure 7.

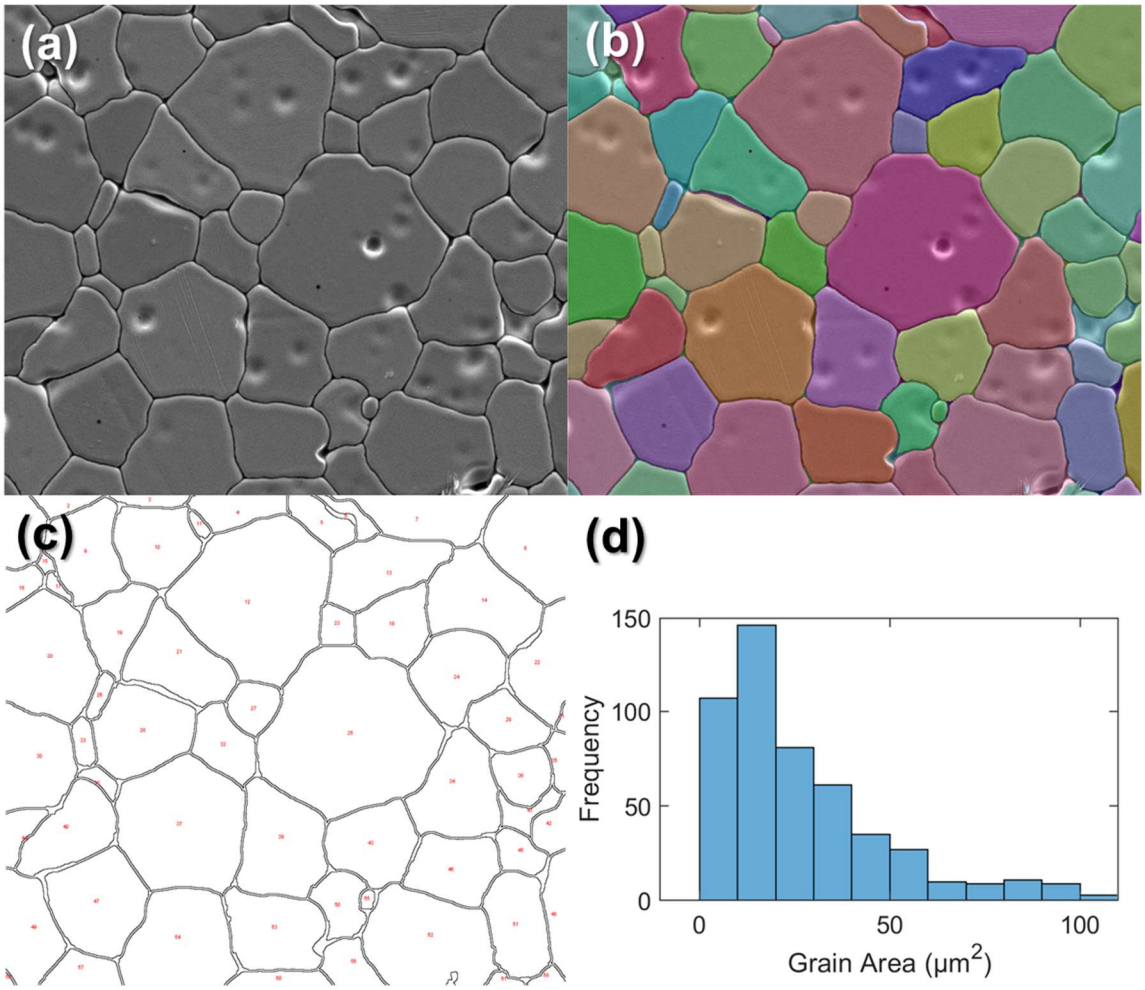

Figure 7: (a) Secondary electron SEM micrograph of a Gd-doped CeO_2 pellet surface. (b) SE micrograph with colour overlay, illustrating the identification of grains through morphological segmentation. (c) Output from particle size analysis in Fiji. (d) Example histogram of measured grain area.

3.2.11 Electron backscatter diffraction

Electron backscattered diffraction (EBSD) is a technique used to create spatially resolved maps revealing the orientation of grains within crystalline solids. EBSD detectors, installed within an SEM chamber, are capable of indexing patterns produced through the diffraction of the electron beam by the specimen surface. Backscatter diffracted electrons collide with a phosphor screen, producing a pattern characteristic of both the crystal structure and grain orientation. These patterns, known as Kikuchi bands, are measured and interpreted by software as the beam is rastered across the specimen surface. The resulting EBSD maps can provide information regarding grain orientation distribution (grain texture), grain boundary angle, grain morphology, and surface strain. EBSD measurements involve firstly tilting the

specimen 70° from the horizonal, allowing backscattered, diffracted electrons to be projected towards the phosphor screen. This process is illustrated in Figure 8.

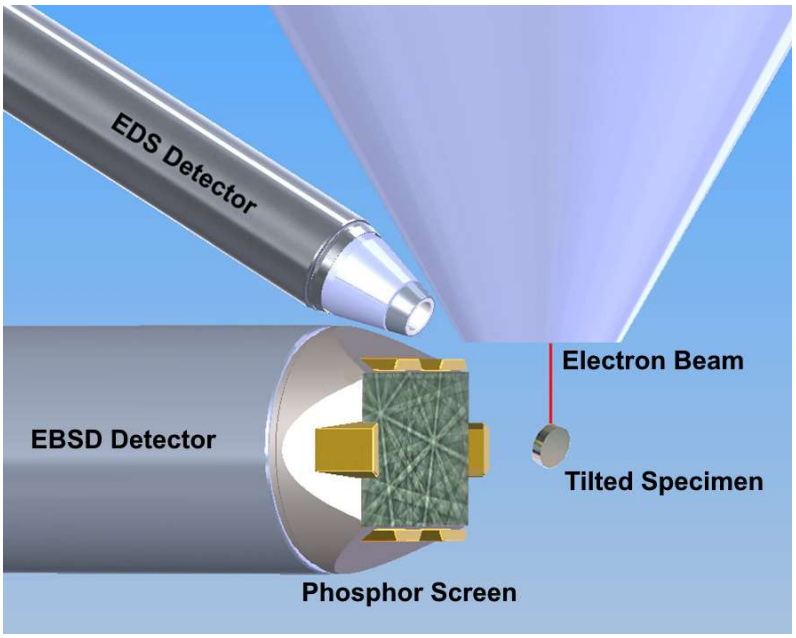

Figure 8: Schematic of SEM chamber equipped with EBSD and EDS detectors, showing the tilted specimen projecting diffracted electrons onto phosphor screen to produce a Kikuchi pattern. Oxford Instruments (2021)[17].

To obtain high-quality EBSD data with good indexing rates (>95%), specimens must be prepared with a relatively flat surface, that crucially must have low surface strain. Surface strain induced during polishing can distort the crystal lattice, resulting in shifts to Kikuchi band edge positions, leading to a lower signal to noise ratio, lowering indexing rates. The standard 1 µm finish used for SEM-EDS or Raman spectroscopy is insufficient, as pellet surface can remain mechanically strained and covered in scratches that will produce an amorphous diffraction pattern under the electron beam. For these reasons, EBSD samples underwent additional polishing steps. Firstly, the pellets were polished with 0.25 µm diamond suspension using the polishing procedure described previously. Following this, the pellets were polished once more using a 0.05 µm colloidal silica and alumina suspension. Colloidal silica is especially effective at removing material damaged and strained by previous polishing steps, as it reacts with the specimen surface to ease mechanical removal of the top layer. For this final polishing step, the applied force was lowered to just 1 N, minimising the mechanical damage induced by the polishing media. Care was taken to avoid over-polishing using colloidal silica, as this can lead to increased surface roughness through heterogenous material removal across the surface[18]. Excessive chemo-polishing can etch grain boundaries, widen pore openings, and remove specific grain orientations at greater rates. Samples were carbon coated to avoid issues with charge-up and drift under the beam. A 4 nm, TEM-grade coat was

applied, to avoid sputtering uneven or thick regions of amorphous carbon, known to be deleterious to indexing quality.

EBSD presented in this work was collected using a JEOL JSM 7900F SEM equipped with an Oxford Instruments AZtec HKL Advanced Symmetry System. Oxford Instruments' AZtec Crystal software was used to calculate grain texture and grain boundary misorientation.

3.2.12 Transmission electron backscatter diffraction

Transmission Electron Backscatter Diffraction (t-EBSD), sometimes referred to as Transmission Kikuchi Diffraction (TKD) is a newer approach to SEM-based diffraction, capable of indexing nanocrystalline materials. In t-EBSD, a focussed electron beam is transmitted through an electron transparent sample. The resulting diffraction pattern is measured by an EBSD detector positioned underneath the sample. Transmission-EBSD boasts a far superior resolution of < 10 nm compared to the typical ~75 nm achievable with conventional EBSD[19]. This high resolution is due to a drastically reduced pattern source interaction volume with the sample. Transmission-EBSD is therefore capable of indexing of materials with high crystalline defect densities, or nanocrystalline (< 100 nm) grains, by avoiding issues with overlapping Kikuchi patterns produced from larger interaction volumes. Electron transparent samples used in t-EBSD were prepared using focussed ion beam (FIB) milling (as described in Section 3.2.14). Transmission-EBSD was also performed using a JEOL JSM 7900F SEM equipped with an Oxford Instruments AZtec HKL Advanced Symmetry System and analysed using Oxford Instruments' AZtec Crystal software.

3.2.13 Transmission electron microscopy

In transmission electron microscopy (TEM), images are formed by a focussed electron beam interacting with a specimen as it passes through it. For this reason, specimens must be electron transparent, which in the case of ceramic samples generally demands thinning below 100 nm. Contrast in TEM imaging indicates variance in beam scattering or diffraction, which can provide information about specimen thickness, microstructure, Z-number, mechanical strain, crystallographic orientation, and crystalline defects[20]. In conventional TEM, apertures with different diameters are used to isolate contributions from electrons diffracted at certain angles. Bright-field (BF) imaging requires the use of an aperture to solely permit contributions from unscattered electrons. Contrast in BF images is influenced by diffraction and absorption of electrons in the specimen. Thicker regions of the sample, or regions with a higher Z-values, will appear dark as the electron beam is absorbed or diffracted. By extension, regions with little to no diffraction of the beam path will appear bright. Conversely, dark-field (DF) imaging uses an aperture to exclude contributions from the unscattered beam, resulting in bright regions where the beam is most diffracted. DF imaging can be useful to increase contrast and

resolve subtle features such as crystalline defects. High-angle annular dark field (HAADF) imaging exclusively detects electrons that have been Rutherford scattered by large angles from the incident beam through coulombic repulsion. By eliminating any signal from Bragg scattering, all of the contrast in the image is dependent on the Z-number of nuclei in the specimen. Electron diffraction (ED) patterns show bright spots where the beam is in phase following Bragg scattering; thus, interpreting them requires understanding of reciprocal space. Diffraction patterns observed in ED micrographs are characteristic of different crystallographic orientations and structures. ED patterns are highly sensitive to defect ordering within the lattice. Scanning transmission electron microscopy (STEM) involves rastering a fine electron beam over the sample in a manner similar to SEM. STEM is a powerful technique for collecting spatially resolved data, especially when paired with electron energy loss spectroscopy (EELS) and EDS detectors. In STEM, scanning coils rather than apertures are used to selectively deflect electrons for detection. Figure 9 illustrates the relative angles of scattering associated with various TEM imaging methods.

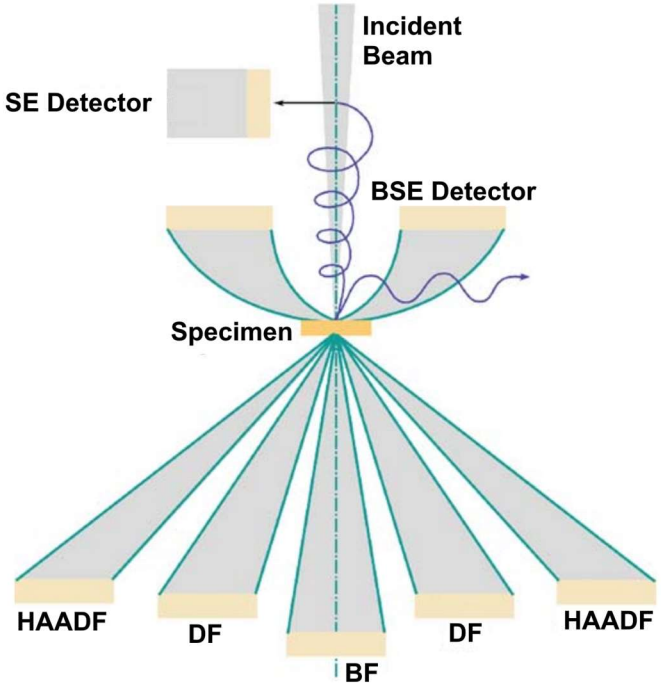

Figure 9: Schematic illustrating various electron detectors that may be found in a (S)TEM. The vast majority of TEM analysis relies on forward-scattered electrons, whilst SE and BSE detectors are rarely used. Adapted from Williams, (2008)[20].

Transmission electron microscopy (TEM) in this work was conducted using both a JEOL F200 and an FEI Tecnai T20 TEM. Both microscopes were operated at 200 keV, BF images and ED patterns were both collected using a charge-coupled device (CCD) camera.

3.2.14 TEM sample preparation

Electron transparent samples for TEM analysis were prepared through two methods, ion polishing a dimpled sample, and lamellar lift-out using a focussed ion beam. Dimpling and ion milling the samples involved firstly sectioning a 2 mm square from a sintered pellet. This square was then mounted to an Al stub using CrystalBond and ground to a thickness of 40 μm using a Gatan Disc Grinder System. The centre of the sample was then dimpled to a depth of around 20 μm using a Gatan Dimple Grinder II. This process involves rotating the sample under a spinning copper wheel coated with 1 μm diamond paste. Once the dimple reached the required 20 μm depth, it was polished for 15 minutes under a felt wheel coated with 0.25 μm diamond paste. This polishing step helps reduce surface roughness of the dimple, allowing more even Ar milling during ion polishing. During the initial dimpling stage, a load of 5 g was applied to the polishing arm, this was increased to 10 g during polishing. Finally, the sample was glued to a Mo grid using Gatan G1 epoxy and hardener. These pre-thinning steps of grinding and dimpling were taken to minimise the time spent ion milling, and improve the evenness of the thinning, resulting in a larger region of electron transparency. Figure 10 illustrates how the sample appears after this pre-thinning stage is complete.

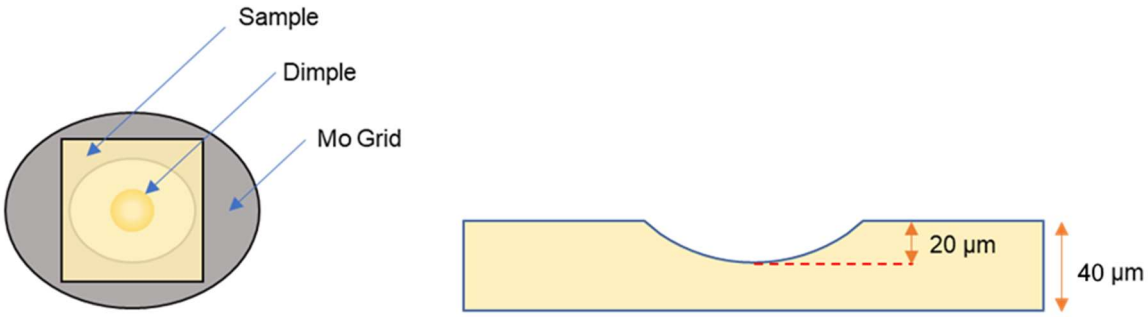

Figure 10: Dimpled sample mounted on molybdenum grid ready for ion milling (left). Cross-section of dimpled sample labelled with typical dimensions (right).

The dimpled sample was then further thinned through ion milling using a Gatan Precision Ion Polishing System (PIPS) II. The PIPS II employs two argon guns that accelerate Ar^+ ions towards the sample, sputtering material in the process. Each gun sputters in a roughly elliptical region, these two regions are perpendicular to one another, resulting in a fine point of intense sputtering at the centre of the dimple, as illustrated in Figure 11.

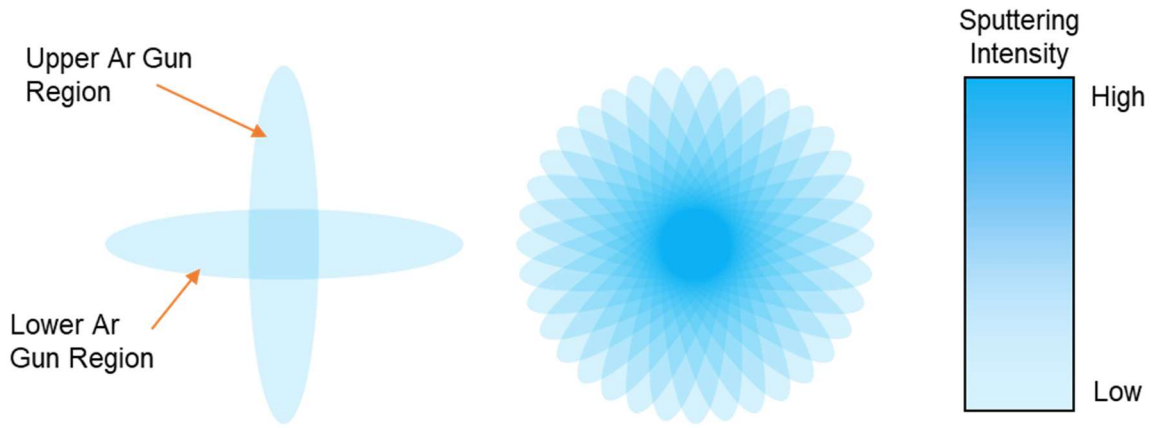

Figure 11: Schematic illustration of dual Ar gun operation in ion milling.

With one Ar gun positioned above the sample and one below, milling tapers the sample thickness towards the centre. Eventually, continued milling forms a hole in the centre of the sample; at this point the sputtering energy and gun angles (θ and ϕ in Figure 12) are lowered in order to remove some of the milling damage induced. The 'donut' region surrounding the hole in the sample, highlighted in Figure 12 (in red), is now electron transparent and therefore ready for TEM analysis.

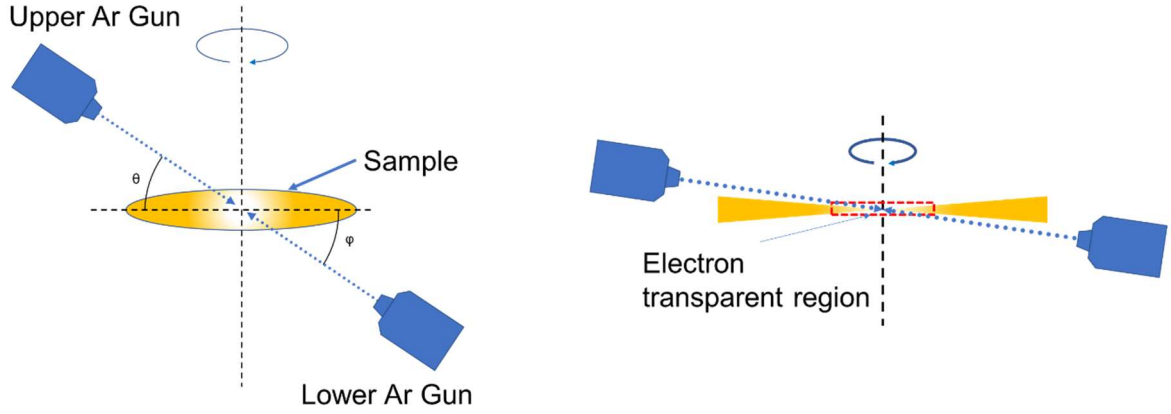

Figure 12: Schematic illustration of how electron transparency is achieved through ion milling.

Focussed ion beam (FIB) milling was also used to prepare TEM samples through lamellar lift-out samples. The lift-out method involved deposition of a protective Pt and C layer before trenches were milled either side of the desired region. The sample was then gradually thinned to ~80 nm, before removal of connecting material at the sides and bottom. The sample was finally mounted to a lift-out grid using deposited Pt.

3.2.15 Electron probe (micro)analysis

Electron Probe (Micro)Analysis (EPMA) is capable of quantitative compositional analysis of monolithic solid specimens. EPMAs operate using a principle similar to that employed in SEM-EDS systems. An electron beam is used to excite electrons, generating X-rays of characteristic energy when electrons drop from higher energy shells to fill the holes. However, EPMA utilises wavelength dispersive spectroscopy (WDS) as opposed to energy dispersive X-ray spectroscopy (EDS). WDS isolates X-ray wavelengths of interest through Bragg diffraction in crystals, before directing these targeted wavelengths to detectors[21], whereas in EDS, X-rays of all wavelengths are detected during accumulations. Whilst this enables EDS spectra to be collected at far greater rates, WDS spectra typically enable far more precise compositional measurements, due to the excellent X-ray peak resolution and higher peak to background ratio. Careful selection of X-ray peaks avoids issues with overlap and interference between elements that can introduce errors. Chemical compositions of samples are determined through comparison of measured X-ray intensities with intensities from standards. Measured X-ray intensities are corrected to account of the depth production of the X-rays, finally yielding quantitative compositions typically quoted in wt%. Figure 13 illustrates the difference between EDS and EPMA maps collected on the same region on the surface of a Gd-doped CeO_2 pellet.

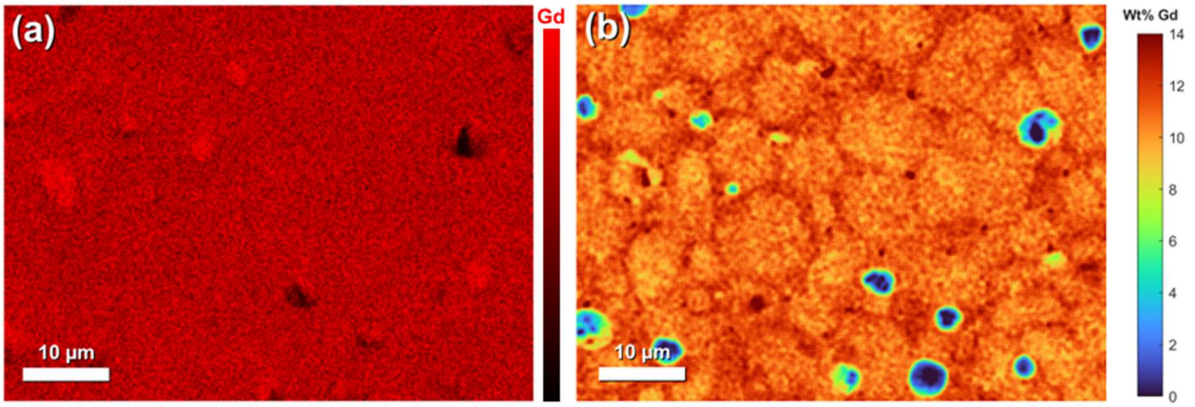

Figure 13: Comparison between and SEM-EDS (a) and EPMA (b) mapping Gd content in the same region of a 10 mol% Gd-doped CeO_2 pellet. Note the quantitative scale available through EPMA, and the vastly improved sensitivity to compositional heterogeneity, revealing Gd segregation towards the grain edge.

Appropriate sample preparation is vital in the collection of accurate EPMA data. The ideal surface for EPMA analysis is perfectly flat, free of any defects or porosity. Matrix corrections are based on the assumption that a consistent interaction volume between the probe and the sample is maintained, and that paths for X-ray release remain the same across the surface. Surface regions where these conditions are not met may lead to an over or underestimation of elemental concentration[22]. This concept is similar in principle to the secondary electron edge effect discussed previously in Section 3.2.9. Pellets polished to just 1 µm can still feature

prominent scratches at higher magnifications, whereas excessive chemo-polishing with 0.05 µm colloidal silica can cause surface roughness. With this in mind, samples analysed with EPMA were polished to 0.05 µm for just 20 minutes under a force of 1 N. All samples were mounted to aluminium stubs using silver dag and carbon coated to avoid charge-up under the electron beam. EPMA data in this work was performed using a JEOL JXA-8530F Plus Hyper Probe. Mapping was conducted in stage mode, allowing the probe angle to remain constant during rastering. A minimum of five quantitative spot measurements were averaged to calculate sample composition. Compositions were firstly calculated in wt% before normalisation and conversion to mol% or molar fraction. Further observational and experimental parameters are listed in the papers contained withing Chapters 5 and 6.

3.2.16 Vertical scanning interferometry

Vertical Scanning Interferometry (VSI) is non-contact three-dimensional (3D) profiling technique, capable of revealing the topography of a specimen surface by measuring its height at number of points across a plane. Interferometry exploits the interference of superimposed waves to precisely measure distances through changes in pathlength. A beam of white (polychromatic) light is split in two; one of these beams travels a known distance to a reference mirror whilst the other is directed towards the sample surface. Both beams are then reflected back towards the beamsplitter, where they are superimposed, generating an interference pattern that reveals any difference in path travelled by the two beams. Figure 14 presents a simple schematic of an interferometer, and an example of data that can be collected through VSI.

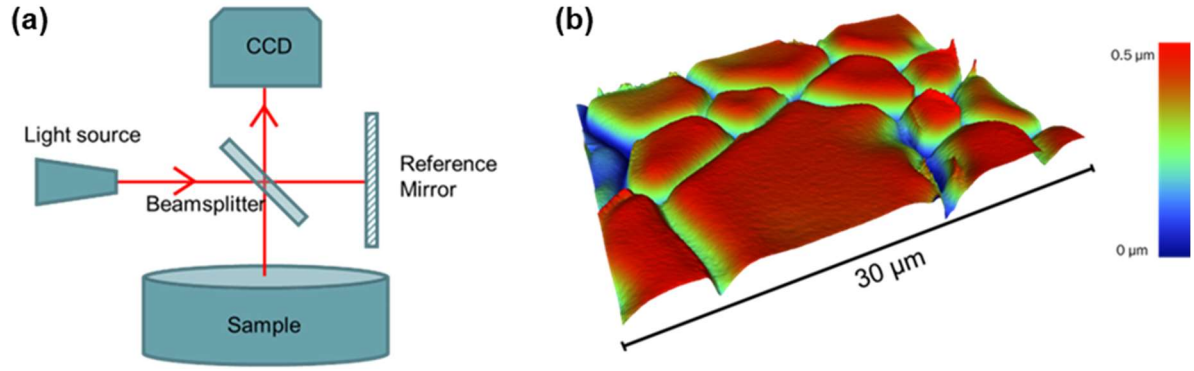

Figure 14: The VSI technique. (a) Schematic diagram illustrating operating principle of an interferometer; (b) 3D surface of a Gd-doped CeO_2 pellet measured using VSI.

Raising and lowering the lens of the VSI adjusts the pathlength of the beam reflected by the sample surface. This adjustment proceeds until the central peak of the interferogram exhibits the greatest contrast with its neighbouring troughs[23]. At this point, the pathlengths to the surface and reference mirror are known to be equal, and the surface height can be measured. Each pixel in the array is assigned a height value corresponding to the position of the lens when the greatest fringe contrast was achieved. Typically, VSI utilises a source of polychromatic white light, although monochromatic green light can also be used. Polychromatic light superimposes various wavelengths to produce a series of fringes with quickly decreasing modulation, as depicted in Figure 15. Monochromatic interferograms by comparison feature a series of fringes with more consistent intensity and gradual modulation.

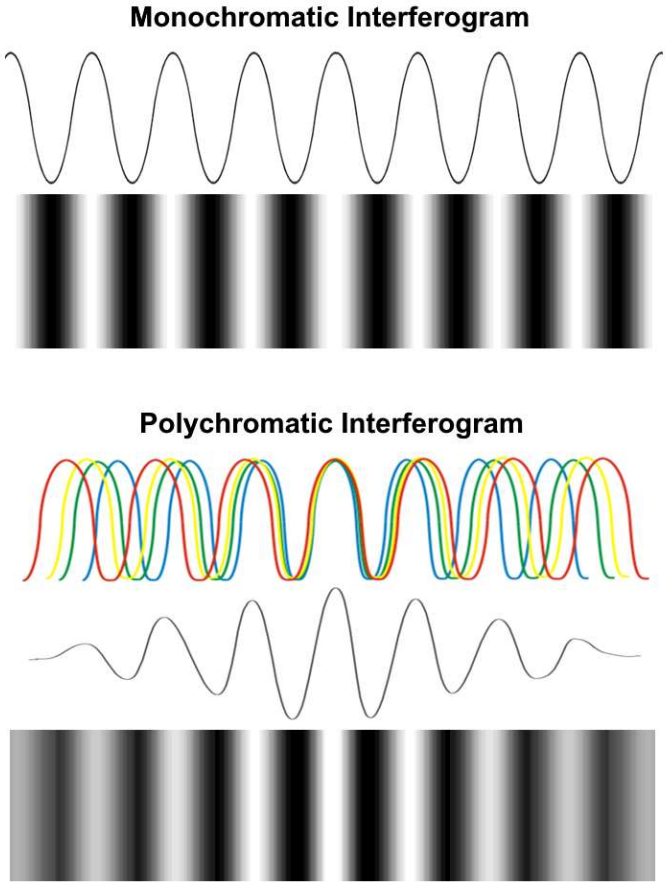

Figure 15: Diagram illustrating the difference in observed fringe contrast between diffractograms generating using monochromatic and polychromatic light.

The pronounced rate of change in fringe contrast caused by superimposition of polychromatic light enables the CCD to reliably detect the height at which the intensity of the central fringe is greatest. This is especially important when measuring rougher surfaces, such as imperfect ceramic samples. The theoretical vertical resolution of VSI approximately 2 nm[24]; however, in

practice the accuracy of VSI measurements is limited by the much lower lateral resolution, which is itself determined by the magnification of the object lens.

3.2.17 VSI-based surface dissolution study

For this work, a novel ex-situ VSI-based dissolution methodology was developed. This method was designed to directly measure the removal of material from a ceramic surface as it dissolved. As no standardised surface profilometry based dissolution tests exist, the following VSI-based dissolution method was developed. Firstly, a sintered ceramic pellet was polished to a 0.05 µm finish following same procedure used for EBSD sample preparation, described in Section 3.2.11. Polished pellets were then mounted to a borosilicate glass slide using CrystalBond to facilitate easy handling and positioning of samples under the VSI. Next, an inert gold mask was sputtered over half of the sample surface using a gold coater. Once masked, a crosshair was scored into the centre of the pellet using a diamond scribe. This crosshair was used as a guide to help relocate the same region for remeasurement post-dissolution. Finally, a cross ('X') was inscribed in the top right quadrant of the pellet, to help avoid potential confusion regarding sample orientation. An example of a pellet prepared with these steps is presented in Figure 16.

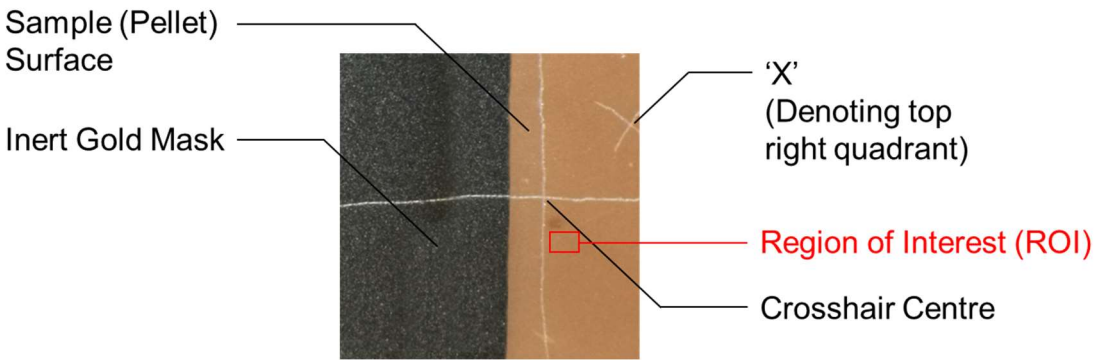

Figure 16: Labelled photograph of a gold coated pellet, featuring an inscribed crosshair and 'X' to aid with relocation of the region of interest (ROI), which is outlined in red (not to scale).

Sample slides were positioned on the VSI stage, with care taken to ensure parallel alignment between slide and stage edge. This alignment helped to minimise rotational differences between repeat measurements post-dissolution. An area of the sample close to the crosshair centre was designated as the region of interest (ROI). Ideally, this region would be free of large pores and grain pull-out. Defects such as these are challenging to measure using VSI, often resulting in loss of data points. Once selected, the ROI was measured with the VSI in its pristine, undissolved state to provide a pre-dissolution reference measurement. An optical microscopy image of the same region was also taken to provide a reference used to relocate the ROI. Several images taken at decreasing magnifications were compiled to provide a

relocation ‘map’. Following collection of the maps, and characterisation of ROIs with EBSD and EPMA maps (detailed in Sections 3.2.11 and 3.2.15, respectively) pellets were ready for dissolution.

Pellets, remaining mounting on borosilicate slides, were placed within PTFE vessels filled with 12 M HCl and left in a 60 °C oven for 7 days. Upon removal, samples were rinsed with UHQ and dried. Following careful repositioning on the VSI stage, ROIs were relocated with the aid of the maps previously described. Precise adjustments of the motorised stage ensured perfect alignment with the initial measurement before another scan was collected post-dissolution. A second measurement was also collected at the gold mask edge to measure the change in step height. Step height measurements were used to estimate average normal retreat of the pellet surface, as illustrated in Figure 17.

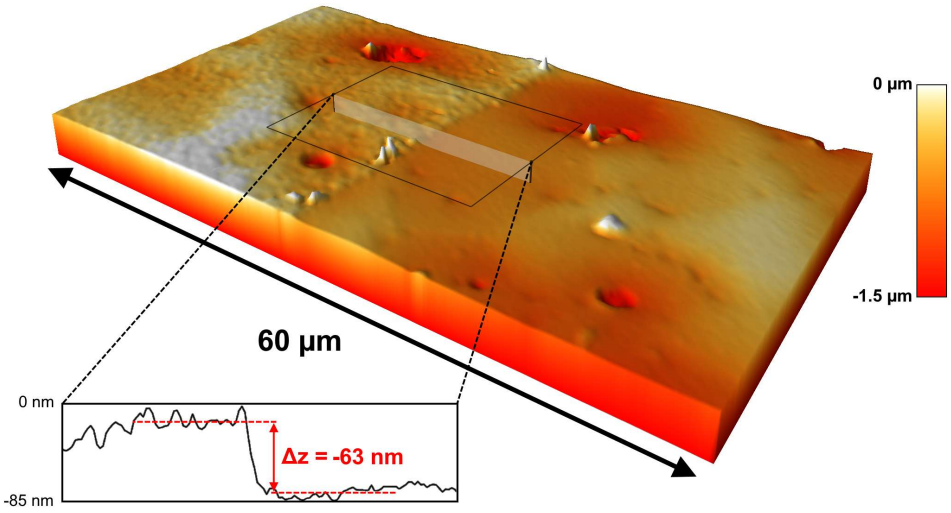

Figure 17: Step height (Δz) measurement between inert gold mask (left) and exposed sample surface (right), allowing for calculation of surface normal retreat.

Bruker’s Vision64 software was used to remove any tilt in the datasets through linear fitting before matrices were exported. A custom MATLAB script was used to calibrate the heights of matrices using the normal retreat estimated from step height measurements. Following this calibration, matrices are subtracted from one another to yield ‘flux’ maps of retreat rate. Flux maps reveal areas of heterogenous retreat rate across a surface by highlighting regions with the greatest difference in height between two measurements. Matrices were presented using pseudo-colour plots, which assign colours to specific pixel values, to reveal surface evolution during dissolution.

For the work presented in Chapter 5, the following observation conditions were used. A Bruker Contour Elite was operated in white light VSI mode at 50x and 115x magnification, using a 1x FOV multiplier and 1x scan speed. The intensity threshold was set to 1%, and back scan and

length were set to 5 and 10 µm respectively. Data processing was performed in both Bruker's Vision64 software and MATLAB.

3.2.18 Proof of concept for VSI-based dissolution study

The novel *ex-situ* VSI-based dissolution methodology used to collect data presented in Chapter 5 was developed iteratively. The results presented below serve as a proof of concept for the method. Note, these data were collected before the latest iteration of the technique (described in Section 3.2.17) was established, meaning an inert mask was not applied to the sample surface prior to dissolution. This earlier version of the technique calibrated each matrix by assigning the height (z-value) of the highest grain in each matrix to the same value. This calibration method is obviously flawed in its assumption that the most durable grain does not retreat through dissolution; in reality this is highly unlikely. The lack of an inert mark providing a reference surface limited the scope of quantitative results the data could provide. For this reason, no retreat or dissolution rates have been calculated. Nevertheless, this preliminary study provided nuanced insight into heterogenous surface dissolution and served as proof of concept for the VSI-based dissolution study. All data, unless stated otherwise, was collected using a Bruker Contour Elite in white light VSI mode at 50x magnification, 1x FOV multiplier, 1x scan speed with a back scan of 5 µm and a length of 25 µm. Data was tilt-removed using Vision64, and matrices were manipulated using MATLAB. Differential 'flux' maps were generated by subtracting matrices obtained from measurements made prior to, and following a period of dissolution.

Preliminary VSI-based dissolution studies were conducted on Cr-doped UO_2, dissolved in 2M HNO_3 at 60 °C. The pellet was removed from solution and measured following 6, 12, 18, 24, and 40 hours of dissolution.

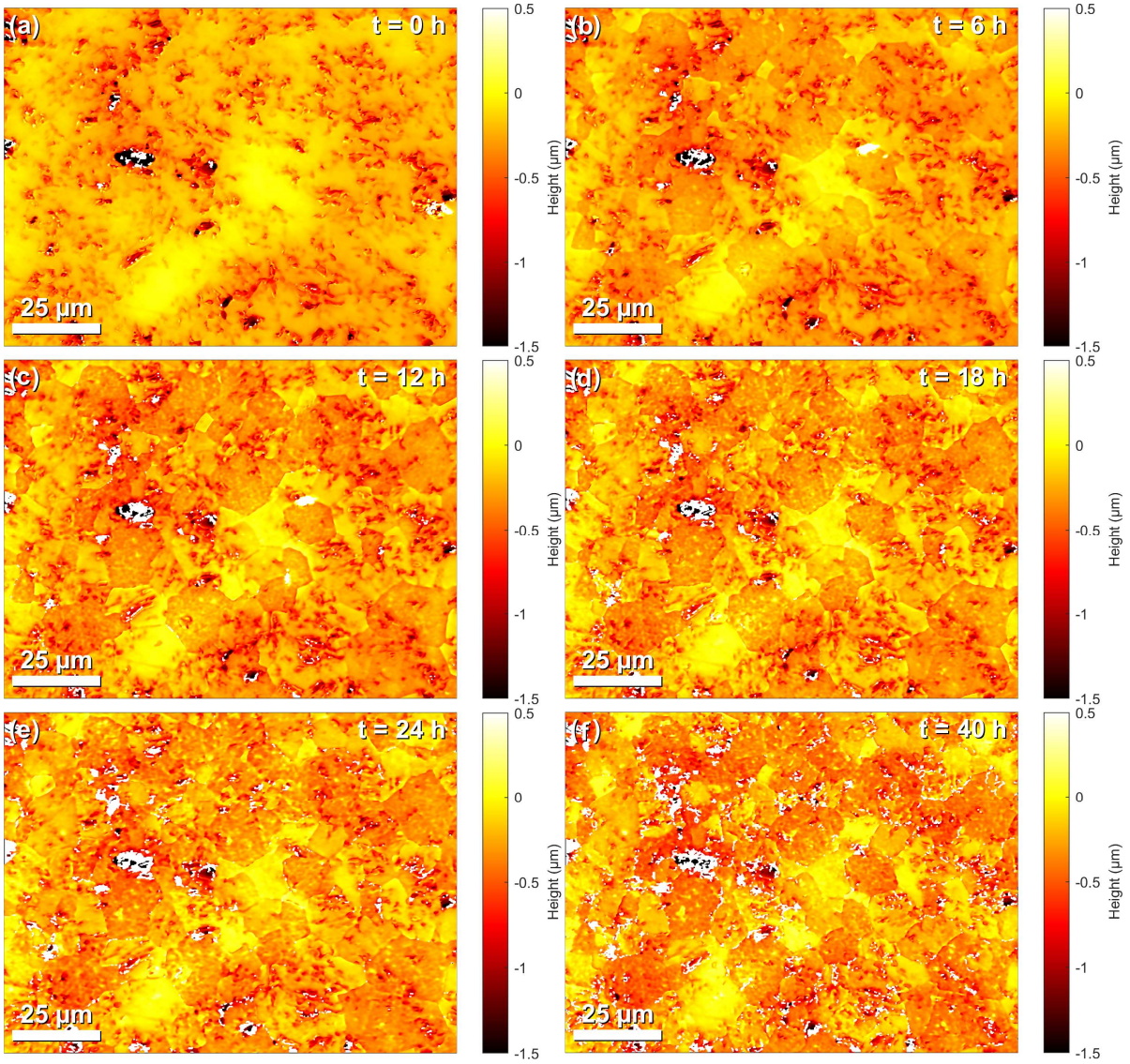

Figure 18: Pseudo-colour plots showing topographical evolution of Cr-doped UO_2 pellet surface during dissolution in 2M HNO_3 at 0 hours (a), 6 hours (b), 12 hours (c), 18 hours (d), 24 hours (e), and 40 hours (f).

The initial scan of the pristine undissolved pellet shown in Figure 18a, revealed significant deviations in height across the sample, including several scratches. These features were likely the result of poor polishing, which was conducted by hand due to laboratory restrictions in radioactive material preparation. Pores are readily observed across entire surface. Following 6 hours dissolution (Figure 18b), the surface topography shows significant alteration. Individual grains are now distinguished by their differing heights; this is caused by the difference in dissolution rates of exposed crystallographic planes[25]. In addition to heterogenous grain retreat, the preferential dissolution of grain boundaries is also indicated by increased retreat towards the grain edge. This rate of this accelerated grain boundary dissolution varies significantly between different boundaries, which may be controlled by the misorientation angle or the local composition. Accompanying EBSD and EPMA maps were

not collected as part of this preliminary study, so the precise cause of this heterogenous retreat remains unclear. This emphasised the requirement for extensive characterisation of the region of interest (ROI) using supplementary techniques, prior to dissolution. Scratches in the surface were found deepen due to accelerated dissolution of highly strained material. This highlighted the importance of consistent polishing procedures in subsequent studies to avoid dissolution rate contributions from extrinsic defects induced during sample preparation. Certain pores also deepened significantly during the first 6 hours of dissolution; this can be observed more easily in the differential flux maps presented in Figure 19. Similar pore dissolution behaviour was observed by Fischer *et al.* in a study on pyrochlore ceramics[26].

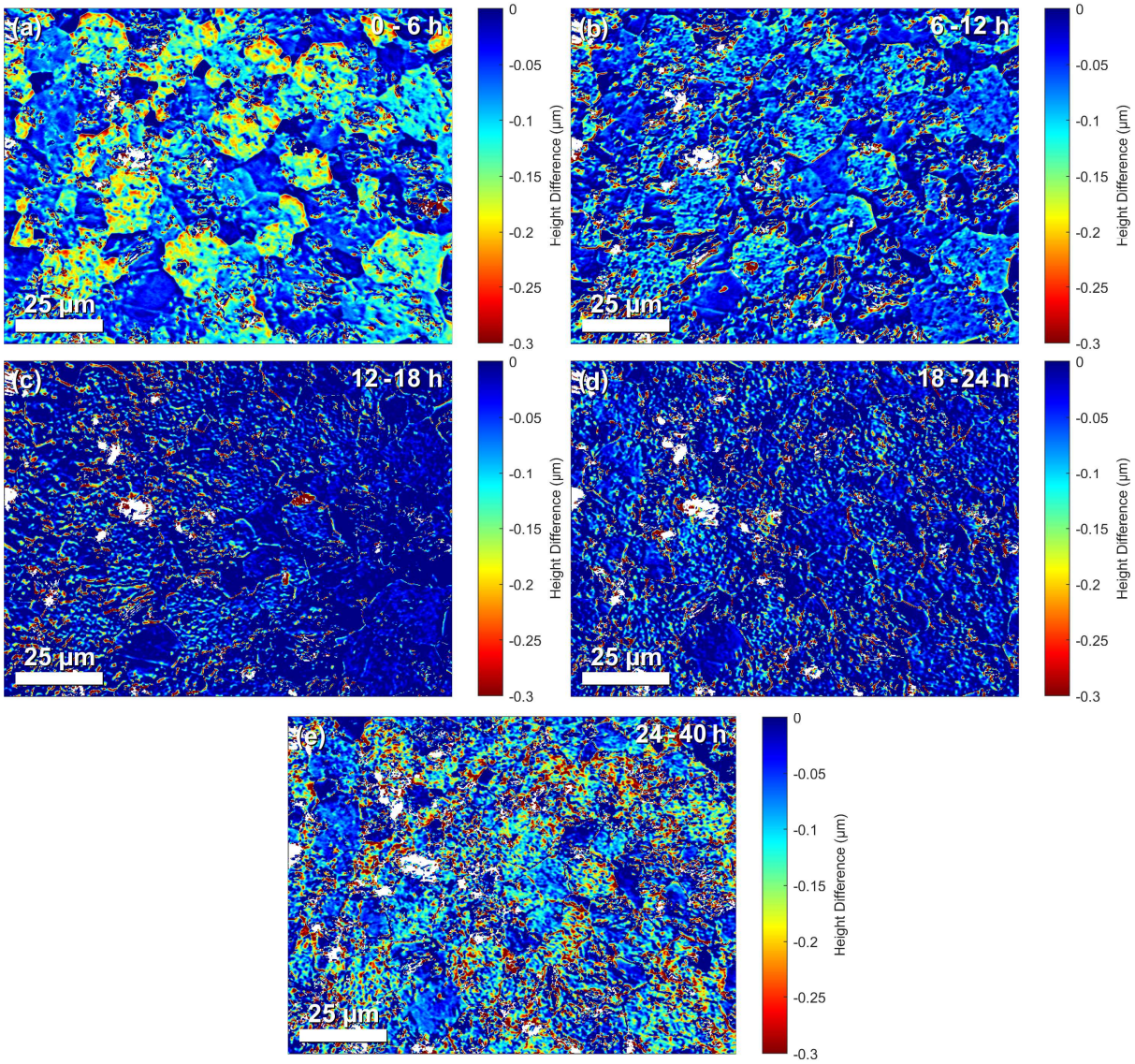

Figure 19: Differential flux maps of revealing heterogenous dissolution of Cr-doped UO_2 in 2M HNO_3 between 0 – 6 hours (a), 6 – 12 hours (b), 12 - 18 hours (c), 18 – 24 hours (d), and 24 – 40 hours (e).

The subsequent 6 hours of dissolution yielded further topographical changes, although these were more subtle compared to the first period. The overall material loss between 6 - 12 hours

was reduced compared to 0 - 6 hours, indicating a decrease in average dissolution rate. The initial enhanced rate could have resulted from surface strain induced during polishing; the topmost region of material will be the most heavily strained, giving rise to lattice defects such as dislocation loops to create a more reactive surface[27]. Certain grains begin to develop a rough texture between 6 – 12 hours of dissolution, which could be attributed to the varying retreat rates of different crystallographic planes with lower surface energy[28,29]. The heterogenous retreat of grains continued as expected, increasing the disparity in grain heights corresponding to the durability of exposed crystallographic planes[25]. Preferential grain boundary dissolution is more pronounced and is especially noticeable on the flux map between 6 - 12 hours; this preferential grain boundary dissolution potentially became more obvious once the effects of high surface strain had subsided. Pores continue to deepen and some intragranular pits begin to form. These pits may be the result more soluble Cr-rich phases being removed; however, EPMA mapping would be necessary to confirm this, reaffirming the importance of further ROI characterisation or the pristine surface. Scratches maintained the accelerated dissolution as the strained material continued to be removed.

The surface evolution in the between 12 - 18 hours follows a similar pattern; overall material loss decreased once more, and changes are predominantly subtle compared to preceding intervals, suggesting a drop in dissolution rate. Certain grains develop further roughness, increasing their reactive surface area. Heterogenous grain retreat is again observed but is far less pronounced, whereas grain boundary retreat becomes more evident. Pores continue to deepen at a comparable rate whilst the scratched area begins to dissolve more slowly as most of the strained material is removed. Similar behaviour is observed between 18 - 24 hours, although by this time the accelerated dissolution of the scratched area has abated almost entirely. The final period of dissolution, between 24 – 40 hours, saw more grains developing a rough texture as the most stable planes within them were revealed. Grain boundaries continued to dissolve preferentially, with some deepening to the point where data was lost due to poor signal in these regions, resulting from low reflected light intensity.

This preliminary study confirmed the *ex-situ* technique was capable of measuring retrain in specific grain boundaries, as shown in Figure 20 through cross-sectional 2D profiles.

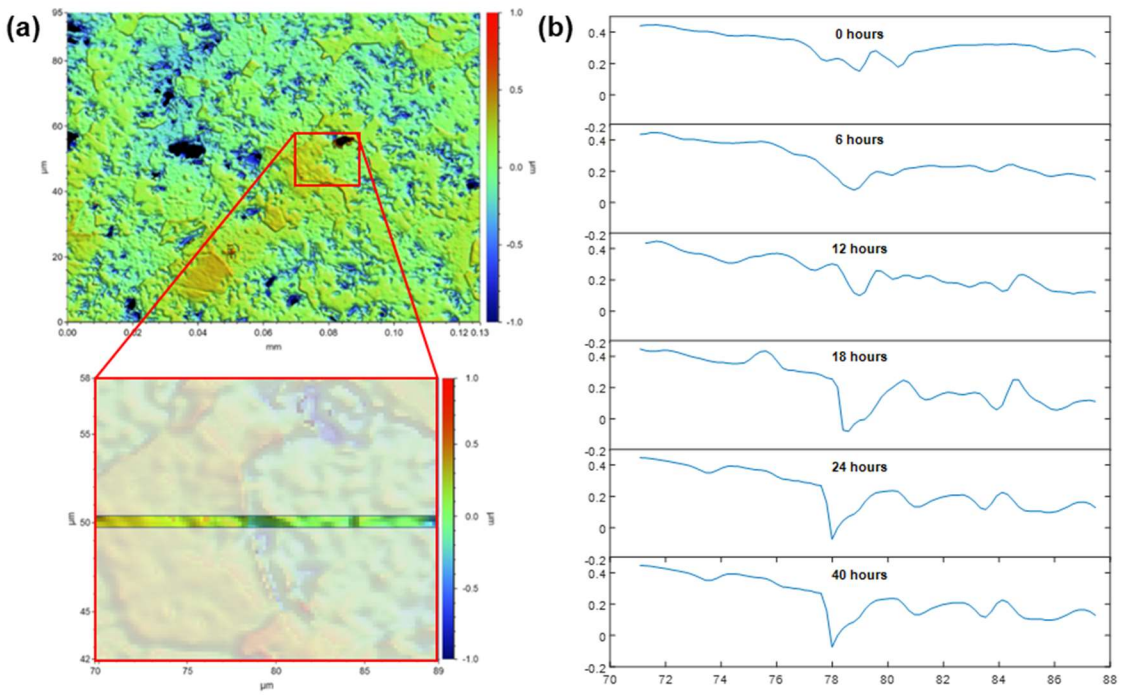

Figure 20: (a) VSI plot with accompanying inset highlighting the selected grain boundary. (b) 2D cross-sectional profiles revealing grain boundary dissolution.

These profiles reveal preferential dissolution within the grain boundary as it deepens over time; the development of the rough texture is also visible. However, the lateral resolution limits the accuracy with which the true geometry of the grain boundary can be measured, as evidenced by the sharp 'V' shape of the valley. As previously mentioned, certain grain boundaries could not be measured at all after extensive recession, as the reflected intensity of light was below the limit of detection by the CCD. These issues obviously represent significant limitations in a method designed to observe and measure the rate of grain boundary dissolution; however, there exist several possible solutions. Preventing the loss of data points in exceptionally rough or steep regions can be achieved by lowering the threshold for the minimum required intensity. Caution must be exercised, however, as very low thresholds risk the acquisition of erroneous signals, producing artefacts. Similarly, increasing the intensity of the white light source will also improve signal, though this increases the risk of diffracted light interfering with the intensity of reflections and producing artefacts. More accurate measurements of grain boundary depth are permitted by a higher magnification objective lens; whilst the theoretical vertical resolution is remains unchanged, the improved lateral resolution enables accurate measurements complex geometries, especially those with steep gradients as illustrated in Figure 21.

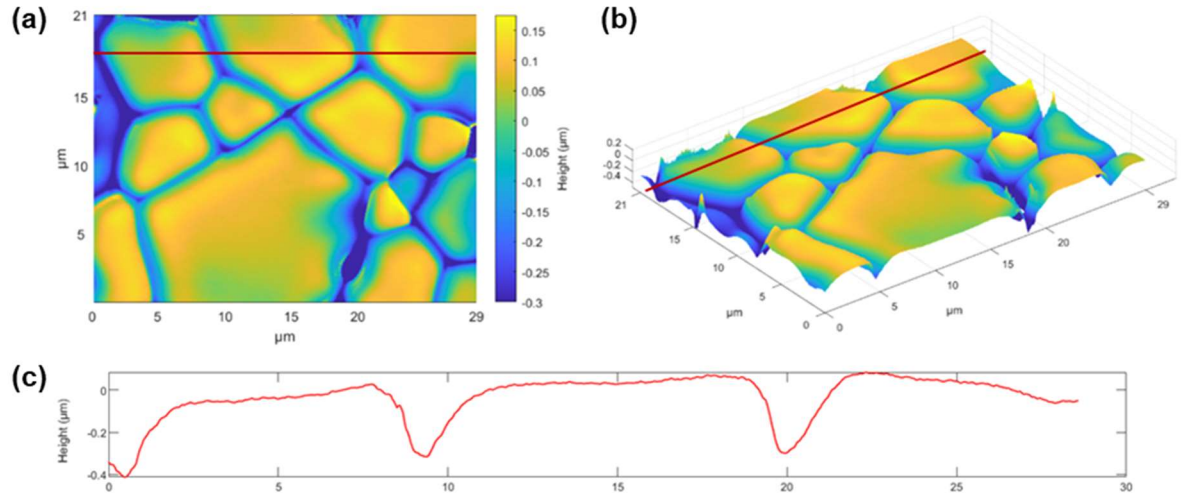

Figure 21: (a) 2D pseudo-colour plot of thermally etched $(Ce,Gd)O_{2-\delta}$ pellet surface. (b) 3D plot of the same data presented in (a) (c) 2D profile across two thermally etched grain boundaries, as indicated by the red lines in (a) and (b).

The increased magnification enabled the accurate resolution of the grain boundary geometry, which could facilitate precise measurements of depth or retreat during dissolution. This finding informed the decision to employ two objective magnifications in subsequent VSI-based dissolution studies. The use of both higher and lower magnification scans would allow observation of macroscopic retreat and precise measurement of grain boundary depth.

The preliminary study of Cr-doped UO_2 using a novel *ex-situ* VSI-based dissolution technique showed the method was capable of monitoring heterogenous retreat during dissolution. Grain orientation, scratches, pores, and grain boundaries were all identified as significant rate contributors. The preliminary study also highlighted the need to extensively characterise the region of interest (ROI) prior to dissolution, using supplementary techniques such as EPMA and EBSD, to fully elucidate the influence of local composition, phase formation and crystallographic orientation on heterogenous dissolution rates.

3.2.19 ASTM C1308 dissolution study

Dissolution studies measure the rate at which materials are leached in contact with solution. Solution analysis then reveals the concentration of elements released through dissolution over a known period, allowing a dissolution rate to be determined. Ceramic dissolution tests typically involve placing sintered pellets (or crushed powders) within inert PTFE vessels filled with acidic solution; these vessels are held at elevated temperatures to encourage accelerated dissolution. This basic concept is illustrated in Figure 22.

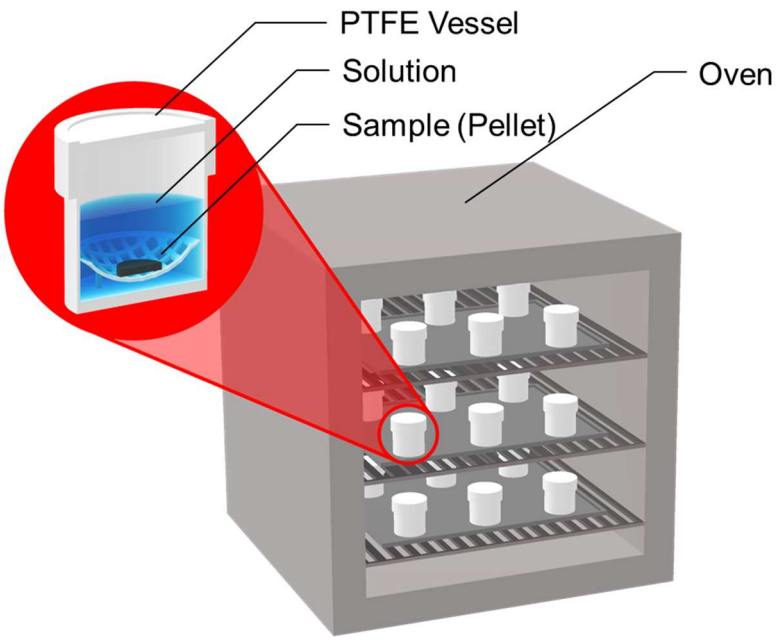

Figure 22: Illustration of apparatus involved in accelerated dissolution testing of ceramic pellets.

The dissolution study presented in this work most closely followed protocol outlined in the ASTM C1308 standard. ASTM C1308 is a semi-dynamic standard test method for the accelerated leaching of solid materials[30]. Semi-dynamic tests involve the complete replacement of dissolution media at each sampling interval, or timepoint. ASTM C1308 tests also require the collection of an acid strip solution. The process of acid stripping ensures residual traces of elemental release adhered to the PTFE vessel post-dissolution are removed and measured in addition to the dissolution leachate. ASTM C1308 is nominally an 11-day test, with sampling taking place at regular 24-hour intervals. For health and safety reasons, out-of-hours access to laboratories was suspended following their reopening under COVID-19 rules, meaning sampling at weekends was not possible. For this reason, the C1308 protocol was adapted to use more convenient sampling intervals. The duration of the test was also extended to 28 days in an effort to investigate longer-term dissolution behaviour.

In the study presented in this work, sintered pellets were dissolved in triplicate at 90 °C in 0.01 M HNO_3 solution. Sampling took place after 1, 2, 3, 4, 7, 10, 14, 21 and 28 days of dissolution. Normalised release of each element was calculated by firstly summing the average concentrations measured in both the dissolution media and acid strip solutions. The average concentration measured in the blanks was then subtracted from this total. Concentrations were converted from ppm to g L^{-1}, then multiplied by the precise volume of measured solution to give the mass of element in solution in g. Normalised elemental mass release in g m^{-2} is finally calculated by multiplying the mass in solution by both the elemental fraction (wt%) in the given composition, and the surface area of the sample.

Nitric acid (HNO_3) solutions used for dissolution, acid stripping and vessel cleaning were prepared using ultrapure, NORMATOM® HNO_3 (VWR Chemicals) to avoid issues with ICP-MS measurements caused by trace metal contaminants. Samples used in the dissolution study were sintered pellets, 10 mm in diameter. Pellets were polished to 1 µm on both sides using polishing procedure detailed in Section 3.1.4. Prior to dissolution, the surface area of each pellet was estimated using measurements made with digital callipers, this was used to calculate the surface area to volume ratio for each sample, ensuring it did not deviate significantly. The mass of each pellet was also recorded.

60 mL PTFE vessels and baskets were cleaned firstly by soaking in 1 vol% Decon90 solution for 24 hours. Vessels were then rinsed three times with UHQ before soaking in 5 vol% technical grade HNO_3 for a further 24 hours. Vessels were then rinsed with UHQ once more before qualification. Qualification of the PTFE vessels involved filling each vessel with UHQ, weighing them, and placing them in a 90 °C oven for 24 hours. Vessels with evaporative losses < 10% were considered qualified and ready for use in the ASTM C1308 study. The same process was repeated for containers used to store the 0.01 M HNO_3 dissolution medium and 2% HNO_3 acid strip solution.

Sampling after each timepoint firstly involved the transferal of pellets to clean PTFE vessels, containing 30 mL of new 0.01 M HNO_3 solution, which were immediately returned to the oven. Replacement HNO_3 solutions were pre-heated to 90 °C to help maintain a consistent dissolution temperature. A 10 mL aliquot of the leachate solution from the removed PTFE pot was then pipetted into centrifuge tubes to collect samples for ICP-MS analysis. A separate 10 mL aliquot was collected for pH measurements, whilst the remaining 10 mL was disposed of. A pH probe was used to confirm solutions of 0.01 M maintained a stable pH of ~2. Empty vessels were then dried prior to acid stripping. The acid strip procedure involved pipetting 30 mL of 2% HNO_3 (equal to the volume of 0.01 M HNO_3 used during dissolution) into PTFE vessels after each dissolution timepoint. The acid strip duration was 2 hours at ambient room temperature. A 10 mL aliquot of this acid strip solution was then pipetted into centrifuge tubes for ICP-MS analysis. All aliquots were collected unfiltered to avoid issues with contamination from the PTFE filters and syringes. Leachate solutions, collected in triplicate, were diluted 10x with HNO_3 prior to measurement. Acid strip and blank solutions, also collected in triplicate, did not require dilution.

3.2.20 Total digest procedure

Performing a total digest allows for accurate determination of a sample's composition through aqueous solution measurements using ICP-OES or ICP-MS. Preparation of total digest solutions involved firstly crushing sintered materials using a pestle and mortar to produce a

fine powder. Small amounts (~20 mg) of crushed material were transferred into 15 mL PTFE vessels, which were filled with 5 mL of 8 M HNO_3. Samples were heated in a 90 °C oven for 7 days under continuous stirring from a magnetic plate, causing complete dissolution of the powders. The resulting total digest solutions were then diluted with HNO_3 and analysed in triplicate using ICP-OES. Relative masses of measured elements were normalised and converted to molar fractions to provide calculated chemical compositions. Quoted errors are the standard deviation between repeat measurements.

3.2.21 Inductively coupled plasma – optical emission spectroscopy

Inductively coupled plasma – optical emission spectroscopy (ICP-OES) is a technique used to determine the concentration of elements in a solution. ICP-OES measurements involve atomising and ionising elements contained within the solution using an Ar^+ plasma torch. The resulting electronic relaxations in the ionised atoms generate a spectrum of visible light unique to each element[31]. The measured emission spectra are compared to spectra of standards with known concentrations, allowing for calculation of the elemental composition within the aqueous solution. In this work, a Thermofisher iCAP 6300 Duo ICP-OES instrument was used to analyse the composition of total digest solutions, relative to a 5-point calibration curve

3.2.22 Inductively coupled plasma – mass spectroscopy

Inductively coupled plasma – mass spectroscopy (ICP-MS) is another technique used to perform compositional analysis of aqueous solutions. ICP-MS exploits the same principles of atomisation and ionisation described for ICP-OES, but instead of measurement of optical emissions, ICP-MS discerns elemental composition *via* separating ions by their mass to charge ratio using a mass spectrometer[32]. Mass spectroscopy is a more precise method of identifying ions than optical emission spectroscopy, allowing for accurate measurements even at extremely low elemental concentrations on the order of parts per trillion. For this reason, leachate solutions from the ASTM C1308 dissolution study were analysed using a Thermofisher RQ ICP-MS instrument, coupled with an ESI-prep Prepfast autosampler. Calibration was performed using a 10 point calibration curve.

3.2.23 X-ray absorption near edge structure spectroscopy

X-ray Absorption Near Edge Structure (XANES) spectroscopy can reveal information about the oxidation state and local coordination of a specific element. XANES involves the analysis of a specific region of the spectra obtained through X-ray absorption spectroscopy (XAS) measurements. XAS spectra are generated by exciting core electrons within a material through the absorption of photons tuned to specific energies. XAS spectra feature characteristic ‘edges’ corresponding to specific photon energies that were most readily

absorbed by the specimen. The energies of these edges correspond to the discrete energy levels associated with orbitals in different shells. The absorption edges associated with electrons within the n = 1 shell are termed K edges, whereas edges associated with n = 2 are termed L, and those associated with n = 3 are referred to as M edges. Energy differences also exist between orbitals within each energy level. The numbers following each letter (K, L, or M) correspond to the orbitals within these energy levels. For example, the M_1 edge is associated with X-ray absorption by electrons in a 3s orbital, M_2 and M_3 are associated with electrons in 3p whilst M_4 and M_5 result from excitation of electrons in 3d. The relative energies of orbitals and their associated edges are outlined in Figure 23.

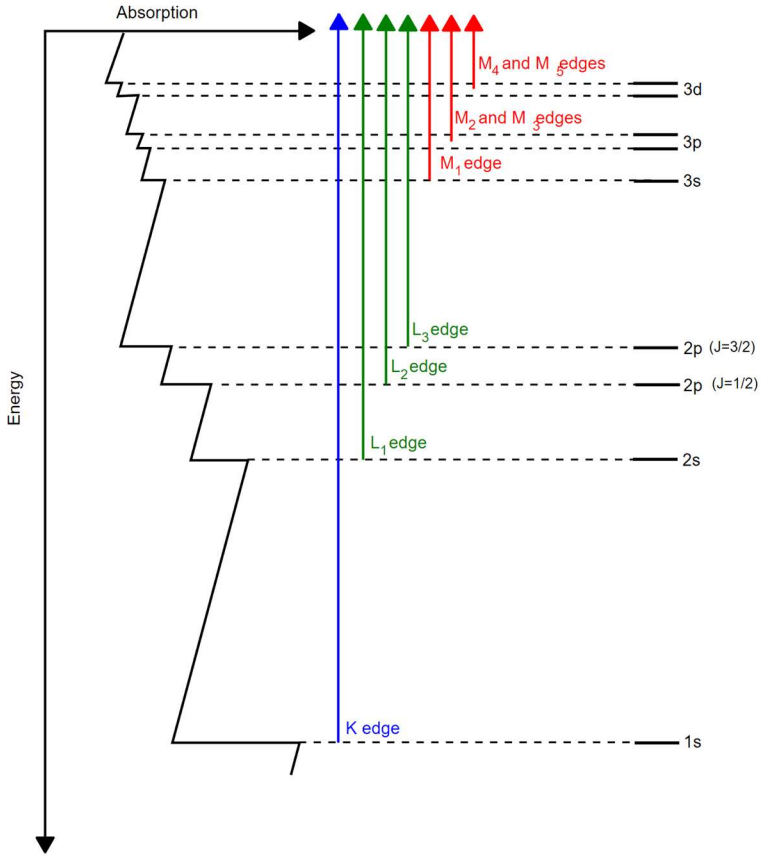

Figure 23: Schematic illustrating the relationship between electron orbital energy and corresponding XAS edges. Tenderholt (2008)[33].

In XAS experiments, specific edges are targeted by tuning the photon energy using a monochromator. The different regions of an XAS spectrum, outlined in Figure 24, can be analysed to reveal a variety of information about the specimen. The XANES region of an XAS spectrum is typically defined up to 50 eV higher than the edge position and encompasses the peaks and shoulders near the absorption edge. Analysis of this region allows for determination of the oxidation state and coordination environment of the absorbing atom.

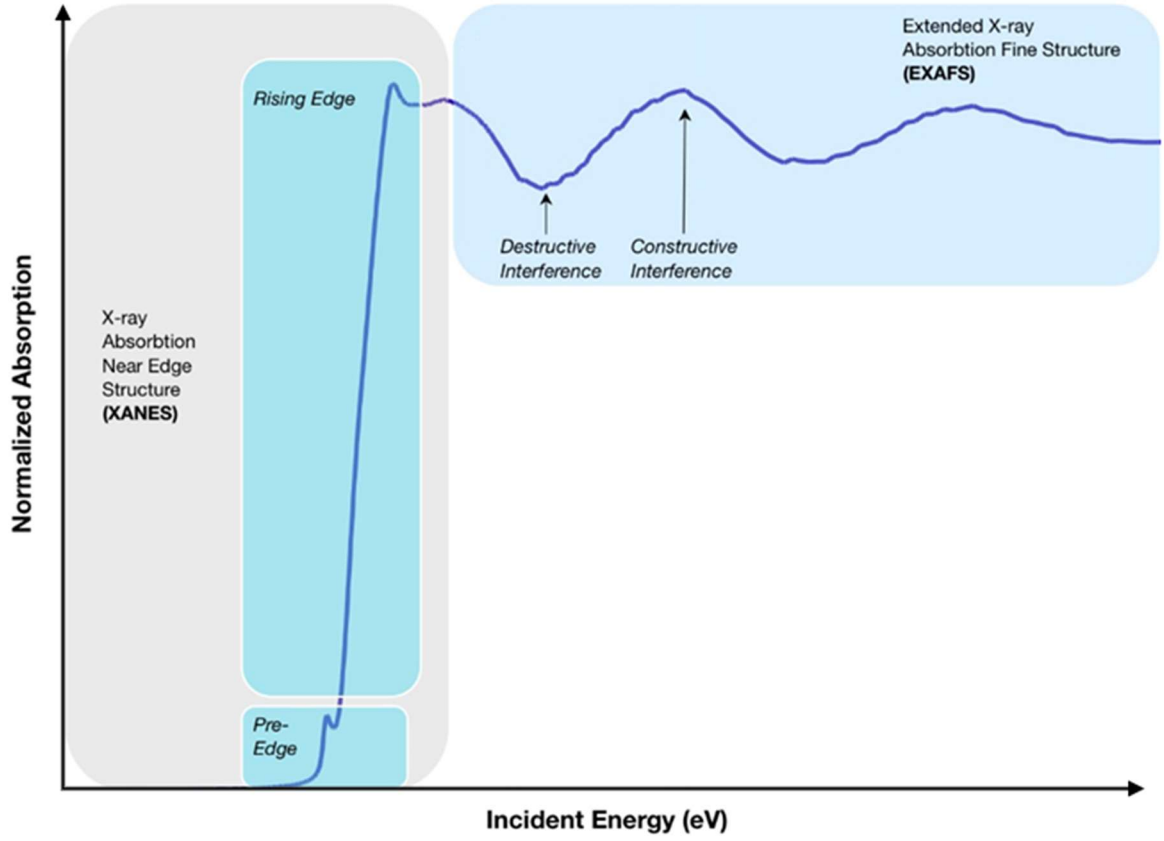

Figure 24: Example XAS spectrum illustrating major regions of XAS analysis. Adapted from Qayyum (2010).

Collection of the U M_4-edge HERFD-XANES data (presented in Chapter 4) was performed at the European Synchrotron Radiation Facility (ESRF) on the Rossendorf ROBL beamline. Fitting was performed using iterative transformation factor analysis[34] (ITFA) and linear combination fitting (LCF). All XAS data was processed and calibrated using Athena from the Demeter Software Package[35]. Further experimental information is detailed in the paper contained within Chapter 6.

References

1. Claparede, L. *et al.* Influence of Crystallization State and Microstructure on the Chemical Durability of Cerium–Neodymium Mixed Oxides. *Inorg. Chem.* **50**, 9059–9072 (2011).
2. Callister, W. D. & Rethwisch, D. G. *Materials science and engineering*. (Wiley, 2015).
3. Buehler. Polishing Application Guide. (2018).
4. *The Rietveld method*. (Oxford Univ. Press, 2002).
5. Thompson, N. B. A., Stennett, M. C., Gilbert, M. R. & Hyatt, N. C. Nuclear forensic signatures and structural analysis of uranyl oxalate, its products of thermal decomposition and Fe impurity dopant. *J Radioanal Nucl Chem* **327**, 957–973 (2021).
6. Gilson, T. R. & Hendra, P. J. *Laser Raman spectroscopy: a survey of interest primarily to chemists, and containing a comprehensive discussion of experiments on crystals*. (Wiley-Interscience, 1970).
7. Orlando, A. *et al.* A Comprehensive Review on Raman Spectroscopy Applications. *Chemosensors* **9**, 262 (2021).
8. Schmitt, R. *et al.* A review of defect structure and chemistry in ceria and its solid solutions. *Chem. Soc. Rev.* **49**, 554–592 (2020).
9. Heath, J. & Taylor, N. Wavelength-dispersive (X-ray) Spectroscopy. (2016).
10. Krumeich, F. SEM: Imaging with Secondary Electrons. (2022).
11. Tokariev, O., Schnetter, L., Beck, T. & Malzbender, J. Grain size effect on the mechanical properties of transparent spinel ceramics. *Journal of the European Ceramic Society* **33**, 749–757 (2013).
12. Öijerholm, J., Pan, J. & Jönsson, B. Influence of Grain-Size on Ionic Conductivity of Pure and Dense α-Al_2O_3 in the Temperature Range 400 - 1000 °C. *MSF* **461–464**, 865–874 (2004).
13. Grover, V. *et al.* Effect of grain size and microstructure on radiation stability of CeO_2 : an extensive study. *Phys. Chem. Chem. Phys.* **16**, 27065–27073 (2014).
14. Clinton, D. J. *A guide to polishing and etching of technical and engineering ceramics*. (Institute of Ceramics, 1987).

15. Legland, D., Arganda-Carreras, I. & Andrey, P. MorphoLibJ: integrated library and plugins for mathematical morphology with ImageJ. *Bioinformatics* btw413 (2016) doi:10.1093/bioinformatics/btw413.
16. Schindelin, J. *et al.* Fiji: an open-source platform for biological-image analysis. *Nat Methods* **9**, 676–682 (2012).
17. Oxford Instruments. Principle Components of an Electron Backscatter Diffraction (EBSD) System. (2021).
18. Rotty, C., Mandroyan, A., Doche, M.-L. & Hihn, J. Y. Electropolishing of CuZn brasses and 316L stainless steels: Influence of alloy composition or preparation process (ALM vs. standard method). *Surface and Coatings Technology* **307**, 125–135 (2016).
19. Koblischka-Veneva, A., Koblischka, M. R., Schmauch, J. & Murakami, M. Transmission EBSD (t-EBSD) as Tool to Investigate Nanostructures in Superconductors. *J Supercond Nov Magn* **32**, 3155–3163 (2019).
20. Williams, D. B. & Carter, C. B. *Transmission electron microscopy: a textbook for materials science*. (Springer, 2008).
21. Llovet, X. Electron Probe Microanalysis. in *Reference Module in Chemistry, Molecular Sciences and Chemical Engineering* B9780124095472143690 (Elsevier, 2018). doi:10.1016/B978-0-12-409547-2.14369-0.
22. Newbury, D. E. Quantitative electron probe microanalysis of rough targets: Testing the peak-to-local background method. *Scanning* **26**, 103–114 (2006).
23. Kumar, A., Reed, J. & Sant, G. Vertical scanning interferometry: A new method to measure the dissolution dynamics of cementitious minerals. *Journal of the American Ceramic Society* **96**, 2766–2778 (2013).
24. Koyuncu, I., Brant, J., Lüttge, A. & Wiesner, M. R. A comparison of vertical scanning interferometry (VSI) and atomic force microscopy (AFM) for characterizing membrane surface topography. *Journal of Membrane Science* **278**, 410–417 (2006).
25. Godinho, J. R. A., Putnis, C. V. & Piazolo, S. Direct Observations of the Dissolution of Fluorite Surfaces with Different Orientations. *Crystal Growth & Design* **14**, 69–77 (2014).

26. Fischer, C., Finkeldei, S., Brandt, F., Bosbach, D. & Luttge, A. Direct Measurement of Surface Dissolution Rates in Potential Nuclear Waste Forms: The Example of Pyrochlore. *ACS Appl. Mater. Interfaces* **7**, 17857–17865 (2015).
27. Saito, T., Hirayama, T., Yamamoto, T. & Ikuhara, Y. Lattice strain and dislocations in polished surfaces on sapphire. *Journal of the American Ceramic Society* **88**, 2277–2285 (2005).
28. Godinho, J. R. A., Piazolo, S. & Evins, L. Z. Effect of surface orientation on dissolution rates and topography of CaF_2. *Geochimica et Cosmochimica Acta* **86**, 392–403 (2012).
29. Cordara, T. *et al.* Kinetics of dissolution of UO_2 in nitric acid solutions: A multiparametric study of the non-catalysed reaction. *Journal of Nuclear Materials* **496**, 251–264 (2017).
30. C26 Committee. *Test Method for Accelerated Leach Test for Diffusive Releases from Solidified Waste and a Computer Program to Model Diffusive, Fractional Leaching from Cylindrical Waste Forms*. http://www.astm.org/cgi-bin/resolver.cgi?C1308-08R17 doi:10.1520/C1308-08R17.
31. He, M., Hu, B., Chen, B. & Jiang, Z. Inductively Coupled Plasma Optical Emission Spectrometry for Rare Earth Elements Analysis. *Physical Sciences Reviews* **2**, (2017).
32. Wilschefski, S. & Baxter, M. Inductively Coupled Plasma Mass Spectrometry: Introduction to Analytical Aspects. *CBR* **40**, 115–133 (2019).
33. Tenderholt, A. L. *et al.* Electronic Control of the “Bailar Twist” in Formally d^0-d^2 Molybdenum Tris(dithiolene) Complexes: A Sulfur K-edge X-ray Absorption Spectroscopy and Density Functional Theory Study. *Inorg. Chem.* **47**, 6382–6392 (2008).
34. Rossberg, A. *et al.* Identification of Uranyl Surface Complexes on Ferrihydrite: Advanced EXAFS Data Analysis and CD-MUSIC Modeling. *Environ. Sci. Technol.* **43**, 1400–1406 (2009).
35. Ravel, B. & Newville, M. *ATHENA* , *ARTEMIS* , *HEPHAESTUS* : data analysis for X-ray absorption spectroscopy using *IFEFFIT*. *J Synchrotron Rad* **12**, 537–541 (2005).

4. Demonstration of the disposal-MOX concept for plutonium immobilisation

The following chapter is a draft manuscript prepared for submission to Scientific Reports.

Demonstration of the disposal-MOX concept for plutonium immobilisation

Max R. Cole[1], Lewis R. Blackburn[1], Latham Haigh[1], Luke T. Townsend[1], Sarah E. Pepper[1], Stuart Creasey-Gray[2], Daniel J. Bailey[1], Kristina O. Kvashnina[3,4], Neil C. Hyatt[1] and Claire L. Corkhill[1]*

[1]NucleUS Immobilisation Science Laboratory, Department of Materials Science and Engineering, University of Sheffield, UK

[2]Sorby Centre for Electron Microscopy, Kroto Research Institute, University of Sheffield, UK

[3]Helmholtz-Zentrum Dresden-Rossendorf (HZDR), Institute of Resource Ecology, PO Box 510119, 01314, Dresden, Germany

[4]The Rossendorf Beamline at ESRF – The European Synchrotron, CS40220, 38043 Grenoble Cedex 9, France

*Corresponding author: c.corkhill@sheffield.ac.uk

Abstract

Disposal Mixed OXide (disposal-MOX) materials offer an alternative route for the immobilisation and disposition of surplus Pu inventories. Simulant disposal-MOX wasteforms, in which U^{4+} cations are substituted with Th^{4+} and Gd^{3+}, were fabricated *via* wet co-precipitation, and solid state synthesis routes, to compare the effects of composition and fabrication method on the phase formation and microstructure. Th^{4+}, employed as a Pu^{4+} surrogate, was added in two different quantities to reflect realistic potential Pu^{4+} loadings. Sufficient quantities of Gd^{3+} were incorporated as a neutron poison to ensure the real system would remain subcritical in the presence of Pu-239. In total, four compositions of disposal-MOX were synthesised, following the general formula $U_{1-(x+y)}Th_xGd_yO_{2-\delta}$, where x = 0.1 or 0.2 and $x:y$ = 1:10 or 1:100. Precursors of the four compositions were synthesised *via* solid state and wet co-precipitation methods to compare the effects of both composition and fabrication route. Upon heat-treatment at 1700°C under a reducing atmosphere, the resulting sintered pellets were characterised as single phase cubic fluorite (Fm-3m). The grain size was similar to $(Pu,U)O_2$ MOX fuel, and was found to be independent of the synthesis route. The relative density of sintered pellets was > 90% but was higher in co-precipitated materials. Th^{4+} and Gd^{3+} additions were distributed more homogenously in co-precipitated samples. Though no unincorporated ThO_2 or Gd_2O_3 was observed in any sample, larger Th^{4+} and Gd^{3+}-rich agglomerates were measured using electron microprobe analysis in materials produced through solid state synthesis. The incorporation of Gd^{3+} within the fluorite lattice was charge balanced *via* the generation of oxygen vacancy defects, as evidenced by Raman spectroscopy

analysis. The proportion of U^{5+}, as determined by high energy resolution fluorescence detection X-ray absorption near edge spectroscopy (HERFD-XANES), was found to be independent of Gd^{3+} content, and was greater in co-precipitated materials. These results demonstrate successful synthesis of single phase disposal-MOX *via* both solid state and wet co-precipitation fabrication routes.

1. Introduction

The United Kingdom inventory of separated Pu is forecast to exceed 140 teHM (tonnes equivalent heavy metal). At present, the long-term management strategy for separated PuO_2, as outlined by the Nuclear Decommissioning Authority (NDA), stipulates that at least some portion of this inventory will require chemical immobilisation to place beyond reach[1]. Therefore, there is a requirement to develop wasteform materials capable of accommodating Pu whilst conferring passive safety that is compatible with geological disposal. Zirconate and titanate ceramics (*e.g.* zirconolite, pyrochlore) have been proposed as suitable wasteforms for Pu and other actinides on the basis of their high chemical durability and radiation stability, in both synthetic and ancient natural specimens[2–5]. Although the feasibility of actinide immobilisation within titanate ceramics has been demonstrated at the laboratory scale, large scale production of these nuclear wasteforms has not yet been demonstrated.

Disposal Mixed Oxide, herein referred to as 'disposal-MOX', and previously referred to as 'storage-MOX', presents a promising alternative for the immobilisation of Pu, not least because the technology to fabricate MOX fuels at an industrial scale for use in nuclear energy generation in certain countries, such as France, is mature[6]. The storage-MOX plan, outlined by Macfarlane *et al.*, would involve fabricating a simple low specification MOX through the addition of separated PuO_2 to UO_2[7]. This material might then be disposed of alongside other high heat generating wastes in a geological disposal environment. Should a pathway of immobilisation and geological disposal be chosen to satisfy long-term management requirements for Pu stockpiles, the incorporation of Pu in disposal-MOX materials will therefore benefit from a wealth of existing knowledge surrounding UO_2 and MOX fuels, including synthesis, dissolution behaviour, effects of water radiolysis, radiation stability, and the generation of gaseous alpha radiation products such as He. The immobilisation of Pu within a disposal-MOX waste package would see dilute concentrations of PuO_2 accommodated in solid solution with UO_2 alongside a requisite quantity of neutron absorbing additive, e.g. Gd_2O_3, to maintain an effective neutron multiplication factor (k_{eff}) < 1. For effective neutron multiplication factor describes the average number of neutrons from one fission that cause another fission, maintaining a value < 1 mitigates the risk of near-field criticality in the disposal environment.

Oxides of Pu and U adopt the cubic fluorite (Fm-3m) with comparable lattice dimensions (a = b = c = 5.470 Å and 5.398 Å for UO_2 and PuO_2, respectively)[8], as shown in Figure 1. Furthermore, UO_2 and PuO_2 have similar densities, of 10.97 and 10.50 g cm^{-3}, respectively, and comparable melting points of 2827 and 2400 °C. At the elevated temperatures used in wasteform processing (~1700 °C), there exists a complete solid solution between UO_2 and PuO_2 (in the form $U_{1-x}Pu_xO_2$), resulting in a relatively homogenous, single phase material[9,10]. The neutron absorbing additive Gd_2O_3, typically adopts a cubic bixbyite (Ia-3) or monoclinic (C2/m) structure in its pure form. However, UO_2 – Gd_2O_3 solid solutions can maintain the fluorite (Fm-3m) structure with the addition of 50 mol% Gd, far above the concentrations necessary to mitigate criticality[11]. Within the context of disposal in a geological facility, the adoption of the fluorite structure is advantageous since UO_2 and MOX fuels are known to retain high aqueous durability under reducing conditions[12,13]. Moreover, the addition of Gd has been shown to reduce U release during dissolution[14,15]. Fluorite type materials also exhibit high tolerance to radiation damage and can readily accommodate He gas generated through alpha decay[16,17].

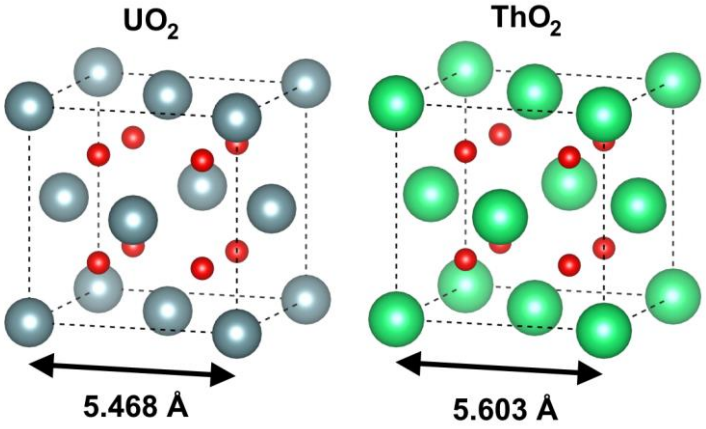

Figure 1: Crystal structures of UO_2 (left) and PuO_2 (right). Both materials adopt the cubic fluorite structure (space group Fm-3m).

To validate the concept of disposal-MOX, we here describe an investigation of several disposal-MOX materials varying in composition and fabrication route. Oxide precursors were prepared through wet co-precipitation and conventional solid state mixed oxide synthesis routes to assess the influence of homogenisation on final sintered materials. Wet co-precipitation yields highly homogenous oxide precursors through liquid mixing, whereas solid state synthesis typically achieves less homogenous oxide mixtures through milling. The solid state fabrication route devised for this study was adapted from the MIMAS (MIcronized MASterblend) process used to fabricate MOX fuel at the MELOX facility in France. This

involves blending and milling UO_2 and PuO_2 powders into a 'master' blend before diluting with additional UO_2 to achieve the desired U:Pu ratio[18].

Samples were characterised to ascertain the control that chemical composition and synthesis route exert on the final sintered microstructure, crystalline defects, distribution of the neutron absorber Gd, and oxidation state of U. Ce is commonly used as Pu surrogate, however, Th was employed in this study for its comparatively stable redox behaviour. The tendency of Ce^{4+} to reduce to Ce^{3+} under the high temperatures and reducing conditions required to sinter disposal-MOX materials[19,20] would render Ce an impractical surrogate in this context. Furthermore, Ce^{3+} is known to readily form at exposed surfaces, even under relatively oxidising conditions[21,22]. Ensuring the Pu surrogate remained in its +4 oxidation state permitted a simpler investigation into the influence of aliovalent Gd^{3+} on the generation of U^{5+} and V_O within the structure. The use of Th^{4+} avoided the complications associated with having multiple redox sensitive cations present in the same system. It must be noted, however, that Th^{4+} has a larger ionic radius than Pu^{4+} in 8-fold co-ordination (1.05 Å and 0.96 Å respectively[8]) whereas the ionic radius of Ce^{4+} (0.97 Å) is far closer to that of Pu^{4+}. Employing a Ce^{4+} surrogate in disposal-MOX analogues will induce a lattice contraction representative of Pu^{4+} when substituted into UO_2 compared to Th^{4+}, which induces lattice expansion as its ionic radius is larger than U^{4+}. This investigation was primarily concerned with understanding the potential influence of Gd^{3+} additions on the generation of U^{5+} and V_O within disposal-MOX materials, as opposed to understanding the effect of Pu^{4+} on the UO_2 unit cell.

2. Experimental methodology and characterisation

2.1 Material synthesis

To investigate the effect of varying Th and Gd loading, four distinct disposal-MOX compositions were formulated, as shown in Table 1. Th was added to UO_2 in amounts of 10 and 20 mol%, while Gd additions were made in two different ratios relative to the Th content: 1:10 and 1:100 (Gd:Th). The Th additions of 10 and 20 mol% represent realistic lower and upper bounds of Pu content that could be incorporated within disposal-MOX. Similarly, the 1:100 ratio of Gd:Th reflects a realistic estimate of the ratio of Gd:Pu required for criticality considerations in a disposal environment based on calculations assuring $K_{eff} < 1$. The greater 1:10 ratio was devised to investigate the effects of excessive Gd addition. The four compositions were produced using two distinct fabrication routes, wet co-precipitation, and solid state mixed oxide synthesis, yielding a total of eight unique samples. Herein, samples will be referred to by their compositions as measured by Inductively Coupled Plasma-Optical Emission Spectroscopy (ICP-OES) following nitric acid digest (Table 1).

Table 1: Details of disposal-MOX compositions. Quoted errors in total digest compositions were derived from the standard deviation of three repeat ICP-OES measurements. Errors in EPMA were derived from the standard deviation of five repeated quantitative spot measurements.

Synthesis method	Target Th/Gd content	Target composition	Measured composition (Total digest)	Measured composition (EMPA)
Co-prec.	$Th_{0.1}$ Gd 1:100	$U_{0.899}Th_{0.100}Gd_{0.001}O_{2-\delta}$	$U_{0.848(7)}Th_{0.146(7)}Gd_{0.006(2)}O_{2-\delta}$	$U_{0.825(3)}Th_{0.174(2)}Gd_{0.001(1)}O_{2-\delta}$
	$Th_{0.1}$ Gd 1:10	$U_{0.890}Th_{0.100}Gd_{0.010}O_{2-\delta}$	$U_{0.835(5)}Th_{0.131(3)}Gd_{0.034(2)}O_{2-\delta}$	$U_{0.827(3)}Th_{0.165(2)}Gd_{0.008(1)}O_{2-\delta}$
	$Th_{0.2}$ Gd 1:100	$U_{0.798}Th_{0.200}Gd_{0.002}O_{2-\delta}$	$U_{0.758(1)}Th_{0.234(9)}Gd_{0.008(0)}O_{2-\delta}$	—
	$Th_{0.2}$ Gd 1:10	$U_{0.780}Th_{0.200}Gd_{0.020}O_{2-\delta}$	$U_{0.666(6)}Th_{0.266(4)}Gd_{0.069(2)}O_{2-\delta}$	$U_{0.655(3)}Th_{0.331(2)}Gd_{0.014(1)}O_{2-\delta}$
Solid state	$Th_{0.1}$ Gd 1:100	$U_{0.899}Th_{0.100}Gd_{0.001}O_{2-\delta}$	$U_{0.889(3)}Th_{0.106(3)}Gd_{0.005(1)}O_{2-\delta}$	$U_{0.779(3)}Th_{0.221(3)}Gd_{0.000(1)}O_{2-\delta}$
	$Th_{0.1}$ Gd 1:10	$U_{0.890}Th_{0.100}Gd_{0.010}O_{2-\delta}$	$U_{0.866(3)}Th_{0.105(2)}Gd_{0.029(2)}O_{2-\delta}$	$U_{0.863(3)}Th_{0.130(1)}Gd_{0.007(1)}O_{2-\delta}$
	$Th_{0.2}$ Gd 1:100	$U_{0.798}Th_{0.200}Gd_{0.002}O_{2-\delta}$	$U_{0.801(4)}Th_{0.192(4)}Gd_{0.008(7)}O_{2-\delta}$	—
	$Th_{0.2}$ Gd 1:10	$U_{0.780}Th_{0.200}Gd_{0.020}O_{2-\delta}$	$U_{0.759(4)}Th_{0.187(4)}Gd_{0.054(2)}O_{2-\delta}$	—

Wet co-precipitated samples were prepared through an oxalic precipitation route. Firstly, $UO_2(NO_3)_2{\cdot}6H_2O$ (British Drug House (BDH). B.D.H Laboratory Chemicals Division, > 98%), $Th(NO_3)_4{\cdot}6H_2O$ (British Drug House (BDH). B.D.H Laboratory Chemicals Division, > 98%) and $GdCl_3{\cdot}6H_2O$ (Sigma Aldrich, > 99%) were dissolved in 1 M HCl to create solutions of known concentrations. Specific volumes of each solution, corresponding to the target chemical formula shown in Table 1, were mixed with the aid of a magnetic stirrer, before the addition of 1 M oxalic acid brought about the instantaneous precipitation of an oxalate precipitate. The precipitates were filtered and dried prior to calcination at temperatures ranging from 400 °C to 800 °C under a 5% H_2 / 95% N_2 atmosphere, yielding a fine oxide powder. Approximately 200 mg of oxide powder calcined at 800 °C was pressed within a 6 mm stainless steel die to form loosely densified green bodies. Green bodies were placed within a zirconia crucible and sintered at 1700 °C for 8 hours under a reducing 5% H_2 / 95% N_2 gas atmosphere, with a heating and cooling rate of 3 °C min^{-1}.

The solid state synthesis route was devised to resemble the MIMAS (MIcronized MASterblend) process developed by BelgoNucleaire, by which the majority of commercial MOX fuels are fabricated[23]. The two-step MIMAS process involves creating a ‘master’ blend of UO_2 and PuO_2, that is subsequently diluted with UO_2 to achieve the desired U:Pu ratio in the final material. For this study, two master blends, corresponding with the two target Th:Gd ratios (1:100 and 1:10), were made by mixing appropriate masses of UO_2 (ABSCO Ltd., > 98%), ThO_2 (calcined from $Th(NO_3)_4{\cdot}6H_2O$, B.D.H Laboratory Chemicals Division, > 98%), and Gd_2O_3 (Sigma Aldrich, > 99.9%) powders. Master blends were mixed and micronised using a pestle and mortar to mimic the homogenisation of real MIMAS blends produced using dry ball milling[24]. The oxide powders were ground and mixed for 30 minutes in propan-2-ol, resulting powder slurries were dried overnight at 80 °C to evaporate excess solvent. Both 1:100 and 1:10 Gd:Th master blends were finally diluted with appropriate masses of UO_2

powder to achieve the four target compositions (detailed in Table 1). UO_2 was mixed into each blend using the same procedure used to produce the master blends.

2.2 Material characterisation

Thermal analysis was performed on the oxalate precipitates using a Netzsch TG 449 F3 Jupiter thermal analyser. Data was collected from simultaneous thermogravimetric (TG) and differential thermal (DT) analysis, in tandem with mass spectroscopy (MS), as oxalates were heated to temperatures of 1000 °C with a temperature ramp rate of 10 °C min^{-1}.

Powder X-ray diffraction (XRD) analysis was performed on all precursors and sintered materials using a Bruker D2 Phaser fitted with a Lynxeye position sensitive detector; data were acquired using a Cu-Kα source (λ = 1.5418 Å, Ni filter) in the ranges $20° \leq 2\theta \leq 80°$ (sintered materials) and $5° \leq 2\theta \leq 60°$ (precursors), with a step size of 0.02°. Sintered powders were mixed with 10 wt% LaB_6 as an internal standard to improve quality of lattice parameter refinements, which were run using the Rietveld method through the Bruker TOPAS software package.

Compositional measurements made using a total digest method involved the complete dissolution of 20 mg of crushed, sintered material in 2 M HNO_3 at 60 °C. Solid samples were completely dissolved after 3 days at 90 °C, with the aid of constant mixing. The total digest solutions were then diluted by a factor of 20 and analysed in triplicate using ICP-OES (ThermoFisher iCAPDuo6300). External calibration was performed using single element standards (NIST traceable). All standards and samples were matrix matched to 1% HNO_3. Quality control samples were run after the calibration and every 10 samples thereafter.

Sintered pellet density was measured using a METTLER TOLEDO ME204 Archimedes balance. Ten repeat measurements were collected for each sample; the quoted error was calculated using the standard deviation of these measurements. Theoretical densities for each composition were calculated using the refined lattice parameters, and the relative density of each pellet was then calculated by dividing its measured density by the theoretical.

Analysis of powder morphology and pellet microstructure was conducted using a Hitachi TM3030 SEM operating in backscattered electron (BSE) mode. EDS maps of powder samples were collected for a minimum of 10 minutes. Sintered pellets were polished to 1 μm and thermally etched at 1630 °C (90% of sintering temperature) to reveal the grain boundaries, allowing for grain size analysis through morphological segmentation using the MorphoLibJ plug-in suite[25] through the Fiji software package[26]. A minimum of 500 grains were analysed across several micrographs taken at random across the pellet surface to obtain a statistical average for each sample.

Electron Probe Micro-analysis (EPMA) was undertaken using a JEOL JXA-8530F Plus Hyper Probe with an accelerating voltage of 15 kV and a probe current 100 nA. Compositions were measured using a minimum of five quantitative spot measurements, each at the centre of grains across the surface. Sintered pellets were polished to 1 µm prior to carbon coating. EPMA maps were collected for U, Th, Gd and O in stage mode, allowing the probe incident angle to remain constant during measurements to avoid errors associated with interaction volume changes. Channels, crystals, and peaks selected for each element can be found in Table S1 in the supplementary information.

A Renishaw inVia microscope was used to conduct Raman spectroscopy on polished, annealed sintered pellets. Five measurements were taken in the centre of grains across the surface of each pellet. Each spectrum consisted of 15 acquisitions, each collected over 30 seconds using a 514 nm laser, set to 5 mW to minimise risk of oxidation. These spectra were baseline subtracted, smoothed using the Savitsky-Golay approach[27] and averaged. Deconvolution of the spectra was performed using Igor Pro software through the application of Gaussian peaks; the position of the U_3 was constrained, all other parameters were left to refine.

Uranium M_4-edge high energy resolution fluorescence detection X-ray absorption near edge spectroscopy (HERFD-XANES) was performed on the BM20 (ROBL) beamline at the European Synchrotron Radiation Facility (ESRF). The U M_4-edge (3.725 keV) was selected with a Si(111) double-crystal monochromator, and HERFD-XANES spectra were collected with five Si(220) crystal analysers at room temperature. Normalised U^{5+} content was determined using iterative transformation factor analysis (ITFA) and linear combination fitting (LCF) methods. All XAS data were processed using the Athena from the Demeter Software Package[28]. Linear combination fitting (LCF) was performed using Athena[28], with KUO_3 and UO_2 spectra (collected at the same beamtime as the samples) chosen as the most suitable standards. The proportion of U^{4+} and U^{5+} was further investigated and defined using the ITFA software package[29].

3. Results and discussion

3.1 Characterisation of oxalate powders

Oxalate powders of each composition were found to crystallise in the monoclinic space groups P21/c, and C2/c, characteristic of uranium and thorium oxalate respectively[30], as shown in Figure 2a. Particles adopted a platelet morphology upon precipitation, with each platelet measuring roughly 5 µm in all samples. EDS mapping indicated that each platelet contained a homogenous distribution of U, Th and Gd (Figure 2b).

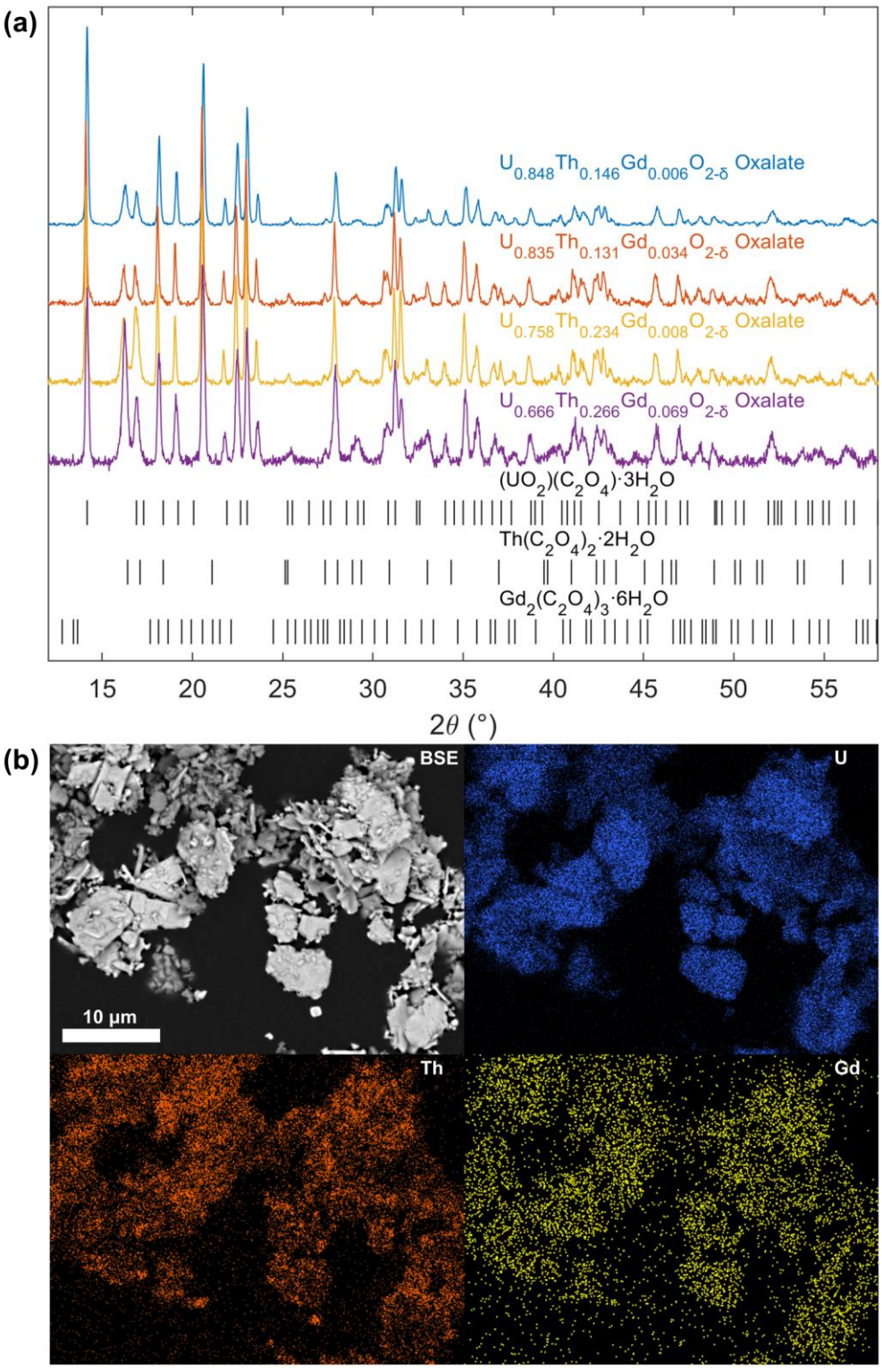

Figure 2: (a) XRD traces of oxalate powders, highlighting reflections indexed to oxalates of U (ICSD 172778), Th (ICSD 248038) and Gd (ICSD 121695). **(b)** BSE micrograph and EDS element distribution maps of the oxalate precursor for the $U_{0.758}Th_{0.234}Gd_{0.008}O_{2-\delta}$ sample, showing homogeneous distribution of each element.

Examination of thermal events during oxalate calcination showed complete decomposition occurred by ~600 °C. Figure 3 shows the thermogravimetric (TG) and differential thermal (DT) data for the decomposition of the oxalate used to produce $U_{0.835}Th_{0.131}Gd_{0.034}O_{2-\delta}$. TG data

revealed two mass losses at temperatures of < 320 °C (T_1 and T_2), corresponding to water loss as the oxalates were dehydrated. A final significant mass loss, at 320 °C (T_3), was attributed to CO_2 evolution during decomposition. Gases were identified using TG-MS presented in Figure S1 in the supplementary information. No further mass losses were measured upon heating beyond 600 °C. DT analysis revealed two endothermic transformations relating to water loss between 90 °C and 320 °C, while exothermic reactions corresponding to CO_2 and CO evolution occurred between 330 °C and 420 °C, in agreement with the TG data. Whilst XRD analysis identified two distinct monoclinic phases (P21/c, and C2/c), neither SEM-EDS nor DT analysis could distinguish two phases in the powders. Thermal events revealed by DT analysis are very similar to those observed in pure $(UO_2)(C_2O_4)\cdot 3H_2O$ [31], and lack the additional endothermic events typically observed around 400 °C in $Th(C_2O_4)_2\cdot 2H_2O$ [32]. It remains unclear whether these precipitates consist of a single mixed (U,Th,Gd) oxalate, or a well homogenised mixture of different oxalate phases with very similar compositions.

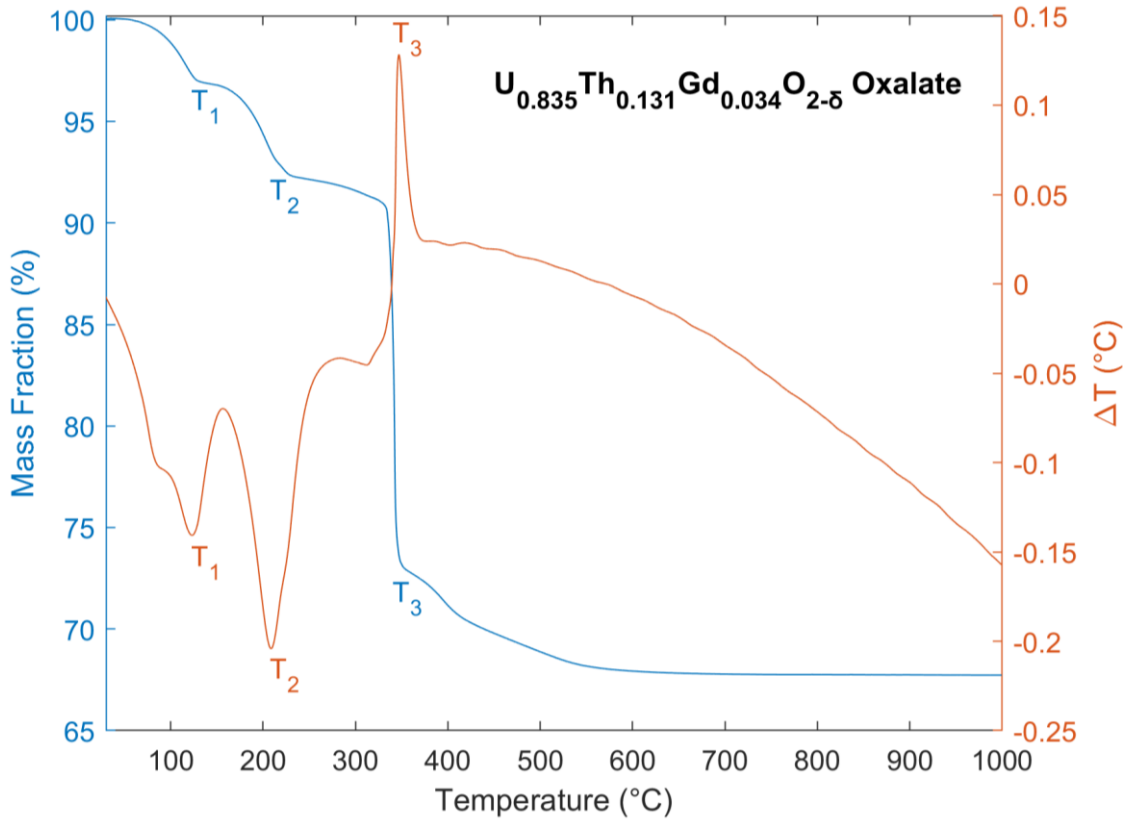

Figure 3: Plot of mass fraction and temperature differential against temperature during decomposition of the uranium, thorium and gadolinium oxalate mixture used to produce the $U_{0.835}Th_{0.131}Gd_{0.034}O_{2-\delta}$ co-precipitated pellets.

Oxide powders of $U_{0.758}Th_{0.234}Gd_{0.008}O_{2-\delta}$ obtained from calcination at 400 °C, 800 °C and 1000 °C were analysed by XRD (Figure 4). Peak broadening observed in the oxide calcined

at 400 °C, when compared with the materials calcined at higher temperature, indicates a significantly smaller crystallite size. Diffraction reflections relating to residual carbon were not observed in either the 800 °C or 1000 °C calcined oxides, suggesting near complete decomposition of the oxalate at these temperatures, in accordance with TG data.

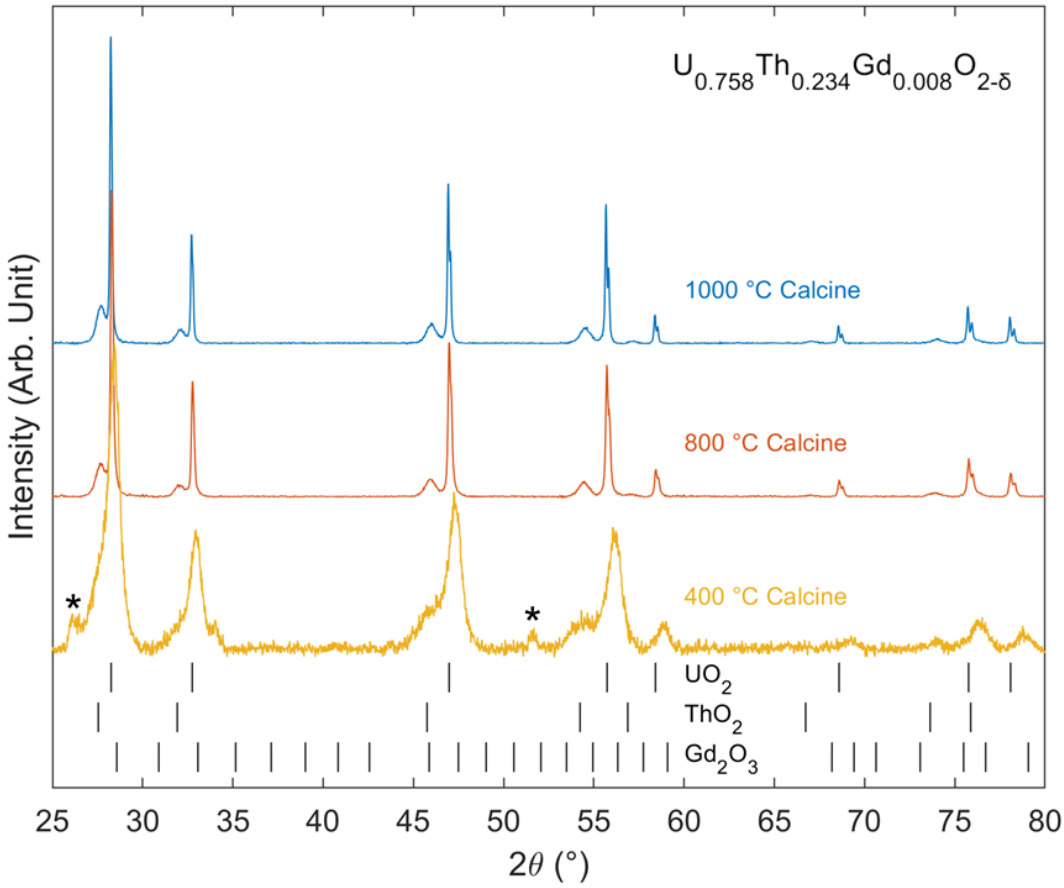

Figure 4: Plot of XRD data collected on $U_{0.758}Th_{0.234}Gd_{0.008}O_{2-\delta}$ oxide powders decomposed from oxalates at 400 °C, 800 °C and 1000 °C. Two sets of fluorite peaks are indexed to UO_2 (ICSD 160814) and ThO_2 (ICSD 253564). Additional peaks denoted with '*' in the 400 °C trace correspond with residual oxalate content, indicating incomplete decomposition. Cubic C-type Gd_2O_3 (ICSD 94892) peaks are absent in all traces.

When determining the optimal calcination temperature, several factors must be considered. Firstly, full decomposition of the oxalate must be ensured; the plateau in mass loss indicates this occurred around 600 °C. Calcination temperature also controls the resulting particle size of the oxide powders, with higher temperatures yielding larger particles. Excessively high calcination temperatures (~1000 °C) will yield powders with decreased reactive surface area, which can inhibit sintering. However, too low a calcination temperature can result in small particles with an excessively high reactive surface area, which can increase the amount of adsorbed gases on the powder surface[33]. Adsorbed gases are released during the subsequent sintering, generating porosity within the final densified pellet. A calcination temperature of 800 °C was used to produce a fully decomposed oxide powder, with a surface area sufficiently

high as to allow adequate sintering, but not excessively high as to avoid extensive gas adsorption. Calcined oxides were re-examined with SEM-EDS, confirming the platelet morphology was maintained following calcination regardless of temperature or composition (Figure S2) and that there was a homogenous distribution of cations.

3.2 Characterisation of calcined oxide powders

For both synthesis routes, the XRD patterns of oxide powders revealed two distinct sets reflections consistent with the cubic fluorite structure (Fm-3m, space group 225), as shown in Figure 5. These reflections were indexed as UO_2 and ThO_2. The peaks corresponding to ThO_2 are visible at lower 2θ angles than UO_2 due to the larger Shannon crystal radius of Th^{4+} compared to U^{4+} in 8-fold coordination (1.19 Å and 1.14 Å, respectively).

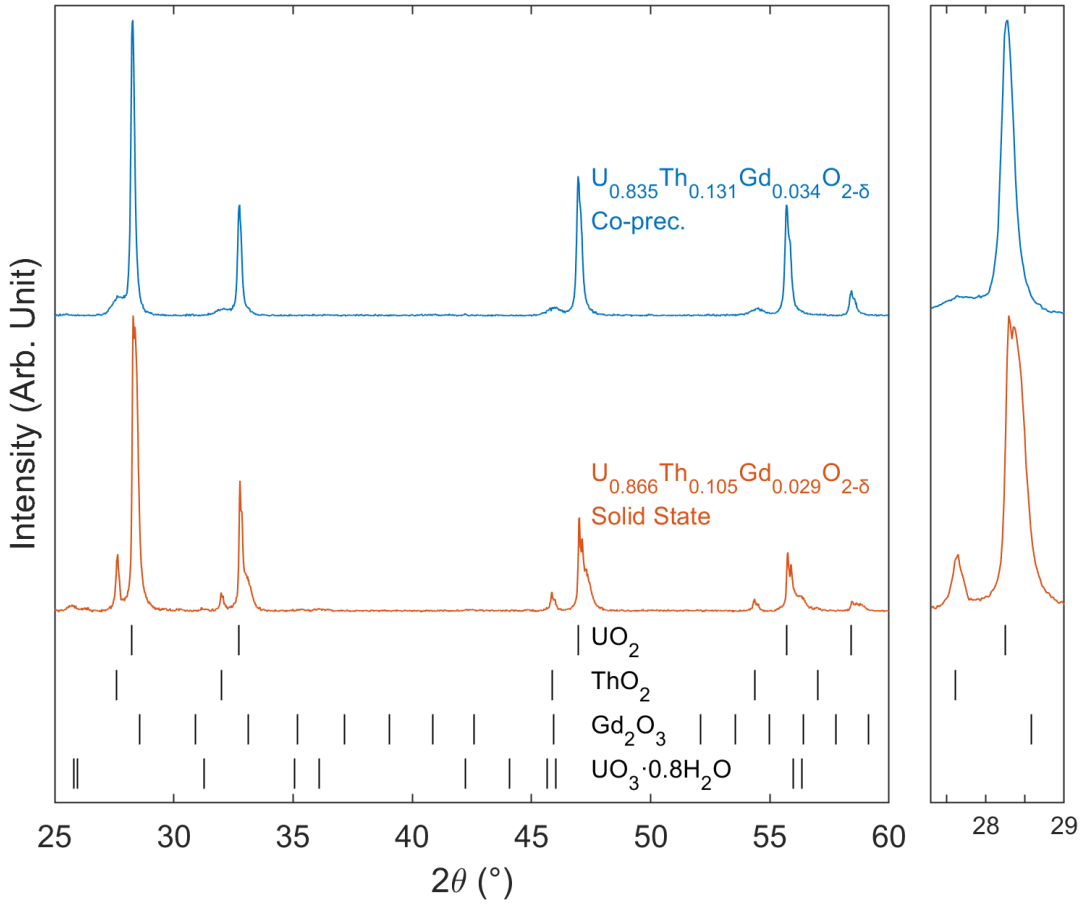

Figure 5: XRD traces of co-precipitated and state milled oxide powders prior to sintering. Two sets of fluorite reflections were indexed to UO_2 (ICSD 160814) and ThO_2 (ICSD 253564). Peak shift in the ThO_2-rich reflections is readily observed in co-precipitated powders due to incorporation of U^{4+} and Gd^{3+}. Additional peaks in solid state oxide powders were indexed to $UO_3{\cdot}0.8H_2O$ (PDF #00-010-0309). No peaks corresponding to cubic C-type Gd_2O_3 (ICSD 94892), or monoclinic Gd_2O_3 were observed.

For the samples prepared *via* the dry synthesis method, no shift in position of the peaks relative to the indexed positions of UO_2 and ThO_2 was observed, confirming the lack of cationic substitution of U, Th, or Gd prior to sintering. Additional peaks associated with monoclinic (C/2m) Gd_2O_3 were not observed in any sample, likely because Gd additions were below the 2 wt% detection limit of the XRD analysis. Some additional peaks corresponding to a small amount of hydrated UO_3 ($UO_3 \cdot 0.8H_2O$) were observed, though this phase was assumed to have no effect on obtained sintered materials.

In samples prepared by oxalic co-precipitation, the set of fluorite reflections corresponding to the ThO_2-rich phase are slightly shifted to higher values of 2θ relative to pure ThO_2. This suggests calcination at 800 °C facilitated partial cationic substitution (U, Th, Gd) through diffusion in the highly homogenous oxalate powders. This shift to higher values of 2θ results from unit cell contraction, likely caused by substitution of Th^{4+} with smaller U^{4+} cations and the generation of oxygen vacancies (V_O) resulting from Gd^{3+} incorporation. By contrast, reflections corresponding to UO_2 did not exhibit shifts indicative of cationic substitution. XRD collected on all four co-precipitated compositions is provided in Figure S3 in the supplementary materials, Rietveld refinements of lattice parameters are presented in Table S2.

3.3 Characterisation of sintered disposal-MOX

3.3.1 Disposal-MOX average composition

Compositional analysis of sintered disposal-MOX materials was performed by completely dissolving samples in nitric acid and analysing the solutions for elemental concentration using ICP-OES. These measurements revealed that all four co-precipitated samples contained excess quantities of Th and Gd relative to the target composition (Table 1). This deviation from nominal stoichiometry may have been due to incomplete conversion of $UO_2(NO_3)_2$ to $UO_2C_2O_4$ during the precipitation reaction. ICP-OES analysis of supernatant solutions following the oxalate precipitation revealed unreacted uranyl nitrate remaining in the solution. This incomplete reaction was likely caused by the low pH of the oxalic solution in which the reaction occurred (pH < 1), which was lower than ideal for the precipitation of uranyl oxalate[34]. In contrast, the solid state compositions were found to be closer to the targeted, nominal compositions. For example, the Th content was within 10% of the desired stoichiometry relative to U in all solid state samples. The Gd additions were less accurate, which is likely due to the very small quantities targeted.

Quantitative EPMA point spectra collected on sintered pellets provided comparison with ICP-OES measurements of the total digest solutions (Table 1). A minimum of 5 spots were

analysed, each within the centre of different grains. The average EMPA quantification corroborated the composition derived from the total digest method, showing that solid state synthesis achieved compositions closest to those targeted. Th and Gd were again measured in excess of desired stoichiometries in all co-precipitated samples, due to incomplete precipitation of uranyl oxalate. It should be noted, however, that there was significant variation in the spatial distribution of elements (discussed later), which may influence the average point EMPA measurements. For this reason, compositions measured by ICP-OES of total digests, rather than EPMA, are quoted in all subsequent discussion. Direct comparison between fabrication routes is made more challenging by this variance in composition; however, where possible, data is plotted as a function of the measured Th and Gd content to deconvolute these factors.

3.3.2 Microstructural analysis of disposal-MOX

The as-sintered disposal-MOX materials exhibited a microstructure similar to that observed for UO_2, ThO_2 and $(U,Pu)O_2$ (Figures 6 and 7), being dense and comprising well-equiaxed grains[35–37]. Pellets produced *via* both wet co-precipitation and solid state fabrication routes exhibited intragranular porosity. Pores typically form at grain boundaries and, in particular, triple points, where diffusion is limited and grain growth ceases; however, most pores in these samples were found within grains. Similar observations of intragranular porosity in $(U,Ce)O_2$ were made by Harrison *et al.*, who proposed oxygen release due to oxygen vacancy formation as the potential cause[35]. In co-precipitated samples, continued CO/CO_2 evolution during sintering may also have resulted in this porosity. Although the TG-MS analysis showed no further gas evolution after temperatures exceeded 600 °C, it is possible that residual carbon remained following calcination at 800 °C. For example, Horlait *et al*. reported at least 0.25 wt% residual carbon in Am-doped UO_2 oxides calcined from oxalates at 750 °C[38]. *In-situ* sintering in an E-SEM could potentially reveal the mechanism behind the pore formation; however, sintering $(U,Th,Gd)O_2$ at the relatively low (~1300 °C) temperatures attainable in high temperature E-SEM experiments would prove challenging due to its refractory nature.

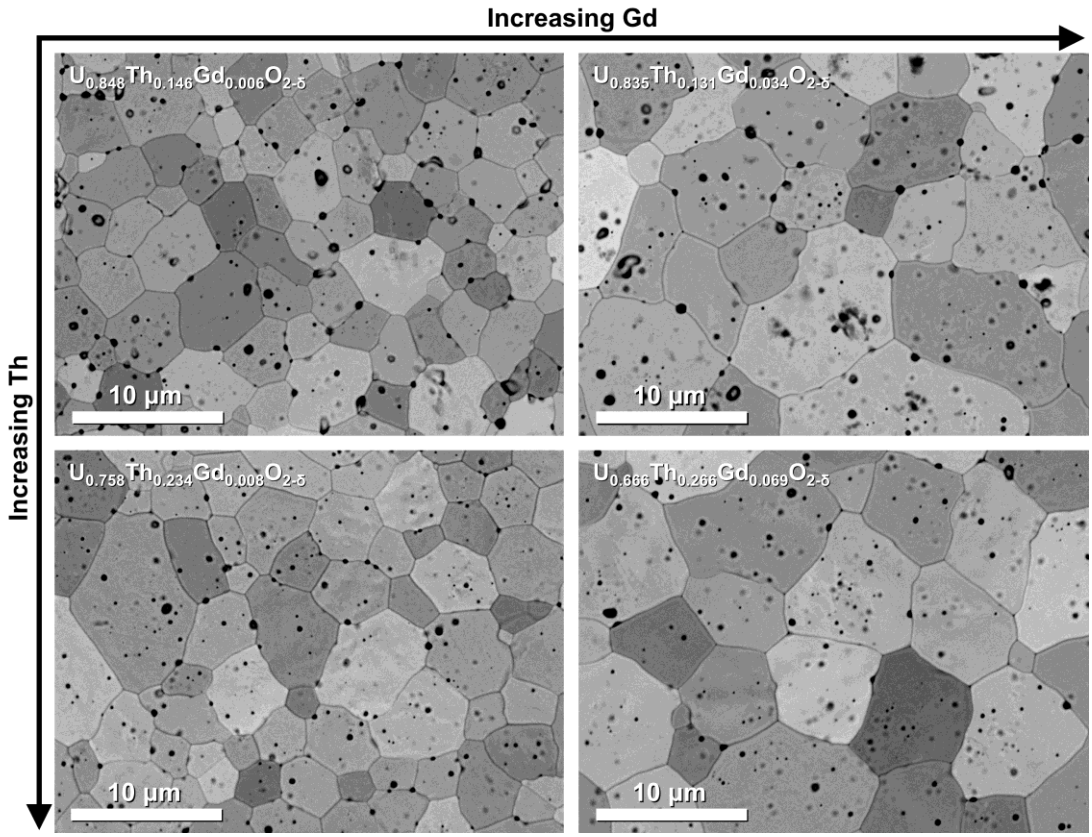

Figure 6: BSE micrographs of polished and annealed surface in co-precipitated pellets.

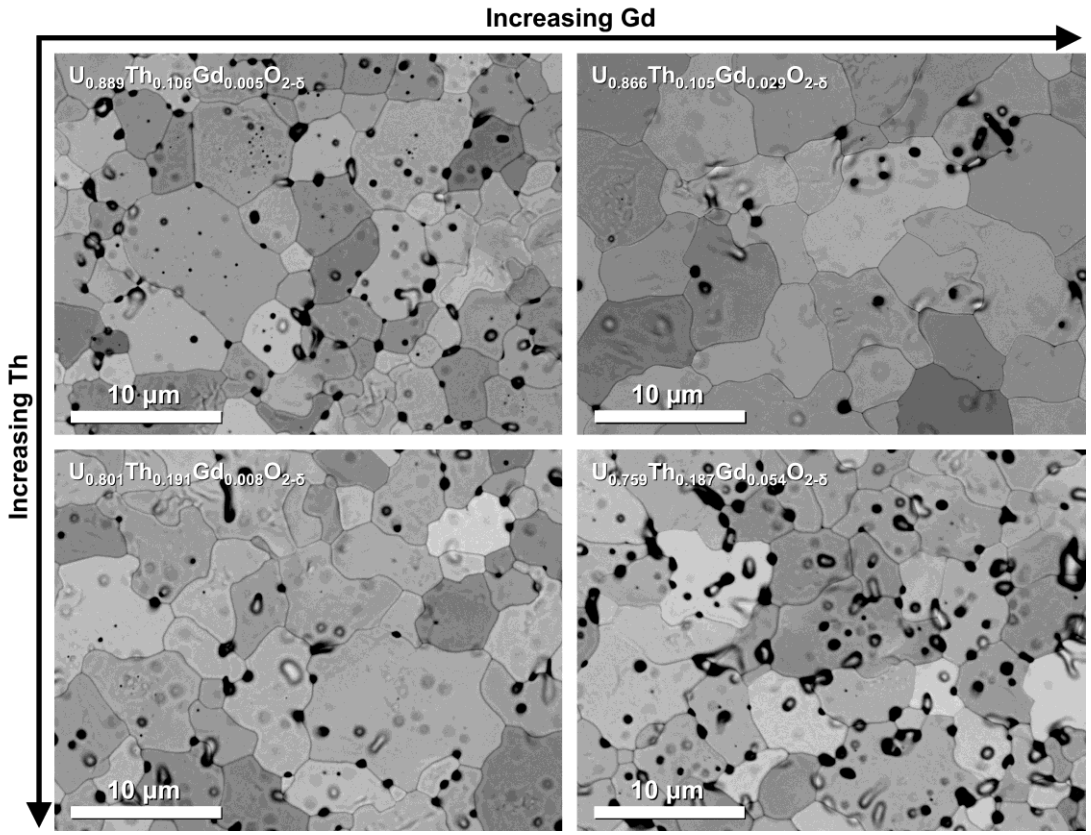

Figure 7: BSE micrographs of polished and annealed surface in solid state pellets.

When compared with co-precipitated samples, the solid state samples showed signs of poorer sinterability, as certain grains adopted an unusual morphology, the grain size showed greater variance and more extensive intergranular porosity was observed. Lower rates of diffusion during the sintering of solid state samples indicates poor homogenisation and lower reactive surface area of the milled oxides compared to those produced *via* wet co-precipitation. In both co-precipitated and solid state samples, the grain size was observed to increase to some extent with increasing Gd concentration, shown in Figure 8(a). Grain size varied significantly across the pellet surface; the largest grains occurred at the pellet edge, likely due to the thermal gradient that exists across the sample during sintering.

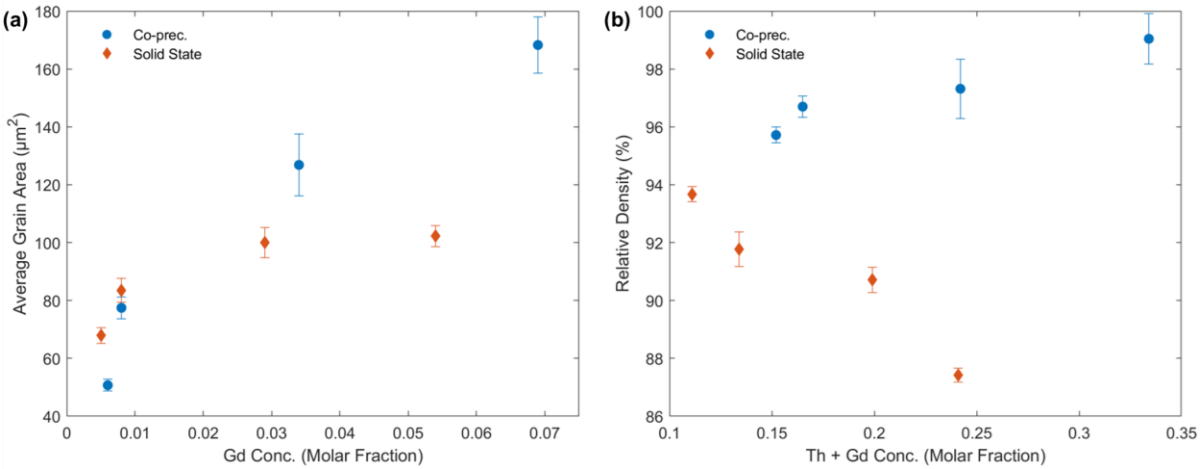

Figure 8: (a) Plot of average grain size of sintered disposal-MOX pellets against molar fraction of Gd. (b) Plot of relative density of sintered disposal-MOX pellets against molar fraction of Th and Gd. Relative density was calculated by dividing the density, as measured by an Archimedes balance, by the theoretical density. Theoretical density was calculated using refined lattice parameters and compositions measured by ICP-OES.

Relative density in the co-precipitated samples increased gradually with greater Th and Gd incorporation, correlating well with the measured grain size increase. However, in solid state pellets, the opposite trend is observed, with relative density decreasing with increasing Th and Gd content. This decrease in density appeared to result from increased levels of intergranular porosity in compositions containing greater amount of Th. Whilst grain size appeared independent of Th incorporation, large pores readily observed between grains in the SEM micrographs (Figure 7) suggest greater quantities of Th inhibited sintering in solid state samples. Figure 8(b) shows the relative density of pellets produced *via* co-precipitation and solid state synthesis as a function of composition. All co-precipitated pellets achieved relative densities of > 95%, despite the intragranular porosity, whereas solid state pellets had relative densities between 87 – 94%. This pronounced difference corresponds with greater intergranular porosity in the solid state pellets, suggesting decreased sinterability of the milled oxide precursors relative to precipitated oxides calcined from an oxalate mixture.

3.3.3 Distribution of Th and Gd in disposal-MOX

Compositional mapping by EPMA revealed greater compositional heterogeneity in the disposal-MOX pellets fabricated *via* solid state synthesis compared to wet co-precipitation. Large (~20 µm) regions heavily enriched with Th were readily observed in solid state samples, whereas Th is distributed far more homogenously in co-precipitated materials, shown in Figure 9. Measured Th content in solid state samples was highest (~80 wt%) at the centre of these Th-rich agglomerates, with the surrounding rim enriched to a lesser extent. This gradient of Th concentration suggests incomplete diffusion of ThO_2 powders into the UO_2 matrix during sintering as a result of poor homogenisation and large particle size. Consequently, large areas of solid state samples were entirely free of Th.

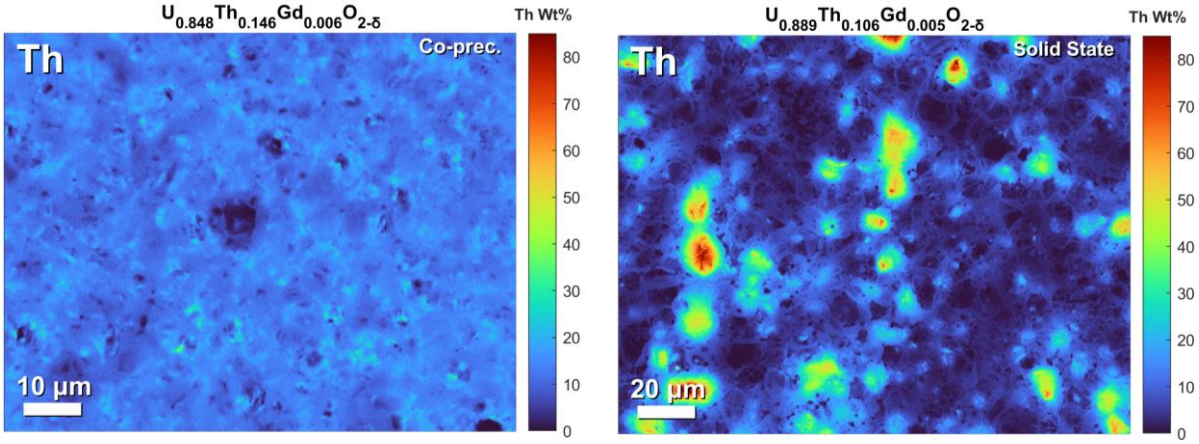

Figure 9: EPMA maps showing Th distribution in co-precipitated and solid state sintered pellets with comparable compositions ($U_{0.848(7)}Th_{0.146(7)}Gd_{0.006(2)}O_{2-\delta}$ and $U_{0.889(3)}Th_{0.106(3)}Gd_{0.005(1)}O_{2-\delta}$ respectively). The same colour bar scale is maintained between both maps to facilitate direct comparison of Th distribution.

Whilst co-precipitated samples exhibited more homogenous elemental distribution compared to those prepared *via* solid state methods, regions enriched with Th and Gd were still readily observed. EPMA mapping of co-precipitated samples revealed smaller regions, around 1 – 5 µm in diameter, containing between 30 - 40 wt% Th. Interestingly, these regions of increased Th content corresponded with regions of increased Gd content, shown in Figure 10. This correlation between Th and Gd distribution could suggest two distinct oxalates, uranyl oxalate, and a separate mixed (Th,Gd) oxalate, formed during precipitation. This potential explanation is supported by XRD analysis previously presented in Figure 2, which revealed the presence of both P21/c, and C2/c phases, associated with uranium and thorium oxalate respectively. Whilst the cause of this coupled Th and Gd distribution remains unclear, in the context of disposal-MOX, close proximity of Th (Pu) with the neutron absorbing Gd would present a considerable advantage in assuring a neutronic state of $k_{eff} < 1$.

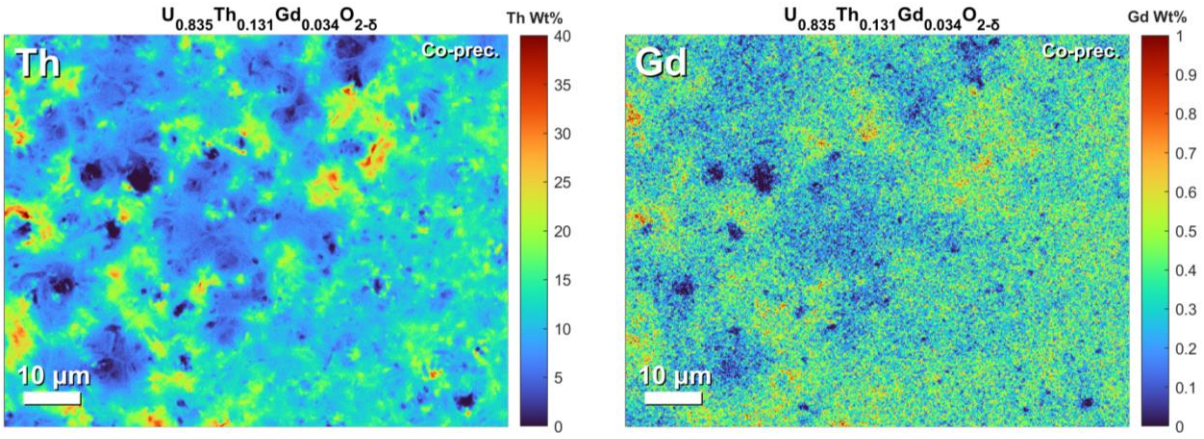

Figure 10: EPMA maps of co-precipitated pellets revealing strong correlation between areas of elevated Th and Gd content. The colour bar scale in Figure 10 has been applied across the range 0 – 40 wt% Th, whereas in Figure 9 the range was 0 – 85 mol% to facilitate a direct comparison between solid state and co-precipitated samples.

Regions of elevated Th did not correlate with Gd-rich regions in the solid state samples, shown in Figure 11, confirming this behaviour was dependent on fabrication route.

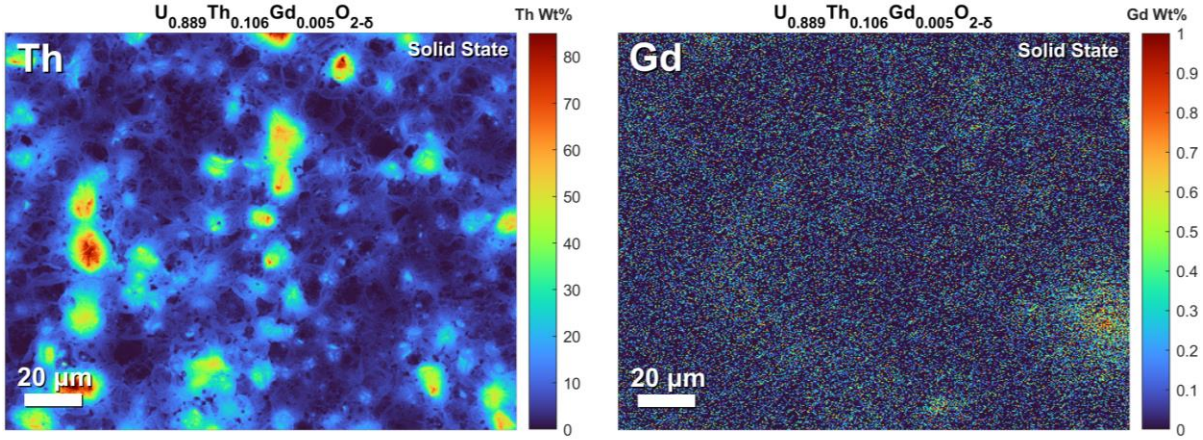

Figure 11: EPMA maps of solid state pellets revealing lack of correlation between areas of elevated Th and Gd content. Note: the colour bar scale has been applied across the range 0 – 85 wt% Th.

EPMA analysis of a thermally etched co-precipitated sample revealed some grain boundaries to be slightly enriched with Th, as shown in Figure 12. Segregation of Th^{4+} cations towards grain boundaries is driven by the large free volume of these 2D defects. Mismatch between the ionic radii of Th^{4+} and U^{4+} (the lattice cation) drives preferential diffusion of Th^{4+} towards grain boundaries during sintering, where it is readily accommodated[39]. It should be noted that EPMA measurements performed on thermally etched pellets cannot be treated as quantitative data due to deviations in interaction volume and absorption paths associated with surface topography[40]. Despite these limitations, these EPMA maps provide strong evidence that measured Th segregation towards grain boundaries is not an artefact resulting from surface topography at these regions. Th enrichment at grain boundaries clearly corresponds with

depleted U content (Figure S4); furthermore, topographic features such a sharp pore edges have discernible influence on measured elemental compositions. Close examination of EPMA maps collected on flat, unetched pellets also reveal signs of Th enrichment at grain boundaries; however, the exact position of grain boundaries is difficult to discern from BSE maps (Figure S3). Evidence of Gd enrichment towards grain boundaries was not observed in the EPMA maps of the co-precipitated samples, likely because the very low concentrations of Gd would result in a very subtle enrichment that would be very challenging to resolve using EPMA.

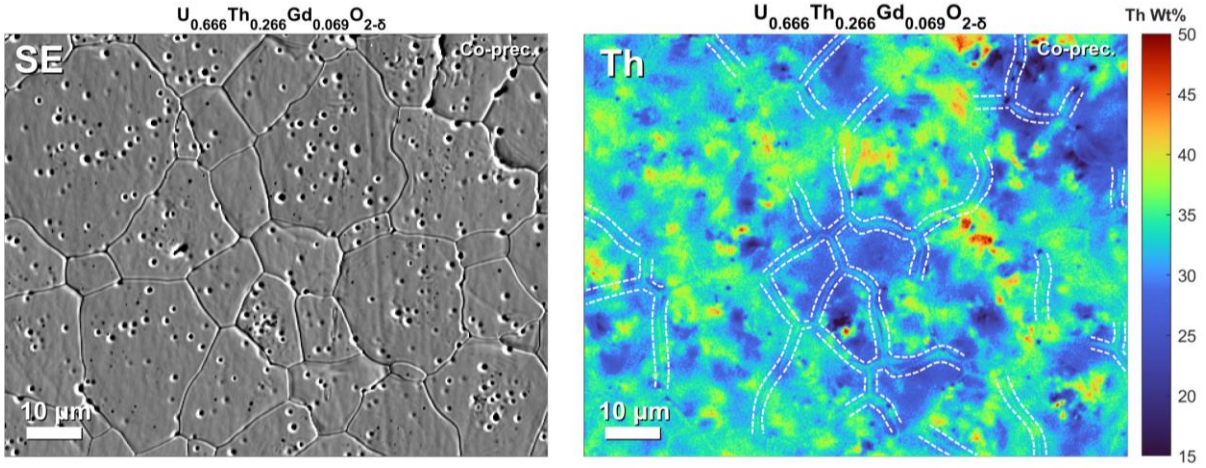

Figure 12: EPMA map of thermally etched pellet produced *via* co-precipitation showing Th segregation towards grain boundaries, highlighted here with white dashed lines. Note: the colour map scale bar has been applied across the range 0 – 50 wt% Th.

3.3.4 Crystal structure and chemistry of disposal-MOX

Following sintering, all materials, regardless of fabrication route, formed a single phase fluorite-structured disposal-MOX (Figures 13 and 14) through complete incorporation of both Th^{4+} and Gd^{3+} into solid solution within the main UO_2 matrix. XRD patterns collected on crushed sintered powders of co-precipitated and solid state samples revealed a single set of reflections characteristic of cubic fluorite. Peak broadening observed in solid state samples was caused by contributions from a gradient of varying (U,Th,Gd) compositions with different lattice parameters. Sharper peaks in co-precipitated materials indicate greater compositional homogeneity in the single fluorite phase; these observations correspond well with analysis of Th and Gd distribution.

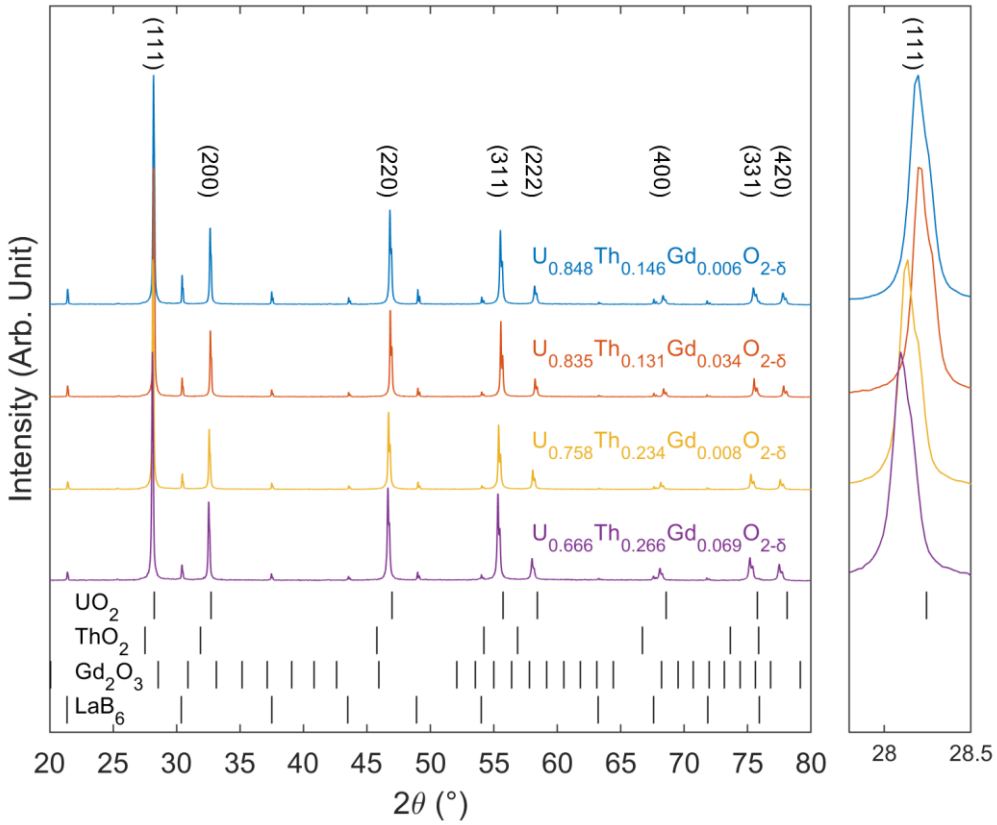

Figure 13: XRD of crushed sintered powders prepared using oxalic co-precipitation. A single set of fluorite reflections corresponding to a solid solution of (U,Th,Gd)$O_{2-\delta}$ is compared to peak positions in pure UO_2 (ICSD 160814) and ThO_2 (ICSD 253564). Additional peaks corresponding to C-type Gd_2O_3 (ICSD 94892) are absent. Additional peaks correspond to internal standard LaB_6 (ICSD 120585).

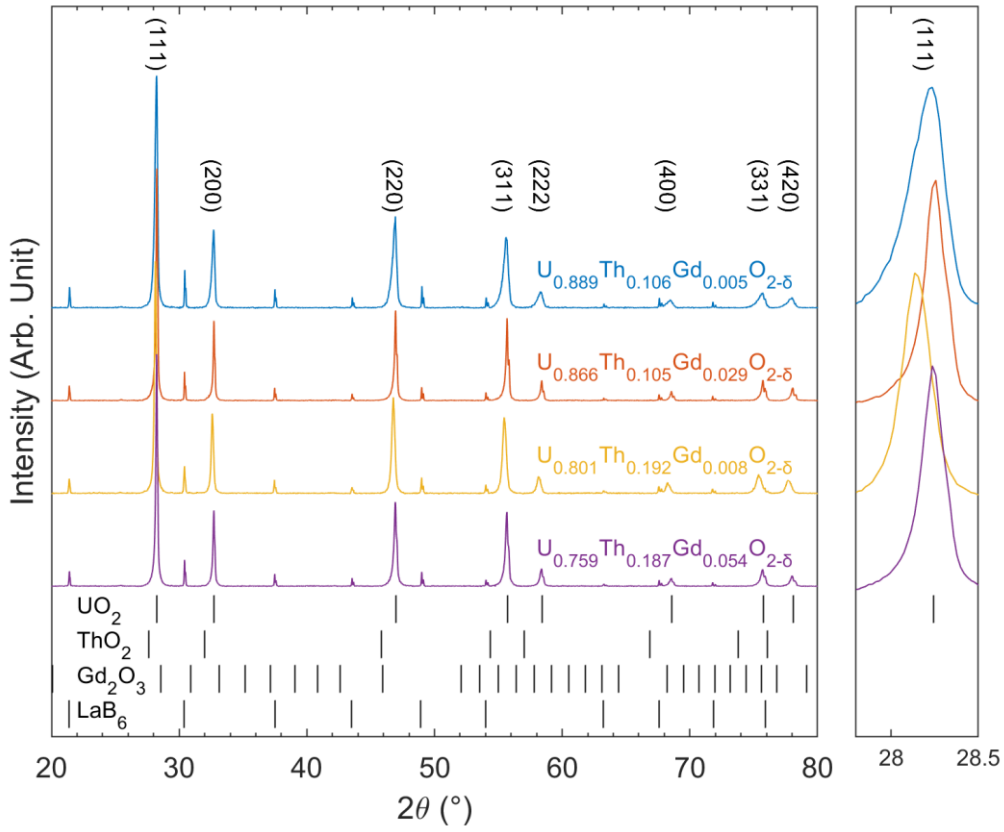

Figure 14: XRD of crushed sintered powders prepared using solid state synthesis. A single set of fluorite reflections corresponding to a solid solution of (U,Th,Gd)$O_{2-\delta}$ is compared to peak positions in pure UO_2 (ICSD 160814) and ThO_2 (ICSD 253564). Additional peaks corresponding to C-type Gd_2O_3 (ICSD 94892) are absent. Additional peaks correspond to internal standard LaB_6 (ICSD 120585).

Rietveld refinements (Table 2) revealed that Th additions resulted in lattice expansion, as shown in Figure 15. The incorporation of Th in UO_2 is expected to increase the lattice parameter since Th^{4+} in 8-fold coordination has a Shannon radius of 1.19 Å, larger than the 1.14 Å of U^{4+}. Conversely, real disposal-MOX materials containing Pu^{4+} exhibit lattice contraction, as the Shannon radius of Pu^{4+} (1.10 Å) is smaller than U^{4+}. Although Gd^{3+} is markedly larger than U^{4+} (1.193 Å), it is known to have the opposite effect on the lattice parameter of UO_2, due to the significant lattice contraction resulting from the generation of oxygen vacancies (V_O)[11]. The incorporation of a trivalent species on a tetravalent site is charge compensated *via* the release of O^{2-}, yielding V_O in the fluorite structure. For this reason, the calculated average crystal radius does not accurately reflect the observed crystal structures, as demonstrated in Figure 16. The addition of Gd^{3+} was shown to result in a decrease in the lattice parameter in sintered materials. This trend is readily observed in solid state samples,

but is is more difficult to obvserve in the co-precipitated samples due to the deviation of Th additions from targeted compositions discussed previously.

Table 2: Summary of Rietveld refinements of XRD data collected on crushed sintered material. Listed compositions are those determined by ICP-OES analysis of total digests.

Synthesis	Composition	a (Å)	Error	Rwp	χ^2
Co-prec.	$U_{0.848(7)}Th_{0.146(7)}Gd_{0.006(2)}O_{2-\delta}$	5.49134	(8)	10.495	1.566
Co-prec.	$U_{0.835(5)}Th_{0.131(3)}Gd_{0.034(2)}O_{2-\delta}$	5.48806	(5)	10.000	1.724
Co-prec.	$U_{0.758(1)}Th_{0.234(9)}Gd_{0.008(0)}O_{2-\delta}$	5.50454	(6)	11.331	2.085
Co-prec.	$U_{0.666(6)}Th_{0.266(4)}Gd_{0.069(2)}O_{2-\delta}$	5.50871	(5)	9.832	1.723
Solid State	$U_{0.889(3)}Th_{0.106(3)}Gd_{0.005(1)}O_{2-\delta}$	5.48019	(13)	14.465	2.343
Solid State	$U_{0.866(3)}Th_{0.105(2)}Gd_{0.029(2)}O_{2-\delta}$	5.47731	(14)	16.764	2.609
Solid State	$U_{0.801(4)}Th_{0.192(4)}Gd_{0.008(7)}O_{2-\delta}$	5.49585	(12)	11.284	1.721
Solid State	$U_{0.759(4)}Th_{0.187(4)}Gd_{0.054(2)}O_{2-\delta}$	5.49042	(18)	16.086	2.576

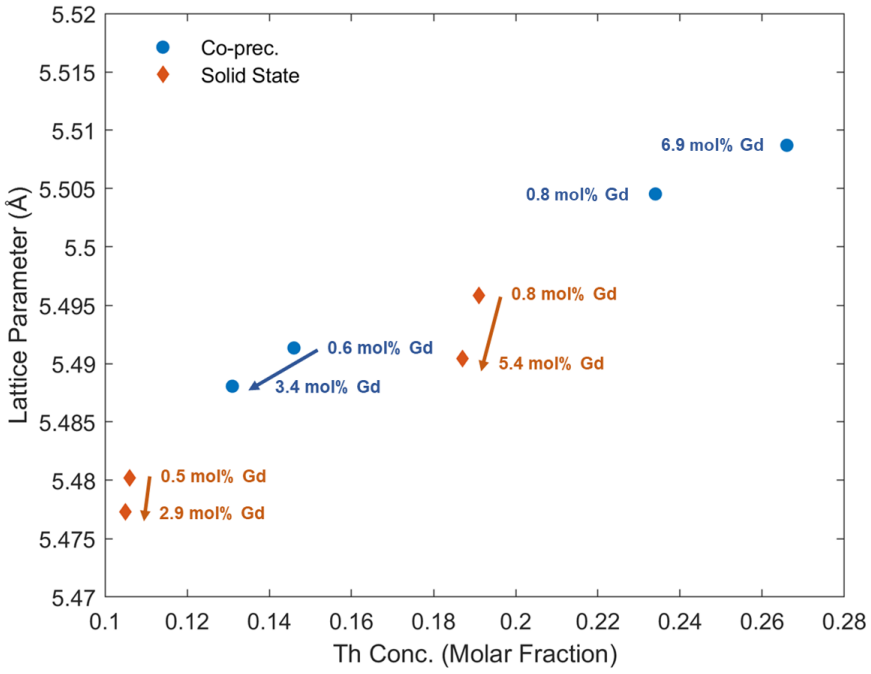

Figure 15: Plot of lattice parameter against Th content. Arrows indicate decrease in lattice parameter corresponding to increased Gd incorporation in comparable compositions.

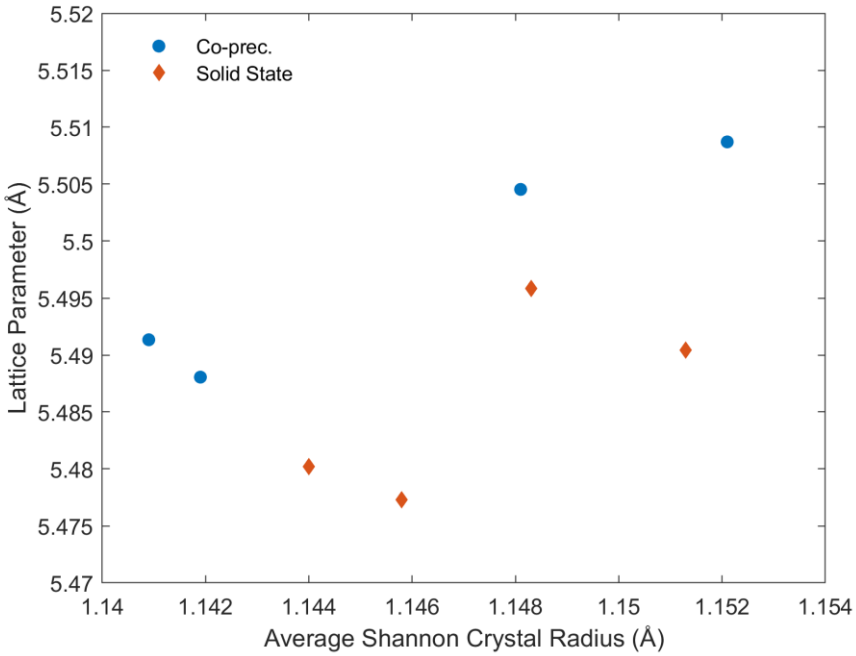

Figure 16: Plot of lattice parameter against average Shannon crystal radius.

The incorporation of Th and Gd within UO_2 was found to increase lattice disorder due to ionic radius mismatch and V_O generation. The deconvoluted Raman spectra collected on both the co-precipitated and solid state synthesised disposal-MOX pellets are shown in Figures 17(a-d). All materials exhibited a sharp T_{2g} Raman mode at 445 cm^{-1}, which is characteristic of the fluorite structure[41]. Lattice disorder was indicated by a shift in T_{2g} mode position to higher wavenumbers; the degree of this shift varied linearly with total Th and Gd additions, as shown in Figure 18(a). Peak broadening of the T_{2g} mode was also observed as total Th and Gd content increased, evidenced by the increase in T_{2g} FWHM, also shown in Figure 18(a). Broadening of the T_{2g} mode is also indicative of greater lattice disorder[42]. Slight asymmetry in the T_{2g} was observed to some extent in all spectra, which was also observed by Rao *et al*.[43] in their Raman study of the UO_2 - ThO_2 solid solution. Such dual-mode behaviour is expected of the T_{2g} peak across the entire solid solution, as the T_{2g} peak in ThO_2 occurs at higher the higher wavenumber of 467 cm^{-1}, leading to this asymmetry.

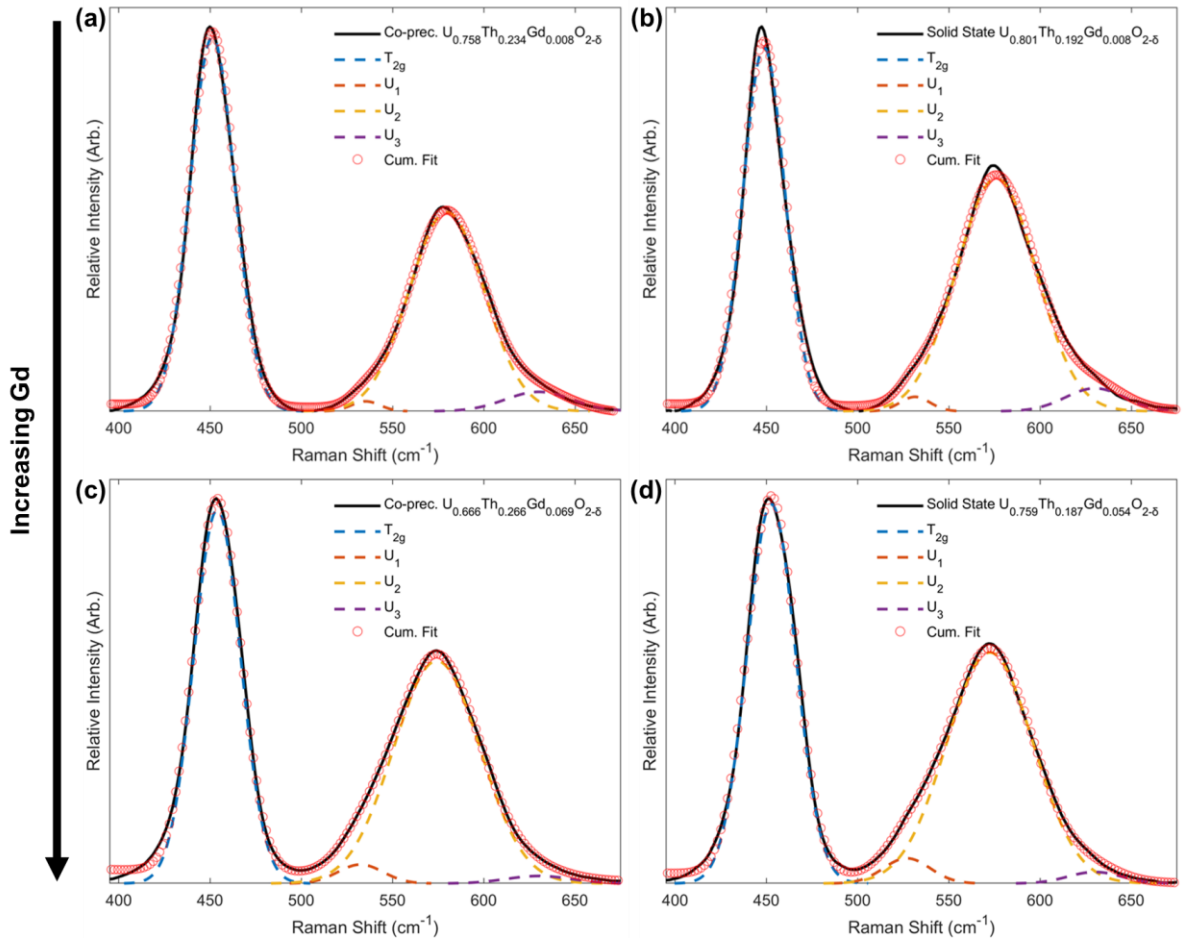

Figure 17: Deconvoluted Raman spectrum of co-precipitated pellet with composition (a) $U_{0.758}Th_{0.234}Gd_{0.008}O_{2-\delta}$, (b) $U_{0.801}Th_{0.192}Gd_{0.008}O_{2-\delta}$, (c) $U_{0.666}Th_{0.266}Gd_{0.069}O_{2-\delta}$, and (d) $U_{0.759}Th_{0.187}Gd_{0.054}O_{2-\delta}$. U_1 results from lattice distortion due to V_O, U_2 results from the breaking of perfect fluorite symmetry, and U_3 results from cuboctahedral symmetry, caused by oxygen interstitials forming a hyper-stoichiometric U_4O_9 structure.

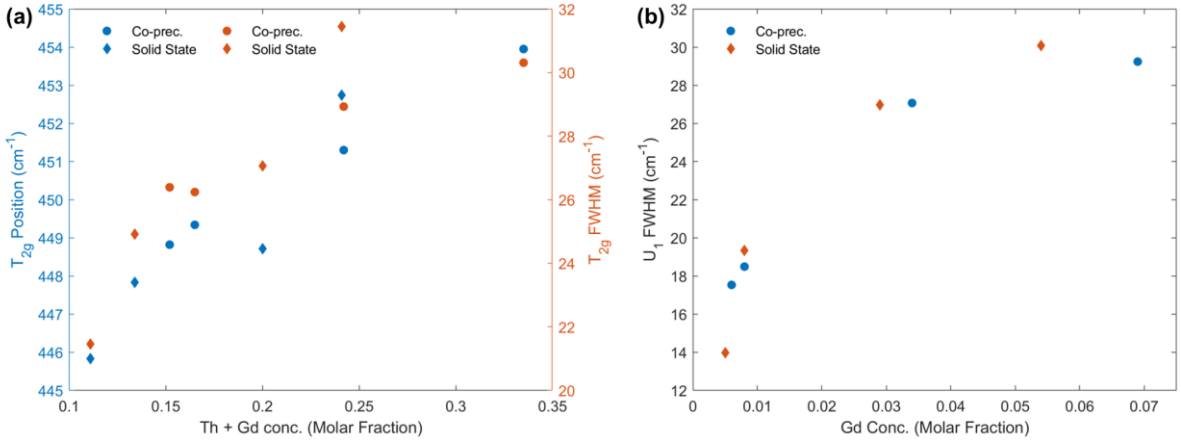

Figure 18: (a) Plot of T_{2g} position and FWHM against total Th and Gd content. (b) Plot of U_1 FWHM against Gd content.

Measured V_O concentration was found to increase with Gd incorporation in sintered pellets of all samples. Raman spectra exhibited a broad set of overlapping peaks at 575 cm^{-1}, often referred to as the defect region. This defect region was deconvoluted to reveal individual contributions from three distinct defect bands: U_1, U_2 and U_3. The U_1 band, which typically occurs around 540 cm^{-1}, results from lattice distortion due to V_O[41,44]. The intensity of the U_1 band, measured by its full width half maximum (FWHM), was found to increase with increasing Gd content, as shown in Figure 18(b). These results confirmed Gd^{3+} incorporation was charge compensated *via* V_O generation regardless of compositions or fabrication route. The U_2 band, also known as the resonant first-order longitudinal optical (1LO) mode, is activated as the perfect fluorite symmetry is broken; this peak was the most intense in samples with greatest Th and Gd content, likely due to contributions from both ionic radius mismatch and oxygen vacancy generation towards increased disorder[41]. The U_3 peak can be assigned to cuboctahedral symmetry, which results from oxygen interstitials forming a hyper-stoichiometric U_4O_9 structure. The low intensity of this band in all spectra confirms the absence of highly oxidised clusters on the pellet surface. Full details of the Raman deconvolutions can be found in Table S3 in the supplementary information; plots for all eight samples are presented in Figure S5.

3.3.5 Proportion of U^{5+} in disposal-MOX

To understand whether any U^{5+} was formed, in addition to V_O, to charge compensate for the incorporation of Gd^{3+}, U M_4-edge HERFD XANES spectra were collected on sintered pellets of disposal-MOX materials. Spectra were fit using linear combination fitting (LCF) and verified with iterative transformation factor analysis (ITFA), as presented in Figure 19(a-d). A greater proportion of U^{5+} was found to be present in the co-precipitated samples, though no relationship between U^{5+} proportion and Gd^{3+} content could be established for samples produced *via* either fabrication route. Greater quantities of U^{5+} measured in co-precipitated samples could possibly be attributed to their increased Gd^{3+} content relative to the solid state samples. However, the measured fraction of U^{5+} did not correlate directly with the Gd content in the co-precipitated samples; in fact, both LCF and ITFA fits agreed that the highest proportion of U^{5+}, roughly 5%, was detected in the sample with the lowest measured Gd content (around 0.6 mol%). Analysis of the solid state samples revealed far lower amounts (0.1-1.2%) of U^{5+} in each sample, again with no correlation between quantities of Gd^{3+} and U^{5+}. XANES analysis suggests that oxidation of U^{4+} to U^{5+} is not influenced by the extent of Gd incorporation but is instead controlled by the synthesis route. These results strongly suggest V_O generation, not oxidation to U^{5+}, is the dominant charge compensation mechanism in all disposal-MOX samples, as illustrated in Figure 20.

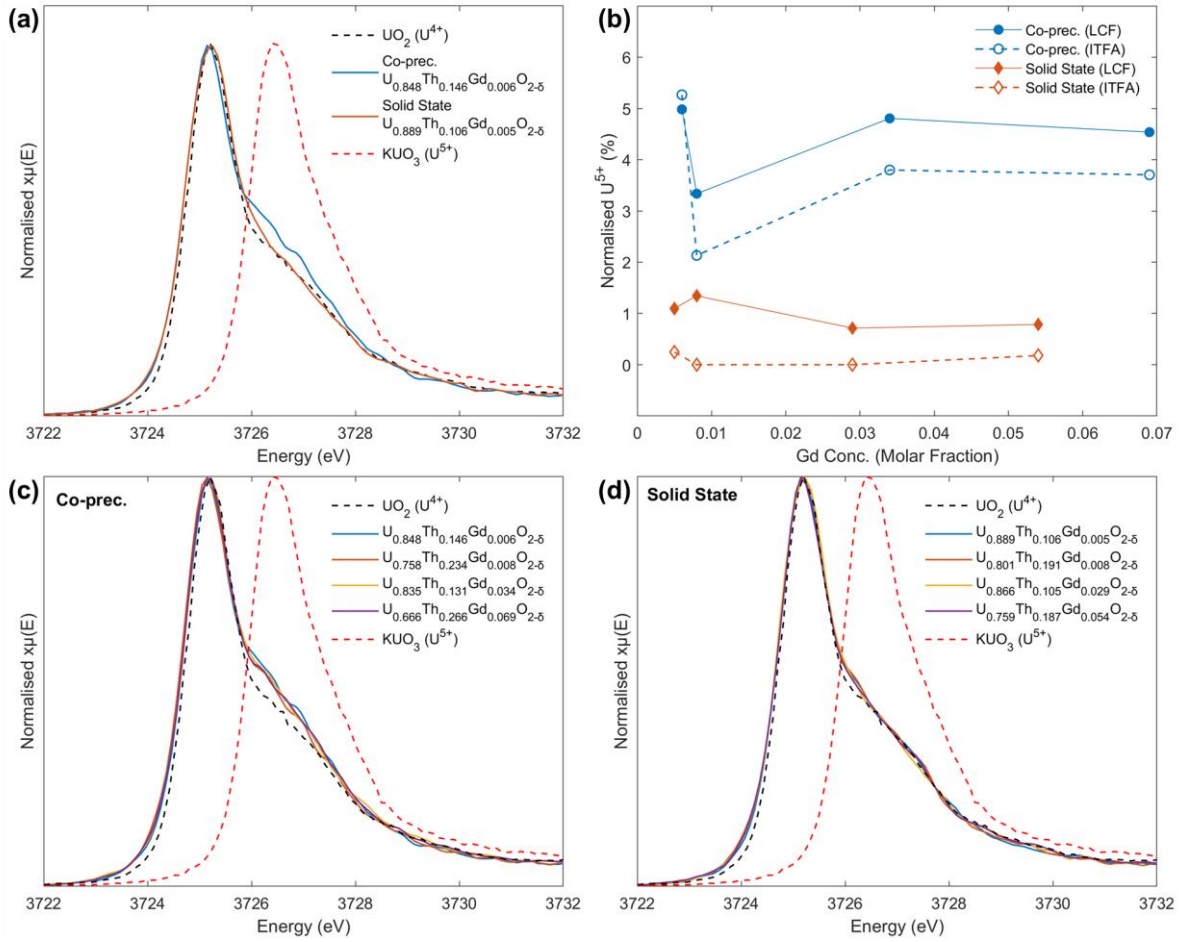

Figure 19: (a) Comparison of U M_4-edge HERFD XANES spectra collected on co-precipitated and solid state samples of similar Gd^{3+} content with U^{4+} and U^{5+} standards, UO_2 and KUO_3. (b) Plot of normalised U^{5+} proportion (%), determined using LCF and ITFA, against Gd^{3+} content. (c) Complete set of U M_4-edge HERFD XANES spectra collected on co-precipitated samples. (d) Complete set of U M_4-edge HERFD XANES spectra collected on solid state samples.

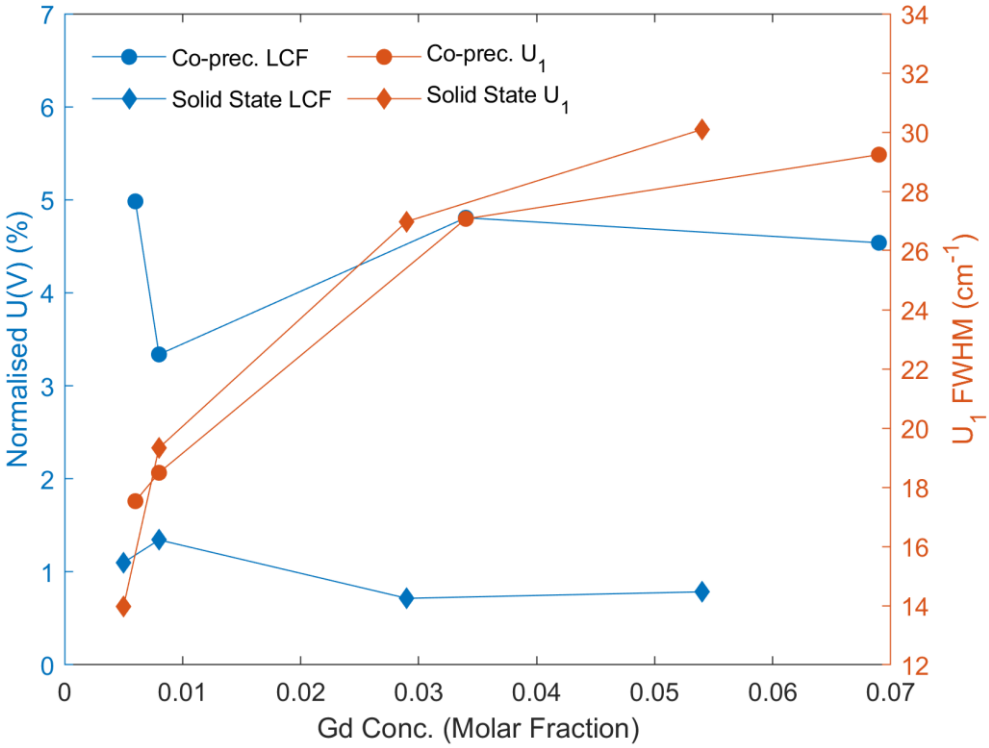

Figure 20: Comparative plot of both U^{5+} proportion (determined by LCF fitting) and U_1 FWHM (a measure of oxygen vacancy concentration) against Gd content, providing strong evidence Gd^{3+} incorporation is charge compensated by V_O formation.

Summary

This study has shown both oxalic co-precipitation and solid state synthesis provide viable routes to fabricate sintered pellets of simulant disposal-MOX in the form of $(U,Th,Gd)O_2$. Sintered disposal-MOX materials achieved relative densities > 90%, and comprised well-equiaxed grains, comparable to those observed for UO_2, ThO_2 and $(U,Pu)O_2$. Grain size was found to increase slightly with greater Gd^{3+} additions, whereas doubling Th content had no discernible impact. In co-precipitated pellets, this subtle increase in grain size was associated with an increase in relative density, whereas density of solid state samples decreased due to significant intergranular porosity. EPMA mapping confirmed greater compositional homogeneity in pellets prepared through co-precipitation, although Th and Gd rich regions were present in all samples. In co-precipitated samples, regions enriched with Th were also enriched with Gd, this relationship was not observed in solid state materials. Th-rich agglomerates in solid state samples were larger and more concentrated with Th. Segregation of Th towards grain boundaries was observed, resulting in slight enrichment at grain edges. Single phase cubic fluorite materials were obtained for all compositions produced using both

synthesis routes, as confirmed by XRD. Rietveld refinements showed Th^{4+} additions caused an expansion of the fluorite lattice in accordance with Vegard's law, whereas Gd^{3+} additions contracted the lattice due to oxygen vacancy generation. Greater asymmetry and peak broadness in XRD patterns of solid state materials suggested these samples, whilst still single phase, comprised a range of $(U,Th,Gd)O_2$ compositions due to poor homogenisation achieved during milling. Raman deconvolutions revealed greater concentrations oxygen vacancies in structures more highly doped with Gd^{3+}, due to charge compensation. U M_4-edge HERFD XANES found a greater proportion of U^{5+} in co-precipitated samples compared to solid state, however in both sample sets, the proportion of U^{5+} showed no correlation with the Gd^{3+} content, suggesting that charge compensation was achieved through oxygen vacancy generation, not oxidation of U^{4+} to U^{5+}.

Acknowledgements

This research utilised the HADES/MIDAS and PLEIADES national nuclear user facilities at the University of Sheffield, established with financial support from EPSRC and BEIS, under grant numbers EP/T011424/1[45] and EP/V035215/1. Collection of the U M_4-edge HERFD-XANES performed at European Synchrotron Radiation Facility (ESRF).

The authors gratefully acknowledge the contributions of Dr Malin D. Wilkins, Dr Ritesh Mohun, Dr Joshua T. Radford, Dr Hannah Smith, and Dr Martin C. Stennett to this work.

References

1. Nuclear Decommissioning Authority (NDA). Progress on Plutonium Consolidation, Storage and Disposition. (2019).
2. Lumpkin, G. R. *et al.* Retention of actinides in natural pyrochlores and zirconolites. *Radiochim. Acta* **66/67**, 469–474 (1994).
3. Lumpkin, G. R. Ceramic waste forms for actinides. *Elements* **2**, 365–372 (2006).
4. Vance, E. R. *et al.* Actinide and rare earth incorporation into zirconolite. *J. Alloys Compd.* **213/214**, 406–409 (1994).
5. Vance, E. R., Begg, B. D., Day, R. A. & Ball, C. J. Zirconolite-rich Ceramics for Actinide Wastes. in *Mat. Res. Soc. Symp. Proc.* vol. 353 767–774 (1995).
6. Kang, J., von Hippel, F. N., MacFarlane, A. & Nelson, R. Storage MOX: A Third Way for Plutonium Disposal? *Sci. Glob. Secur.* **10**, 85–101 (2002).
7. Macfarlane, A. M. Another option for separated plutonium management: Storage MOX. *Prog. Nucl. Energy* **49**, 644–650 (2007).
8. Shannon, R. D. Revised Effective Ionic Radii and Systematic Studies of Interatomic Distances in Halides and Chalcogenides. *Acta Cryst* **A 32**, 751–767 (1976).
9. Böhler, R. *et al.* Recent advances in the study of the UO_2 – PuO_2 phase diagram at high temperatures. *J. Nucl. Mater.* **448**, 330–339 (2014).
10. Bingham, P. A., Hand, R. J., Stennett, M. C., Hyatt, N. C. & Harrison, M. T. The Use of Surrogates in Waste Immobilization Studies: A Case Study of Plutonium. in *Mater. Res. Soc. Symp. Proc.* vol. 1107 (2008).
11. Durazzo, M., Oliveira, F. B. V., Urano de Carvalho, E. F. & Riella, H. G. Phase studies in the UO_2 – Gd_2O_3 system. *J. Nucl. Mater.* **400**, 183–188 (2010).
12. Shoesmith, D. W. Fuel corrosion processes under waste disposal conditions. *J. Nucl. Mater.* **282**, 1–31 (2000).
13. Leenaers, A., Sannen, L., Van den Berghe, S. & Verwerft, M. Oxidation of spent UO_2 fuel stored in moist environment. *J. Nucl. Mater.* **317**, 226–233 (2003).

14. Casella, A., Hanson, B. & Miller, W. The effect of fuel chemistry on UO_2 dissolution. *J. Nucl. Mater.* **476**, 45–55 (2016).
15. Razdan, M. & Shoesmith, D. W. Influence of Trivalent-Dopants on the Structural and Electrochemical Properties of Uranium Dioxide (UO_2). *J. Electrochem. Soc.* **161**, H105–H113 (2014).
16. Garrido, F., Moll, S., Sattonnay, G., Thomé, L. & Vincent, L. Radiation tolerance of fluorite-structured oxides subjected to swift heavy ion irradiation. *Nucl. Instrum. Methods Phys. Res. Sect. B Beam Interact. Mater. At.* **267**, 1451–1455 (2009).
17. Wiss, T. *et al.* Evolution of spent nuclear fuel in dry storage conditions for millennia and beyond. *J. Nucl. Mater.* **451**, 198–206 (2014).
18. Talip, Z. *et al.* Characterization of un-irradiated MIMAS MOX fuel by Raman spectroscopy and EPMA. *J. Nucl. Mater.* **499**, 88–97 (2018).
19. Schmitt, R. *et al.* A review of defect structure and chemistry in ceria and its solid solutions. *Chem. Soc. Rev.* **49**, 554–592 (2020).
20. Dixon Wilkins, M. C., Maddrell, E. R., Stennett, M. C. & Hyatt, N. C. The Effect of Temperature on the Stability and Cerium Oxidation State of $CeTi_2O_6$ in Inert and Oxidizing Atmospheres. *Inorg. Chem.* **59**, 17364–17373 (2020).
21. Chueh, W. C. *et al.* Highly Enhanced Concentration and Stability of Reactive Ce^{3+} on Doped CeO_2 Surface Revealed In Operando. *Chem. Mater.* **24**, 1876–1882 (2012).
22. Loche, D. *et al.* Determining the maximum lanthanum incorporation in the fluorite structure of La-doped ceria nanocubes for enhanced redox ability. *RSC Adv.* **9**, 6745–6751 (2019).
23. Bairiot, H. OVERVIEW OF MOX FUEL FABRICATION ACHIEVEMENTS. 21.
24. Warin, D., Bauer, M., Seiss, M. & Lorenzelli, R. Mechanisms of dry ball milling in MOX fabrication. *IAEA N P* (1997).
25. Legland, D., Arganda-Carreras, I. & Andrey, P. MorphoLibJ: integrated library and plugins for mathematical morphology with ImageJ. *Bioinformatics* btw413 (2016) doi:10.1093/bioinformatics/btw413.

26. Schindelin, J. *et al.* Fiji: an open-source platform for biological-image analysis. *Nat. Methods* **9**, 676–682 (2012).
27. Savitzky, Abraham. & Golay, M. J. E. Smoothing and Differentiation of Data by Simplified Least Squares Procedures. *Anal. Chem.* **36**, 1627–1639 (1964).
28. Ravel, B. & Newville, M. *ATHENA* , *ARTEMIS* , *HEPHAESTUS* : data analysis for X-ray absorption spectroscopy using *IFEFFIT*. *J. Synchrotron Radiat.* **12**, 537–541 (2005).
29. Rossberg, A. *et al.* Identification of Uranyl Surface Complexes on Ferrihydrite: Advanced EXAFS Data Analysis and CD-MUSIC Modeling. *Environ. Sci. Technol.* **43**, 1400–1406 (2009).
30. Tyrpekl, V. *et al.* Low temperature decomposition of U(IV) and Th(IV) oxalates to nanograined oxide powders. *J. Nucl. Mater.* **460**, 200–208 (2015).
31. Thompson, N. B. A., Stennett, M. C., Gilbert, M. R. & Hyatt, N. C. Nuclear forensic signatures and structural analysis of uranyl oxalate, its products of thermal decomposition and Fe impurity dopant. *J. Radioanal. Nucl. Chem.* **327**, 957–973 (2021).
32. Aybers, M. T. Kinetic study of the thermal decomposition of thorium oxalate dihydrate. *J. Nucl. Mater.* **252**, 28–33 (1998).
33. White, G. D., Bray, L. A. & Hart, P. E. Optimization of thorium oxalate precipitation conditions relative to derived oxide sinterability. *J. Nucl. Mater.* **96**, 305–313 (1981).
34. Shin, Y. J., Kim, I. S., Lee, W. K., Shin, H. S. & Ro, S. G. Precipitation behavior of uranium in multicomponent solution by oxalic acid. *J. Radioanal. Nucl. Chem. Artic.* **209**, 217–223 (1996).
35. Harrison, R. W. *et al.* Spark plasma sintering of $(U,Ce)O_2$ as a MOx nuclear fuel surrogate. *J. Nucl. Mater.* **557**, 153302 (2021).
36. Cherkaski, Y., Clavier, N., Brissonneau, L., Podor, R. & Dacheux, N. Densification behavior and microstructure evolution of yttrium-doped ThO 2 ceramics. *J. Eur. Ceram. Soc.* **37**, 3381–3391 (2017).
37. Hingant, N. *et al.* Preparation of morphology controlled $Th_{1-x}U_xO_2$ sintered pellets from low-temperature precursors. *Powder Technol.* **208**, 454–460 (2011).

38. Horlait, D. *et al.* Americium-based oxides: Dense pellet fabrication from co-converted oxalates. *J. Nucl. Mater.* **444**, 181–185 (2014).
39. Yan, M. F., Cannon, R. M. & Bowen, H. K. Space charge, elastic field, and dipole contributions to equilibrium solute segregation at interfaces. *J. Appl. Phys.* **54**, 764–778 (1983).
40. Newbury, D. E. Quantitative electron probe microanalysis of rough targets: Testing the peak-to-local background method. *Scanning* **26**, 103–114 (2006).
41. Guimbretière, G. *et al.* Determination of in-depth damaged profile by Raman line scan in a pre-cut He^{2+} irradiated UO_2. *Appl. Phys. Lett.* **100**, 251914 (2012).
42. Karcher, S. *et al.* Benefits of using multiple Raman laser wavelengths for characterizing defects in a UO_2 matrix. *J. Raman Spectrosc.* **53**, 988–1002 (2022).
43. Rao, R., Bhagat, R. K., Salke, N. P. & Kumar, A. Raman Spectroscopic Investigation of Thorium Dioxide–Uranium Dioxide (ThO_2 –UO_2) Fuel Materials. *Appl. Spectrosc.* **68**, 44–48 (2014).
44. Lee, J. *et al.* Raman study on structure of $U_{1-y}Gd_yO_{2-x}$ (y=0.005, 0.01, 0.03, 0.05 and 0.1) solid solutions. *J. Nucl. Mater.* **486**, 216–221 (2017).
45. Hyatt, N. C. *et al.* The HADES Facility for High Activity Decommissioning Engineering & Science: part of the UK National Nuclear User Facility. *IOP Conf. Ser. Mater. Sci. Eng.* **818**, 012022 (2020).

Supplementary Information

Table S1: Comprehensive details of EPMA experimental conditions.

Element	Channel	Crystal	Peak Pos. (mm)	Peak	Order
U	2	PETL	125.147	Ma	1
Th	3	PETH	132.231	Ka	1
Gd	3	LIFH	142.347	La	1
O	1	LDE1	109.973	Ka	1

Table S2: Summary of Rietveld refinements performed on calcined oxides produced *via* co-precipitation.

Composition	UO_2-rich a (Å)	ThO_2-rich a (Å)
$U_{0.848}Th_{0.146}Gd_{0.006}O_{2-\delta}$	5.472(14)	5.59(194)
$U_{0.835}Th_{0.131}Gd_{0.034}O_{2-\delta}$	5.471(15)	5.59(192)
$U_{0.758}Th_{0.234}Gd_{0.008}O_{2-\delta}$	5.471(13)	5.594(71)
$U_{0.666}Th_{0.266}Gd_{0.069}O_{2-\delta}$	5.472(18)	5.58(120)

Table S3: Comprehensive details of deconvoluted Raman spectra.

Synthesis	Composition	T_{2g} Pos. (cm^{-1})	T_{2g} FWHM (cm^{-1})	U_1 Pos. (cm^{-1})	U_1 FWHM (cm^{-1})	U_2 Pos. (cm^{-1})	U_2 FWHM (cm^{-1})	U_3 Pos. (cm^{-1})	U_3 FWHM (cm^{-1})	X^2
Co-prec.	$U_{0.848}Th_{0.146}Gd_{0.006}O_{2-\delta}$	448.82±0.09	26.39±0.23	532.84±2.74	17.53±7.28	579.29±0.48	50.39±1.42	630±0.00	38.73±8.25	0.09
Co-prec.	$U_{0.835}Th_{0.131}Gd_{0.034}O_{2-\delta}$	449.34±0.08	26.24±0.23	531.01±1.07	27.07±2.41	574.80±0.27	50.70±1.32	630±0.00	36.95±8.81	0.09
Co-prec.	$U_{0.758}Th_{0.234}Gd_{0.008}O_{2-\delta}$	451.30±0.05	28.93±0.14	535.30±1.82	18.49±4.91	579.64±0.39	48.52±1.04	630±0.00	43.04±8.35	0.03
Co-prec.	$U_{0.666}Th_{0.266}Gd_{0.069}O_{2-\delta}$	453.95±0.03	30.31±0.09	532.44±1.49	29.24±3.71	574.24±0.22	55.81±1.36	630±0.00	41.56±13.96	0.01
Solid State	$U_{0.889}Th_{0.106}Gd_{0.005}O_{2-\delta}$	445.83±0.09	21.46±0.23	528.24±3.74	13.98±10.13	573.45±0.59	52.31±1.83	630±0.00	40.81±7.06	0.12
Solid State	$U_{0.866}Th_{0.105}Gd_{0.029}O_{2-\delta}$	447.83±0.09	24.91±0.25	527.43±1.39	26.98±3.31	573.55±0.36	54.38±1.68	630±0.00	34.10±7.63	0.11
Solid State	$U_{0.801}Th_{0.192}Gd_{0.008}O_{2-\delta}$	448.71±0.08	27.06±0.23	531.44±2.09	19.33±5.64	575.94±0.32	51.38±1.26	630±0.00	38.09±7.80	0.08
Solid State	$U_{0.759}Th_{0.187}Gd_{0.054}O_{2-\delta}$	452.74±0.04	21.45±0.13	526.98±1.27	30.09±2.84	572.48±0.22	55.89±0.95	630±0.00	34.43±6.89	0.02

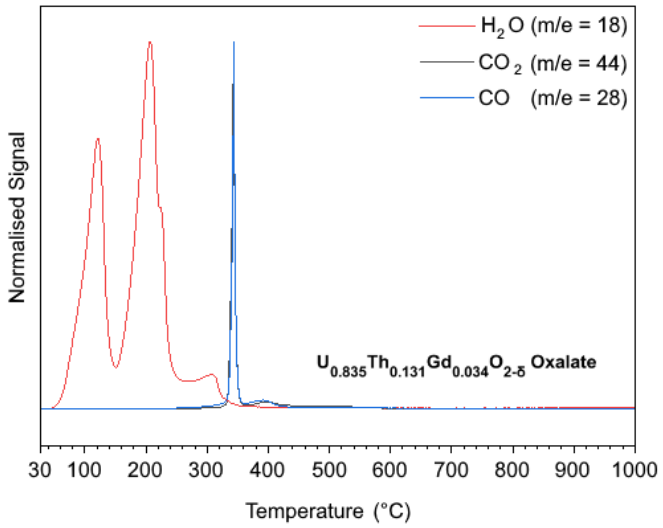

Figure S1: TG-MS data collected during calcination of $U_{0.835(5)}Th_{0.131(3)}Gd_{0.034(2)}O_{2-\delta}$.

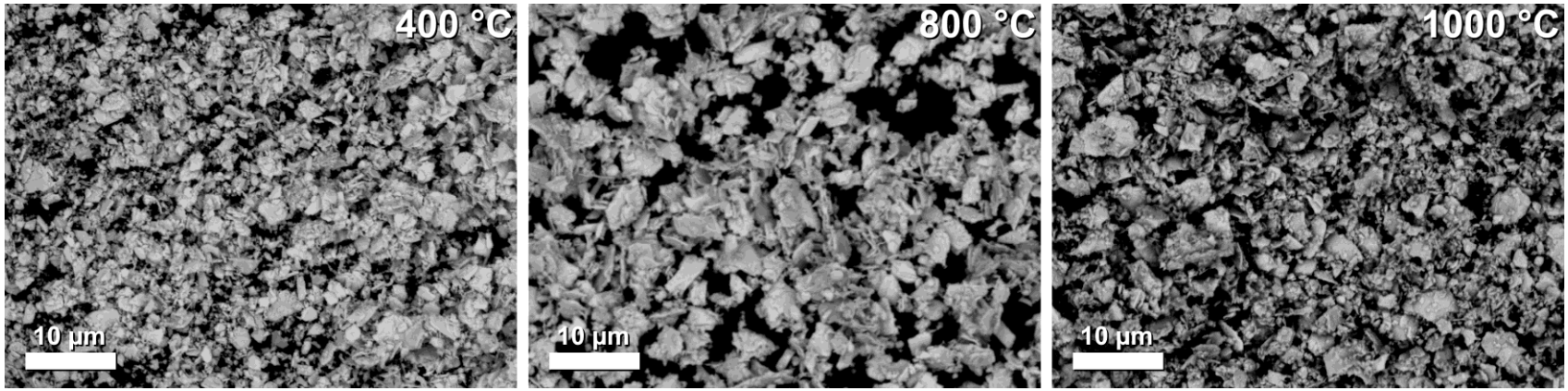

Figure S2: SEM micrographs revealing platelet morphology of $U_{0.758(1)}Th_{0.234(9)}Gd_{0.008(0)}O_{2-\delta}$ oxide powders maintained following calcination.

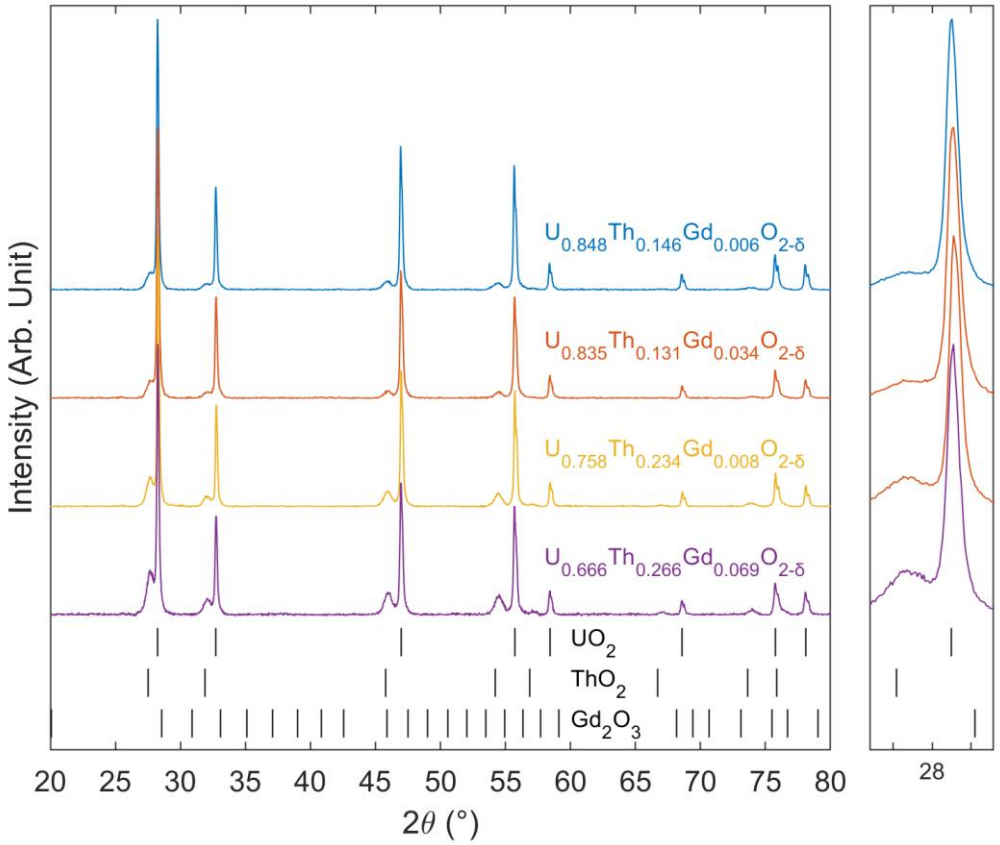

Figure S3: XRD traces collected on calcined oxide powders produced *via* wet co-precipitation. Two sets of fluorite reflections were indexed to UO_2 (ICSD 160814) and ThO_2 (ICSD 253564). Relative intensity of ThO_2-rich peaks corresponds with measured compositions. Peak shift in the ThO_2-rich reflections is readily observed due to incorporation of U^{4+} and Gd^{3+}. No peaks corresponding to cubic C-type Gd_2O_3 (ICSD 94892), or monoclinic Gd_2O_3 were observed.

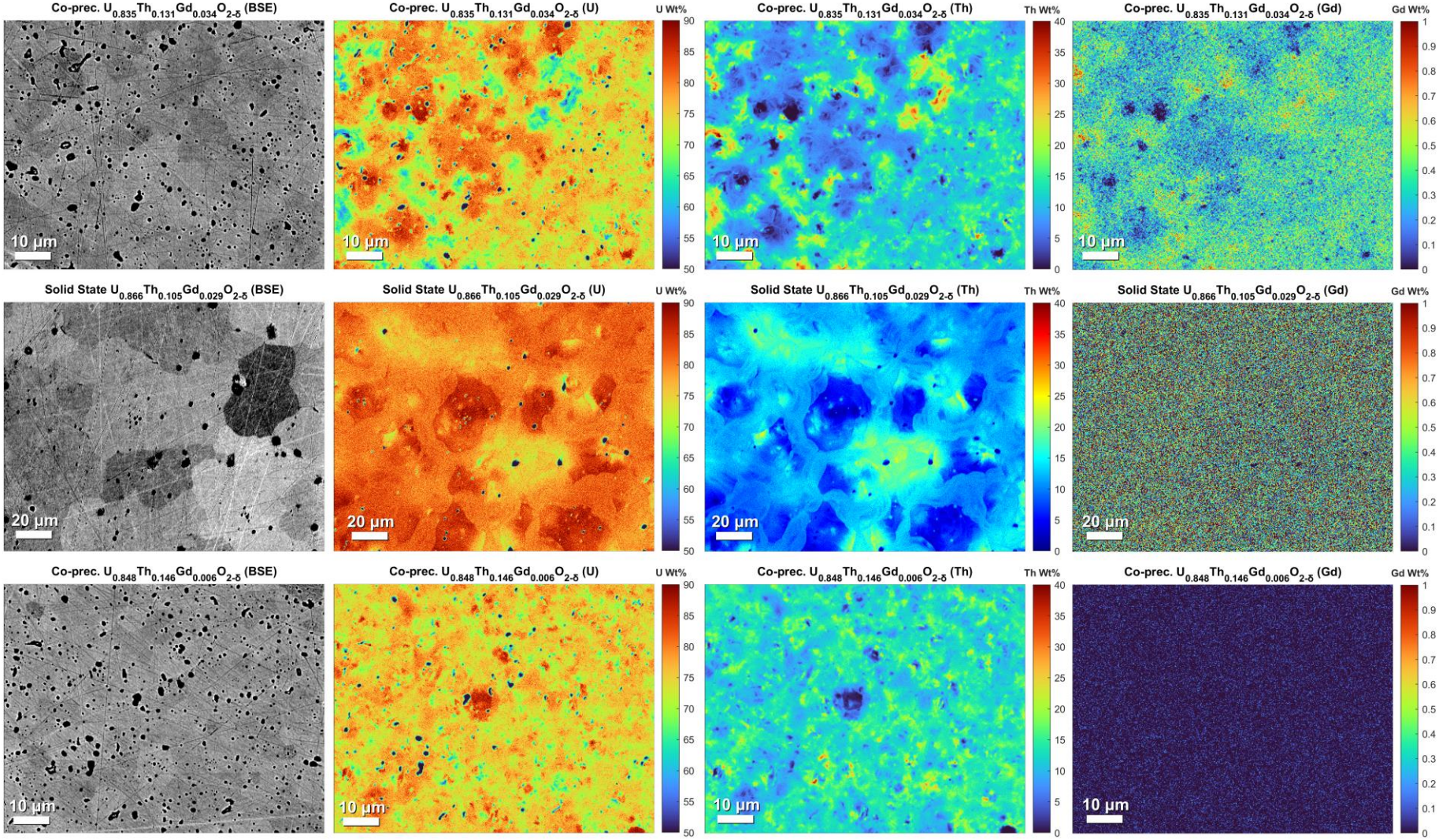
Co-prec. $U_{0.835}Th_{0.131}Gd_{0.034}O_{2-\delta}$ (BSE)
Co-prec. $U_{0.835}Th_{0.131}Gd_{0.034}O_{2-\delta}$ (U)
U Wt%
Co-prec. $U_{0.835}Th_{0.131}Gd_{0.034}O_{2-\delta}$ (Th)
Th Wt%
Co-prec. $U_{0.835}Th_{0.131}Gd_{0.034}O_{2-\delta}$ (Gd)
Gd Wt%
Solid State $U_{0.866}Th_{0.105}Gd_{0.029}O_{2-\delta}$ (BSE)
Solid State $U_{0.866}Th_{0.105}Gd_{0.029}O_{2-\delta}$ (U)
Solid State $U_{0.866}Th_{0.105}Gd_{0.029}O_{2-\delta}$ (Th)
Solid State $U_{0.866}Th_{0.105}Gd_{0.029}O_{2-\delta}$ (Gd)
Co-prec. $U_{0.848}Th_{0.146}Gd_{0.006}O_{2-\delta}$ (BSE)
Co-prec. $U_{0.848}Th_{0.146}Gd_{0.006}O_{2-\delta}$ (U)
Co-prec. $U_{0.848}Th_{0.146}Gd_{0.006}O_{2-\delta}$ (Th)
Co-prec. $U_{0.848}Th_{0.146}Gd_{0.006}O_{2-\delta}$ (Gd)
10 µm
20 µm

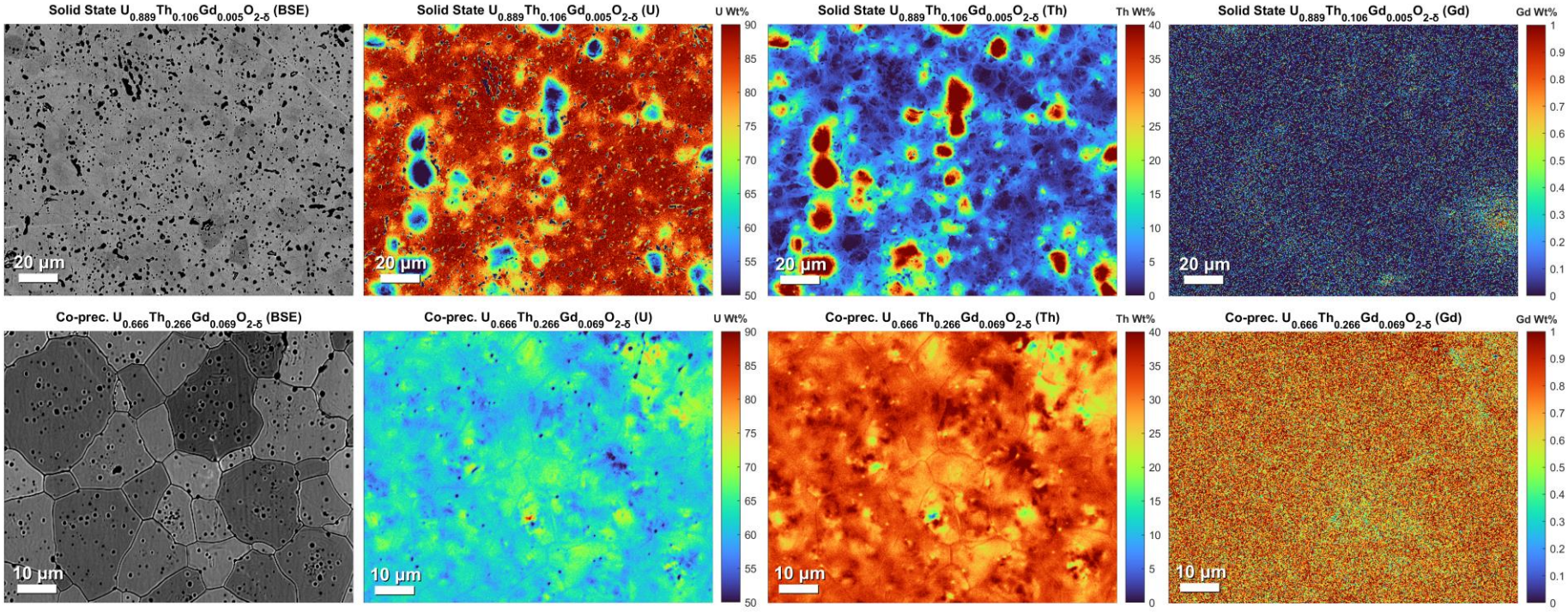

Figure S4: Complete set EPMA maps revealing U, Th and Gd distribution in disposal-MOX pellets.

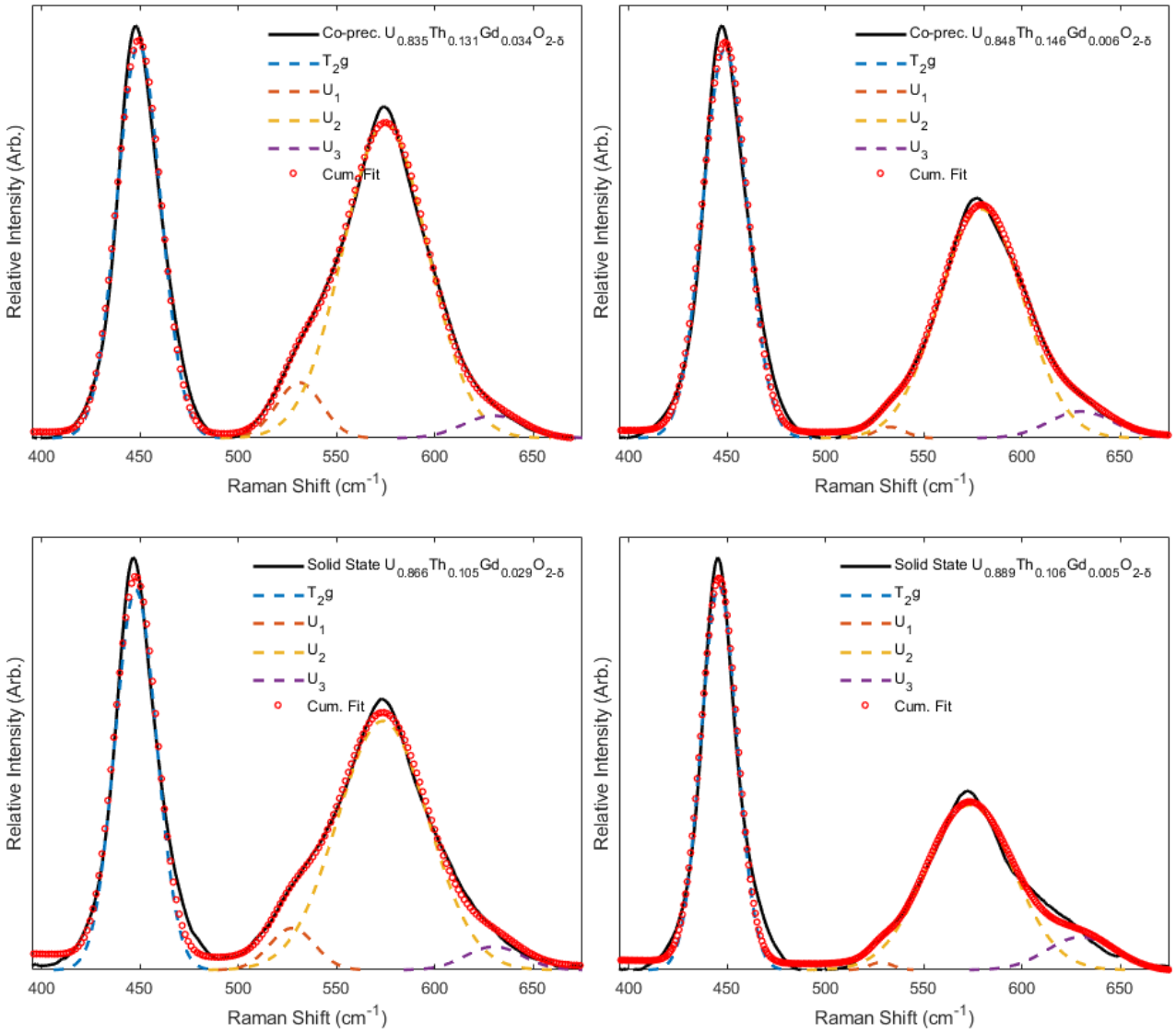
Co-prec. U0.835Th0.131Gd0.034O2-δ
T2g
U1
U2
U3
Cum. Fit
Co-prec. U0.848Th0.146Gd0.006O2-δ
Solid State U0.866Th0.105Gd0.029O2-δ
Solid State U0.889Th0.106Gd0.005O2-δ
Relative Intensity (Arb.)
Raman Shift (cm-1)
400
450
500
550
600
650

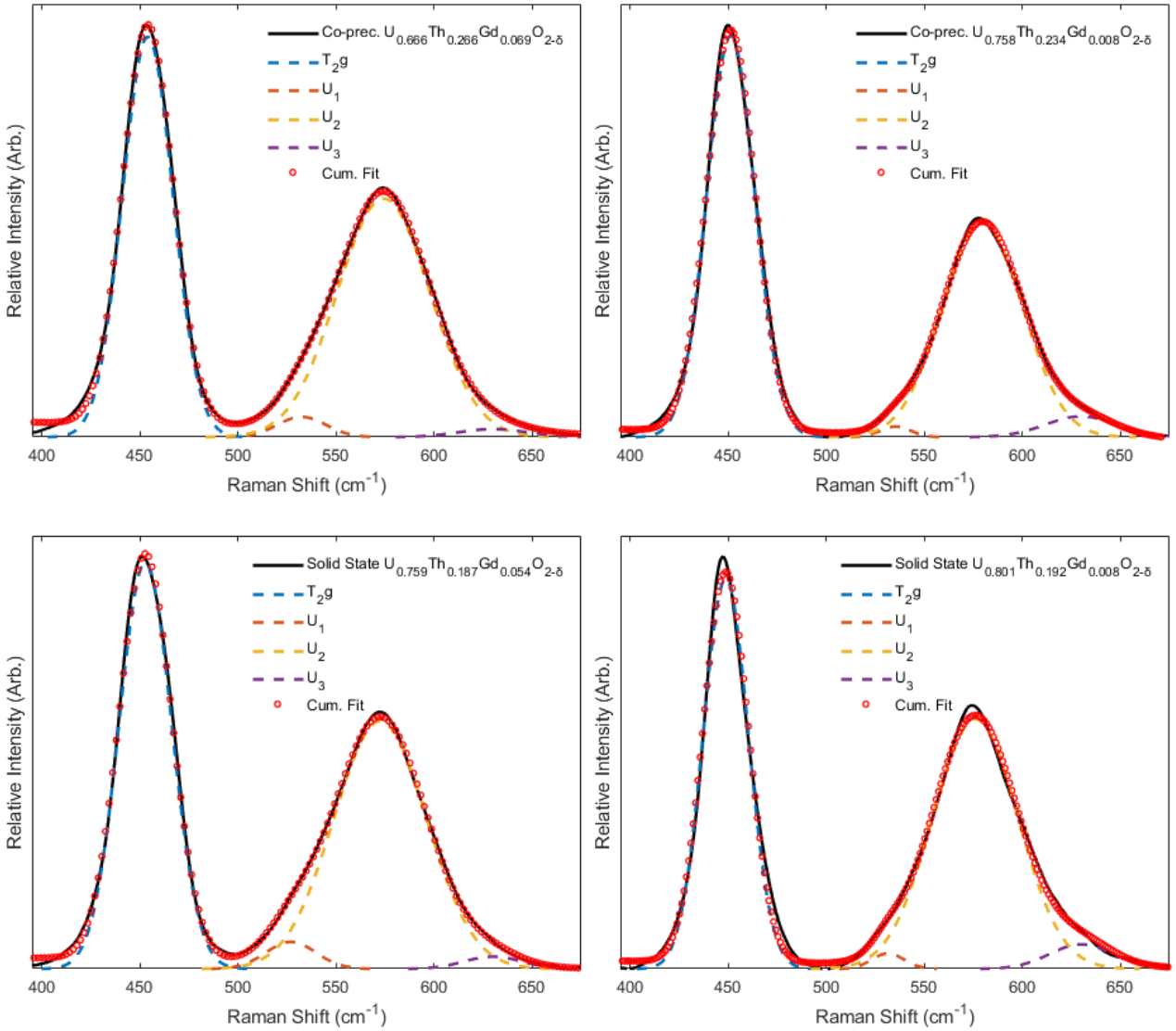

Figure S5: Complete set of deconvoluted Raman spectra collected on sintered disposal-MOX of each composition produced *via* both fabrication routes.

5. (Micro)structure-dissolution relationships in the $Ce_{1-x}Gd_xO_{2-x/2}$ system

The following chapter is a draft manuscript intended for publication.

(Micro)structure-dissolution relationships in the $Ce_{1-x}Gd_xO_{2-x/2}$ system

Max R. Cole[1], Laura J. Gardner[1], Sarah E. Pepper[1], Sebastian M. Lawson[1], Stuart Creasey-Gray[2], Le Ma[2], Colm O' Regan[2] and Claire L. Corkhill[1]

[1]NucleUS Immobilisation Science Laboratory, Department of Materials Science and Engineering, University of Sheffield, UK
[2]Sorby Centre for Electron Microscopy, Kroto Research Institute, University of Sheffield, UK

*Corresponding author: c.corkhill@sheffield.ac.uk

Abstract

Ceramic dissolution is controlled at the surface – solution interface by the surface energy of the material. This energy can vary greatly across the surface, and is influenced by grain boundaries, grain orientation, pores, and secondary phases. Understanding the contribution of high energy surface sites to dissolution is important in reducing uncertainty surrounding the behaviour of nuclear ceramics, such as UO_2 and $(U,Pu)O_2$, prior to their long-term disposal. In this work, a series of $CeO_2 – Gd_2O_3$ mixed oxides, following the general formula $Ce_{1-x}Gd_xO_{2-x/2}$ (where $0.00 \geq x \leq 1.00$), were synthesised *via* oxalic precipitation. Sintered pellets were characterised through XRD, SEM-EDS, Raman spectroscopy, EBSD, EPMA and TEM to investigate the effects of Gd incorporation on crystal structure, secondary phase formation, microdomain formation, compositional homogeneity of the matrix, grain texture, grain size and density. The dissolution behaviour was examined using both leachate-based methodology (ASTM C1308) and a novel vertical scanning interferometry (VSI)-based surface dissolution test. Compositions of $Ce_{1-x}Gd_xO_{2-x/2}$ where $x \leq 0.30$ adopted single-phase fluorite determined by XRD, with the matrix adopting a C-type (Ia-3) structure for $x \geq 0.40$. Examination of compositions where $x \leq 0.15$ revealed incorporation of trivalent Gd^{3+} generated oxygen vacancies (V_O) in the structure. Gd-rich C-type secondary phases formed within the fluorite matrix for x = 0.10 – 0.30. C-type nanodomains may have formed, even in samples where x = 0.05. Gd additions were found to segregate towards grain boundaries, and form larger agglomerates within fluorite grains, though this heterogeneity did not influence localised dissolution rates. Gd additions exerted strong control over dissolution rates; the greatest Ce and Gd normalised release was measured for x = 0.15. Incongruent release of Ce and Gd, observed in all compositions, is suspected to have resulted from preferential dissolution of Gd-enriched grain boundaries and Gd-rich secondary phases. Spatial Gd distribution within fluorite $Ce_{1-x}Gd_xO_{2-x/2}$ was found to exert no discernible control over localised dissolution rates. Grain boundary misorientation was also found to have no influence on rate of grain boundary dissolution, regardless of composition. These findings suggest that the most significant impact of Gd additions on CeO_2 dissolution result from changes to crystal structure; Gd additions do not influence the role of reactive surface sites within the microstructure on localised dissolution rates.

1. Introduction

The widely supported policy for the safe long-term management of spent nuclear fuel is permanent disposal within a geological facility. Transport in groundwater represents the most likely mechanism for spent fuel radionuclide release into the biosphere. Comprehensive understanding of the factors influencing spent nuclear fuel dissolution is paramount for its safe disposal. Spent fuel is a complex, heterogenous ceramic, predominantly comprised of UO_2 (> 95%), with an array of fission products and actinides constituting the remainder. Insoluble fission products precipitate into separated ceramic and metallic phases, and fission gas release generates voids in the microstructure[1]. The microstructural and compositional complexity of real spent fuel makes deconvolution of dissolution mechanics very challenging. In addition, highly radioactive isotopes cause radiolysis of leachate solutions. U^{4+} in the fluorite matrix is readily oxidised to its more soluble U^{6+} state, further complicating the elucidation of dissolution processes. The UO_2 matrix of spent fuel incorporates, amongst other fission products, soluble rare-earth elements, such as Gd, within its lattice. Rare-earth additions are estimated to constitute 22% of moderate burn-up spent fuel after 100 years of cooling[2], and are known to influence to structure and dissolution behaviour of UO_2 [3,4]. Gd-doped UO_2 fuels have also been developed, with Gd providing a burnable poison used to control burnup[5]. The high neutron capture cross-section of Gd has also sparked research into its potential use for criticality mitigation in disposal mixed-oxide (MOX) materials[6,7].

In this work, CeO_2 was employed as a surrogate for UO_2, in a highly simplified interpretation of spent fuel. CeO_2 is a well-established inactive surrogate for UO_2. CeO_2 surrogates can facilitate simplified dissolution experiments that are not influenced by immiscible phases, radiolysis or redox sensitivities associated with UO_2 [8]. CeO_2 microstructure is similar to that of UO_2, featuring randomly oriented, equiaxed grains[9]. CeO_2 crystallises as fluorite (Fm-3m), which is the same structure adopted by both UO_2 and PuO_2. Furthermore, Ce in CeO_2 assumes a highest oxidation state of 4+ (i.e. it cannot be oxidised further), the tetravalent state is also observed for U and Pu in their respective stoichiometric oxides. The crystal radius of Ce^{4+}, U^{4+}, and Pu^{4+} in 8-fold coordination are also very similar (1.11, 1.14, and 1.10 Å respectively[10]). Gd-doped CeO_2 ceramics, of general composition $Ce_{1-x}Gd_xO_{2-x/2}$, are widely studied materials, most prevalently due to their suitability as solid electrolytes in solid oxide fuel cells[11]. Existing studies on the $Ce_{1-x}Gd_xO_{2-x/2}$ system have investigated the effects of Gd^{3+} on the crystal structure, grain size, density, electrical and thermal properties. Very limited investigation into the aqueous dissolution behaviour of $Ce_{1-x}Gd_xO_{2-x/2}$ has been performed, with no existing studies conducted on sintered pellets of $Ce_{1-x}Gd_xO_{2-x/2}$.

The surface – solution surface interaction is key to understanding dissolution in ceramic materials. The presence of certain microstructural features, for example, grain boundaries, results in heterogeneous rates of material removal, or retreat, as they have greater interfacial surface energies. Crystallographic orientation is also known to exert strong control over dissolution rate in fluorite oxides such as CaF_2 and CeO_2 [12,13]. Corkhill *et al.* found high-angle grain boundaries dissolved faster when compared to their low-angle equivalents, which was attributed to high concentrations of defects incorporated into highly disordered structure of high-angle (~60°) grain boundaries[14]. Spatially resolved studies of surface retreat measured using vertical scanning interferometry (VSI), a form of 3D optical profilometry, permit examination of relative contributions from specific microstructural regions. VSI surface measurements were paired with EBSD and EPMA maps of the same regions to investigate relationships between grain orientation, grain boundary misorientation, Gd segregation with localised retreat rates.

The entire CeO_2 – Gd_2O_3 solid solution ($Ce_{1-x}Gd_xO_{2-x/2}$ solid solutions, where x = 0, 0.1, 0.2, 0.3, 0.4, 0.5, 0.6, 0.7, 0.8, 0.9 and 1.0) was firstly investigated to ascertain crystal structure and secondary phase formation in sintered materials. Additional $Ce_{1-x}Gd_xO_{2-x/2}$ compositions with lower Gd concentrations more relevant to spent fuel (x = 0.0, 0.05, 0.10 and 0.15) were studied in further detail to additionally investigate the influence of Gd segregation, C-type nanodomain formation, oxygen vacancy (V_O) generation, and grain texture on the aqueous dissolution behaviour as a function of Gd concentration. Conventional 'bulk' dissolution studies were supplemented with 3D measurements of surface retreat in an effort to deconvolute the complex factors controlling dissolution.

2. Experimental

2.1 Materials synthesis

Mixed oxides of $Ce_{1-x}Gd_xO_{2-x/2}$, where x = 0, 0.1, 0.2, 0.3, 0.4, 0.5, 0.6, 0.7, 0.8, 0.9 and 1.0, were prepared using an oxalic precipitation route. Hydrated salts of Ce and Gd, $CeCl_3 \cdot 7H_2O$ and $GdCl_3 \cdot 7H_2O$, (>99% purity, Sigma-Aldrich) were dissolved in 1 M hydrochloric acid (HCl) to produce 1 M and 0.5 M solutions of $CeCl_3$ and $GdCl_3$ respectively. The appropriate volume of each solution for the desired composition was then pipetted into an excess of 1 M oxalic acid ($C_2H_2O_4$) and stirred, resulting in instantaneous precipitation of mixed (Ce,Gd) oxalates according to:

$$(1-x)Ce^{3+} + xGd^{3+} + \frac{3}{2}H_2C_2O_4 + yH_2O \xrightarrow{1\,M\,HCl} Ce_{1-x}Gd_x(C_2O_4)_{1.5} \cdot yH_2O + 3H^+$$

This reaction was allowed to continue for five minutes, under continuous mixing conferred by a magnetic stirrer. The oxalate precipitate was then placed within a vacuum filtration system for 5 minutes and dried at 90 °C for 12 hours. The dried precipitate was then calcined in air at 1000 °C for 4 hours, converting the oxalates to oxides through the oxidation of Ce^{3+} to Ce^{4+}. Calcination temperatures approaching 1000 °C ensure complete decomposition of the oxalate, higher temperatures also yield larger oxide particles with greater sinterability[9]. The decomposition reaction is described by Equation 2.

$$Ce_{1-x}^{III}Gd_x^{III}(C_2O_4)_{1.5} \cdot yH_2O \xrightarrow{1000\,^{\circ}C,\ 4h} Ce_{1-x}^{IV}Gd_x^{III}O_{2-\frac{x}{2}} + \left(2-\frac{x}{2}\right)CO + \left(1+\frac{x}{2}\right)CO_2 + yH_2O$$

Equation 2: Decomposition of a mixed oxalate to yield a mixed oxide powder in the form $Ce_{1-x}Gd_xO_{2-x/2}$.

Following the calcination, the oxide powders were sieved using a 212 μm sieve to create a finer, more freely flowing powder with a high surface area. This step allowed for more effective pressing and sintering, resulting in denser pellets[9]. The oxide powder was compacted into pellets using a uniaxial hydraulic press; 0.5 g of powder was pressed under 2 tons into a 10 mm die and held for 2 minutes to consolidate each pellet. Green bodies were then placed within a zirconia crucible and sintered in air at a temperature of 1700 °C for 10 hours, with approximate heating rates of 5 °C min^{-1}.

2.2 Materials characterisation

X-ray Diffraction (XRD) was performed on calcined oxides, sintered pellets and crushed sintered material using a Bruker D2 Phaser diffractometer fitted with a Lynxeye position sensitive detector; traces were acquired in the ranges $20° \leq 2\theta \leq 80°$ using a Cu- Kα source (λ = 1.5418 Å, Ni filter) with a step-size of 0.02°. Sintered powders obtained through crushing with pestle and mortar were mixed with 10 wt% LaB_6 to provide an internal standard for higher quality Rietveld refinements, which were run through the Bruker TOPAS package.

Scanning Electron Microscopy (SEM), paired with Energy Dispersive X-ray Spectroscopy, (EDS) was conducted using Hitachi TM3030 and FEI Inspect F50 instruments. The Hitachi TM3030 was operated in back-scattered electron (BSE) mode, using an accelerating voltage of 15 kV at a working distance of approximately 8 mm. The Inspect F50 was primarily operated in secondary electron (SE) mode; observation conditions varied depending on the sample, however, the microscope was typically operated at accelerating voltages of 15 or 20 kV, using spots size 4-5, with a working distance of approximately 10 mm. EDS maps and point spectra were collected in a minimum of 10 regions across the surface of each pellet for compositional analysis. Sintered pellets were polished to 1 μm and carbon coated using a Quorum Q150T Sputter Coater prior to examination. EDS spectra collected on the Hitachi TM3030 and FEI

Inspect F50 were analysed using the Bruker Quantax and Oxford Instrument AZtec software packages, respectively.

Electron Back Scatter Diffraction (EBSD) analysis was performed using a JEOL JSM 7900F SEM equipped with an Oxford Instruments AZtec HKL Advanced Symmetry System. An accelerating voltage of 20 kV was used at a working distance of 13 mm to collect 120,000 μm^2 maps with 0.5 µm stepsize, 16,500 μm^2 maps with 0.2 µm and 4900 μm^2 maps with a stepsize of 0.1 µm. For all maps the dwell time was 10 µs. Transmission electron backscatter diffraction (t-EBSD) was conducted with an accelerating voltage of 30 kV at a working distance of 4.2 mm, mapping 50 μm^2 with a stepsize of 9 nm and a dwell time of 3 µs. Oxford Instruments' AZtec Crystal software was used to calculate grain texture and grain boundary misorientation.

The average grain size was obtained through image analysis of SEM micrographs and also EBSD analysis. Grain size analysis of SEM micrographs firstly requires thermally annealing flat polished pellets to etch and deepen the surface at grain boundaries; pellets were heated to 90% of their sintering temperature (1630 °C) and held for 2 hours. Individual grains captured within SEM micrographs were isolated by morphological segmentation using MorphoLibJ plug-in suite[15] in the Fiji software package[16], allowing for their areas to be measured. This process was repeated until a minimum of 500 grains had been analysed. EBSD data analysed using Oxford's AZtec Crysal software also provided a measurement of average grain area, enabling measurement of 1000s of grains for each composition.

Raman spectroscopy was performed using a Renishaw inVia microscope on polished and annealed sintered pellets. A minimum of five measurements were taken within the centre of grains across the surface of each pellet; each spectrum comprised 15 one-second static acquisitions collected in the range 170 – 850 cm^{-1} made using a 514 nm laser at 10 mW power. The spectra were baseline removed, smoothed using the Savitsky-Golay approach[17], and averaged. Deconvolution of Raman bands was carried out using Igor Pro, assigning Lorentzian peaks to T_{2g} whereas Gaussian peaks were used for both D_1 and D_2. No constraints were applied to the position of FWHM in any fits.

Density measurements were conducted using both a METTLER TOLEDO ME204 Archimedes balance and a Micromeritics AccuPyc II gas pycnometer. 10 repeat Archimedes measurements were used to calculate average densities of sintered pellets. 10 repeat pycnometry measurements were used to calculate average densities of calcined oxide powders, powdered sintered material, and sintered pellets. In both instances, the quoted errors correspond to the standard deviation of these measurements. Theoretical densities were calculated using lattice parameters obtained through Rietveld refinements.

Electron Probe Micro-analysis (EPMA) was undertaken using a JEOL JXA-8530F Plus Hyper Probe with an accelerating voltage of 15 kV and a probe current 100 nA. Pellets were polished flat to 0.25 µm using diamond suspension, then to 0.05 µm using colloidal alumina/silica suspension before carbon coating. Five quantitative spot measurements, taken within grain centres across the surface of each pellet, were averaged for compositional analysis. A 12 wt% Ce glass standard (Ca, Si, Al, O), and 12 wt% Gd glass standard (Ca, Si, Al, O) were used to quantify the wt% of Ce and Gd respectively. Additional standards $CeAl_2$ and Al_2O_3 were used to verify intensity ratios for Ce and O respectively. In addition to Ce, Gd and O, measurements of Al and Si were also made to diminish the impact of any residual polishing media on the accuracy of the quantitative results. Channels, crystals, and peaks selected for each element can be found in the Supplementary information in Table S1.

Scanning Transmission Electron Microscopy (STEM) analysis was performed using a JEOL F200 with an accelerating voltage of 200 kV. Electron diffraction micrographs were captured with an exposure time of 0.1 s, using apertures ranging from 10 – 100 µm in diameter. STEM-EDS maps and line scans were collected using an accelerating voltage of 300 kV.

Vertical Scanning Interferometry (VSI) measurements were collected using a Bruker Contour Elite, operated in white light VSI mode at 50x and 115x magnification using a 1x FOV multiplier and 1x scan speed. The intensity threshold was set to 1%, with back scan and length set to 5 and 10 µm respectively. Tilt removal was performed in both Bruker's Vision64 software, whilst matrices were aligned and subtracted using Mathworks' MATLAB software.

Semi-dynamic aqueous dissolution experiments using the ASTM C1308 [18] were performed on sintered pellets, in triplicate, at 90 °C in 0.01 M HNO_3 solution. While not representative of spent nuclear fuel disposal conditions, it was necessary to use aggressive leaching media to observe dissolution of the highly durable materials investigated. Sampling took place after 1, 2, 3, 4, 7, 10, 14, 21 and 28 days of dissolution. Concentrations of Ce and Gd removed in aliquots of leachate, in addition to solutions recovered after acid stripping the vessels, were measured using Inductively Coupled Plasma-Mass Spectrometry (ICP-MS). Elemental concentrations were blank subtracted and converted to normalised elemental mass release in g m^{-2} according to Equation 3.

$$NL_i = \frac{m_i}{SA \times EF_i}$$

Equation 3: Calculation of normalised elemental mass release for a given element 'i', where NL_i is the normalised elemental mass loss/release, m_i is the mass of the given element measured in solution, SA is the surface area of the sample in solution, and EF_i is the elemental mass fraction of the given element in the sample.

A Thermo iCAP RQ ICP-MS with an ESI PrepFast 4DX autosampler was used to measure solutions diluted 10x in ultrapure HNO_3. External calibration used single element standards (NIST traceable). All standards and samples were matrix matched to 2% HNO_3. Internal standards of V-51, Rh-103, Tb-159 and Ir-193, were measured simultaneously. Quality control samples were analysed after the calibration and then every 10 samples, giving confidence limits of ± 20%.

3. Results and discussion on CeO_2 – Gd_2O_3 solid solution

3.1 $Ce_{1-x}Gd_xO_{2-x/2}$ compositions

Material compositions measured by SEM-EDS indicate successful synthesis of desired Ce:Gd stoichiometries (Table 1). Individual EDS spectra are available in the Supplementary information (Figure S1). Compositions of $Ce_{1-x}Gd_xO_{2-x/2}$, where $x \geq 0.50$, are further from the nominal desired composition, likely resulting from greater error associated with adding large amount of 1 M $CeCl_3$ to 0.5 M $GdCl_3$. These solutions were prepared at different concentrations to ensure most accurate additions of Gd, as this study was primarily concerned with the implications of Gd incorporation within CeO_2, not *vice versa*. As measurements were in generally good agreement with nominal compositions, samples will be referred to by their nominal compositions for the remainder of this work.

Table 1: Summary of nominal and obtained $Ce_{1-x}Gd_xO_{2-x/2}$ solid solutions.

Nominal Composition	Measured Composition (SEM-EDS)
CeO_2	CeO_2
$Ce_{0.90}Gd_{0.10}O_{2-\delta}$	$Ce_{0.90(6)}Gd_{0.09(6)}O_{2-\delta}$
$Ce_{0.80}Gd_{0.20}O_{2-\delta}$	$Ce_{0.79(9)}Gd_{0.20(9)}O_{2-\delta}$
$Ce_{0.70}Gd_{0.30}O_{2-\delta}$	$Ce_{0.69(8)}Gd_{0.30(8)}O_{2-\delta}$
$Ce_{0.60}Gd_{0.40}O_{2-\delta}$	$Ce_{0.5(23)}Gd_{0.4(23)}O_{2-\delta}$
$Ce_{0.50}Gd_{0.50}O_{2-\delta}$	$Ce_{0.4(12)}Gd_{0.5(12)}O_{2-\delta}$
$Ce_{0.40}Gd_{0.60}O_{2-\delta}$	$Ce_{0.3(24)}Gd_{0.6(24)}O_{2-\delta}$
$Ce_{0.30}Gd_{0.70}O_{2-\delta}$	$Ce_{0.2(12)}Gd_{0.7(12)}O_{2-\delta}$
$Ce_{0.20}Gd_{0.80}O_{2-\delta}$	$Ce_{0.13(7)}Gd_{0.86(7)}O_{2-\delta}$
$Ce_{0.10}Gd_{0.90}O_{2-\delta}$	$Ce_{0.06(2)}Gd_{0.93(2)}O_{2-\delta}$
Gd_2O_3	Gd_2O_3

3.2 Crystal structure of CeO_2 – Gd_2O_3 solid solution

Oxides of $Ce_{1-x}Gd_xO_{2-x/2}$, obtained *via* calcination of oxalates at 1000 °C, crystallised as single-phase cubic fluorite (Fm-3m) structure when $x \leq 0.30$. Gd additions beyond $x = 0.30$ resulted in additional reflections characteristic of cubic bixbyite (Ia-3), often referred to as the C-type structure[19]. Figure 1 shows XRD traces collected on calcined oxide powders across the entire CeO_2-Gd_2O_3 solid solution.

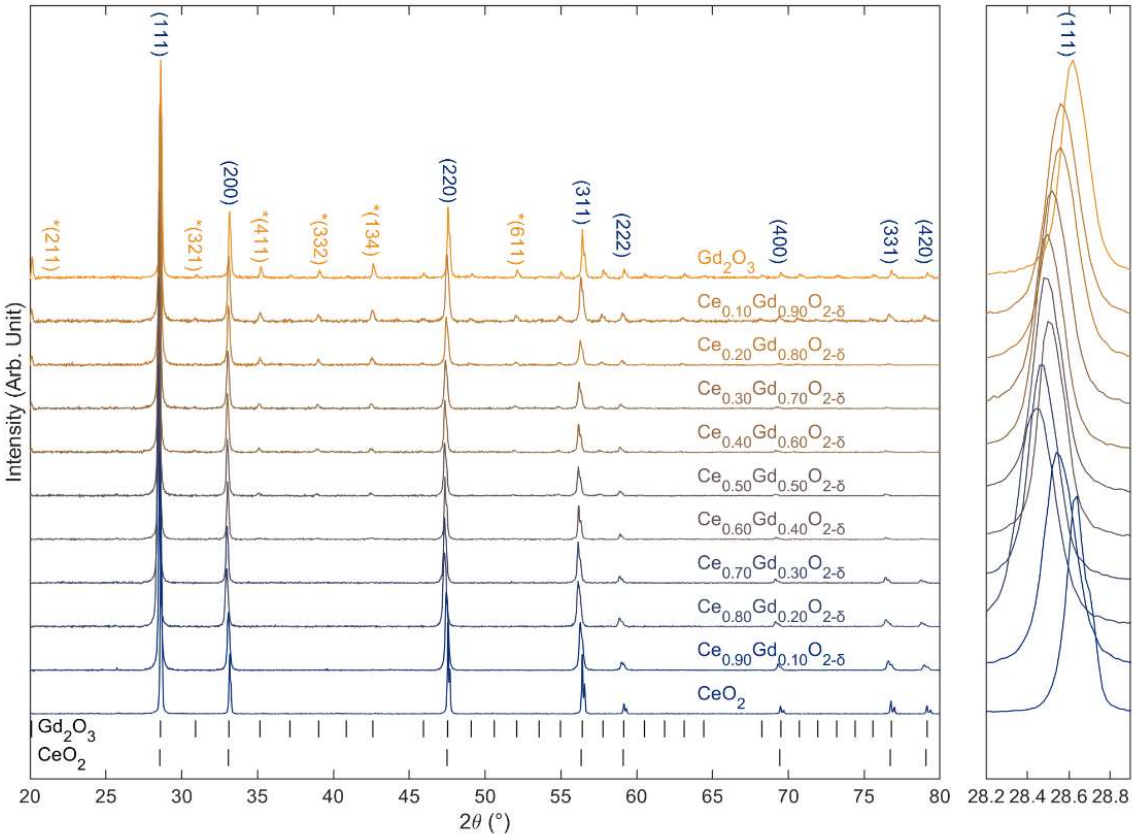

Figure 1: Stacked XRD plot of traces collected on calcined powders of $Ce_{1-x}Gd_xO_{2-x/2}$, where x = 0.00 – 1.00. Subplot highlights shift on (111) reflection. Reference XRD patterns taken from the Inorganic Crystal Structure Database (ICSD). CeO_2: ICSD 155604, Ia-3 Gd_2O_3: ICSD 40473[20].

The transition from fluorite to C-type is evidenced by reflections in the range 35° – 43° 2θ, denoted with asterisks in Figure 1. This C-type structure is maintained throughout the remainder of the solid solution of calcined mixed oxides, including in pure Gd_2O_3. The C-type structure is formed when a sufficient concentration of oxygen vacancies (V_O), generated to compensate for trivalent Gd^{3+}, are present within the fluorite lattice. V_O, which were previously randomly distributed through the lattice, become ordered through the removal of O^{2-} at each position in the (111) plane. Widespread V_O ordering displaces cations to new crystallographic sites. These displacements break the symmetry of the fluorite unit cell, doubling the lattice parameter through creation of a new cubic superlattice, known as the C-type structure[21,22]. The C-type structure remains very similar to fluorite, so distinguishing between the two structures can prove challenging. In XRD analysis, many C-type reflections are superposed with those of fluorite, with additional reflections being less intense peaks resulting from the superlattice. XRD is not sensitive to V_O and can only detect the presence of C-type phases once formed in sufficient quantities when the intensity of the addition reflections caused by atomic displacements is sufficiently high. For this reason, certain compositions of

$Ce_{1-x}Gd_xO_{2-x/2}$ characterised as single-phase by XRD were examined further with more sensitive techniques including Raman spectroscopy, EBSD and TEM (see Sections 4.4, 4.5 and 4.6).

Lattice expansion in calcined oxides of $Ce_{1-x}Gd_xO_{2-x/2}$ is observed for $x \leq 0.20$, evidenced by peak shift to lower values of *2θ*. This is due to the larger ionic radius of Gd^{3+} relative to Ce^{4+} (1.053 Å and 0.97 Å respectively[10]). Lattice contraction is observed with Gd additions where $x > 0.20$, with peak shift to higher values of 2θ. This contraction is caused by V_O generation decreasing the extent of O – O repulsion, resulting in unit cell contraction[23]. This reverse in peak shift suggests the dominant influence on the lattice volume of calcined oxides of $Ce_{1-x}Gd_xO_{2-x/2}$ for $x \leq 0.20$, is the increased ionic radius of Gd. However, the reduction in O – O repulsion outweighs the increased ionic radius, resulting in lattice contraction. In compositions where $x \geq 0.40$, formation of C-type phases consolidates this contraction, as the C-type structure has a smaller lattice volume compared to fluorite. Horlait *et al.* found this behaviour occurred for calcined oxides of $Ce_{1-x}Gd_xO_{2-x/2}$ between $x = 0.30 – 0.60$ [23].

3.3 Crystal structure of sintered $CeO_2 – Gd_2O_3$ solid solution

Existing studies of the $Ce_{1-x}Gd_xO_{2-x/2}$ system have found the formation of fluorite and C-type phases is strongly dependent on synthesis route and heat treatment of samples. For this reason, XRD analysis was repeated on compositions sintered at 1700 °C.

Figure 2 shows XRD traces collected on sintered pellets across the entire $CeO_2 – Gd_2O_3$ solid solution.

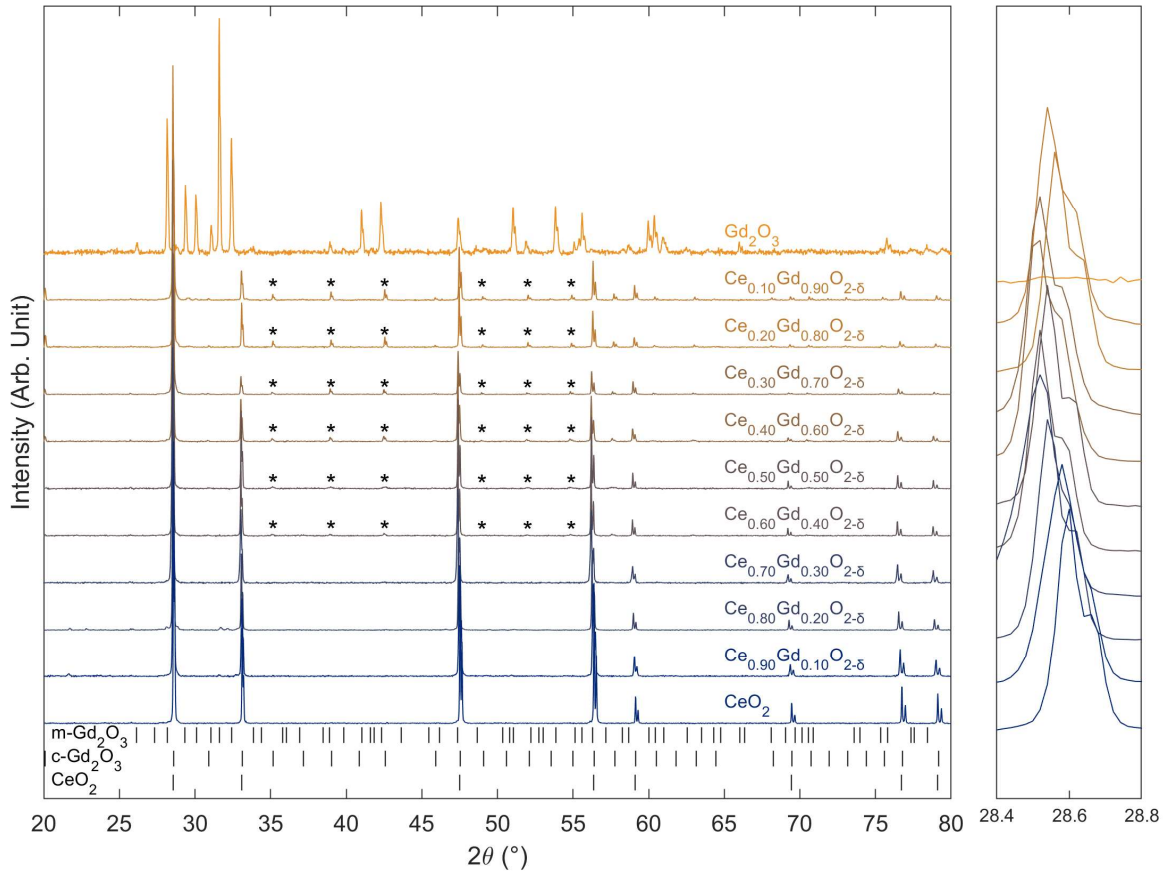

Figure 2: Stacked XRD plot of traces collected on sintered pellets of $Ce_{1-x}Gd_xO_{2-x/2}$, where x = 0.00 – 1.00. Subplot highlights the shift on the (111) reflection. Reference XRD patterns taken from the Inorganic Crystal Structure Database (ICSD). CeO_2: ICSD 155604, c-Gd_2O_3 (Ia-3): ICSD 40473, m-Gd_2O_3 (C2/m), ICSD 636103 [20]. Asterisks denote additional peaks corresponding to C-type (Ia-3) phases.

Crystal structures of $Ce_{1-x}Gd_xO_{2-x/2}$ sintered at 1700 °C were similar to those observed in oxides calcined at 1000 °C. As with the calcined oxide powders, reflections characteristic of the single-phase cubic fluorite (Fm-3m) structure are observed in sintered pellets where x ≤ 0.30, whereas for x = 0.40 – 0.90 the compositions adopted a C-type (Ia-3) structure. This transition is evidenced by additional reflections in the range 35° – 43° 2θ, denoted with asterisks in Figure 2. Ye *et al.* and Horlait *et al.* also reported formation of a single fluorite phase, as determined by XRD, for compositions of $Ce_{1-x}Gd_xO_{2-x/2}$ where x ≤ 0.30[21,23]. Beyond this threshold, the CeO_2 – Gd_2O_3 system is generally considered to transition entirely from fluorite to C-type, bypassing a biphasic regime[24–27]. In their synchrotron X-ray diffraction study of $Ce_{1-x}Gd_xO_{2-x/2}$, Artini *et al.* found for x > 0.30, peaks associated with C-type increased in intensity, as observed in present study. Whilst this might initially suggest the formation of a biphasic region, peak splitting was not observed, despite the technique resolution being sufficient to distinguish between the near identical fluorite and C-type. Furthermore, they noted an absence of lattice parameter saturation at the onset of these additional C-type peaks, with

the lattice expanding until x = 0.50[26]. Grover *et al.* also observed an immediate transition from fluorite to C-type, but instead occurring for x > 0.40, they too noted a subsequent increase in lattice parameter with additional Gd, and used this lack of saturation to support their claim that the system was not biphasic. Near identical behaviour is observed in XRD analysis presented in this study, with intensity in C-type reflections increasing for x > 0.30, beyond which the lattice parameter continues to increase. Artini *et al.* hypothesised that C-type nanodomains grow within the fluorite structure using it as a matrix, and when x > 0.30 previously randomly distributed domains become ordered, triggering the coherent growth of C-type phase. However, it must be noted that due their structural similarity, small quantities of C-type phases cannot be measured using XRD, and the instrument is unable to detect additional phases, monoclinic Gd_2O_3-rich phases, comprising less than ~2 wt% of the total material. For this reason, XRD analysis can only be considered to represent an average of the bulk phase and should not be interpreted as evidence that samples are truly single-phase, or that no biphasic region exists.

Pellets of pure Gd_2O_3 (x = 1.00) adopted a monoclinic (C2/m) structure after sintering, in contrast to the C-type structure observed in the calcined oxide. Gd_2O_3 is known to crystallise in C-type structure at temperatures below 1200 °C, but transforms to monoclinic (C2/m) at higher temperatures[28], explaining why oxides calcined at 1000 °C conformed to C-type but pellets sintered at 1700 °C crystallised in monoclinic structure. Close examination of patterns collected on compositions where x ≤ 0.30 reveals the presence of very low intensity reflections that could be indexed to monoclinic Gd_2O_3; secondary phase formation is discussed further in Section 3.5.

Lattice expansion due to the increased ionic radius of Gd^{3+} is observed for x ≤ 0.40, as indicated by peak shift to lower values of 2θ. This was verified by Rietveld refinements presented in Figure 3 and summarised in Table 2. In compositions where x ≥ 0.50, increase in average ionic radius is completely negated by the reduction in O – O repulsion and widespread C-type phase formation. In pellets where x ≥ 0.50, the lattice parameter is reduced with increasing Gd^{3+} content. In this region, C-type Gd_2O_3 is the host phase, therefore, following Vegard's law, reducing the quantity of smaller Ce^{4+} ions should increase the lattice parameter. However, the opposite effect is observed in the Gd_2O_3 – CeO_2 system; incorporation of Ce^{4+} into Gd_2O_3 instead causes lattice expansion, due to ionic repulsion between excess interstitial atoms[24]. This explains why reducing the quantity of Ce^{4+} in the C-type Gd_2O_3 causes a reduction in the lattice parameter.

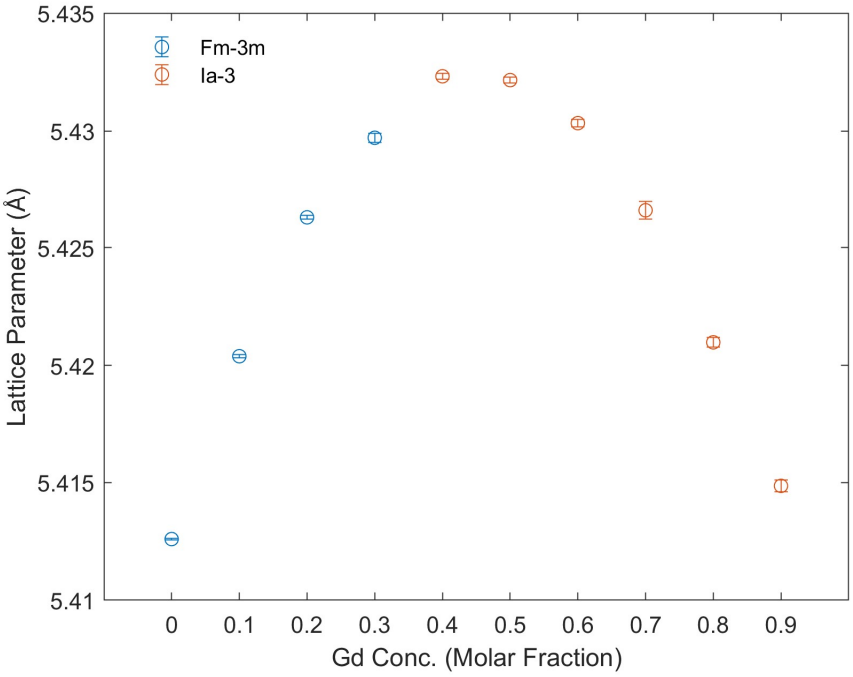

Figure 3: Plot of refined lattice parameters against Gd concentration for sintered pellets of $Ce_{1-x}Gd_xO_{2-x/2}$ where $0.00 \leq x \geq 0.90$. Where $x \geq 0.40$, lattice parameters have been halved to aid comparison between samples Fm-3m and Ia-3

Table 2: Summary of Rietveld refinements performed on entire CeO_2-Gd_2O_3 solid solution.

Composition	Space group	a (Å)	b (Å)	c (Å)	Rwp
CeO_2	Fm-3m	5.4125(4)	—	—	12.452
$Ce_{0.9}Gd_{0.1}O_{2-\delta}$	Fm-3m	5.4204(8)	—	—	11.889
$Ce_{0.8}Gd_{0.2}O_{2-\delta}$	Fm-3m	5.4262(8)	—	—	15.304
$Ce_{0.7}Gd_{0.3}O_{2-\delta}$	Fm-3m	5.429(19)	—	—	10.899
$Ce_{0.6}Gd_{0.4}O_{2-\delta}$	Ia-3	5.432(12)*	—	—	10.961
$Ce_{0.5}Gd_{0.5}O_{2-\delta}$	Ia-3	5.432(12)*	—	—	9.843
$Ce_{0.4}Gd_{0.6}O_{2-\delta}$	Ia-3	5.430(17)*	—	—	11.395
$Ce_{0.3}Gd_{0.7}O_{2-\delta}$	Ia-3	5.426(38)*	—	—	21.258
$Ce_{0.2}Gd_{0.8}O_{2-\delta}$	Ia-3	5.420(20)*	—	—	12.295
$Ce_{0.1}Gd_{0.9}O_{2-\delta}$	Ia-3	5.414(24)*	—	—	11.55
Gd_2O_3	C2/m	14.093(88)	3.576(21)	8.76(385)	8.977

*Divided by 2 to ease comparison with Fm-3m compositions.

3.4 Density of CeO_2 – Gd_2O_3 solid solution

The density of sintered $Ce_{1-x}Gd_xO_{2-x/2}$ increased considerably between x = 0.00 and x = 0.10. This was followed by a steady decrease in density in compositions where $0.20 \leq x \leq 0.40$.

Additions of x > 0.40 were accompanied by a steady increase in density. Further small increases in density were measured in the range 0.70 ≤ x ≥ 0.90. Figure 4 illustrates the influence of composition on the evolution of pellet density in the CeO_2 – Gd_2O_3 solid solution.

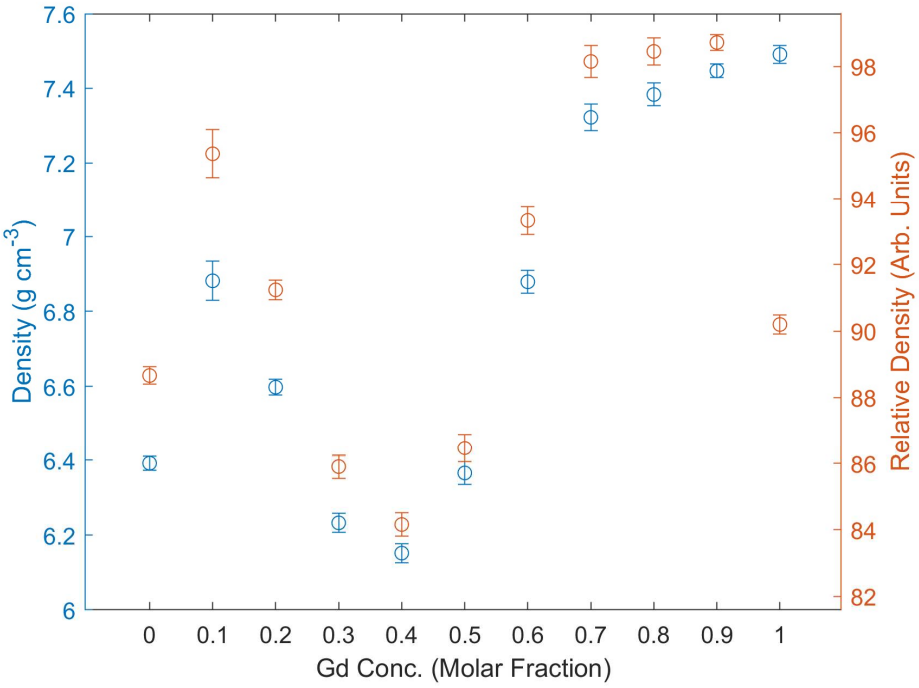

Figure 4: Plot of absolute and relative density against Gd content for CeO_2 – Gd_2O_3 solid solution.

The same trend is observed in both absolute and relative densities, with the exception of monoclinic Gd_2O_3. The low relative density of monoclinic Gd_2O_3 may indicate inaccuracy in the lattice parameter refinement. Alternatively, it could indicate partial C-type phase formation, as C-type Gd_2O_3 has a lower theoretical density of 7.51 g cm^{-3} compared to monoclinic Gd_2O_3 (8.05 g cm^{-3}).

Obtained densities for the majority of composition were slightly lower than the 95.5% relative density expected average burn-up spent fuel[29]. Parallels can be drawn between the evolution of density and the crystal structure with Gd additions in pellets of $Ce_{1-x}Gd_xO_{2-x/2}$. The lowest relative densities are achieved when x = 0.40, which is also the maximum measured lattice parameter. This point represents the transition between domination of the fluorite and C-type matrix, where x = 0.00 – 0.30, samples are mostly fluorite, Clearly, in samples with roughly equal quantities of Ce and Gd, sintering behaviour is worse, as neither fluorite or C-type structure is dominant, leading to poorer diffusion and greater levels of porosity. Poor density obtained in pure CeO_2 may be due to pore formation caused by partial auto-reduction to Ce^{3+} at high temperatures[30]. Yasuda *et al.* noted a decrease in pellet density as sintering temperature was increased from 1200 °C to 1400 °C. They hypothesised this decrease

corresponded with pore formation resulting from O_2 release caused by the auto-reduction of Ce at high temperatures during sintering. In contrast, Stennett *et al.* reported the greatest obtained densities in CeO_2 pellets at 1700 °C, with increased porosity noted instead upon increase to 1750 °C [9]. TGA-MS analysis is required to confirm whether significant O_2 release played a role in excessive pore formation in the materials examined in this work.

3.5. Microstructure and phase formation

Typical microstructures obtained in sintered pellets across the entire solid solution are presented in Figure 5.

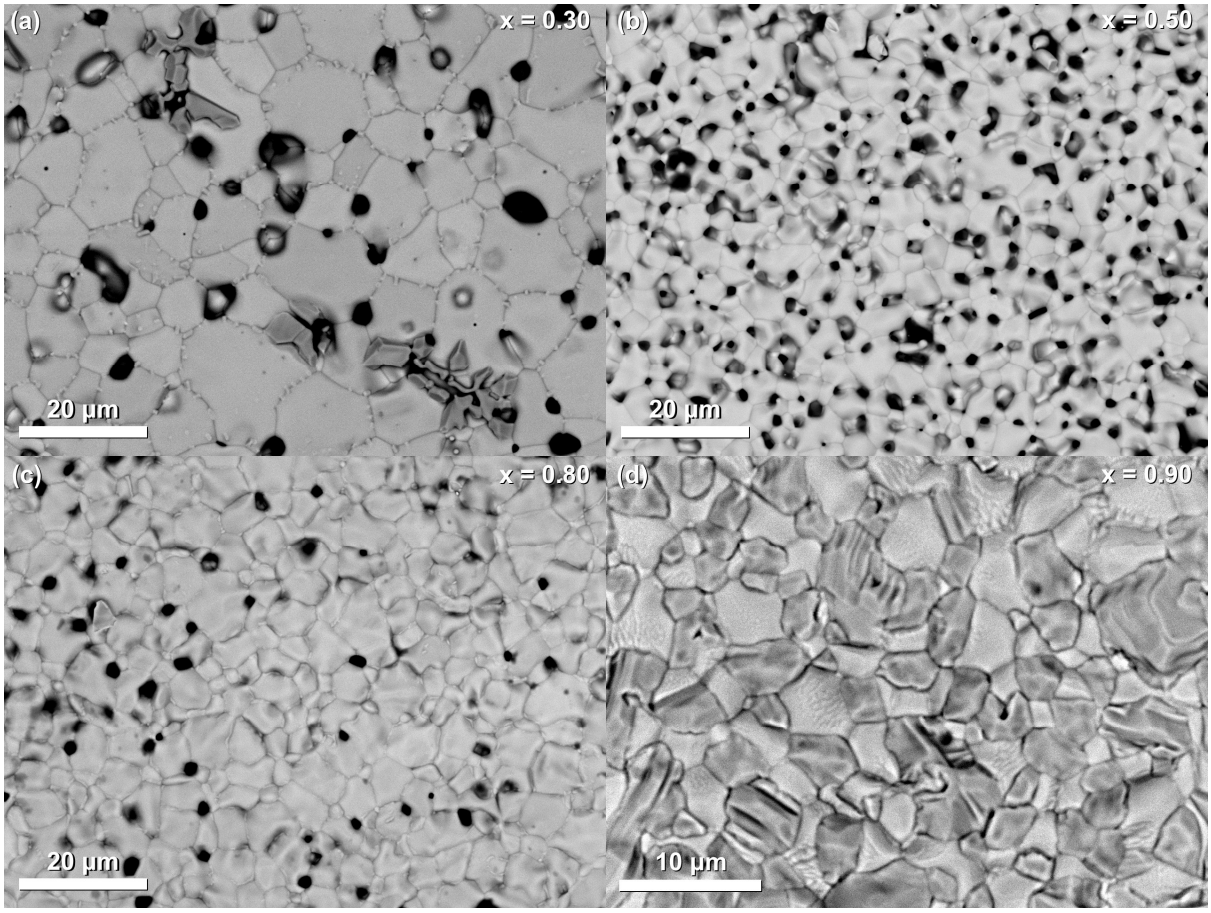

Figure 5: BSE micrographs illustrating typical microstructures in sintered pellets of $Ce_{1-x}Gd_xO_{2-x/2}$ where x = 0.30 (a), 0.50 (b), 0.80 (c) and 0.90 (d).

Microstructures exhibited increasing porosity with x > 0.10, best illustrated by the highly porous microstructure shown in the x = 0.50 sample in Figure 5b. Gd-rich secondary phases formed on the surface of sintered pellets in $Ce_{1-x}Gd_xO_{2-x/2}$ compositions where $0.10 \leq x \leq 0.90$. The system can be assumed to have reached equilibrium during the 10-hour dwell at 1700 °C, which is significantly longer than the 6-hour dwell typically considered be sufficient for sintering Gd-doped CeO_2[27,31,32]. Despite this, regions exhibiting different grain morphologies and compositions, herein referred to as secondary phases, were observed using SEM-EDS,

presented in Figure 6a-d. In Section 3.4, it was discussed how XRD analysis suggested sintered pellets where $x < 0.40$ formed a single fluorite phase, and that no biphasic region was observed with the onset of C-type reflections for $x \geq 0.40$. XRD analysis of this system can therefore only be considered to represent an average of the bulk fluorite phase and should not be interpreted as evidence that samples are truly single-phase.

Gd-rich secondary phases were found to take three distinct forms: (1) individual, highly faceted grains around 10 – 20 μm in diameter (Figure 5a and Figure 6a), (2) larger spherical regions, 50 – 100 μm, especially porous, comprised of a network of lathe-like grains (Figure 6b), and (3) even larger (100 – 300 μm) spherical regions, featuring a dense outer rim comprised of small (< 5 μm) grains (Figure 6c and Figure 6d). Form (1) was most readily observed in compositions with lower Gd concentrations, $x = 0.10 – 0.30$, that were ostensibly single-phase fluorite *via* XRD. Form (2) was observed predominantly in pellets where $0.20 \leq x \leq 0.40$. For $x > 0.40$, most secondary phases adopted form (3).

Whilst many existing studies have analysed the CeO_2 – Gd_2O_3 solid solutions using SEM-EDS[27,33,34], none discuss the appearance of secondary phases. Horlait *et al.* reported a secondary phase of hexagonal Nd_2O_3 forming in $Ce_{0.24}Nd_{0.76}O_{1.62}$ [35]. These secondary phases formed in lathe-like morphologies between grains of the C-type matrix, unlike the phases observed in this work. Iwasaki *et al.* observed large, spherical Gd-rich regions in their study of 10 wt% Gd-dispersed UO_2 pellets, which were prepared by mixing large (25–53 μm) Gd_2O_3 particles into UO_2 powders. These regions were very similar in morphology to form (3) described in this work.

A potential explanation for secondary phase formation, even where $x \leq 0.20$, is the very high sintering temperature (1700 °C) used for the pellets. This high temperature promotes greater rates of Gd diffusion, facilitating extensive movement of Gd^{3+} ions towards V_O, and other Gd^{3+}, which are known to preferentially bind[36]. Extensive segregation of Gd^{3+} and V_O can eventually lead to precipitation of C-type domains within the fluorite phase[37]. An alternative explanation is poor homogenisation of Gd in the mixed oxalate, however, this seems unlikely given that oxalate precipitation is widely accepted as a very reliable route to achieving fine, well homogenised powders. These secondary phases are likely to be C-type rather than monoclinic, however, XRD analysis (Section 3.3) revealed very low intensity reflections in samples where $x \leq 0.30$ potentially indicative of a monoclinic phase. Further characterisation with additional techniques such as TEM, EBSD or Raman spectroscopy would be necessary to confirm the crystal structure of the secondary phases. Formation of monoclinic phases has previously been reported in studies of $Ce_{1-x}Gd_xO_{2-x/2}$, but only for quenched samples, where $x > 0.90$ [24,38]. Even small quantities of Ce^{4+} will stabilise Gd_2O_3 within a C-type phase[38], however,

as established previously, monoclinic transitions can be facilitated by high temperatures, the 1700 °C sintering step undertaken for this work is in excess of typical sintering temperatures employed by most studies in the CeO_2 – Gd_2O_3 system (1200 °C – 1600 °C). In UO_2, very high Gd concentrations (x > 0.90) have been reported to form monoclinic phases after sintering at 1650 °C [39].

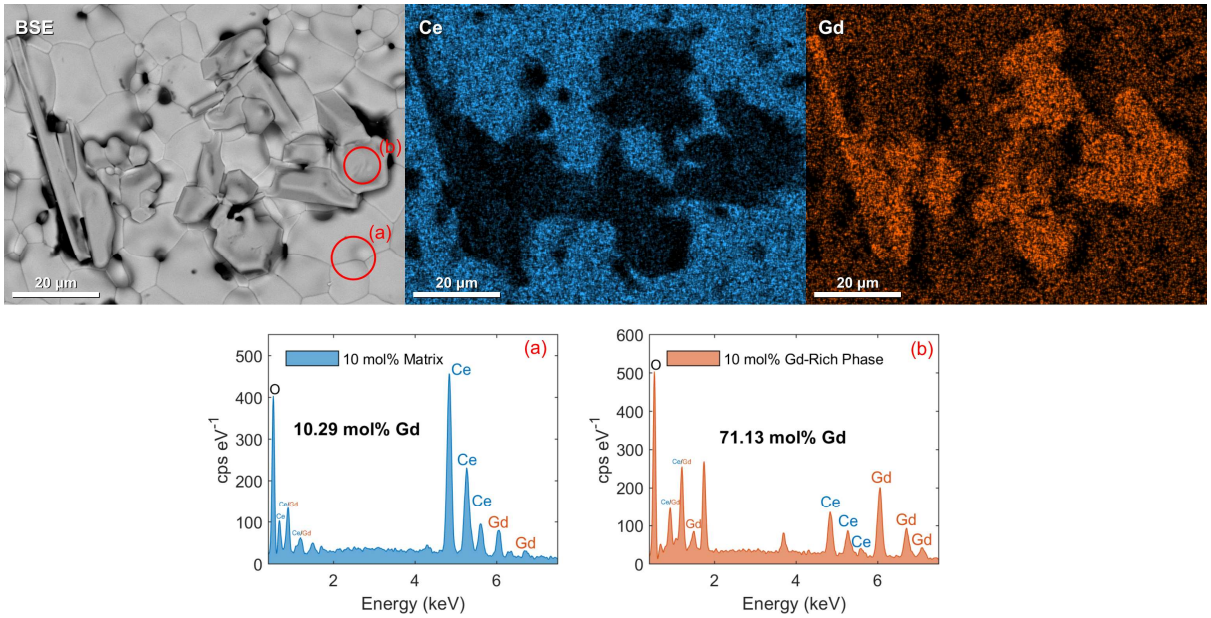

Figure 6a: $Ce_{0.9}Gd_{0.1}O_{2-\delta}$: BSE micrograph, EDS maps and accompanying spectra.

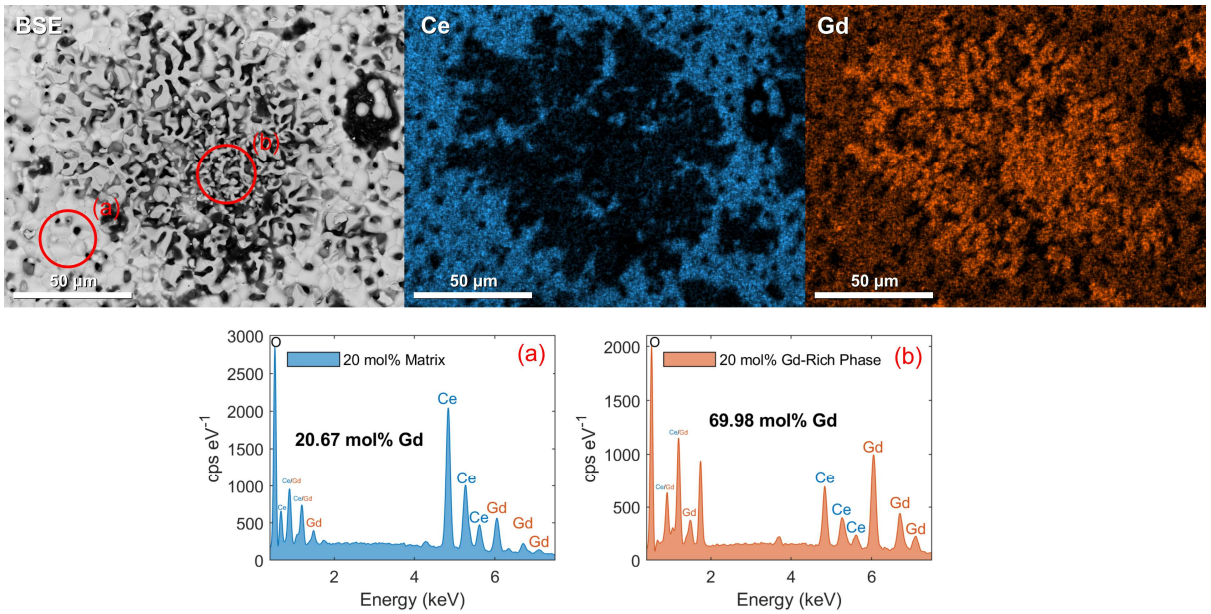

Figure 6b: $Ce_{0.8}Gd_{0.2}O_{2-\delta}$: BSE micrograph, EDS maps and accompanying spectra.

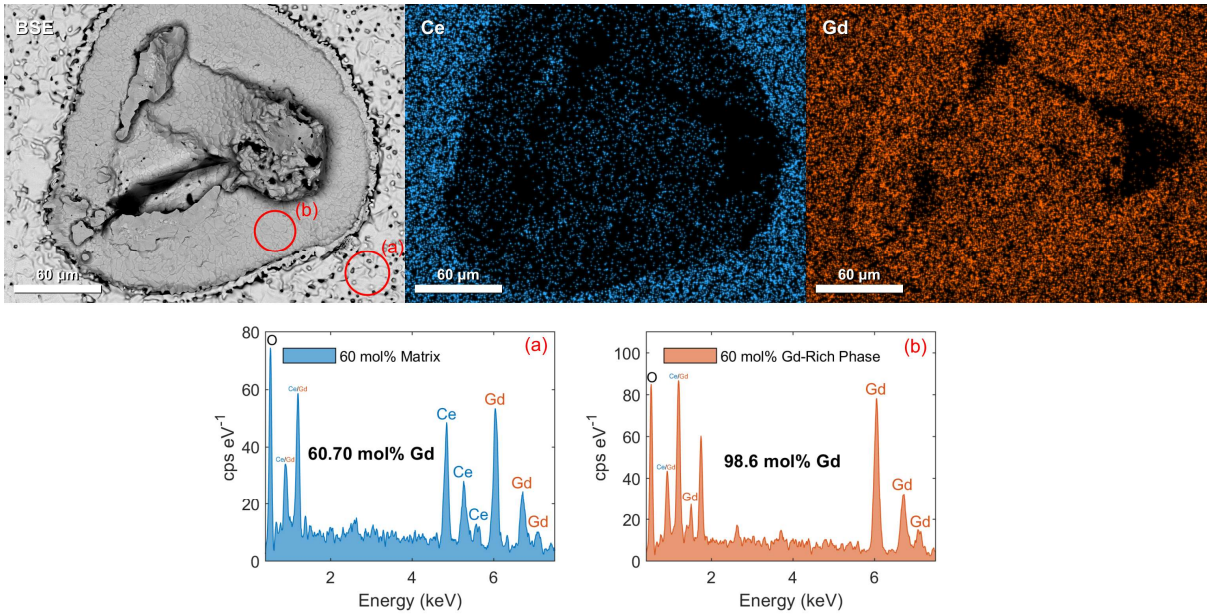

Figure 6c: $Ce_{0.4}Gd_{0.6}O_{2-\delta}$: BSE micrograph, EDS maps and accompanying spectra.

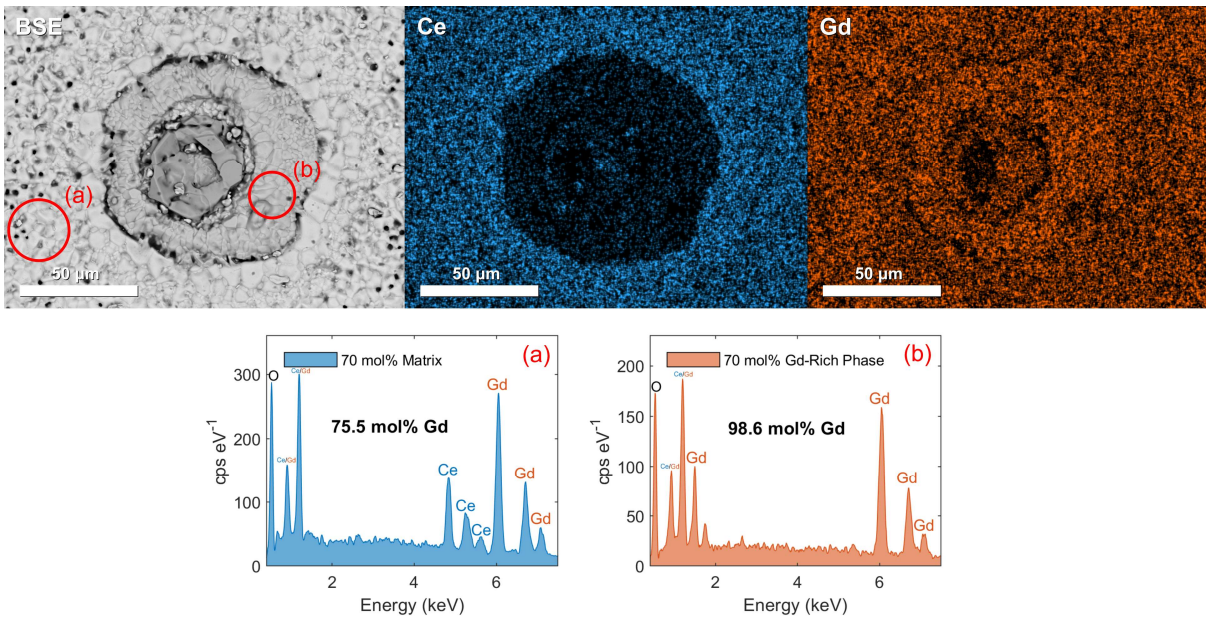

Figure 6d: $Ce_{0.3}Gd_{0.7}O_{2-\delta}$: BSE micrograph, EDS maps and accompanying spectra.

Table 3 presents a comparison of averaged point spectra collected within the matrix and secondary phases in sintered pellets of $Ce_{1-x}Gd_xO_{2-x/2}$.

Table 3: Summary of compositional analysis of CeO_2 – Gd_2O_3 samples measured by SEM-EDS. EDS spectra for each composition are available in Figure S1 in the supplementary information.

Nominal Composition	Matrix Composition by SEM-EDS	Secondary Phase Composition by SEM-EDS
CeO_2	CeO_2	—
$Ce_{0.90}Gd_{0.10}O_{2-\delta}$	$Ce_{0.90(6)}Gd_{0.09(6)}O_{2-\delta}$	$Ce_{0.31(2)}Gd_{0.68(2)}O_{2-\delta}$
$Ce_{0.80}Gd_{0.20}O_{2-\delta}$	$Ce_{0.79(9)}Gd_{0.20(9)}O_{2-\delta}$	$Ce_{0.34(5)}Gd_{0.65(5)}O_{2-\delta}$
$Ce_{0.70}Gd_{0.30}O_{2-\delta}$	$Ce_{0.69(8)}Gd_{0.30(8)}O_{2-\delta}$	$Ce_{0.16(9)}Gd_{0.83(9)}O_{2-\delta}$
$Ce_{0.60}Gd_{0.40}O_{2-\delta}$	$Ce_{0.5(23)}Gd_{0.4(23)}O_{2-\delta}$	$Ce_{0.07(4)}Gd_{0.92(4)}O_{2-\delta}$
$Ce_{0.50}Gd_{0.50}O_{2-\delta}$	$Ce_{0.4(12)}Gd_{0.5(12)}O_{2-\delta}$	—
$Ce_{0.40}Gd_{0.60}O_{2-\delta}$	$Ce_{0.3(24)}Gd_{0.6(24)}O_{2-\delta}$	$Ce_{0.01(1)}Gd_{0.98(1)}O_{2-\delta}$
$Ce_{0.30}Gd_{0.70}O_{2-\delta}$	$Ce_{0.2(12)}Gd_{0.7(12)}O_{2-\delta}$	$Ce_{0.02(3)}Gd_{0.97(3)}O_{2-\delta}$
$Ce_{0.20}Gd_{0.80}O_{2-\delta}$	$Ce_{0.13(7)}Gd_{0.86(7)}O_{2-\delta}$	—
$Ce_{0.10}Gd_{0.90}O_{2-\delta}$	$Ce_{0.06(2)}Gd_{0.93(2)}O_{2-\delta}$	$Ce_{0.04(2)}Gd_{0.95(2)}O_{2-\delta}$
Gd_2O_3	Gd_2O_3	—

4. Results and discussion on (micro)structure – dissolution relationship in fluorite $Ce_{1-x}Gd_xO_{2-x/2}$

Four additional $Ce_{1-x}Gd_xO_{2-x/2}$ solid solutions, where x = 0.00, 0.05, 0.10, 0.15, were synthesised using the oxalic precipitation method described previously. The nuclear context of this study concerned the influence of Gd fission product incorporation within the UO_2 matrix of spent fuel, and the potential effects of adding Gd to $(U,Pu)O_2$ to produce disposal-MOX. Global Gd content in both scenarios is expected to be relatively low (< 1 mol%); however, increased localised concentrations of Gd^{3+} may result from inhomogeneous mechanical mixing of disposal-MOX[40,41], and fission product segregation in spent fuel[42]. The remainder of this study aimed to examine the effects of Gd incorporation on the crystal structure and microstructure of fluorite CeO_2, and to relate these effects to changes in dissolution behaviour.

4.1 Compositional analysis of $Ce_{1-x}Gd_xO_{2-x/2}$ (x = 0.00 – 0.15)

Measurements of elemental composition of sintered pellets *via* EPMA and SEM-EDS confirmed successful synthesis of the nominal compositions (Table 4), with Gd additions within 1 mol% of the desired amount in all samples except x = 0.15, which had a somewhat higher Gd content than anticipated. However, it should be noted that the EMPA measurements are highly sensitive to local distribution in Gd concentration which, as shown in Section 4.7, was highly variable. Samples are referred to by their nominal compositions for the remainder of this work.

Table 4: Summary of nominal and measured compositions of $Ce_{1-x}Gd_xO_{2-x/2}$ solid solutions, where x = 0, 0.05, 0.10, 0.15.

Nominal Composition	Measured Composition (EPMA)	Measured Composition (SEM-EDS)
CeO_2	$Ce_{1.00(7)}O_{2-\delta}$	$Ce_{1.0(21)}O_{2-\delta}$
$Ce_{0.95}Gd_{0.05}O_{2-\delta}$	$Ce_{0.94(8)}Gd_{0.06(2)}O_{2-\delta}$	$Ce_{0.9(29)}Gd_{0.06(6)}O_{2-\delta}$
$Ce_{0.90}Gd_{0.10}O_{2-\delta}$	$Ce_{0.89(9)}Gd_{0.11(6)}O_{2-\delta}$	$Ce_{0.9(42)}Gd_{0.1(12)}O_{2-\delta}$
$Ce_{0.85}Gd_{0.15}O_{2-\delta}$	$Ce_{0.82(8)}Gd_{0.18(9)}O_{2-\delta}$	$Ce_{0.8(25)}Gd_{0.17(6)}O_{2-\delta}$

4.2 Effect of Gd on microstructure of $Ce_{1-x}Gd_xO_{2-x/2}$ (x = 0.00 – 0.15)

Sintered pellets of $Ce_{1-x}Gd_xO_{2-x/2}$ exhibited a dense microstructure comprised of randomly oriented, well-equiaxed grains. This microstructure is representative of those observed in UO_2 fuels [9]. Secondary electron (SE) SEM micrographs presented in Figure 7 present typical microstructures observed in polished and annealed pellets. Porosity was prevalent in all samples, with most pores occurring at triple points between adjoining grains.

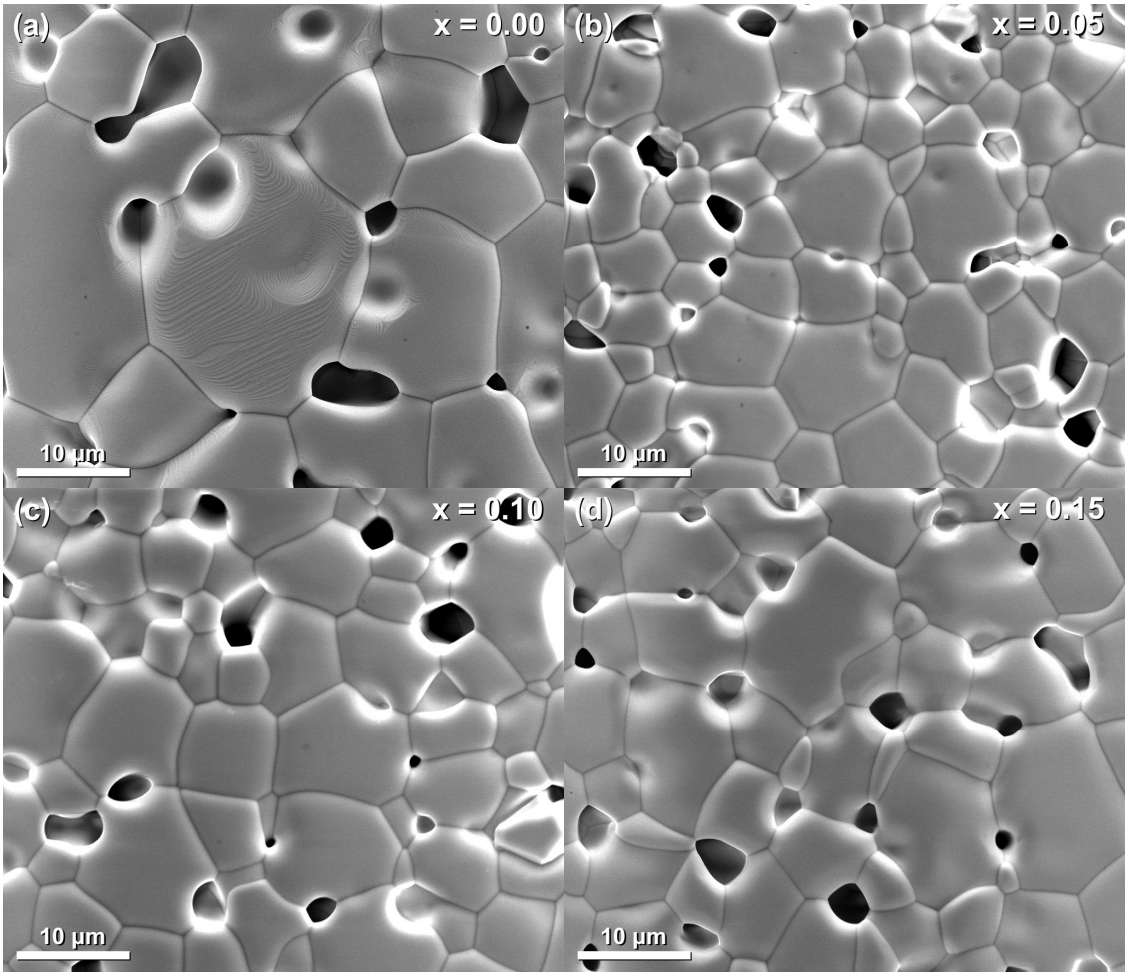

Figure 7: SE micrographs of microstructures obtained in sintered pellets of $Ce_{1-x}Gd_xO_{2-x/2}$. Surfaces were polished to 1 µm and thermally etched to reveal grain boundaries.

Grain size decreases drastically with the initial addition of from x = 0.00 to x = 0.05; however, subsequent additions to x = 0.10 and 0.15 were found to increase the grain size slightly. This trend is observed in grain size measurements made through both SEM image segmentation and EBSD analysis, as shown in Figure 8.

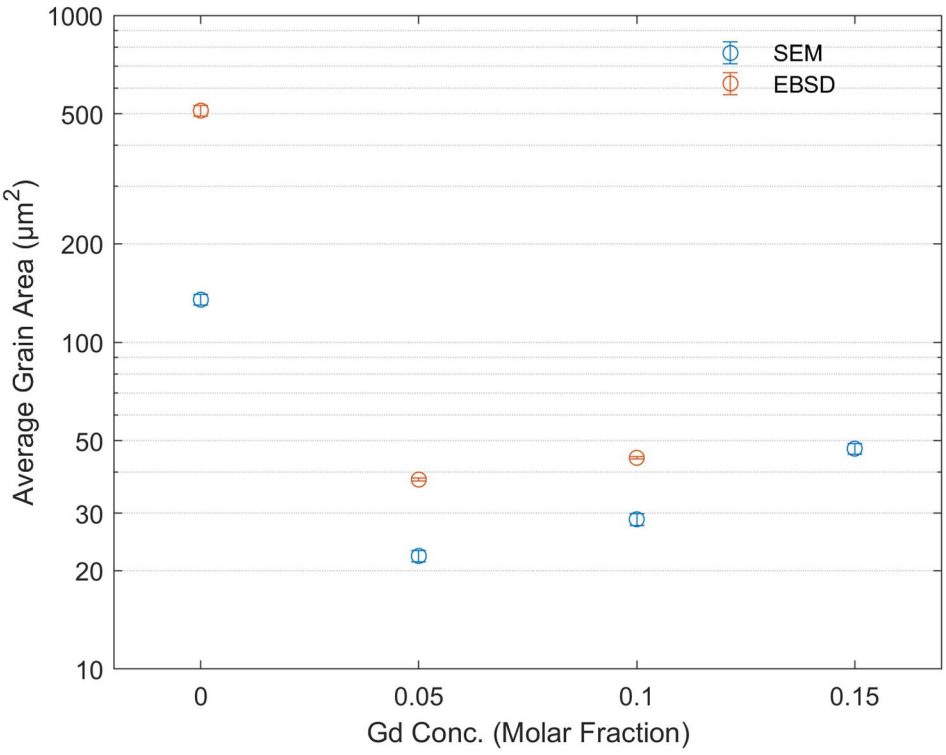

Figure 8: Plot of average size, as measured by SEM image analysis and EBSD, against Gd concentration. Note, EBSD measurements could not be collected on x = 0.15.

Decreased grain size can be attributed to the solute drag effect, which limits the grain boundary mobility necessary for grain growth. Preferential migration of dopant cations towards the grain edge during sintering can hinder cationic diffusion necessary for grain boundary movement[43]. Similar decreases in grain size have been observed in previous studies on $Ce_{1-x}Gd_xO_{2-x/2}$ [27,33], as well as other $Ce_{1-x}RE_xO_{2-x/2}$ [43,44] systems. Small additions (≤ 1 mol%) of Gd^{3+} are known to promote improved grain boundary mobility through the enhanced diffusivity facilitated by oxygen vacancies. Beyond ~ 1 mol% Gd, the deleterious effect of solute drag on grain growth is dominant. The cause of gradual grain size increase observed between x = 0.05 to x = 0.15 is unclear. Van Mao *et al.* noted approximately equal grain sizes in pellets of 5, 10 and 15 wt% Gd-doped CeO_2 [33], whereas Chourashiya *et al.* measured a slight decrease in grain size between 10 and 20 mol% Gd-doped CeO_2 [45]. The relationship between grain growth

and Gd^{3+} is expected to be controlled by several factors, including synthesis of oxides precursors[9] and sintering temperature[46].

Grain area measurements were performed through SE micrograph image analysis and EBSD mapping. Average grain area measurements from SE image analysis results in systematic underestimation of grain area. This may result from a flaw in the methodology, where a significant number of grains within each sampled image are partially cropped by the border. The same limitation does not occur for the large montaged EBSD maps (presented in Figure S2 in the Supplementary information), which by comparison have far fewer grains occupying this edge region. Similarly, the limited FOV of a single SE micrograph at relatively high magnifications (~5000x) will prevent imaging the entirety of the largest grains in the microstructure, this is made clear by the significantly greater maximum grain areas measured through EBSD (shown in the histograms presented in Figure S3).

The density of the sintered pellets was found to increase with Gd content. Archimedes density measurements of sintered pellets presented in Figure 9 revealed that both absolute and relative densities with Gd additions of x = 0.05, and again for x = 0.10, whilst a slight further increase was measured for x = 0.15.

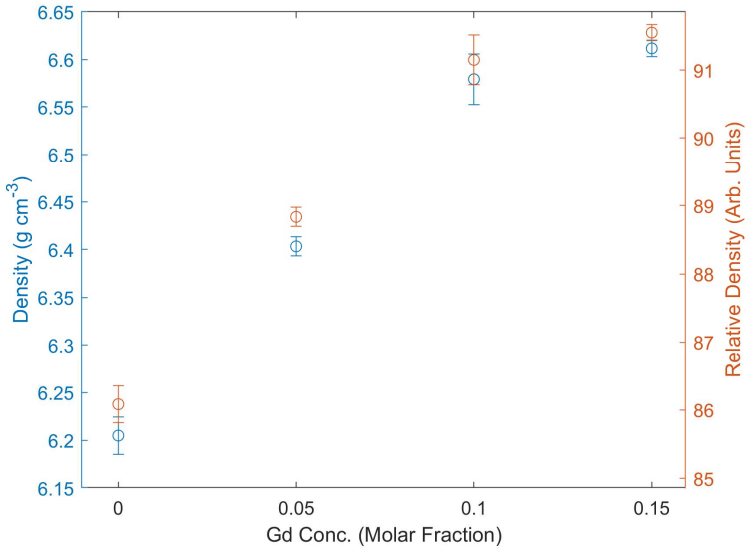

Figure 9: Plot of density and relative density of sintered pellets against Gd concentration as measured by Archimedes balance.

The same trend was observed in Archimedes measurements on the entire $CeO_2 – Gd_2O_3$ solution discussed previously. Density increased linearly as x increased from 0.00 to 0.05 and 0.10. The final Gd addition to x = 0.15 yielded a slight further increase. Van Mao *et al.* observed a similar increase in pellet density of CeO_2 with increasing Gd content (5, 10 and 15 wt%)[33]. Similar trends in density were observed in previous studies of $Ce_{1-x}Gd_xO_{2-x/2}$ [33,45].

Gas pycnometry of the sintered pellets also revealed an increase in density with Gd content. However, where x > 0.10, density decreased slightly. The true density of $Ce_{1-x}Gd_xO_{2-x/2}$ materials was measured by gas pycnometry of crushed sintered powders. Figure 10 illustrates the significantly higher densities measured on crushed powders, which avoid underestimation caused by closed porosity in sintered pellets.

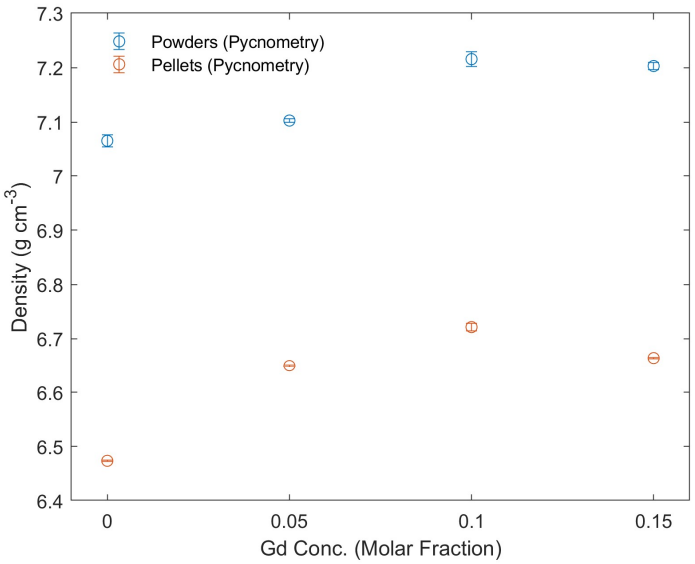

Figure 10: Plot comparing pellet and powder densities of sintered $Ce_{1-x}Gd_xO_{2-x/2}$ against Gd concentration.

Addition of Gd was found to exert no control over grain texture, with random crystallographic orientation maintained in all compositions of $Ce_{1-x}Gd_xO_{2-x/2}$ for x = 0.00 – 0.10. This was confirmed by EBSD analysis. Figure 11 shows grain orientation was randomly distributed between the major planes <001>, <101> and <111>.

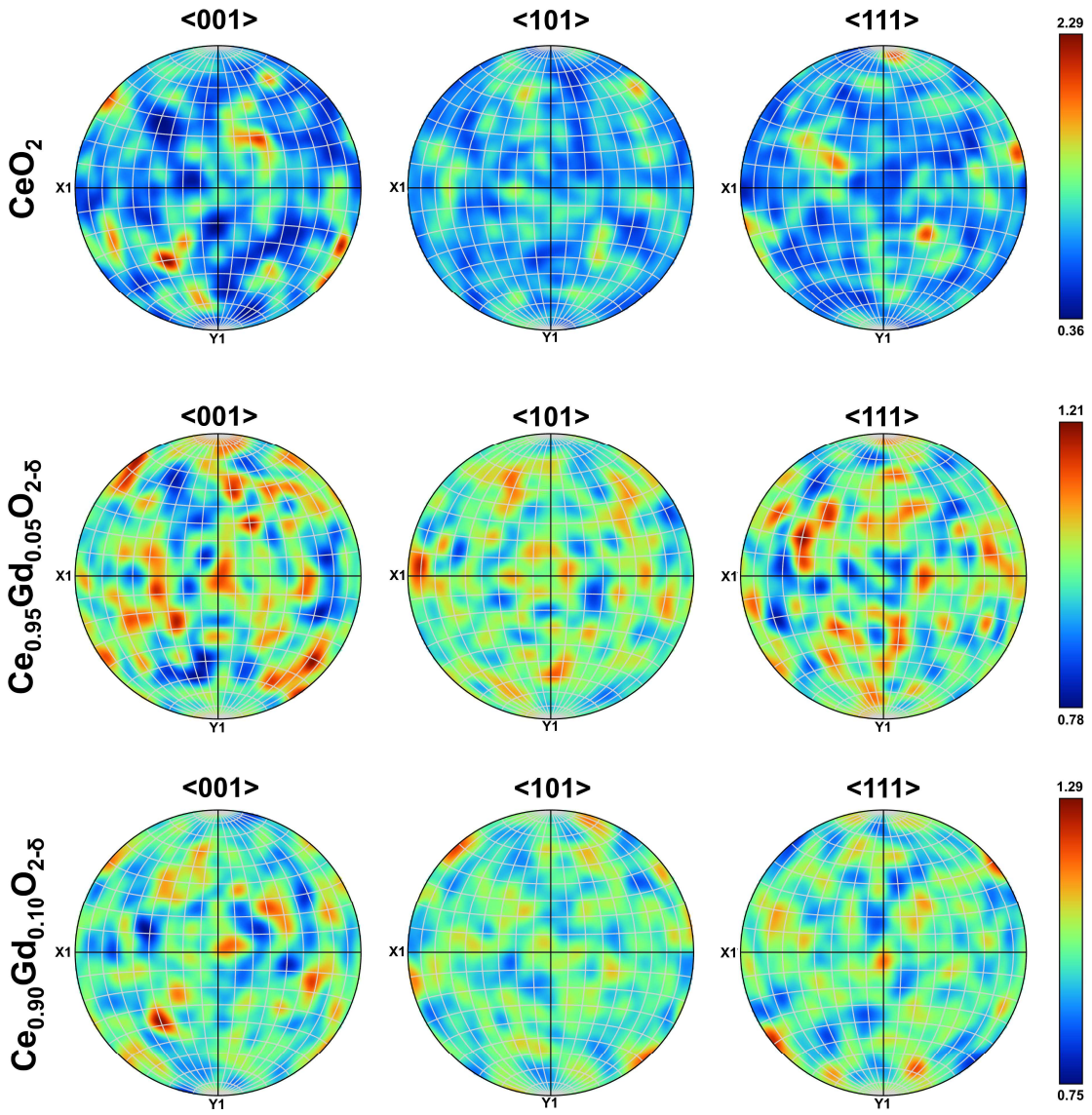

Figure 11: Pole figures of EBSD data confirming lack of grain texture in pellets of $Ce_{1-x}Gd_xO_{2-x/2}$.

Values of Multiple of Uniform Density (MUD) averaged around 1, confirming random orientation. Textured microstructures are indicated by MUD values significantly greater than 1. The greatest MUD range was measured in CeO_2, likely as a result the smaller dataset of total analysed grains resulting from the significantly larger grain size. 1200 grains of CeO_2 were analysed compared to ~10,000 in the smaller grained x = 0.05 and 0.10 samples, Euler colour EBSD maps of all three samples are presented in Figure S2. Large-scale EBSD analysis of the x = 0.15 sample was not possible due to the C-type nanodomain formation, discussed in detail Section 4.5.

EBSD analysis also confirmed that Gd incorporation did not exert significant control over grain boundary misorientation. Figure 12 shows that the distribution of grain boundary angles was consistent between the three measured compositions.

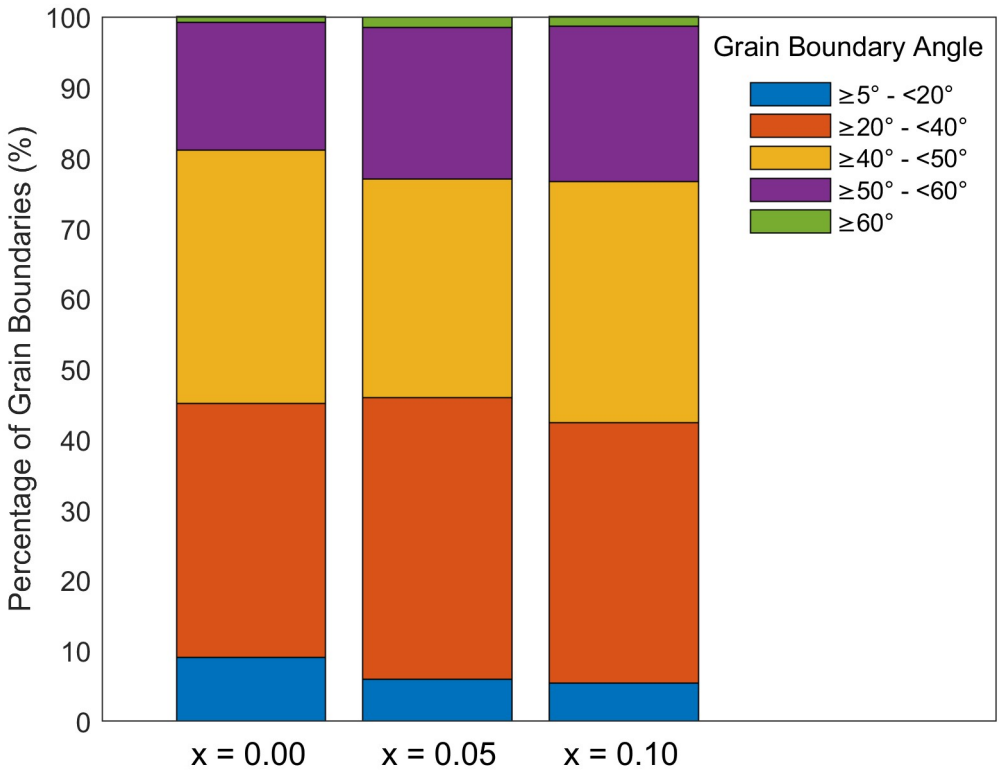

Figure 12: Bar chart showing distribution of grain boundary misorientation angles in $Ce_{1-x}Gd_xO_{2-x/2}$ where x = 0.00, 0.05 and 0.10.

4.3 Secondary phase formation in $Ce_{1-x}Gd_xO_{2-x/2}$ (x = 0.00 – 0.15)

Secondary phases were observed through SEM-EDS in sintered pellets of $Ce_{1-x}Gd_xO_{2-x/2}$ where x ≥ 0.10. SEM-EDS analysis presented in Figure 13a-b confirms the presence of Gd-rich (~70 – 80 mol%) phases, exhibiting the same faceted morphologies described previously as 'form (1)'. The frequency and size of secondary phases was greater in x = 0.15 compared to 0.10. Large porous Gd-rich secondary phases, described previously as 'form (2)', were present in x = 0.15 but not in 0.10. These phases, shown in Figure 14a-d, were most prevalent on as-sintered surfaces and were less readily observed following grinding and polishing, as shown in Figure 15. This observation suggests secondary phase formation may have been aided by these exposed surfaces during initial the sintering and subsequent thermal annealing.

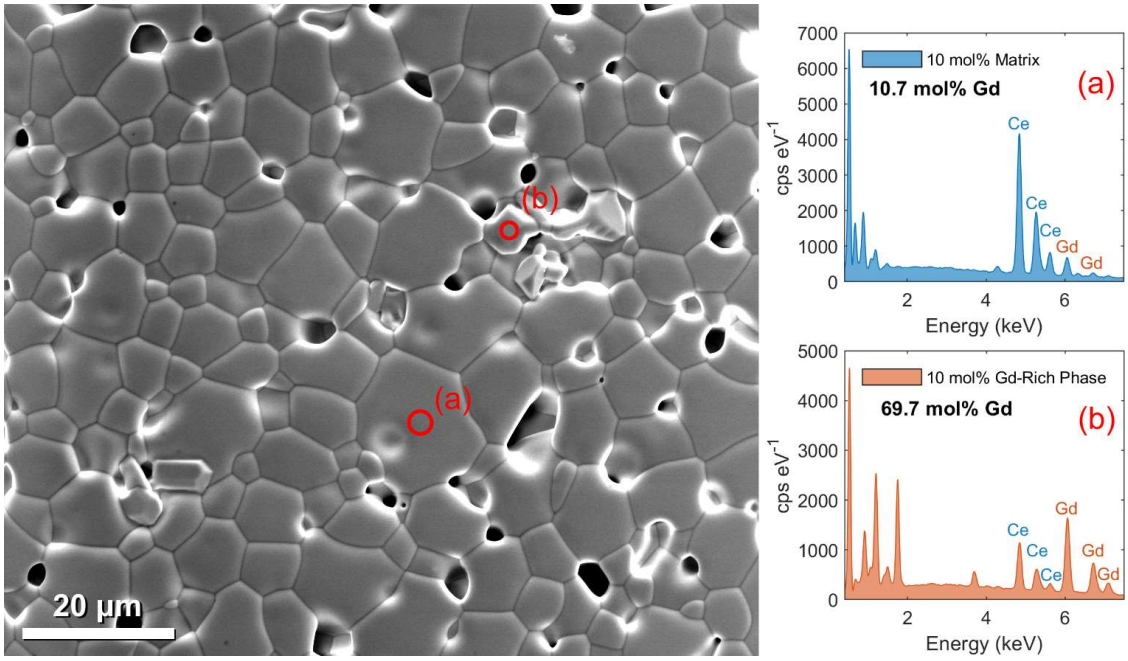

Figure 13a: Secondary electron image of polished and annealed surface of an x = 0.10 ($Ce_{0.90}Gd_{0.10}O_{2-\delta}$) pellet, accompanied by EDS spectra taken from matrix and segregated Gd-rich phase.

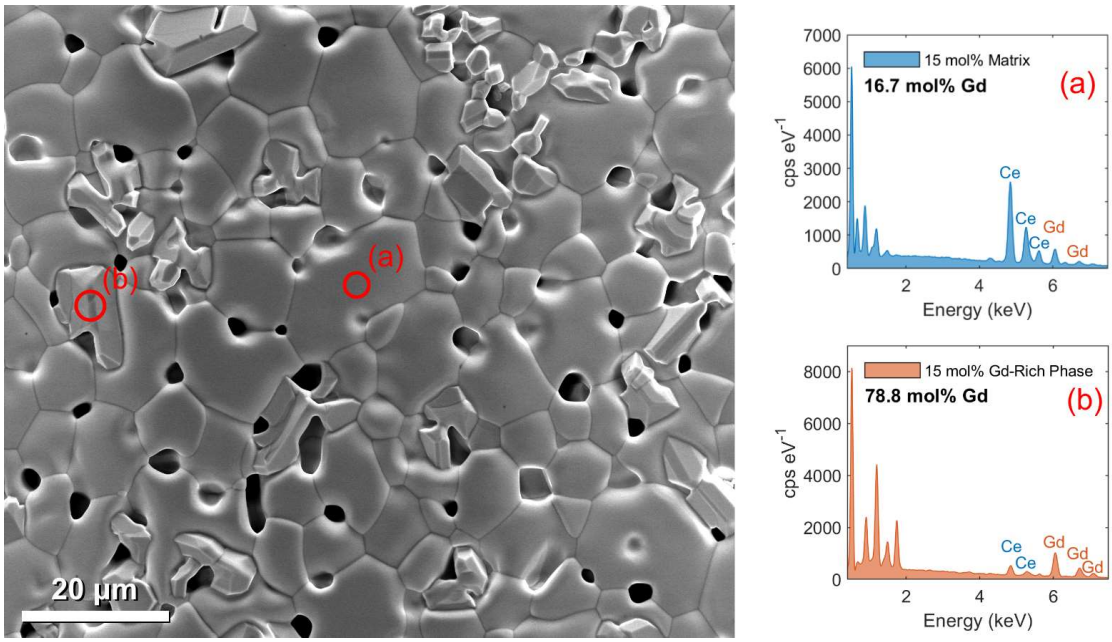

Figure 13b: Secondary electron image of polished and annealed surface of an x = 0.15 ($Ce_{0.85}Gd_{0.15}O_{2-\delta}$) pellet, accompanied by EDS spectra taken from matrix and segregated Gd-rich phase.

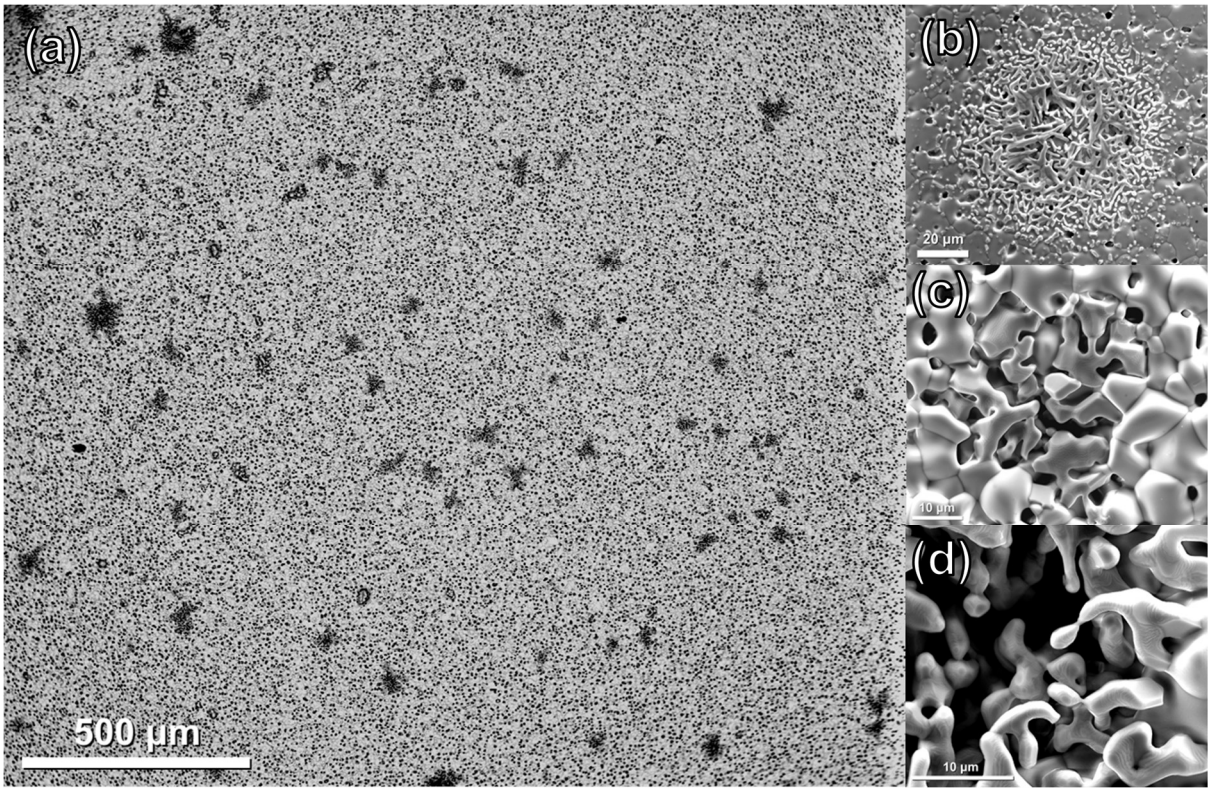

Figure 14: (a) Back scattered electron image of as-sintered surface of an x = 0.15 ($Ce_{0.85}Gd_{0.15}O_{2-\delta}$) pellet, illustration relative abundance of secondary phases (dark spots) on surface prior to grinding and polishing. (b-d) Examples different morphologies adopted by Gd-rich secondary phases.

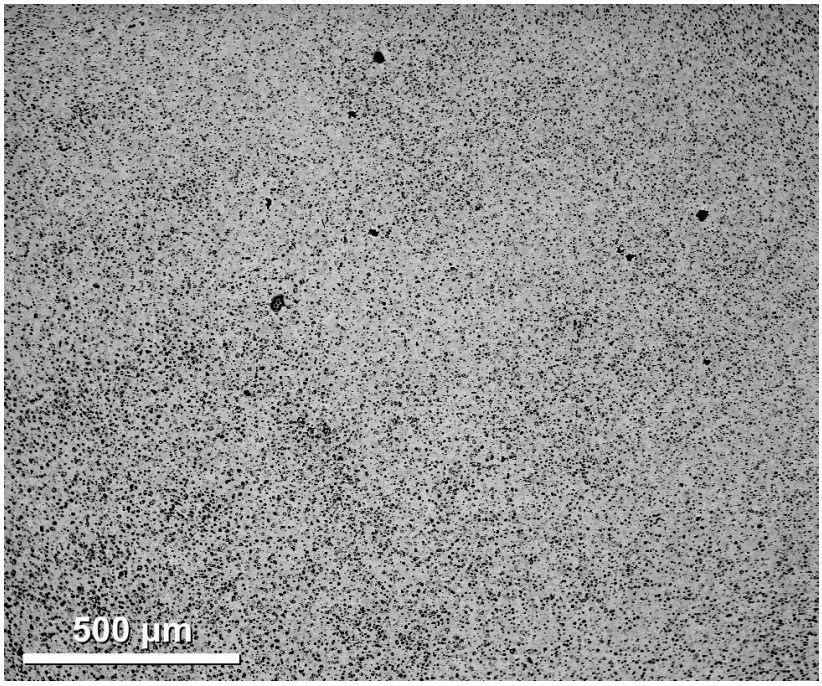

Figure 15: BSE image of polished surface of an x = 0.15 ($Ce_{0.85}Gd_{0.15}O_{2-\delta}$) pellet. Note the lack of darker, Gd-rich secondary phases observed on the polished and unannealed surface, suggesting these phases were predominantly formed on the exposed surfaces of pellets during heat treatments.

4.4 Examination of fluorite structure in $Ce_{1-x}Gd_xO_{2-x/2}$ (x = 0.00 – 0.15)

XRD analysis suggested all samples of $Ce_{1-x}Gd_xO_{2-x/2}$, where x = 0.00 – 0.15, crystallised as single-phase fluorite. This is evidenced by a single set of reflections characteristic of the crystal structure Fm-3m (Figure 16), additional reflections characteristic of C-type and monoclinic Gd_2O_3 phases are absent in all traces. However, it must be restated that due their structural similarity, small quantities of C-type phases cannot be measured using XRD. Furthermore, this instrument is incapable of resolving very small (< 2 wt%) quantities of additional phases that may be present, such as monoclinic Gd_2O_3-rich phases. For this reason, XRD analysis of this system can only be considered to represent an average of the bulk fluorite phase and should not be interpreted as evidence that samples are truly single-phase. Figure 16 presents powder XRD collected on crushed sintered pellets of each composition. LaB_6 additions (10 wt.%) provided an internal standard for more accurate Rietveld refinements.

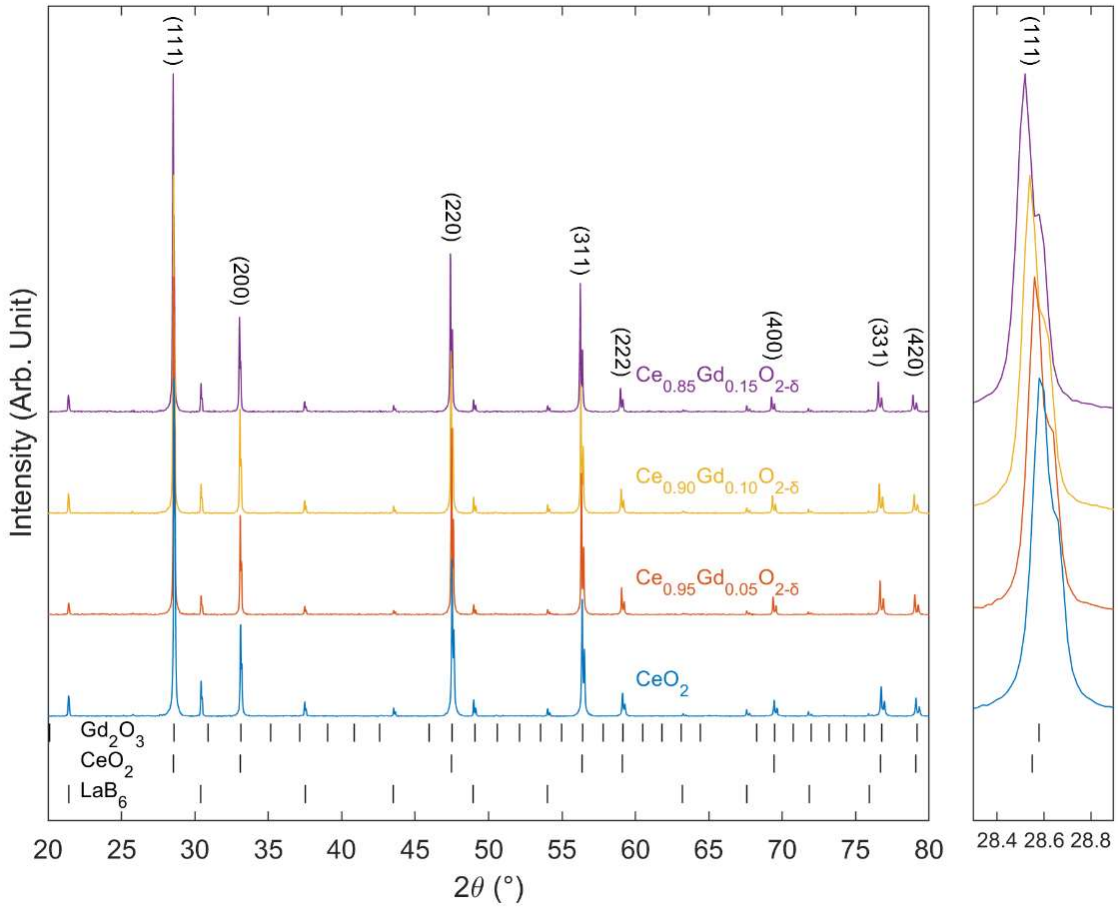

Figure 16: Stacked XRD plot of $Ce_{1-x}Gd_xO_{2-x/2}$, where x = 0.00 – 0.15. Reference XRD patterns taken from the Inorganic Crystal Structure Database (ICSD). CeO_2: ICSD 155604, Gd_2O_3 (Ia-3): ICSD 40473, LaB_6: ICSD 120585[20].

Expansion of the fluorite lattice is observed with increasing Gd content, as shown by peak shift towards lower values of 2θ. This is in agreement with the trends observed for x = 0.00 – 0.20 compositions in the CeO_2 – Gd_2O_3 solid solution discussed previously. This expansion is due to the larger ionic radius of Gd^{3+} compared to Ce^{4+} in 8-fold coordination, the effect of which outweighs the slight contraction from reduction in O – O repulsion caused by oxygen vacancy generation. The linear relationship between Gd content and lattice parameter (Figure 17) is in accordance with Vegard's law, confirming successful substitution of Ce^{4+} with Gd^{3+} on the A-site within the FCC sub-lattice of the fluorite structure in all compositions. As discussed in Section 3.3, where x < 0.40, the absence of widespread C-type phase formation yields a steady increase in lattice parameter with increasing Gd content.

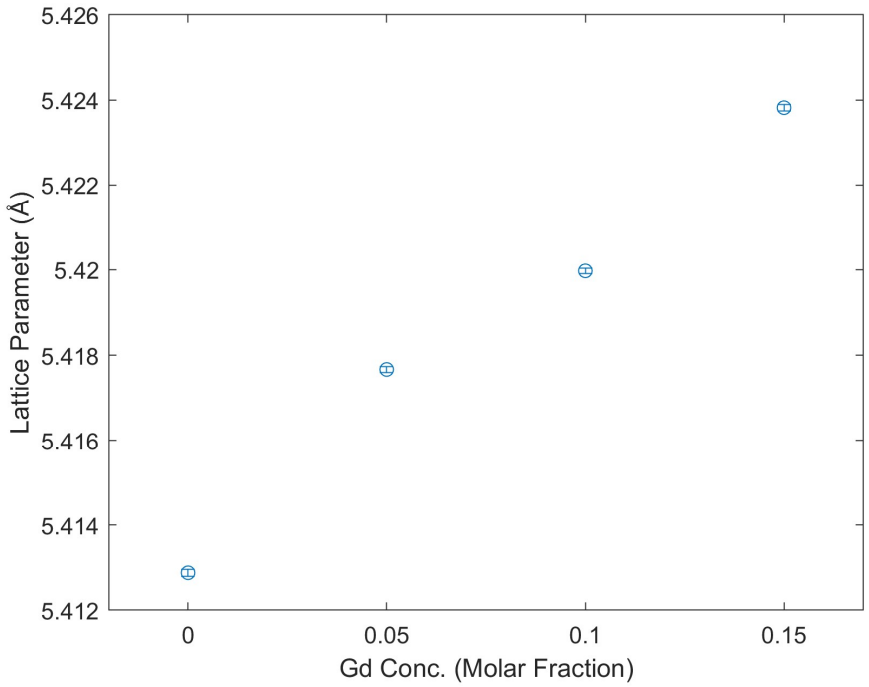

Figure 17: Plot of refined lattice parameters against Gd molar fraction in $Ce_{1-x}Gd_xO_{2-x/2}$ pellets.

4.5 C-type nanodomain formation in $Ce_{1-x}Gd_xO_{2-x/2}$ (x = 0.00 – 0.15)

Whilst XRD provides evidence that fluorite phase was formed in the bulk for x ≤ 0.15, further interrogation of the crystal structure and lattice defects is necessary to adequately characterise this complex system. As previously discussed, replacement of Ce^{4+} with Gd^{3+} generates V_O, strong binding energies between V_O – V_O and V_O – Gd^{3+} result in segregation and eventually ordering[32,36,47]. Over sufficient length scales, widespread V_O ordering yields transition to a cubic C-type phase in $Ce_{1-x}Gd_xO_{2-x/2}$ [26,37,38]. However, V_O ordering over far smaller length scales (> 100 nm) can result in temporary discontinuities within fluorite crystallites, known as nanodomains, which would not be apparent in XRD analysis[26,27]. C-type nanodomains have

been found to form in Gd-doped CeO_2 where x > 0.10 [21,32]; the structure of C-type nanodomains can be distinguished from true C-type phases by their differing degrees of ionic displacement, as illustrated in Figure 18.

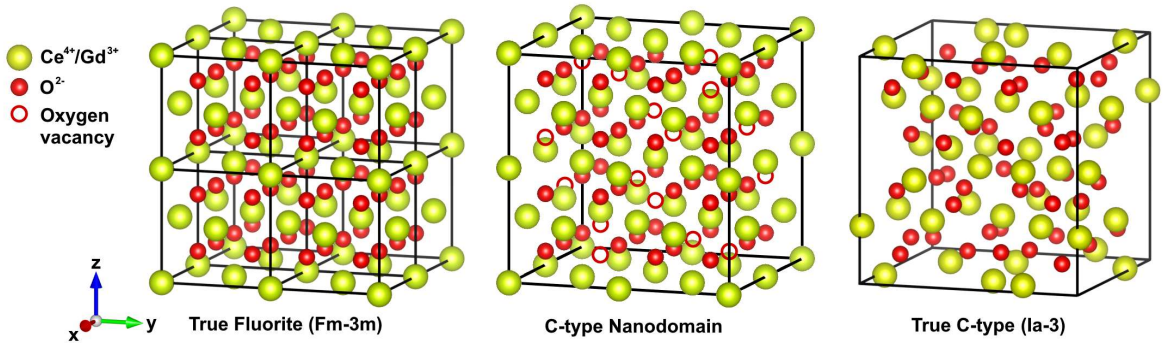

Figure 18: Schematic illustrating the formation of C-type superlattices through V_O ordering in fluorite. C-type nanodomain structures are distinguished from true C-type structures by their lack of significant atomic displacements from the fluorite positions.

Ou *et al.* proposed that given the high stability of the fluorite lattice, and the relatively small scale of local ordering, the atomic shift associated with true C-type phases is insignificant in C-type nanodomains[48, 49]. For this reason, nanodomains are not readily detected *via* XRD due to their small sizes and subtle atomic displacements. The size and frequency of nanodomains is known to increase with Gd content in CeO_2 [50], the agglomeration of these nanodomains over large regions is suspected to provide the main mechanism for secondary phase formation in Gd-doped CeO_2 [37].

Potential evidence of C-type nanodomain formation in fluorite $Ce_{1-x}Gd_xO_{2-x/2}$ investigated in the present study was observed using TEM. Electron diffraction patterns collected on a sample of $Ce_{0.95}Gd_{0.05}O_{2-\delta}$, presented in Figure 19b, exhibit diffuse scattering of the beam in addition to strong fluorite reflections. Diffuse scattering is indicative of lattice disorder, potentially caused by C-type nanodomains within the fluorite lattice. This diffuse scattering is absent in ED patterns collected on pure CeO_2, as shown in Figure 19a.

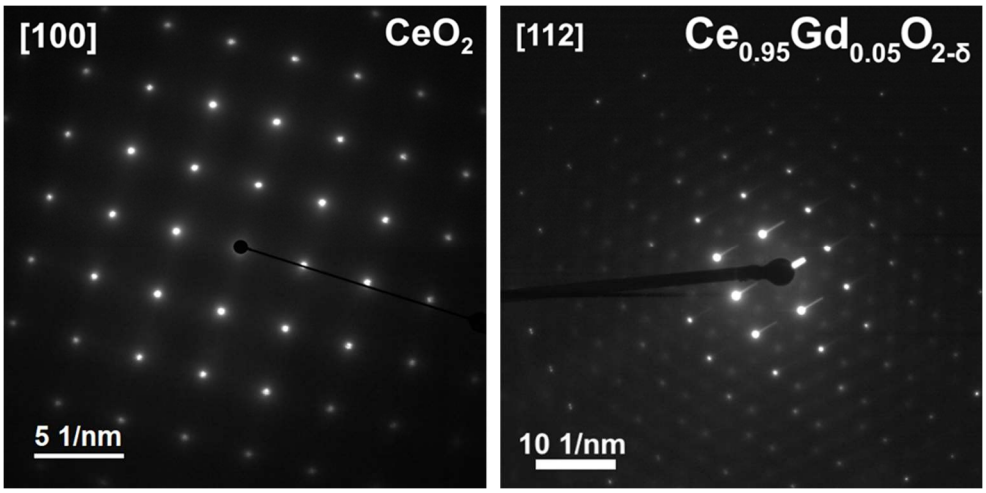

Figure 19: (a) left, ED pattern collected on sample of CeO_2 down the [100] zone axis. (b) right, ED pattern collected on sample of $Ce_{0.95}Gd_{0.05}O_{2-\delta}$ down the [112] zone axis.

Whilst diffuse scattering might indicate presence of C-type nanodomains, double diffraction by both fluorite and C-type structures was not observed in any compositions. Additional cubic reflections corresponding to C-type domains have been shown to produce double diffraction patterns in several TEM studies of $Ce_{1-x}Gd_xO_{2-x/2}$ [21,32,47]. For example, Yan *et al.* simulated ED patterns in the [112] plane of Yt-doped CeO_2, which featured additional C-type reflections although nanodomain formation is most widely reported for $x \geq 0.30$. Sintering temperature is believed to play in a role in the formation of nanodomains in $Ce_{1-x}Gd_xO_{2-x/2}$, with greater temperatures facilitating greater Gd^{3+} and V_O segregation, resulting in more clustering and domain growth during sintering[47].

HRTEM analysis of the same $Ce_{0.95}Gd_{0.05}O_{2-\delta}$ sample revealed subtle dislocations in the fluorite structure indicative of C-type nanodomain formation, shown in Figure 20.

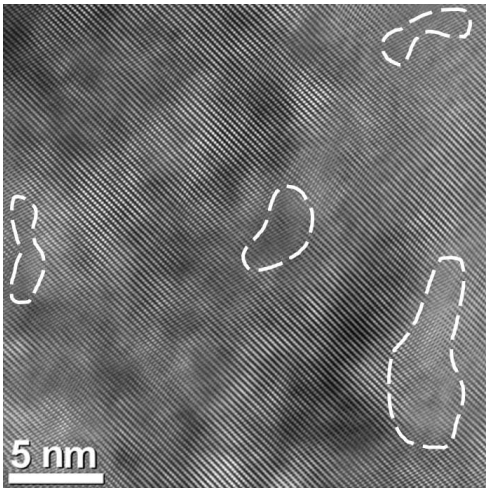

Figure 20: HRTEM micrograph of $Ce_{0.95}Gd_{0.05}O_{2-\delta}$. Dashed white lines outline suspected nanodomains.

Direct observation of nanodomains can prove challenging, due to their small size and lack of periodicity. Observation down zone is very important, as without clear repeating fluorite structure for reference, there is no repeat structured for C-type nanodomains to deviate from. BF TEM imaging revealed contrast variance in nanosized regions within grains when viewed down zone. Dark regions ~10 nm in diameter indicate greater scattering of the beam, potentially associated with the greater Z-number of Gd (Z_{Gd} = 64, Z_{Ce} = 58). In HAADF imaging, which removes contributions from Bragg scattering, these same nanosized regions yield bright areas on the micrograph, confirming the source of contrast to be Z-number. This could indicate the presence of Gd-rich C-type domains, embedded within the fluorite grain. Figures 21a-b present HAAFD and BF micrographs featuring suspected nanodomains in $Ce_{0.95}Gd_{0.05}O_{2-\delta}$.

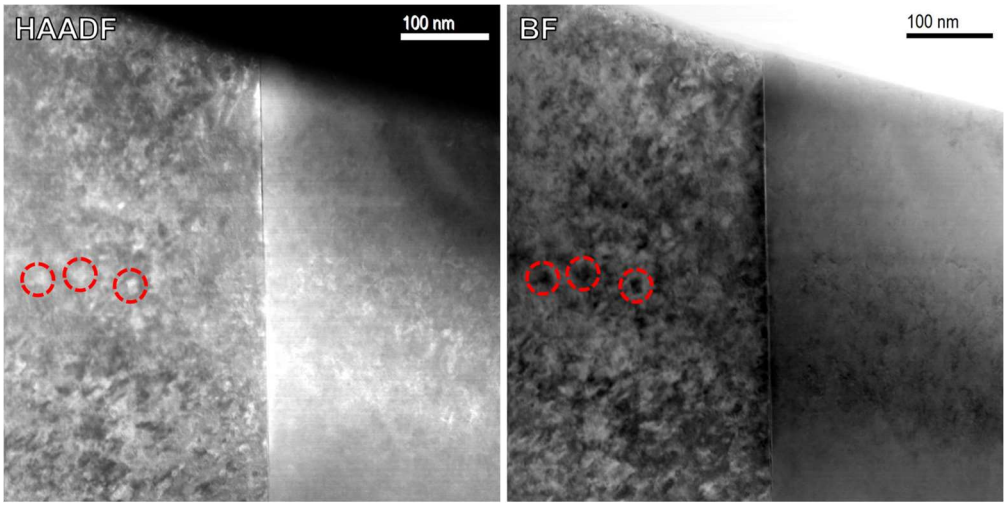

Figure 21: (a) left, HAADF micrograph of suspected nanodomains in $Ce_{0.95}Gd_{0.05}O_{2-\delta}$. (b) right, BF micrograph of suspected nanodomains in $Ce_{0.95}Gd_{0.05}O_{2-\delta}$.

As discussed in Section 4.2, bulk EBSD measurements were not possible in compositions where x > 0.10, as neither fluorite (Fm-3m) nor C-type (Ia-3) phases could be indexed. This may have resulted from C-type nanodomain disrupting the long-range fluorite ordering. To explore this further, transmission-EBSD mapping was conducted on a TEM sample taken from the same x = 0.15 material (Figure S4). T-EBSD of x = 0.15 achieved excellent indexing rates, likely due to the significantly reduced interaction volume between a more focussed electron beam and thinner sample. This smaller interaction volume enabled t-EBSD to successfully resolve the fluorite structure as there were fewer nanodomain contributions for each measured pixel.

4.6 Disorder and defects in fluorite lattice of $Ce_{1-x}Gd_xO_{2-x/2}$ (x = 0.00 – 0.15)

The lattice disorder and defect concentration within fluorite $Ce_{1-x}Gd_xO_{2-x/2}$ was found to increase with Gd^{3+} content. Raman spectra were collected within grain centres on polished,

sintered pellets, with care taken to avoid regions of obvious secondary phases, focussing Raman analysis purely on the structural evolution of the matrix. Figure 22 presents Raman spectra for each of the four compositions of $Ce_{1-x}Gd_xO_{2-x/2}$, where $0.00 \leq x \leq 0.15$. Deconvoluted modes, D_1 and D_2 are plotted over the defect band range. The D_1 band can be assigned to V_O generation, and the D_2 band to MO_8-type complexing[51]. Fits used to determine T_{2g} position and FWHM are available in Figure S5. A full summary of Raman deconvolution is available in Table S2.

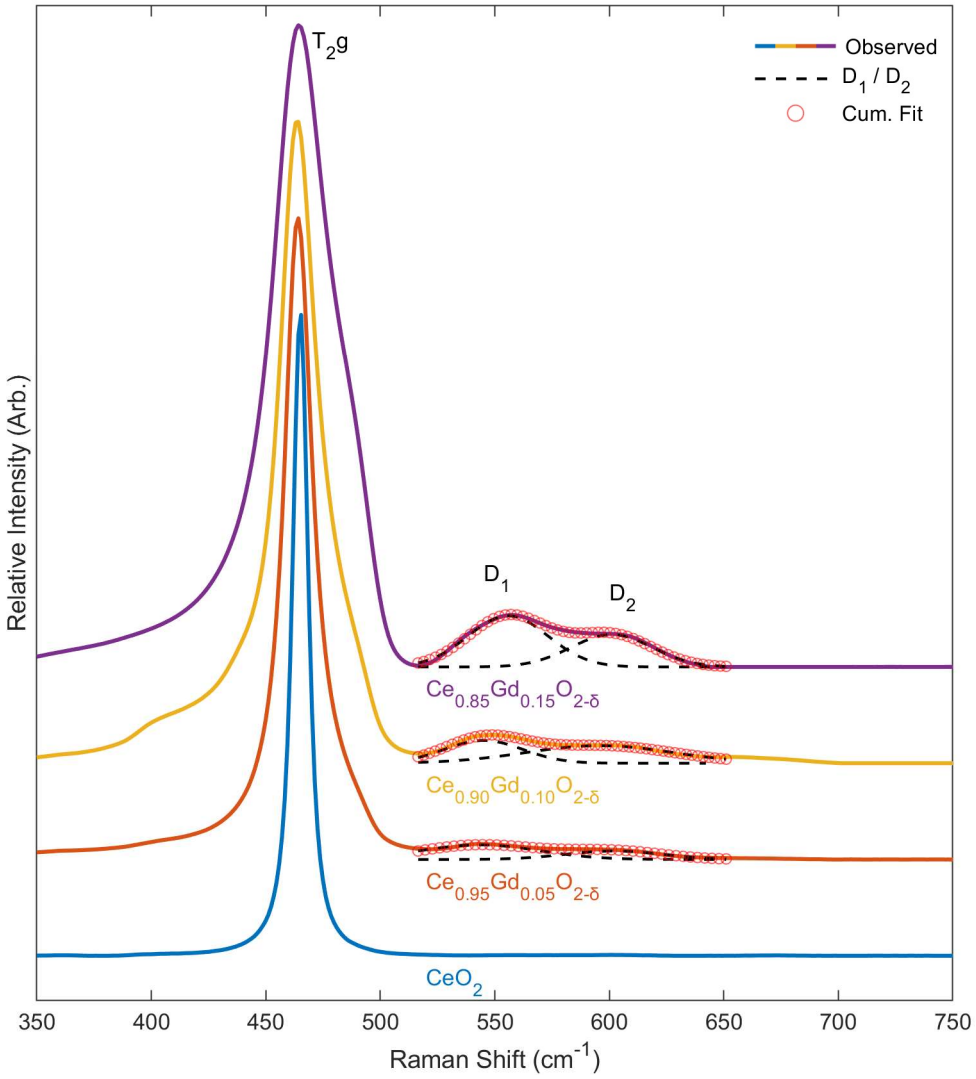

Figure 22: Raman spectra collected on sintered pellets of composition $Ce_{1-x}Gd_xO_{2-x/2}$ where x = 0.00, 0.05, 0.10 and 0.15.

The sharp T_{2g} peak at ~465 cm^{-1} observed in spectra collected on all compositions arises from the oscillation of Ce – O bonds in Fm-3m [52–54]. Bands characteristic of monoclinic (C/12) Gd_2O_3 (218, 268, 300, 386, 417, 430, 483 and 590 cm^{-1} [28]), and C-type Gd_2O_3 (Ia-3) (315, 361 480 and 568 cm^{-1} [28]) are absent in all spectra. Lattice expansion due to incorporation of larger Gd^{3+} ions is observed in compositions where $x \leq 0.10$. This is indicated by a shift in T_{2g} position

towards lower wavenumbers [55,56]. However, in samples of x = 0.15 T_{2g} position increases slightly to ~465.7 cm^{-1}; similar behaviour was observed in La-doped CeO_2 by Lee *et al.* with the increase from 11 to 15 mol% La doping[57]. Kainbayev *et al.* also reported a shift towards lower wavenumbers (462 cm^{-1} to 459 cm^{-1}) as Gd content in CeO_2 was increased from 10 to 20 mol%[56]. This reverse in T_{2g} shift for x > 0.10 is the result of increased V_O concentration, which is known to shift the T_{2g} position towards higher wavenumbers[56]. Measurements of T_{2g} position were plotted against Gd^{3+} content, presented in Figure 23.

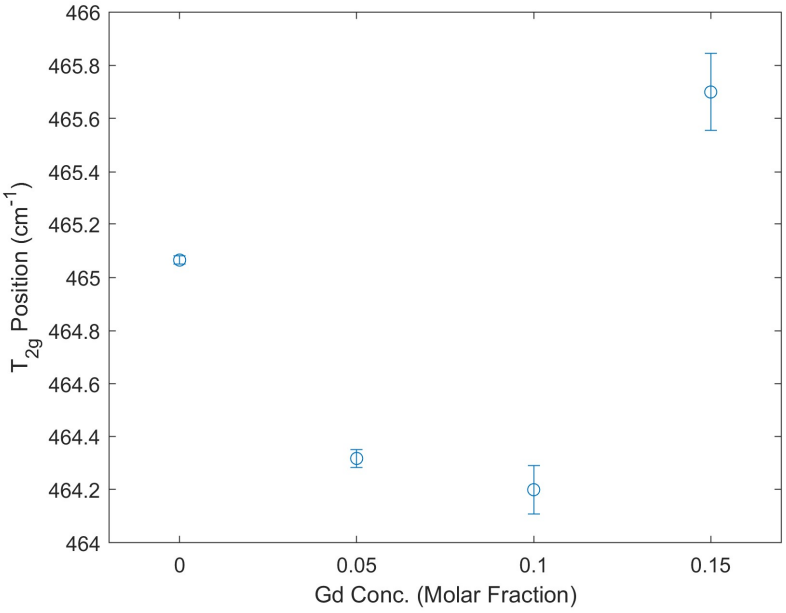

Figure 23: Plot of T_{2g} position against Gd concentration.

This suggests that where x ≤ 0.10, the expansion of the fluorite lattice is the dominant factor in controlling T_{2g} shift; however, Gd additions beyond this threshold generate a sufficient concentration of V_O to outweigh the influence of lattice expansion, shifting T_{2g} to higher wavenumbers. As no spectra were collected on grains of the Gd-rich secondary phases, this T_{2g} shift is unlikely to be related to a true C-type phase transition. Whilst T_{2g} shift can provide a useful indication of lattice expansion, the sensitivity of Raman spectroscopy to the oxygen sublattice renders it a less useful tool for examination of lattice parameters in defect-rich systems compared to XRD.

Total lattice disorder was found to increase with Gd^{3+} content. Disorder of the fluorite lattice arises from both the increased ionic radius of Gd^{3+} and V_O generation, which cause the T_{2g} mode to broaden. Measurements of the full width half maximum (FWHM) of the T_{2g} mode were found to vary linearly with Gd additions, as shown in Figure 24.

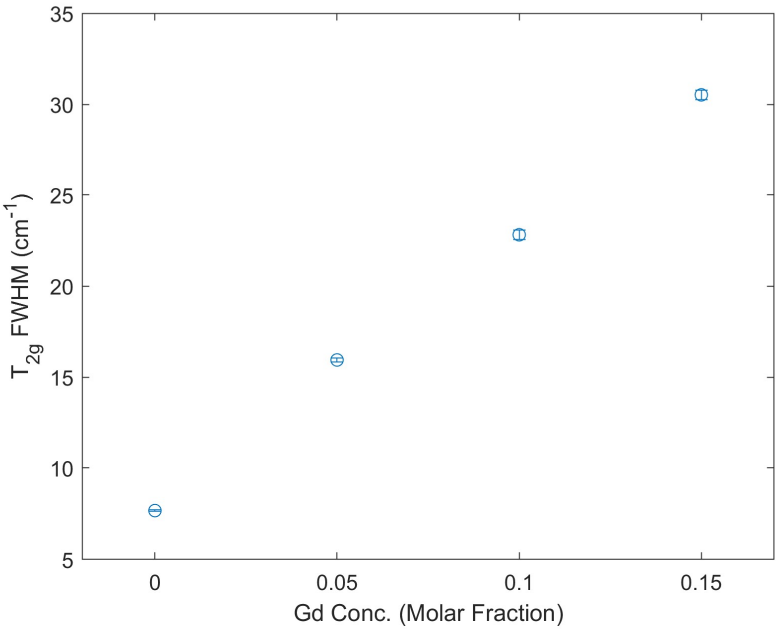

Figure 24: Plot of full width half maximum (FWHM) of T_{2g} mode against Gd concentration.

The FWHM of the T_{2g} mode may also be affected by peak splitting, evidenced by the subtle shoulder at ~480 cm^{-1}, which is most clearly observed in the x = 0.15 sample. This weakly separated vibrational mode has been noted in various studies of Ln-doped CeO_2 and its origin is much debated. Aškrabić *et al.* assigned this mode at ~480 cm^{-1} to a segregated monoclinic (C/12) Gd_2O_3 phase[58]; however, no additional modes characteristic of the C/12 structure were observed. Tyagi *et al.*, suggested the ~480 cm^{-1} mode is caused by vibration of O^{2-} around Gd^{3+} in the fluorite lattice, this attribution is also uncertain, as the position of this ~480 cm^{-1} peak is independent of the ionic radius of the dopant. Whilst assignment of this mode remains unclear, it is unlikely to have resulted from the 483 cm^{-1} or 480 cm^{-1} modes associated with C-type and monoclinic Gd_2O_3 phases respectively, as the spectra did not exhibit any additional modes associated with those structures.

The concentration of both V_O and GdO_8-type complexes in $Ce_{1-x}Gd_xO_{2-x/2}$ was found to increase with Gd additions up to x = 0.15. This is indicated by increases in the relative areas of the D_1 and D_2 modes. The broad defect band between 510 – 650 cm^{-1}, clearly observable in compositions of x = 0.05, 0.10, and 0.15, was deconvoluted to quantify relative contributions from defect band D_1 and D_2, attributed to V_O – Gd^{3+} and GdO_8 complexes respectively. V_O and GdO_8 complexes are manifested by separate modes, D_1 and D_2, located around 560 and 610 cm^{-1} respectively (Figure 22). GdO_8-type complexes describe the positions of dopant Gd^{3+} cations in 8-fold coordination with O^{2-} in regions with low V_O concentration[52]. The intensity of the D_1 and D_2 modes was plotted as a function of Gd content, presented in Figure 25.

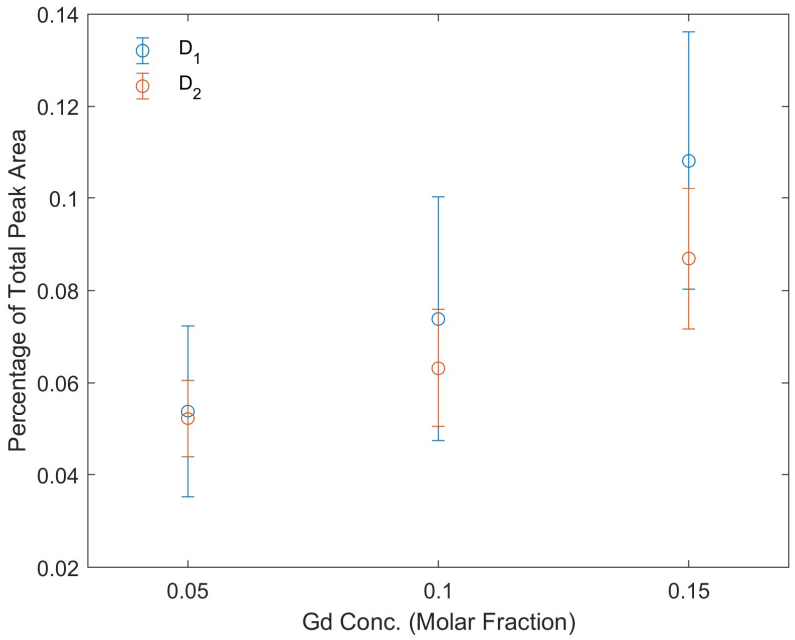

Figure 25: Plot of D_1 and D_2 peak areas relative to total peak area against Gd concentration.

Both V_O – Gd^{3+} and GdO_8 complexing increase with the addition of Gd. This is expected, as with greater amounts of Gd^{3+}, more V_O must be generated to charge balance, but greater numbers of Gd^{3+} also increases the likelihood of finding Gd^{3+} in 8-fold coordination. However, as Gd content is increased, V_O – Gd^{3+} complexing occurs at a greater rate than GdO_8 complexing, as shown by the increasing disparity in relative peak areas of D_1 and D_2. Lee *et al.* reported a similar increase in the intensity ratio of D_1:D_2 with increasing La doping in CeO_2. As Gd content increases, so too does V_O generation, meaning there are fewer regions in which V_O concentration is low enough to permit the formation of GdO_8 complexes[57]. Despite this, the concentration of GdO_8 complexes continues to increase with Gd additions.

The D_1 mode was found to shift to higher wavenumbers with increasing Gd^{3+} concentration, as shown in Figure 26.

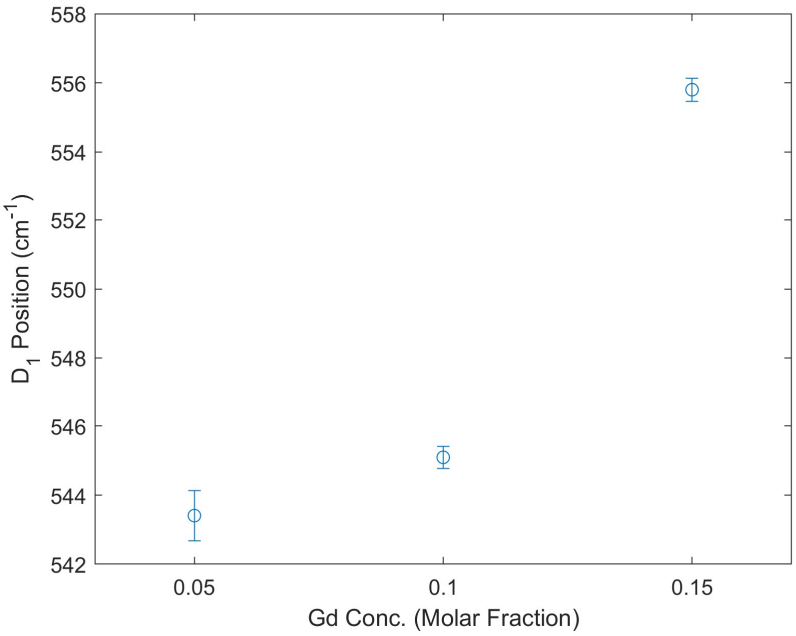

Figure 26: Plot of D_1 mode position against Gd concentration.

This same D_1 shift was observed by Lee *et al.* in their study of nanocrystalline CeO_2 doped with La, Gd, Pr and Y, and was attributed to an increase in the number of $2Gd'_{Ce} – V_O$ complexes compared to $Gd'_{Ce} – V_O$ complexes[57].

4.7 Gd Distribution within fluorite $Ce_{1-x}Gd_xO_{2-x/2}$ (x = 0.00 – 0.15)

Segregation of Gd^{3+} cations was observed in all compositions of $Ce_{1-x}Gd_xO_{2-x/2}$, where x = 0.00 – 0.15. This segregation occurred on both the micro and nanoscale, as evidenced by EPMA and STEM-EDS mapping respectively. Gd enriched regions were found to form both within grains and at grain boundaries.

Figure 27 reveals Gd distribution measured through EPMA mapping of sintered pellets. A consistent colour bar scale has been maintained to aid comparisons between samples.

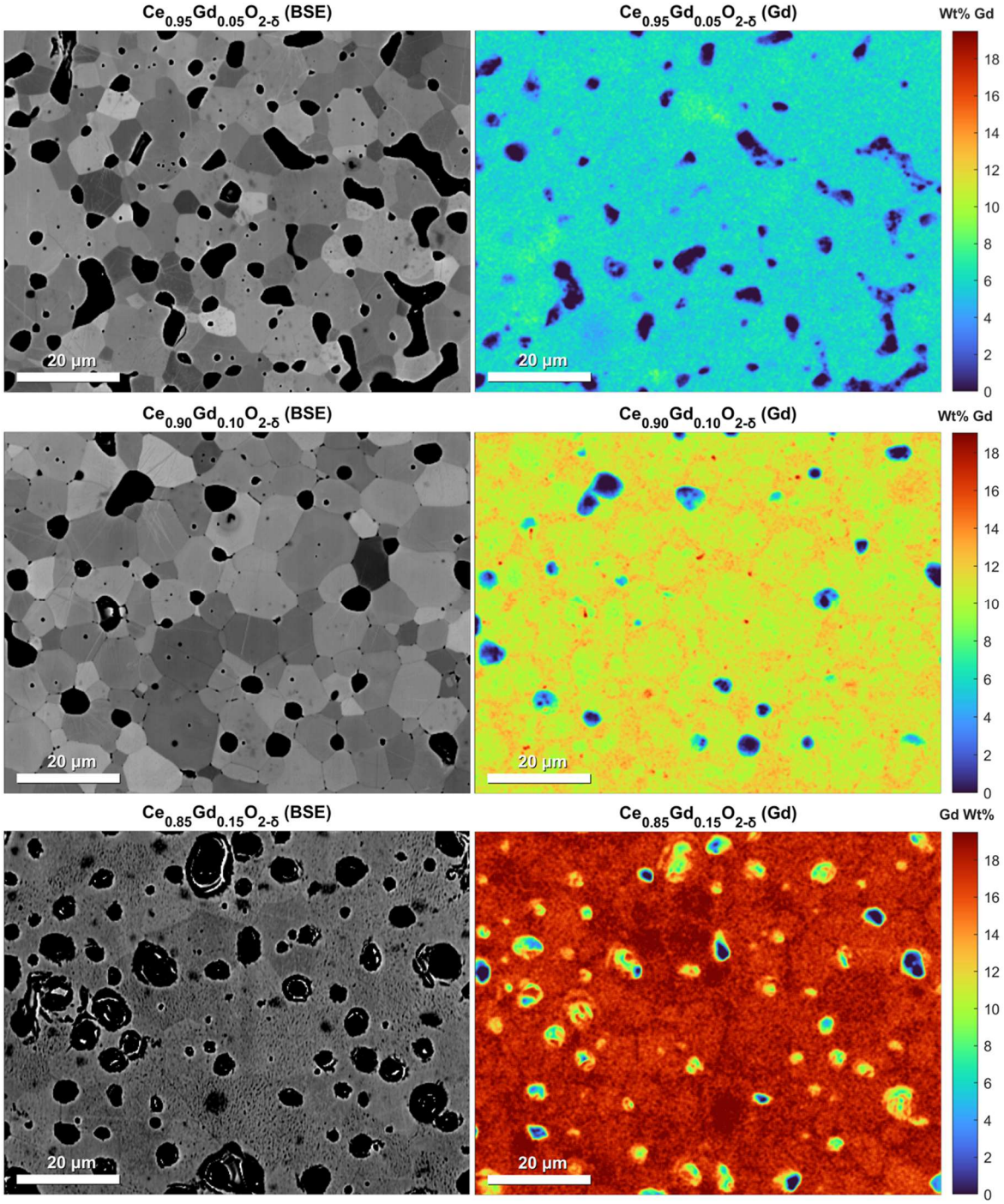

Figure 27: EPMA maps of $Ce_{1-x}Gd_xO_{2-x/2}$, where x = 0.05, 0.10 and 0.15, revealing heterogenous Gd distribution within the fluorite phase.

In the x = 0.05 sample, Gd is relatively well distributed across the surface, with concentrations generally varying between 5 – 7 wt%. However, some Gd-rich regions containing ~9 wt% were also revealed. Diameters of these regions ranged between 5 – 20 µm, Gd enrichment within fluorite grains may have resulted from preferential segregation of Gd^{3+} towards ordered V_O clusters, driven by strong V_O – Gd^{3+} binding[22]. These regions were confirmed by EBSD (presented in 4.9, Figure 37) to be fluorite, so cannot be considered a secondary phase.

Compositional heterogeniety is unlikely to have resulted from imperfect homogenisation of oxides precursors, as they were calcined from co-precipitated oxalate precipitates, known to have excellent cationic homoegeniety[59]. Gd distribution made no discernible contribution to Z-contrast in the BSE images for all samples, however Bragg contrast in the BSE images clearly reveals individual grain within the flat polished pellet surfaces.

For x = 0.10, there are clear signs of Gd enrichment along grain boundaries. Dopant segregation towards grain boundaries is driven by the large free volume of these 2D defects. Aliovalent dopants, especially those with significantly different ionic radii compared to the lattice cation, preferentially diffuse towards these regions during sintering, where they are readily accommodated[60]. Additionally, V_O concentration is known to increase within grain boundaries, further promoting Gd^{3+} segregation through V_O – Gd^{3+} association. Feng *et al*. proposed segregation towards specific sites within disordered grain boundaries provides the initial driving force behind dopant segregation, whereas subsequent segregation is promoted by dopant interactions with V_O clusters at the grain boundary[61].

Whilst Gd is generally most concentrated in the channels along grain boundaries, there do exist a few larger (~10 μm) Gd-rich regions within and across grains in the x = 0.10 sample. As with x = 0.05 sample, EBSD analysis of the same region (4.9, Figure 40) confirmed the absense of secondary phases in these Gd-rich regions. The x = 0.15 sample similarly shows Gd-rich regions within grains (~10 μm) and enrichment along grain boundaries. Poor Bragg contrast in the BSE image, resulting from disordered lattice discussed previously, makes distinguishing grains more challenging, evidence of grain boundary enrichment is still apparent.

The full series of EPMA maps on these samples, which also included Ce, O, Al, and Si, is presented in Figure S6, found in the Supplmentary information.

Closer examination of Gd distribution in fluorite $Ce_{1-x}Gd_xO_{2-x/2}$ revealed evidence of grain boundary segregation for x = 0.05 that was not observed *via* EPMA. STEM-EDS mapping, presented in Figure 28, shows a porous, Gd-rich region situated between two grains. Surprisingly, this Gd enriched region appeared entirely depleted in Ce, suggesting potential formation of a Gd_2O_3 secondary phase localised along the grain boundary. Extensive solute segregation has been linked to potential phase transitions in the vicinity of grain boundaries[61], though further analysis through ED or t-EBSD would be necessary to confirm this.

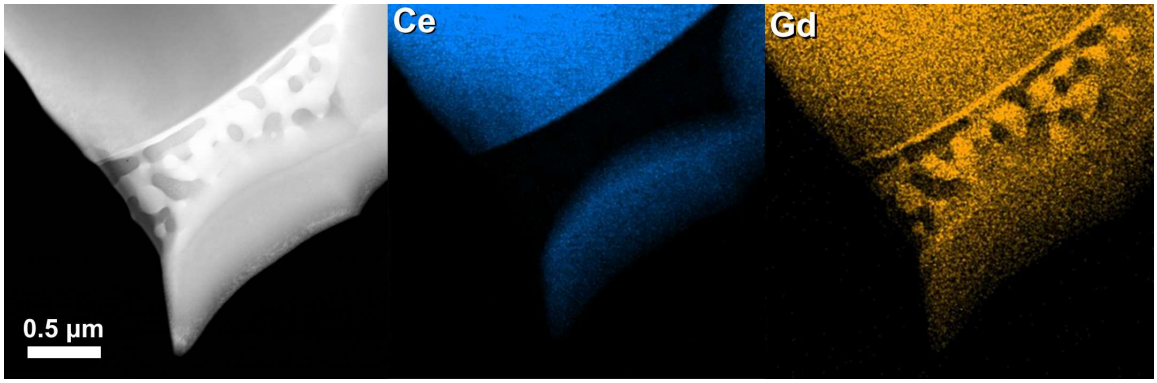

Figure 28: STEM-EDS maps of Ce and Gd distribution across a grain boundary in $Ce_{0.95}Gd_{0.05}O_{2-\delta}$.

At higher magnifications still, it is possible to find evidence of Gd^{3+} occupying sites within the grain boundary structure. Figure 29 shows a STEM-EDS line-scan revealing Gd enrichment, corresponding with Ce depletion, approximately 3 nm either side of a grain boundary.

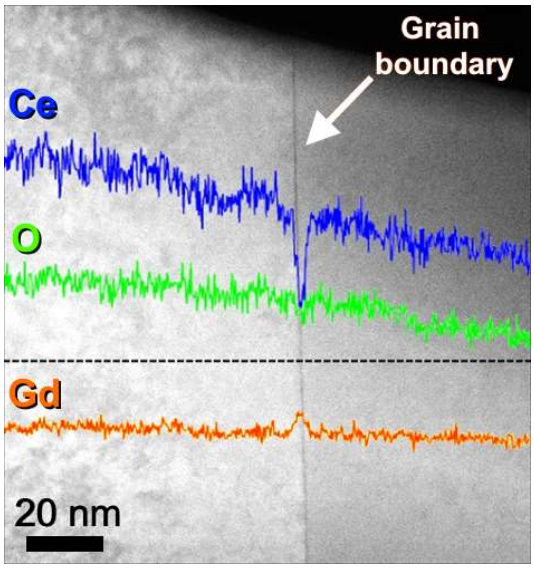

Figure 29: STEM-EDS line scan across $Ce_{0.95}Gd_{0.05}O_{2-\delta}$ grain boundary.

TEM conducted by Li *et al.* also found evidence of Gd ions occupying sites within grain boundaries in 25 mol% Gd-doped CeO_2. Despite the large free volume and high V_O concentration driving Gd^{3+} cations towards grain boundaries, the largest regions of segregated Gd generally occurs within grains. Li *et al.* proposed this phenomenon resulted from grain boundary movement during sintering [32]. Gd is initially randomly distributed the fluorite matrix, high temperatures reached during sintering enhance the mobility and interactions of dopants and associated oxygen vacancies. This enhanced movement of V_O and Gd^{3+} allows both to segregate towards grain boundaries during the early stages of sintering, where they may form C-type nanodomains. Grains continue to grow as sintering continues, leaving the nanodomains to reside within the newly formed grain interior.

4.8 Bulk dissolution behaviour in $Ce_{1-x}Gd_xO_{2-x/2}$ (x = 0.00 – 0.15)

Semi-dynamic aqueous dissolution experiments were performed on sintered pellets of $Ce_{1-x}Gd_xO_{2-x/2}$ at 90 °C in 0.01 M HNO_3 solution; sampling took place after 1, 2, 3, 4, 7, 10, 14, 21 and 28 days of dissolution. Normalised release rates of Ce and Gd were greatest during the first four days of dissolution, this was followed by decrease in rate for the remaining 24 days. Two dissolution regimes, termed 'Rate 1' and 'Rate 2', were calculated using linear fits (shown in Figure S7) of normalised release across days 1-4 and 5-28 respectively. Elemental release of Ce and Gd in each composition is summarised in Table 5. The incongruity factor '*r*' was calculated by dividing the normalised release rate of Gd by that of Ce (NL_{Gd}/NL_{Ce}).

Table 5: Summary of normalised mass loss in $Ce_{1-x}Gd_xO_{2-x/2}$ during Rate 1 and Rate 2.

Composition ($Ce_{1-x}Gd_xO_{2-x/2}$)	Rate 1 (Days 1 – 4)			Rate 2 (Days 5 – 28)		
	NL_{Ce} (g m^{-2} d^{-1})	NL_{Gd} (g m^{-2} d^{-1})	r	NL_{Ce} (g m^{-2} d^{-1})	NL_{Gd} (g m^{-2} d^{-1})	r
x = 0.00	$(1.29 \pm 0.048) \times 10^{-3}$	-	-	$(5.01 \pm 0.049) \times 10^{-4}$	-	-
x = 0.05	$(9.54 \pm 0.914) \times 10^{-4}$	$(1.18 \pm 0.001) \times 10^{-1}$	123.7	$(2.42 \pm 0.027) \times 10^{-4}$	$(7.55 \pm 0.008) \times 10^{-2}$	312.0
x = 0.10	$(1.98 \pm 0.126) \times 10^{-3}$	$(4.40 \pm 0.133) \times 10^{-2}$	22.22	$(3.78 \pm 0.202) \times 10^{-4}$	$(1.14 \pm 0.105) \times 10^{-2}$	30.16
x = 0.15	$(6.91 \pm 0.569) \times 10^{-3}$	$(1.95 \pm 0.201) \times 10^{-1}$	28.22	$(1.01 \pm 0.149) \times 10^{-3}$	$(2.53 \pm 0.394) \times 10^{-2}$	25.05

The decrease in elemental release between Rate 1 and Rate 2 is primary caused by solubility-related effects. During the first 4 days of dissolution, the solution was replaced every day, whereas during the subsequent 24 days of dissolution, solution was replaced less frequently (reasons for this deviation from the ASTM standard are detailed in Section 3.2.19). The thermodynamic driving force behind Ce and Gd release decreases as their concentration in solution increases. In a completely static dissolution experiment, the duration of the initial rate is shortened, as solutions are not replaced even after saturation is reached, resulting in a slower, residual rate. A semi-dynamic dissolution test was used to mitigate solution saturation effects, allowing data to reveal more information about intrinsic factors affecting dissolution rates, which might otherwise be concealed by solubility-related effects. However, as sampling every 24 hours was not possible, longer intervals elapsed between sampling and solution renewal after 4 days of dissolution. This change to sampling frequency is likely to have decreased leaching rates due to solution effects. For this reason, Rate 1 and Rate 2 must be considered separately.

Gd incorporation apparently influenced the aqueous dissolution of sintered pellets of $Ce_{1-x}Gd_xO_{2-x/2}$. Normalised Ce release was similar for x = 0.00, 0.05 and 0.10, but for x = 0.15, Ce release during Rate 1 was around 3 times greater. Figure 30 below presents a plot of cumulative normalised release of Ce over time.

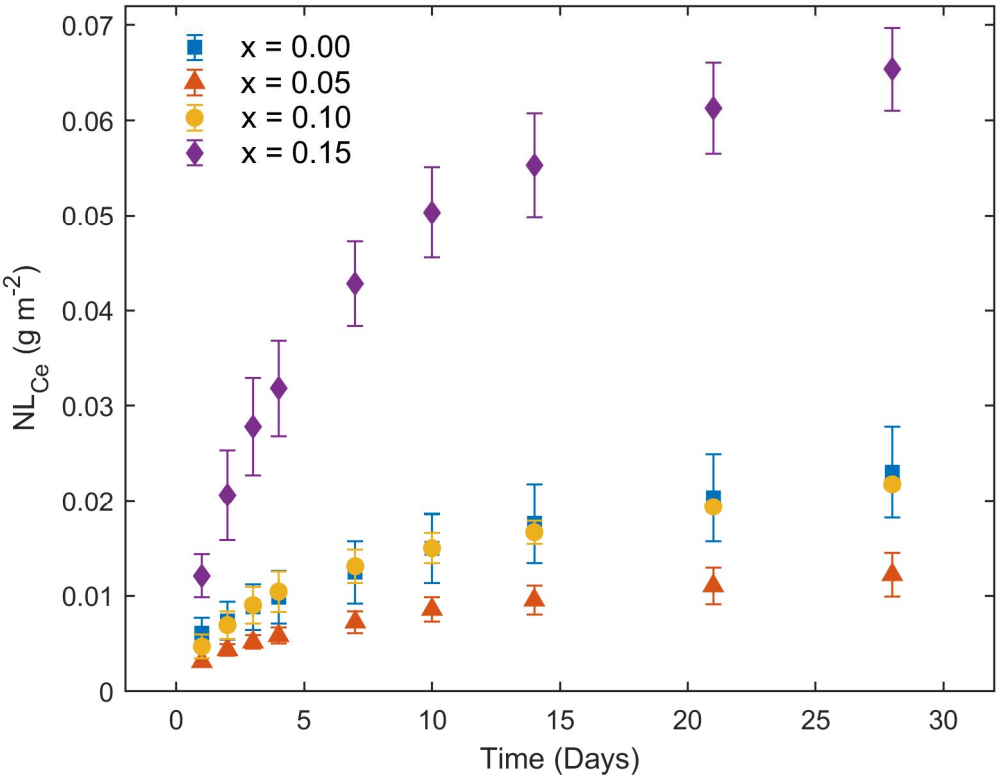

Figure 30: Plot of normalised Ce release in $Ce_{1-x}Gd_xO_{2-x/2}$ (where x = 0.00 - 0.15) against time. Dissolution took place in 0.01 HNO_3 at 90 °C. Errors presented are the standard deviation in measurements on triplicate/duplicate pellets.

Normalised Ce release during Rate 2 was significantly higher for x = 0.15 compared to all compositions where x < 0.15. This bi-modal behaviour between compositions where x < 0.15 and x = 0.15 could be attributed greater contributions from secondary phases, which were found to be most prevalent for x = 0.15. Whist these phases were Gd-rich, they contained a significant quantity of Ce, and, if rapidly dissolved compared to the fluorite matrix, would result in pronounced increases to Ce normalised release. However, these same secondary phases were also observed, albeit to a lesser extent, in compositions where x = 0.10. If these phases were responsible for greater rates of Ce release, it should follow that x = 0.10 would exhibit a significantly greater Ce release compared to x = 0.00 and x = 0.05, however this was not the case. Alternatively, the marked 3-fold increase in Ce release for x = 0.15 may be related to changes in the crystal structure induced for x > 0.10. As previously discussed, samples of x = 0.15 could not be indexed as either fluorite (Fm-3m) or C-type (Ia-3) in bulk EBSD measurements; this is believed to be because of V_O ordering inducing slight cation displacements that broke long-range order and symmetry in the structure. Similarly, Raman analysis revealed extensive V_O concentrations for x > 0.10 that reversed the trend in T_{2g}

position shift, and significantly increased the number of $2Gd'_{Ce} – V_O$ complexes compared to $Gd'_{Ce} – V_O$ complexes.

A clear relationship between composition and dissolution rate was observed by Horlait *et al.* in their study of Ln^{3+}-doped CeO_2. They noted an approximate 10-fold increase in Ce release rates with every 10 mol% of Ln^{3+} incorporated within CeO_2, which was attributed to a weakening of the crystal lattice due to V_O generation[62]. In the present study, incorporation of x = 0.05 was shown to distort the fluorite lattice, induce V_O, and form small regions enriched with segregated Gd^{3+}. Despite this, Ce release was lower in x = 0.05 compared to x = 0.00. This discrepancy could have resulted from underestimation of the surface area of CeO_2 in contact with solution. Pellets of CeO_2 exhibited greater porosity, as observed through SE imagining and density measurements discussed previously. However, surface area measurements, which were used to calculate the normalised release, considered pellets to have simple cylindrical geometries. This unaccounted increase in reactive surface area, facilitated by a greater quantity of open pores in CeO_2, may have resulted in overestimation of normalised Ce release.

Corkhill *et al.* noted a normalised release of $(7.40 \pm 0.2) \times 10^{-2}$ g m^{-2} d^{-1} in polished CeO_2 pellets, and $(7.26 \pm 0.2) \times 10^{-5}$ g m^{-2} d^{-1} annealed CeO_2 pellets, dissolved at in 0.01 HNO_3 at 90 °C [14]. Stennett *et al.* measured an initial rate in crushed CeO_2 powders of $(4.85 \pm 0.01) \times 10^{-4}$ g m^{-2} d^{-1}. In this work, the 'initial' Rate 1 was $(1.29 \pm 0.048) \times 10^{-3}$ g m^{-2} d^{-1}. Despite the studies taking place at the same temperature and using the same dissolution media, vastly different rates of dissolution are observed. Complex factors involved in dissolution testing can exert a strong influence on measured rates. For example, in dissolution tests using sintered pellets, deviations in sample grinding and polishing can induce different quantities of defects and strain the surface. Annealing can help to alleviate this surface strain, however the heat treatment introduces greater topography in samples, potentially affecting their surface area in contact with solution. Comparing dissolution data collected on pellets with powder samples can prove especially challenging, as crushing powders typically introduces greater uncertainty in surface area to volume ratio, and introduces sharp features known to encourage more rapid dissolution. Furthermore, certain studies may involve dissolving samples of unsintered material, such as Horlait *et al.* investigation into Ln^{3+}-doped CeO_2, in which calcined oxide powders were used. For these reasons, direct comparison of rates between studies is very challenging, often discussing trends and relative relationships is more meaningful and useful.

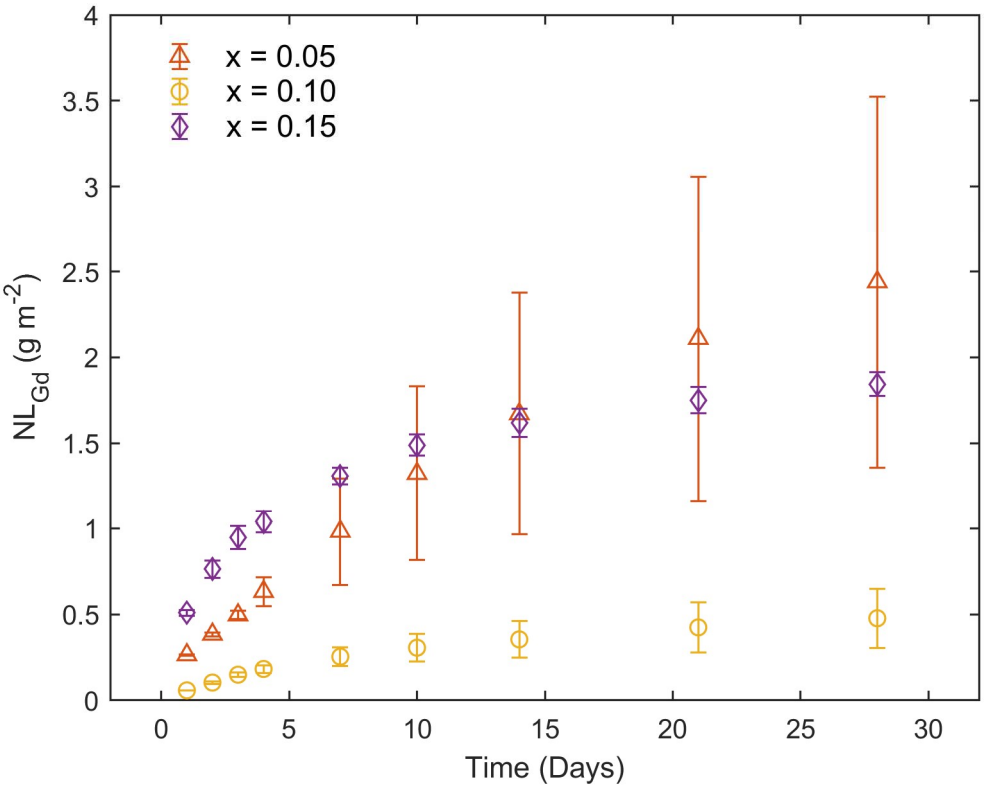

Figure 31: Plot of normalised Gd release in $Ce_{1-x}Gd_xO_{2-x/2}$ (where x = 0.00 - 0.15) against time. Dissolution took place in 0.01 HNO_3 at 90 °C. Errors presented are the standard deviation in measurements on duplicate pellets.

Normalised Gd release rates presented in Figure 31 reveal no obvious trends with increasing Gd additions in x = 0.05, 0.10, and 0.15. Gd release during Rate 1 was greatest for x = 0.15, in accordance with the relative rates of Ce release. Samples where x = 0.10 showed the lowest normalised Gd release during both Rate 1 and Rate 2. For x = 0.05, Rate 2 of Gd release is only slightly slower than Rate 1, falling from $(1.18 \pm 0.001) \times 10^{-1}$ to $(7.55 \pm 0.008) \times 10^{-2}$ g m^{-2} d^{-1}. During Rate 2, Gd release for x = 0.05 was greater than for x = 0.15 ($(1.01 \pm 0.149) \times 10^{-3}$ g m^{-2} d^{-1}).

Normalised Gd release was found to be incongruent with Ce release in all Gd-containing compositions, as illustrated in Figure 32. This incongruous dissolution was most prevalent where x = 0.05. The contributing factors toward this incongruity are believed to vary with composition. Incongruity for x = 0.10 and x = 0.15 may have resulted from the enhanced dissolution of Gd-rich secondary phases. These secondary phases were identified in both samples, and were characterised to contain 70-80 mol% Gd, and 20-30 mol% CeO_2. The

relative quantities of these phases are believed to be far higher for x = 0.15, but despite this the degree of incongruity in both x = 0.10 and 0.15 was very similar.

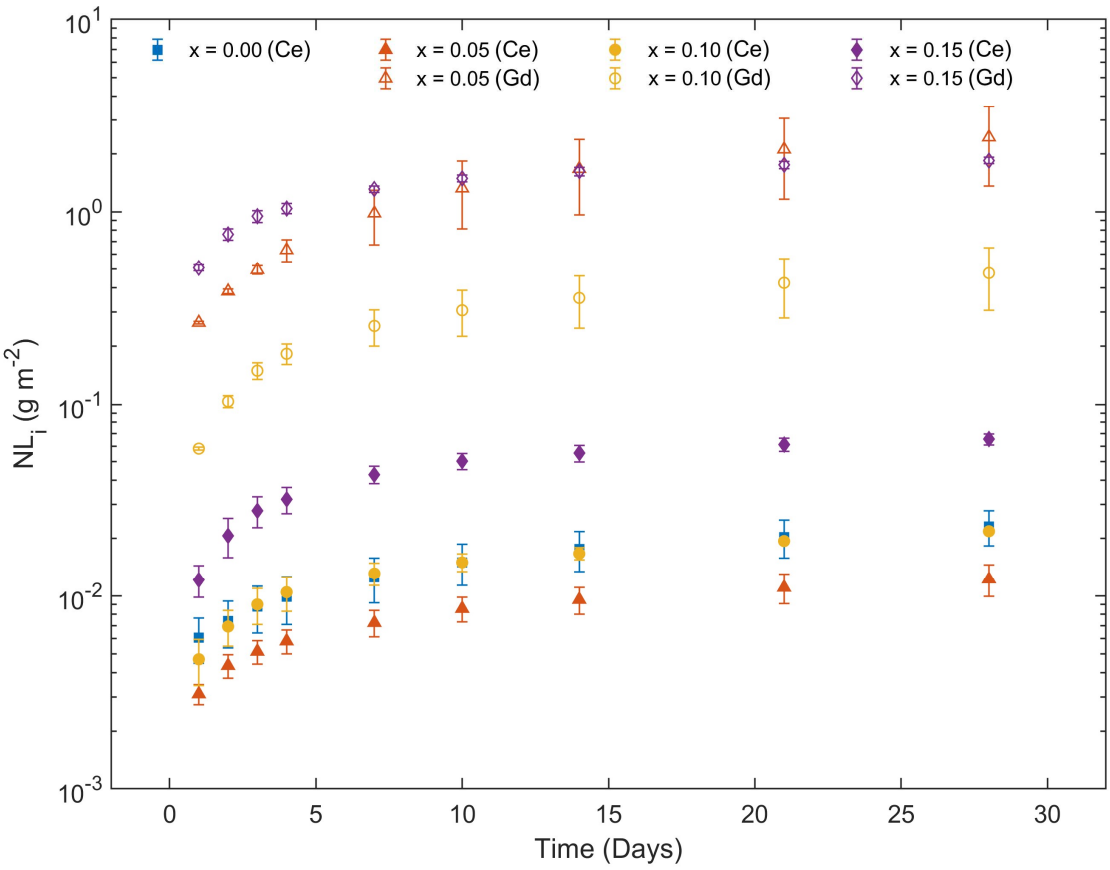

Figure 32: Log plot of normalised Ce and Gd release during ASTM C1308 dissolution of $Ce_{1-x}Gd_xO_{2-x/2}$

Incongruent release could also be caused by rapid grain boundary dissolution. Channels between grains were found to be enriched with Gd in both x = 0.10 and 0.15 samples. The extent of grain boundary segregation was greatest however for x = 0.10 (Figure 27), perhaps suggesting this was the dominant factor behind the 30-fold faster release of Gd compared to Ce. Analysis of post-dissolution surfaces using SEM and VSI, however, revealed no discernible grain boundary deepening through preferential dissolution. Incongruent behaviour was most pronounced however for x = 0.05. During Rate 1, Gd was released at a rate over 100 times greater than Ce. In Rate 2, the incongruity was more pronounced still, with Gd released at over 300 times the rate of Ce. The cause of this incongruity is unclear, as these samples showed no signs of secondary phase formation or extensive grain boundary segregation of Gd.

The effects of change in reactive surface area, resulting from material removal during dissolution, must also be considered[13]. Surface areas of each pellet were measured using VSI prior to and following dissolution, revealing no measurable difference. Overall, surfaces

showed no real signs of dissolution when observed with VSI, as shown in Figure 33. In their study of $Ce_{0.24}Nd_{0.76}O_{1.62}$, Horlait *et al.* used E-SEM images to readily observe rapid dissolution of hexagonal secondary phases, leaving behind large pits and pores in the microstructure[35] which increased the total reactive surface area as dissolution progressed. No such observations were made in the present work.

The low normalised release rate of Gd in x = 0.10 sample was surprising, given EPMA revealed this composition to exhibit the most obvious signs of grain boundary segregation. VSI and SEM observation of pellet surfaces post-dissolution revealed no evidence of grain boundary retreat, this is likely because the relatively dilute (0.01 M) HNO_3 solution dissolves a very small amount of material, even after 28 days at 60 °C.

Whilst triplicate pellets were dissolved for each solution, normalised release was calculated using ICP-MS data collected on just two of the three pellets of x = 0.05. 0.10, and 0.15, as the third pellet displayed anomalous dissolution behaviour. Individual plots of normalised release from each pellet shown in Figure S8 in the Supplementary information. Pellets of x = 0.10 and 0.15 that dissolved at a markedly faster rates were analysed with VSI, revealing a large, recessed regions on the surface with a very porous microstructure, shown in Figure S9. Extensive porosity can increase the surface area in contact with solution during dissolution tests, resulting in inaccuracy when calculating normalised elemental release rates. These porous regions possibly resulted from large-scale formation of secondary phases, however the exact cause of this variation between samples is unclear.

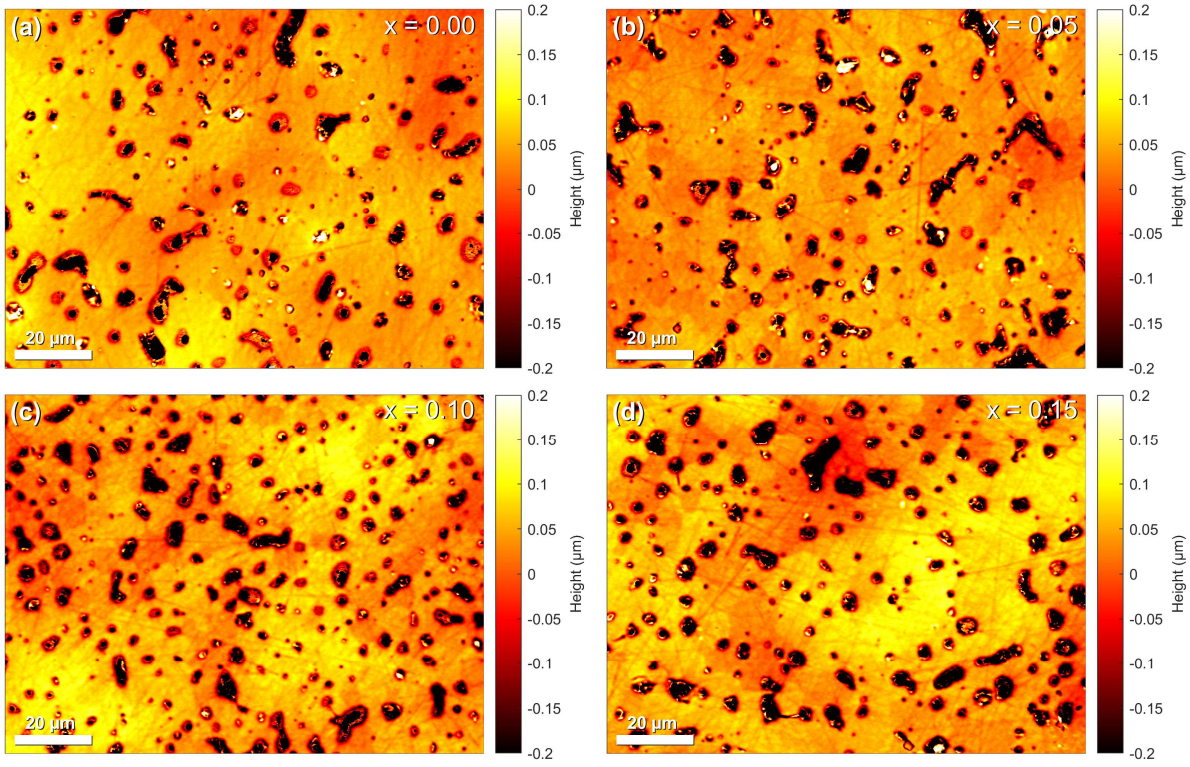

Figure 33: VSI scans showing post-dissolution (0.01 M HNO_3 at 60 °C) surfaces of pellets where: (a) x = 0.00, (b) x = 0.05, (c) x = 0.10, (d) x = 0.15.

4.9 Influence of microstructural and compositional heterogeneity on dissolution in $Ce_{1-x}Gd_xO_{2-x/2}$ (x = 0.00 – 0.15)

The effects of microstructural features and local composition on the surface dissolution of $Ce_{1-x}Gd_xO_{2-x/2}$ pellets was investigated using vertical scanning interferometry (VSI). Specific regions of interest (ROI) were marked on the surface of each sample (x = 0.00, 0.05, 0.10 and 0.15). These regions were characterised using EBSD and EPMA prior to dissolution in 12 M HCl at 60 °C for 7 days; these aggressive conditions were required to accelerate the rate dissolution and produce measurable surface retreat within a month. This technique aimed to deconvolute the various factors controlling the dissolution rate in fluorite $Ce_{1-x}Gd_xO_{2-x/2}$.

Average surface normal retreat rate (relative to the inert mask) measured for each composition is summarised in Table 6.

Table 6: Summary of surface normal retreat rate measured in VSI-base dissolution study. Values were calculated using the average step height measured between masked and unmasked regions across each pellet surface.

Composition	Surface Normal Retreat Rate (nm day^{-1})
CeO_2	105.4 ± 12.14
$Ce_{0.95}Gd_{0.05}O_{2-\delta}$	81.56 ± 5.286
$Ce_{0.90}Gd_{0.10}O_{2-\delta}$	89.53 ± 7.029
$Ce_{0.85}Gd_{0.15}O_{2-\delta}$	52.54 ± 4.857

Interestingly, average surface retreat was slowest for x = 0.15, which in bulk dissolution testing showed the greatest rates of normalised Ce release. It should be noted however, that direct comparisons between the bulk C1308 tests and the VSI-based surface dissolution tests may be misleading. In C1308 tests, pellets were dissolved in 0.01 M HNO_3 solutions, whereas in the VSI-study, a far stronger 12 M HCl solution was required to promote significant dissolution, introducing significant surface evolution that was more readily measured using VSI. To simplify subsequent discussion, only high-magnification flux (difference) maps are presented for each composition. Individual VSI measurements of pellet surfaces prior to, and following dissolution are available in Figure S11 in the Supplementary information.

4.9.1 Surface Dissolution of CeO_2

Heterogenous surface retreat in CeO_2 was influenced by grain orientation, grain boundaries and pores. Figure 34 presents a flux map, highlighting differences in surface height surface pre- and post-dissolution.

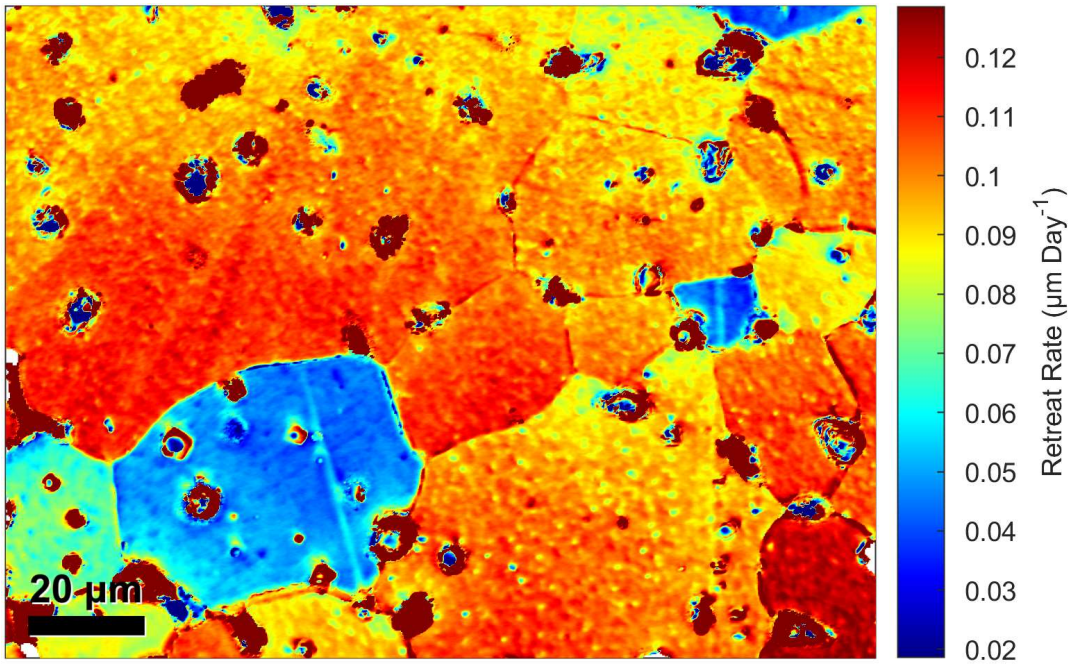

Figure 34: Flux map heterogenous revealing rates of surface retreat in x = 0.00 pellet dissolved in 12 M HCl at 60 °C.

The most pronounced differences in retreat rate are observed between different grains. Crystallographic orientation varies between grains, meaning different crystallographic planes are exposed at the surface. These planes differ in their surface energies; <001> and <111> are known to be the most stable. The least stable planes, with the largest surface energies, are known to dissolve more rapidly. Godinho *et al.* found the <112> plane to dissolve at 33 times the rate of <111> in their study of CaF_2 (fluorite) [13]. EBSD mapping, presented in Figure

35, revealed the same trend in CeO_2. The slowest dissolving grains, corresponding to blue regions of low retreat in the flux map, were indexed as <104> or <114>. Both orientations are closely aligned with <001>, as illustrated by their red colouring on the Euler plot in the EPMA map. The surface energy relationships between the three orientations that provide poles in Euler projection used in the EBSD plots, <001>, <111>, and <101>, are presented in Figure 36.

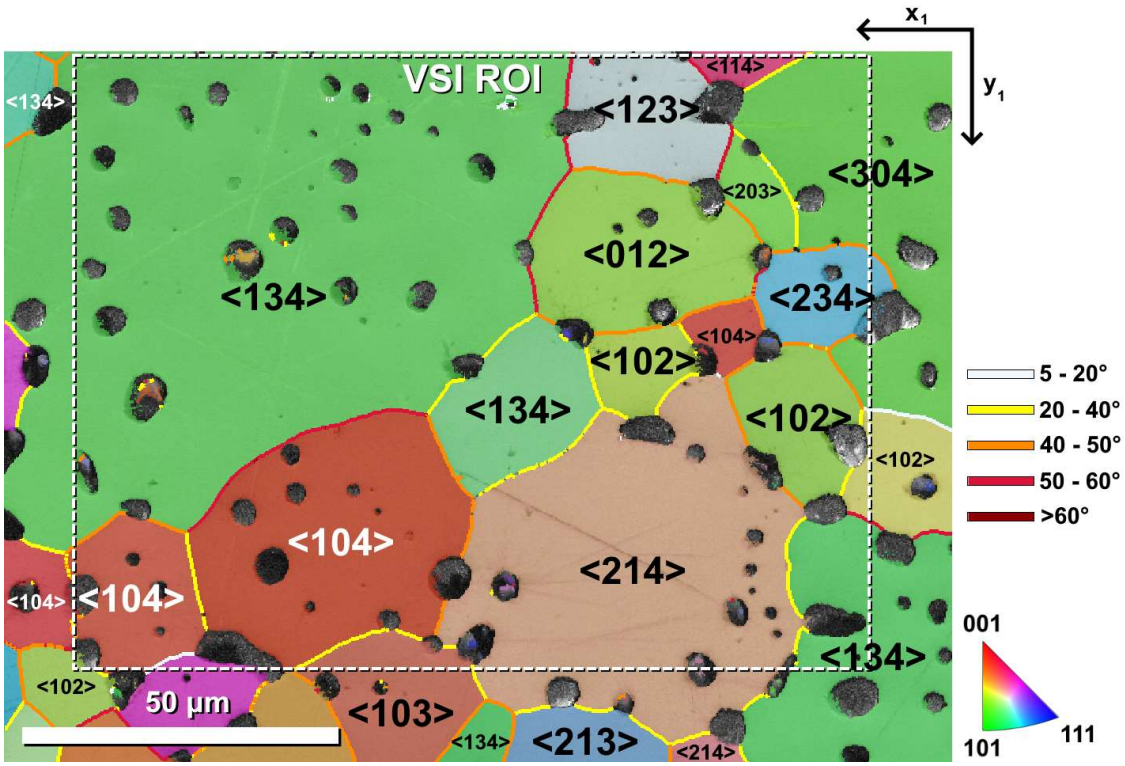

Figure 35: Euler angle colouring EBSD map of x = 0.00 pellet. The dashed white border indicates the region of interest over which surface dissolution was monitored using VSI (Figure 34).

Corkhill *et al.* also observed the lowest rates of dissolution in <111> grain surfaces in their study of CeO_2 [14], in accordance with this work. Grains developed roughness through facet formation during dissolution. This faceting was also found to be crystallographically controlled, and most prevalent in the rapidly dissolved grains. Corkhill *et al.* noted the formation of triangular facets, indicative of <111> plane terminations, suggesting that surfaces that dissolve more slowly are the most stable, and persist during dissolution.

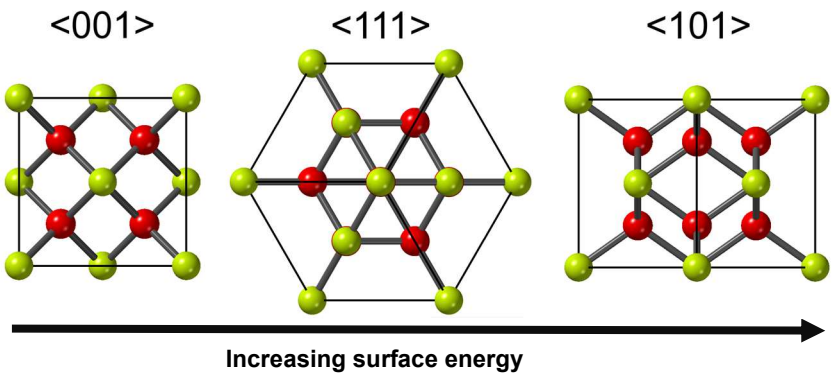

Figure 36: Illustration of orientations that provide poles in Euler projection used in the EBSD plots and their relative surface energies.

Preferential grain boundary dissolution was also readily observed in CeO_2, in agreement with observations in several existing studies[12,14,35]. However, no clear relationship between grain boundary misorientation could be established, in contrast with observations made by Corkhill *et al.* in their study of CeO_2 and ThO_2 [14]. Subtle differences in grain boundary retreat rates caused by differences in misorientation may have been obscured by the extensive heterogenous retreat of grain surfaces themselves. In the Corkhill study, grain boundary depth was measured more frequently during the very earliest stages of dissolution, when grain boundary deepening the only significant area of retreat within the microstructure.

Measurement of pore dissolution was not possible due to several limiting factors. Polishing samples in preparation for EBSD and EPMA involved the use of colloidal silica, this polishing media is readily trapped within pores, and proved very challenging to remove despite additional polishing with clean pads in UHQ, and ultrasonication in isopropanol. In addition, the technique of VSI is poorly suited to measurement of sharp geometries and deep pores. For this reason, the retreat rates of pores will not be discussed further.

EPMA maps revealing Ce distribution in CeO_2 (x = 0.00), x = 0.05, x = 0.10, and x = 0.15 are not presented here, but are available in Figure S10 in the Supplementary information.

4.9.2 Surface Dissolution of $Ce_{0.95}Gd_{0.05}O_{2-\delta}$

Surface retreat for x = 0.05 (Figure 39) was also largely governed by the crystallographic orientation (Figure 37) of grains. The same relationship is observed as with x = 0.00 (CeO_2), grains aligned towards <101> dissolved fastest, whilst those oriented closer to <001> and <111> directions showed slower retreat. No clear relationship between Gd distribution (Figure 38) and heterogenous retreat was observed. Low level Gd segregation does not appear to either encourage or inhibit dissolution. The most Gd-rich region revealed by *via* EPMA is contained within a <014> oriented grain at the very top of the region of interest. This grain retreated 50% faster compared to an equally sized grain with the same orientation. As

discussed previously, EPMA mapping of this region revealed several Gd-rich regions, which did not correspond to specific grains or phases.

As discussed in Section 4.2, the Gd addition were not found to exert a grain texture (preferential alignment) in the microstructure, so the relative quantities of high and low energy exposed crystallographic planes are not expected to vary with composition.

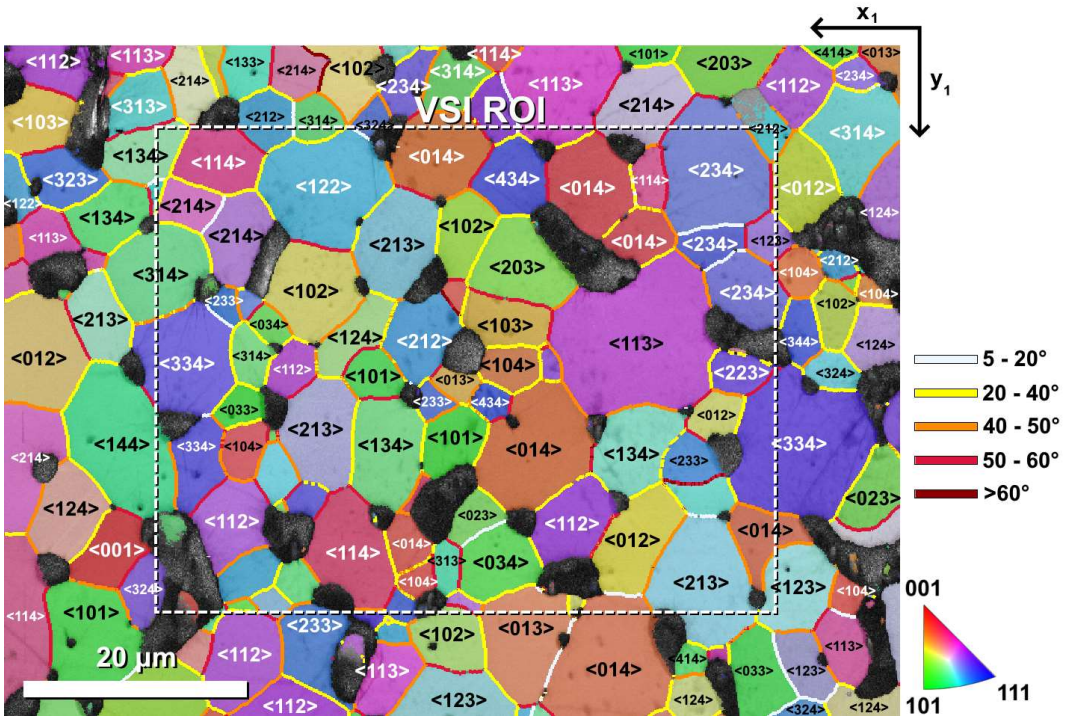

Figure 37: Euler angle colouring EBSD map of x = 0.05 pellet. The dashed white border indicates the region of interest over which surface dissolution was monitored using VSI (Figure 39).

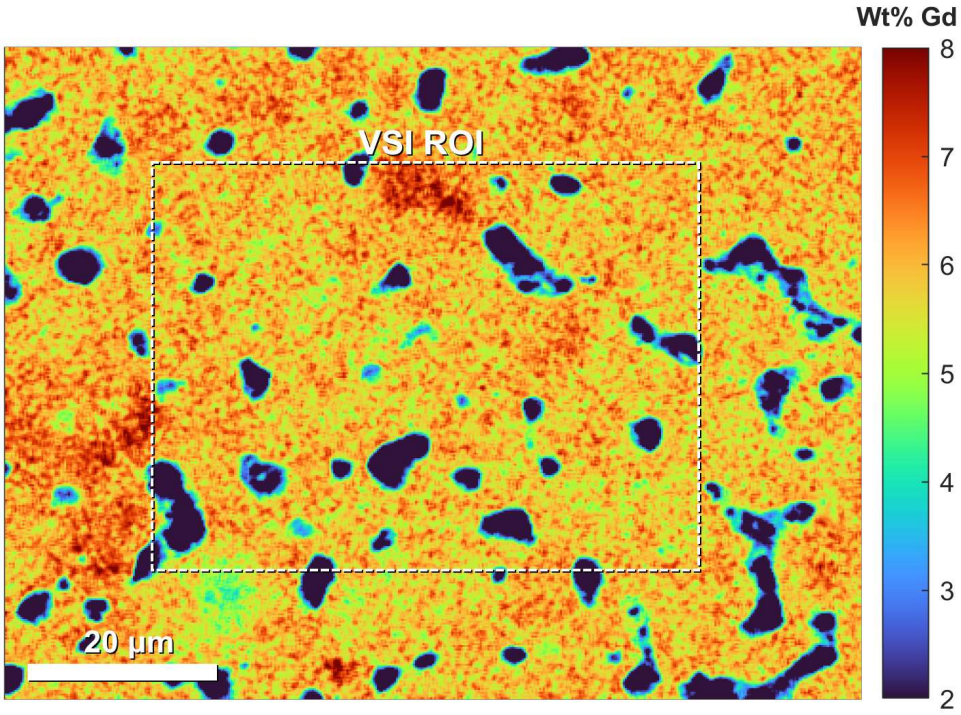

Figure 38: EPMA map of x = 0.05 pellet, revealing spatial distribution of Gd. The dashed white border indicates the region of interest over which surface dissolution was monitored using VSI (Figure 39).

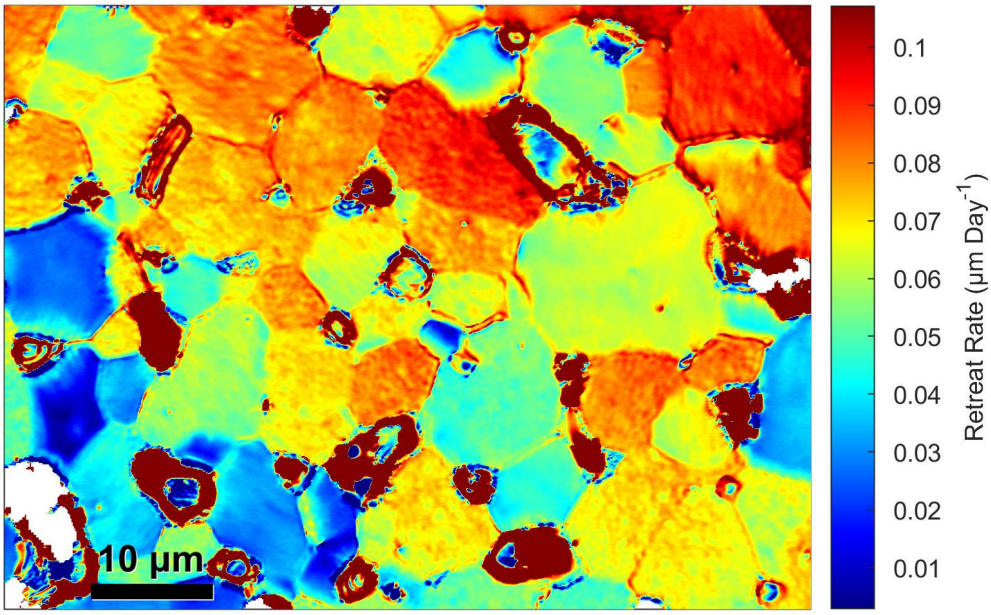

Figure 39: Flux map heterogenous revealing rates of surface retreat in x = 0.05 pellet dissolved in 12 M HCl at 60 °C.

4.9.3 Surface Dissolution of $Ce_{0.90}Gd_{0.10}O_{2-\delta}$

As with x = 0.00 and x = 0.05, heterogenous surface dissolution in x = 0.10 (Figure 42) was dominated by crystallographic orientation effects (Figure 40).

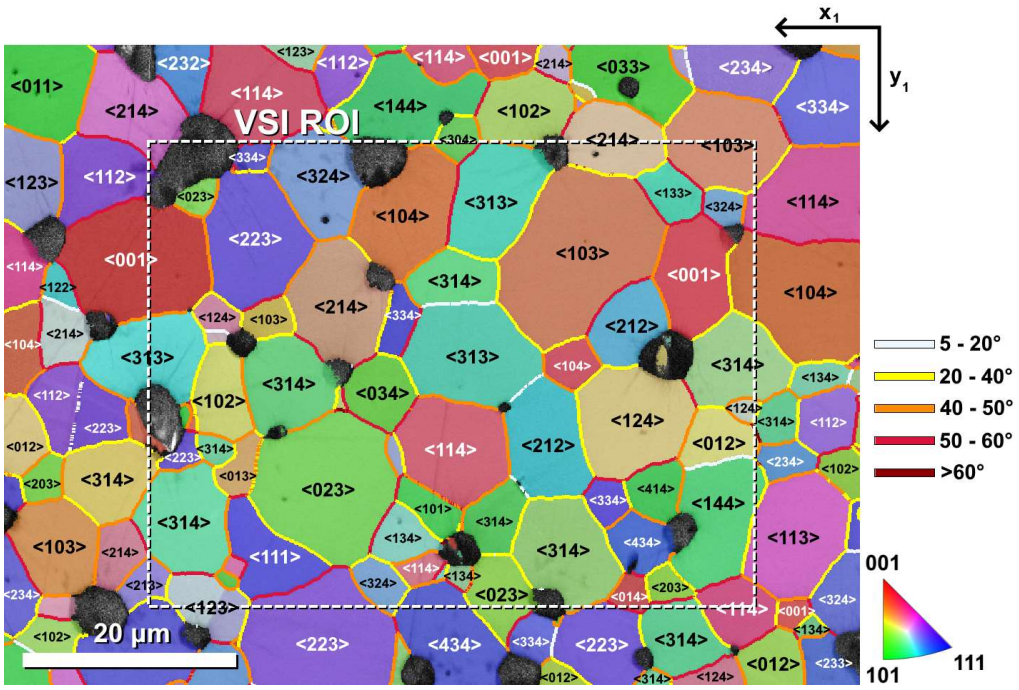

Figure 40: Euler angle colouring EBSD map of x = 0.10 pellet. The dashed white border indicates the region of interest over which surface dissolution was monitored using VSI (Figure 42).

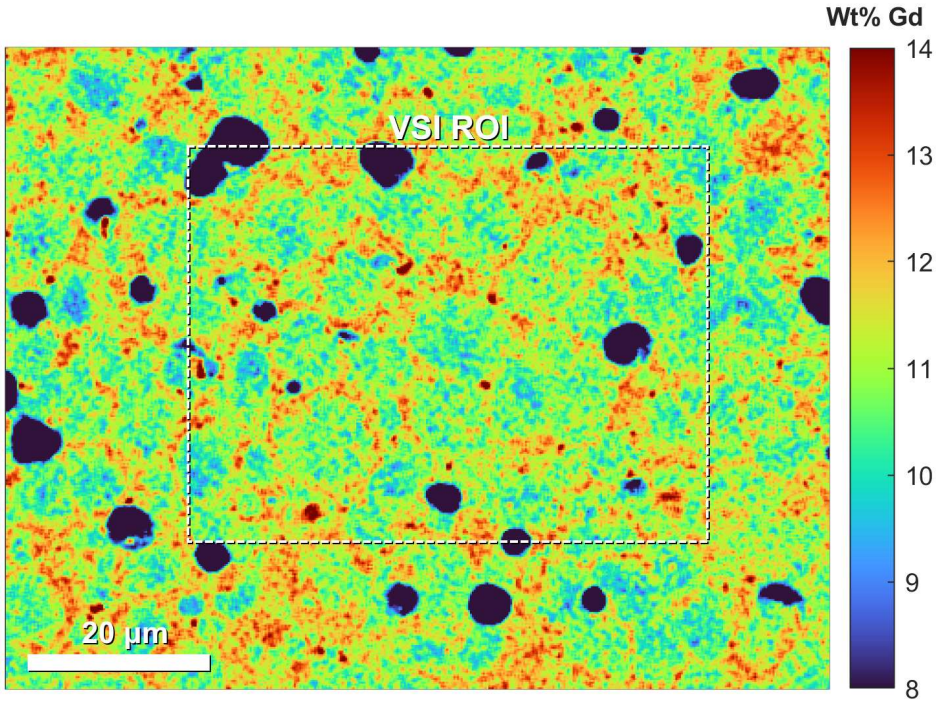

Figure 41: EPMA map of x = 0.10 pellet, revealing spatial distribution of Gd. The dashed white border indicates the region of interest over which surface dissolution was monitored using VSI (Figure 42).

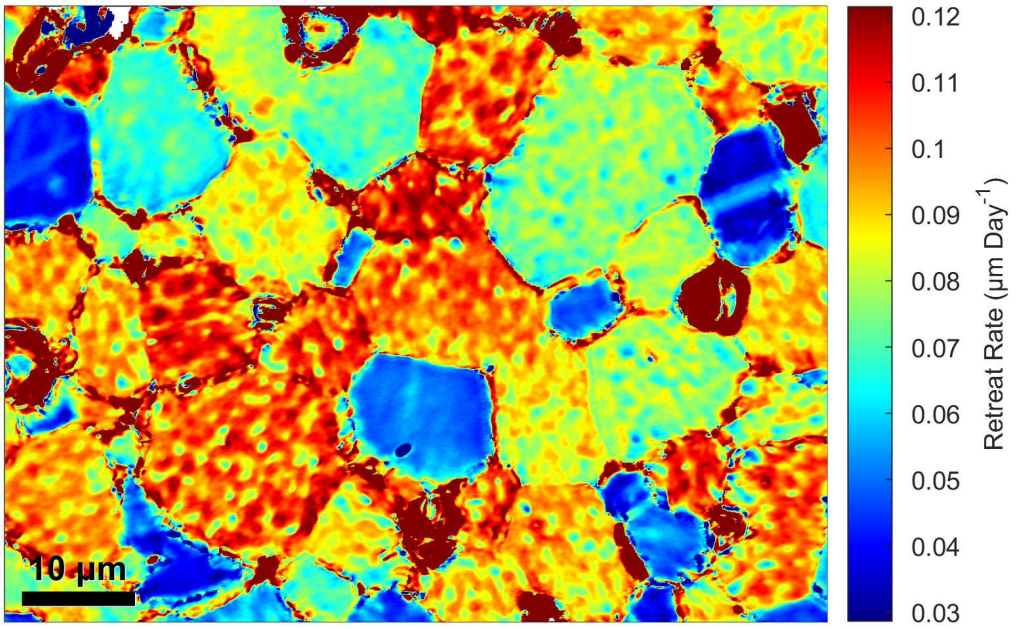

Figure 42: Flux map heterogenous revealing rates of surface retreat in x = 0.10 pellet dissolved in 12 M HCl at 60 °C.

EPMA mapping of the x = 0.10 sample revealed significant enrichment of the grain boundaries with Gd (Figure 41). As with x = 0.00 and 0.05, preferential grain boundary dissolution is apparent, once more no clear relationship was observed between the misorientation angle and retreat rate of specific grain boundaries. Furthermore, no correlation between Gd enrichment and grain boundary retreat rate was noted. However, the confirmation that grain boundaries are both enriched with segregated Gd, and preferentially dissolved provides further insight into the incongruous dissolution of Ce and Gd previously described in the bulk C1308 studies.

4.9.4 Surface Dissolution of $Ce_{0.85}Gd_{0.15}O_{2-\delta}$

Crystallographic orientation appeared to exert strong control over surface dissolution for x = 0.15 (Figure 44). In the absence of a EBSD map (for reasons discussed in Section 4.5) it cannot be stated with complete confidence that the retreat rates corresponded surface energies for exposed crystallographic planes, as was observed with all previous compositions (x = 0.00, 0.05, and 0.10).

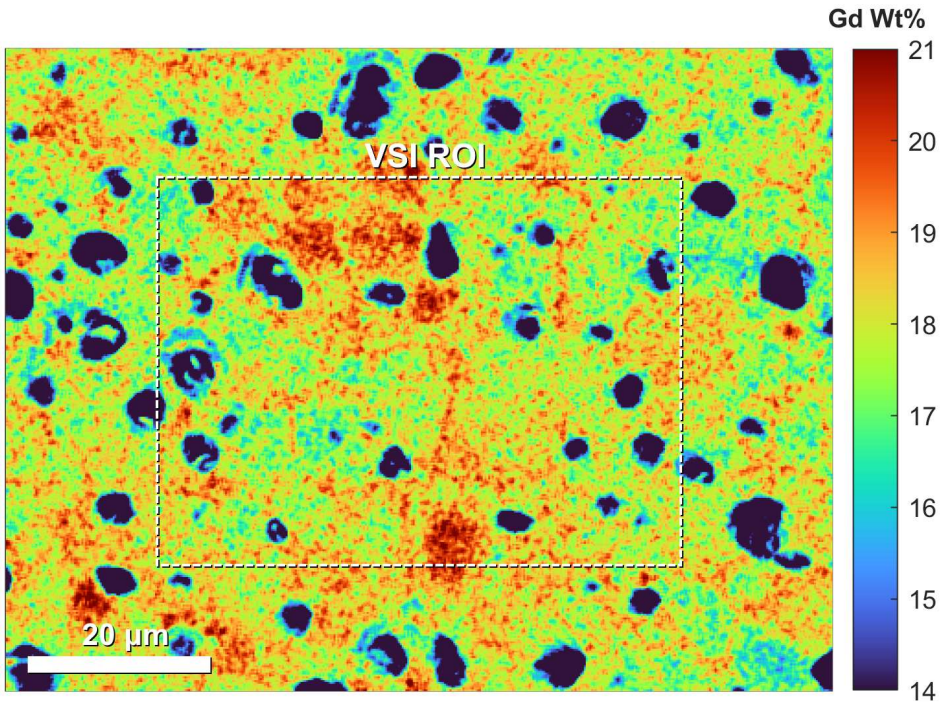

Figure 43: EPMA map of x = 0.15 pellet, revealing spatial distribution of Gd. The dashed white border indicates the region of interest over which surface dissolution was monitored using VSI (Figure 44).

EPMA mapping (Figure 43) revealed some indication of grain boundary enrichment, but the greatest Gd concentrations were measured in within grains. These enriched regions did not appear to be confined to specific grains. Preferential grain boundary dissolution is again observed for x = 0.15.

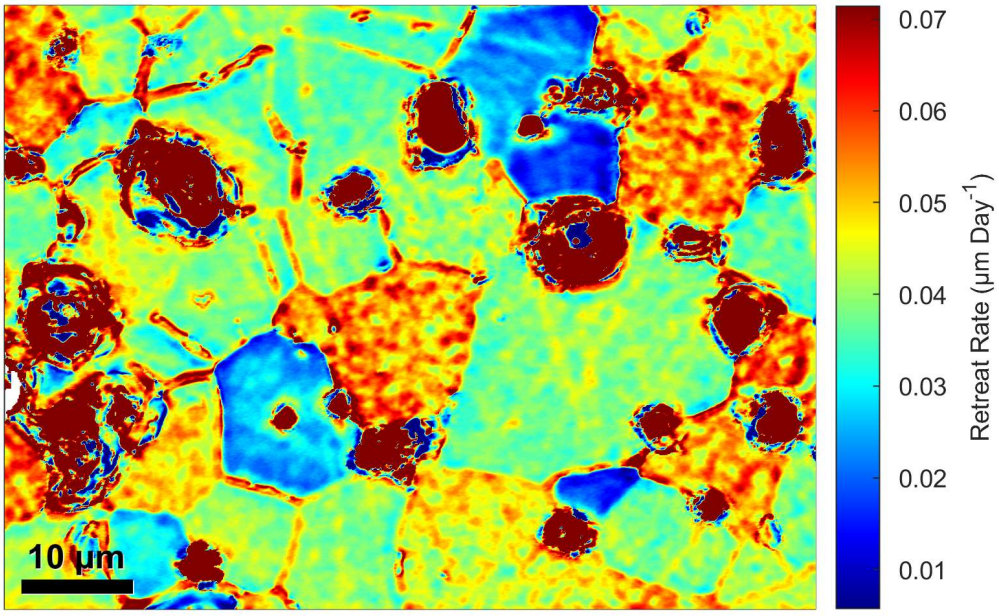

Figure 44: Flux map heterogenous revealing rates of surface retreat in x = 0.15 pellet dissolved in 12 M HCl at 60 °C.

4.9.5 Summary of grain boundary dissolution

Figure 45 presents a scatter plot of retreat rate against grain boundary misorientation, illustrating the lack of correlation observed in samples of all compositions. Corkhill *et al.* measured greater retreat rates in high-angle (60°) grain boundaries compared to lower (30°) boundaries in CeO_2, which was attributed to the higher interfacial energies of high-angle boundaries resulting from the increased concentration of defects housed within them[14]. It is plausible this relationship between misorientation, and retreat can only be measured in the earliest stages dissolution, when subtle differences grain boundary retreat will be more pronounced. If this is the case, grain boundary misorientation could prove to have little influence on long-term durability of CeO_2 and may only exert control on localised rates at the onset of dissolution.

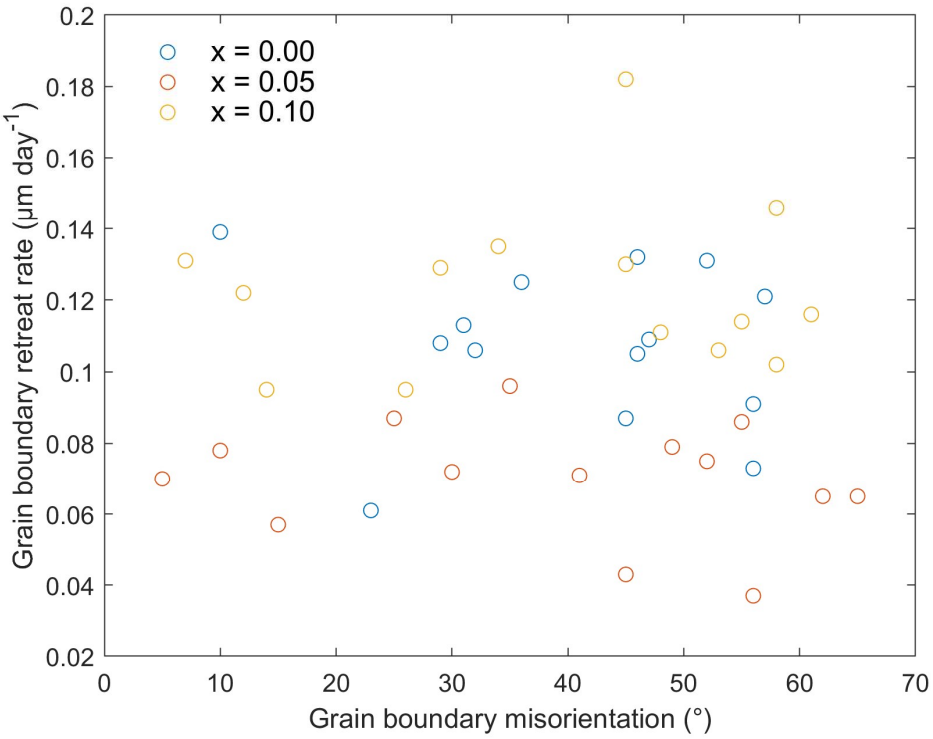

Figure 45: Scatter plot of grain boundary retreated (determined by VSI) against grain boundary misorientation (determined by EBSD) for samples where x = 0.00, 0.05 and 0.10.

5. Summary

Sintered pellets of $Ce_{1-x}Gd_xO_{2-x/2}$, exhibiting similar microstructure to that observed in UO_2, ThO_2 and $(U,Pu)O_2$, were produced *via* the oxalic co-precipitation route. Gd incorporation was found to influence the microstructure, crystal lattice and dissolution behaviour of CeO_2. X-ray diffraction suggested that, for $x < 0.40$, $Ce_{1-x}Gd_xO_{2-x/2}$ adopted the fluorite (Fm-3m) structure in the bulk, whilst Gd additions beyond this threshold induced a widespread transformation to

a cubic C-type (Ia-3) matrix. Where $x < 0.40$, additional reflections corresponding to secondary phases were undetected by XRD, however quantities of Gd-rich secondary phases were observed *via* SEM-EDS in all compositions where $x \geq 0.10$. The volume and quantity of these secondary phases increased with further Gd additions. The incorporation of trivalent Gd^{3+} was found to induce a linearly proportional concentration of V_O defects within the lattice. Potential evidence of C-type nanodomain formation within the fluorite lattice was identified via electron diffraction in compositions where $x \geq 0.05$. Total lattice disorder was found to increase linearly with Gd incorporation. Gd additions exerted strong control over dissolution rates, with the greatest Ce and Gd normalised release measured for $x = 0.15$. Incongruent release of Ce and Gd, observed in all compositions, is suspected to have primarily resulted from preferential dissolution of Gd-rich secondary phases, however, accelerated dissolution of Gd-rich grain boundaries may have contributed to this incongruity. Grain boundary misorientation was found to have no influence on rate of grain boundary dissolution, regardless of composition. Gd distribution within fluorite $Ce_{1-x}Gd_xO_{2-x/2}$ was also found to exert no discernible control over localised dissolution rates. Grain orientation was however found to strongly influence localised dissolution rates, although the incorporation of Gd did not appear to affect the relative surface energies of exposed planes. These findings suggest that the most significant impact of Gd additions on CeO_2 dissolution result from changes to crystal structure. Gd additions do not appear influence the role reactive surface sites play in controlling localised dissolution rates.

Acknowledgements

This research utilised the HADES/MIDAS and PLEIADES national nuclear user facilities at the University of Sheffield, established with financial support from EPSRC and BEIS, under grant numbers EP/T011424/1[63] and EP/V035215/1.

References

1. Bruno, J. & Ewing, R. C. Spent Nuclear Fuel. *Elements* **2**, 343–349 (2006).
2. Buck, E. C., Hanson, B. D. & McNamara, B. K. The geochemical behaviour of Tc, Np and Pu in spent nuclear fuel in an oxidizing environment. *Geol. Soc. Lond. Spec. Publ.* **236**, 65–88 (2004).
3. Liu, N. *et al.* Influence of Gd Doping on the Structure and Electrochemical Behavior of UO_2. *Electrochimica Acta* **247**, 496–504 (2017).
4. Barreiro Fidalgo, A. & Jonsson, M. Radiation induced dissolution of $(U,Gd)O_2$ pellets in aqueous solution – A comparison to standard UO_2 pellets. *J. Nucl. Mater.* **514**, 216–223 (2019).
5. Iwasaki, K. *et al.* Effect of Gd_2O_3 Dispersion on the Thermal Conductivity of UO_2. *J. Nucl. Sci. Technol.* **46**, 673–676 (2009).
6. Kang, J., von Hippel, F. N., MacFarlane, A. & Nelson, R. Storage MOX: A Third Way for Plutonium Disposal? *Sci. Glob. Secur.* **10**, 85–101 (2002).
7. Macfarlane, A. M. Another option for separated plutonium management: Storage MOX. *Prog. Nucl. Energy* **49**, 644–650 (2007).
8. Godinho, J. R. A., Piazolo, S., Stennett, M. C. & Hyatt, N. C. Sintering of CaF_2 pellets as nuclear fuel analog for surface stability experiments. *J. Nucl. Mater.* **419**, 46–51 (2011).
9. Stennett, M. C., Corkhill, C. L., Marshall, L. A. & Hyatt, N. C. Preparation, characterisation and dissolution of a CeO_2 analogue for UO_2 nuclear fuel. *J. Nucl. Mater.* **432**, 182–188 (2013).
10. Shannon, R. D. Revised effective ionic radii and systematic studies of interatomic distances in halides and chalcogenides. *Acta Crystallogr. Sect. A* **32**, 751–767 (1976).

11. Hussain, S. & Yangping, L. Review of solid oxide fuel cell materials: cathode, anode, and electrolyte. *Energy Transit.* **4**, 113–126 (2020).
12. Godinho, J. R. A., Putnis, C. V. & Piazolo, S. Direct Observations of the Dissolution of Fluorite Surfaces with Different Orientations. *Cryst. Growth Des.* **14**, 69–77 (2014).
13. Godinho, J. R. A., Piazolo, S. & Evins, L. Z. Effect of surface orientation on dissolution rates and topography of CaF_2. *Geochim. Cosmochim. Acta* **86**, 392–403 (2012).
14. Corkhill, C. L. *et al.* Contribution of Energetically Reactive Surface Features to the Dissolution of CeO_2 and ThO_2 Analogues for Spent Nuclear Fuel Microstructures. *ACS Appl. Mater. Interfaces* **6**, 12279–12289 (2014).
15. Legland, D., Arganda-Carreras, I. & Andrey, P. MorphoLibJ: integrated library and plugins for mathematical morphology with ImageJ. *Bioinformatics* btw413 (2016) doi:10.1093/bioinformatics/btw413.
16. Schindelin, J. *et al.* Fiji: an open-source platform for biological-image analysis. *Nat. Methods* **9**, 676–682 (2012).
17. Savitzky, Abraham. & Golay, M. J. E. Smoothing and Differentiation of Data by Simplified Least Squares Procedures. *Anal. Chem.* **36**, 1627–1639 (1964).
18. C26 Committee. *Test Method for Accelerated Leach Test for Diffusive Releases from Solidified Waste and a Computer Program to Model Diffusive, Fractional Leaching from Cylindrical Waste Forms*. http://www.astm.org/cgi-bin/resolver.cgi?C1308-08R17 doi:10.1520/C1308-08R17.
19. Gaboriaud, R. J., Paumier, F. & Lacroix, B. Disorder–order phase transformation in a fluorite-related oxide thin film: In-situ X-ray diffraction and modelling of the residual stress effects. *Thin Solid Films* **601**, 84–88 (2016).
20. Levin, I. NIST Inorganic Crystal Structure Database (ICSD). (2020) doi:10.18434/M32147.
21. Ye, F., Ou, D. R. & Mori, T. Microstructural Evolution in a CeO_2 -Gd_2O_3 System. *Microsc. Microanal.* **18**, 162–170 (2012).

22. Wang, B., Lewis, R. J. & Cormack, A. N. Computer simulations of large-scale defect clustering and nanodomain structure in gadolinia-doped ceria. *Acta Mater.* **59**, 2035–2045 (2011).

23. Horlait, D. *et al.* Stability and Structural Evolution of $Ce^{IV}_{1-x}Ln^{III}_{x}O_{2-x/2}$ Solid Solutions: A Coupled μ-Raman/XRD Approach. *Inorg. Chem.* **50**, 7150–7161 (2011).

24. Grover, V. & Tyagi, A. K. Phase relations, lattice thermal expansion in CeO_2–Gd_2O_3 system, and stabilization of cubic gadolinia. *Mater. Res. Bull.* **39**, 859–866 (2004).

25. Grover, V. & Tyagi, A. K. Investigations of Ternary Phase Relations in a CeO_2 –Gd_2O_3 – ThO_2 System. *J. Am. Ceram. Soc.* **89**, 2917–2921 (2006).

26. Artini, C., Costa, G. A., Pani, M., Lausi, A. & Plaisier, J. Structural characterization of the CeO_2/Gd_2O_3 mixed system by synchrotron X-ray diffraction. *J. Solid State Chem.* **190**, 24–28 (2012).

27. Tianshu, Z., Hing, P., Huang, H. & Kilner, J. Ionic conductivity in the CeO_2–Gd_2O_3 system (0.05VGd/CeV0.4) prepared by oxalate coprecipitation. *Solid State Ion.* 7 (2002).

28. Le Luyer, C., García-Murillo, A., Bernstein, E. & Mugnier, J. Waveguide Raman spectroscopy of sol-gel Gd_2O_3 thin films: Sol-gel Gd_2O_3 thin films. *J. Raman Spectrosc.* **34**, 234–239 (2003).

29. Lucuta, P. G., Verrall, R. A., Matzke, Hj. & Palmer, B. J. Microstructural features of SIMFUEL — Simulated high-burnup UO_2-based nuclear fuel. *J. Nucl. Mater.* **178**, 48–60 (1991).

30. Yasuda, K., Uemura, K. & Shiota, T. Sintering and mechanical properties of gadolinium-doped ceria ceramics. *J. Phys. Conf. Ser.* **339**, 012006 (2012).

31. Arabacı, A. & Öksüzömer, M. F. Preparation and characterization of 10 mol% Gd doped CeO_2 (GDC) electrolyte for SOFC applications. *Ceram. Int.* **38**, 6509–6515 (2012).

32. Li, Z.-P., Mori, T., Auchterlonie, G. J., Zou, J. & Drennan, J. Direct evidence of dopant segregation in Gd-doped ceria. *Appl. Phys. Lett.* **98**, 093104 (2011).

33. Van Mao, P., Arima, T., Inagaki, Y. & Idemitsu, K. Evaluation of Structural and Thermal Properties of $Ce_{1-y}Gd_yO_{2-x}$ Solid Solution. *Int. J. Thermophys.* **41**, 111 (2020).

34. Jadhav, L. D., Pawar, S. H. & Chourashiya, M. G. Effect of sintering temperature on structural and electrical properties of gadolinium doped ceria ($Ce_{0.9}Gd_{0.1}O_{1.95}$). *Bull. Mater. Sci.* **30**, 97–100 (2007).
35. Horlait, D. *et al.* Environmental SEM monitoring of $Ce_{1-x}Ln_xO_{2-x/2}$ mixed-oxide microstructural evolution during dissolution. *J Mater Chem A* **2**, 5193–5203 (2014).
36. Arora, G. & Aidhy, D. S. Segregation and binding energetics at grain boundaries in fluorite oxides. *J. Mater. Chem. A* **5**, 4026–4035 (2017).
37. Scavini, M. *et al.* Percolating hierarchical defect structures drive phase transformation in $Ce_{1-x}Gd_xO_{2-x/2}$: a total scattering study. *IUCrJ* **2**, 511–522 (2015).
38. Žguns, P. A., Ruban, A. V. & Skorodumova, N. V. Phase diagram and oxygen–vacancy ordering in the CeO_2 – Gd_2O_3 system: a theoretical study. *Phys. Chem. Chem. Phys.* **20**, 11805–11818 (2018).
39. Durazzo, M., Oliveira, F. B. V., Urano de Carvalho, E. F. & Riella, H. G. Phase studies in the UO_2–Gd_2O_3 system. *J. Nucl. Mater.* **400**, 183–188 (2010).
40. Leyva, A. G., Vega, D., Trimarco, V. & Marchi, D. Homogeneity characterisation of sintered $(U,Gd)_{O2}$ pellets by X-ray diffraction. *J. Nucl. Mater.* **303**, 29–33 (2002).
41. Oudinet, G. *et al.* Characterization of plutonium distribution in MIMAS MOX by image analysis. *J. Nucl. Mater.* **375**, 86–94 (2008).
42. Hong, M. *et al.* The role of charge and ionic radius on fission product segregation to a model UO_2 grain boundary. *J. Appl. Phys.* **113**, 134902 (2013).
43. Chen, P.-L. & Chen, I.-W. Grain Growth in CeO_2: Dopant Effects, Defect Mechanism, and Solute Drag. *J. Am. Ceram. Soc.* **79**, 1793–1800 (1996).
44. Bellière, V., Joorst, G., Stephan, O., de Groot, F. M. F. & Weckhuysen, B. M. Phase Segregation in Cerium−Lanthanum Solid Solutions. *J. Phys. Chem. B* **110**, 9984–9990 (2006).
45. Chourashiya, M. G., Patil, J. Y., Pawar, S. H. & Jadhav, L. D. Studies on structural, morphological and electrical properties of $Ce_{1-x}Gd_xO_{2-(x/2)}$. *Mater. Chem. Phys.* **109**, 39–44 (2008).

46. Ahmad, S. I., Koteshwar Rao, P. & Syed, I. A. Sintering temperature effect on density, structural and morphological properties of Mg- and Sr-doped ceria. *J. Taibah Univ. Sci.* **10**, 381–385 (2016).
47. Ye, F. *et al.* Compositional and structural characteristics of nano-sized domains in gadolinium-doped ceria. *Solid State Ion.* **179**, 827–831 (2008).
48. Ou, D. R. *et al.* Oxygen-vacancy ordering in lanthanide-doped ceria: Dopant-type dependence and structure model. *Phys. Rev. B* **77**, 024108 (2008).
49. Ou, D. R. *et al.* Oxygen vacancy ordering in heavily rare-earth-doped ceria. *Appl. Phys. Lett.* **89**, 171911 (2006).
50. Ou, D. R. *et al.* Microstructures and electrolytic properties of yttrium-doped ceria electrolytes: Dopant concentration and grain size dependences. *Acta Mater.* **54**, 3737–3746 (2006).
51. Nakajima, A., Yoshihara, A. & Ishigame, M. Defect-induced Raman spectra in doped CeO_2. *Phys. Rev. B* **50**, 13297–13307 (1994).
52. Li, L., Chen, F., Lu, J.-Q. & Luo, M.-F. Study of Defect Sites in $Ce_{1-x}M_xO_{2-\delta}$ (x = 0.2) Solid Solutions Using Raman Spectroscopy. *J. Phys. Chem. A* **115**, 7972–7977 (2011).
53. Loridant, S. Raman spectroscopy as a powerful tool to characterize ceria-based catalysts. *Catal. Today* **373**, 98–111 (2021).
54. Fang, P. *et al.* Effect of phase structure on electrical conductivity of $Ce_xGd_{1-x}O_{2-\delta}$ solid electrolytes. *Mater. Sci. Eng. B* **164**, 101–105 (2009).
55. Pikalova, E. Yu. *et al.* CeO2 based materials doped with lanthanides for applications in intermediate temperature electrochemical devices. *Int. J. Hydrog. Energy* **36**, 6175–6183 (2011).
56. Kainbayev, N. *et al.* Raman Study of Nanocrystalline-Doped Ceria Oxide Thin Films. *Coatings* **10**, 432 (2020).
57. Lee, W., Chen, S.-Y., Tseng, E., Gloter, A. & Chen, C.-L. Study of Defect Structure in Ferromagnetic Nanocrystalline CeO_2: Effect of Ionic Radius. *J. Phys. Chem. C* **120**, 14874–14882 (2016).

58. Aškrabić, S., Dohčević-Mitrović, Z. D., Radović, M., Šćepanović, M. & Popović, Z. V. Phonon-phonon interactions in $Ce_{0.85}Gd_{0.15}O_{2-\delta}$ nanocrystals studied by Raman spectroscopy. *J. Raman Spectrosc.* **40**, 650–655 (2009).
59. Horlait, D., Clavier, N., Dacheux, N., Cavalier, R. & Podor, R. Synthesis and characterization of $Th_{1-x}Ln_xO_{2-x/2}$ mixed-oxides. *Mater. Res. Bull.* **47**, 4017–4025 (2012).
60. Yan, M. F., Cannon, R. M. & Bowen, H. K. Space charge, elastic field, and dipole contributions to equilibrium solute segregation at interfaces. *J. Appl. Phys.* **54**, 764–778 (1983).
61. Feng, B. *et al.* Atomically ordered solute segregation behaviour in an oxide grain boundary. *Nat. Commun.* **7**, 11079 (2016).
62. Horlait, D., Clavier, N., Szenknect, S., Dacheux, N. & Dubois, V. Dissolution of Cerium(IV)–Lanthanide(III) Oxides: Comparative Effect of Chemical Composition, Temperature, and Acidity. *Inorg. Chem.* **51**, 3868–3878 (2012).
63. Hyatt, N. C. *et al.* The HADES Facility for High Activity Decommissioning Engineering & Science: part of the UK National Nuclear User Facility. *IOP Conf. Ser. Mater. Sci. Eng.* **818**, 012022 (2020).

Supplementary information

Table S1: Comprehensive details of crystals and peaks selected for EPMA.

Element	Channel	Crystal	Peak Pos. (mm)	Peak	Order
Ce	1	PETJ	81.549	La	1
Si	2	PETL	228.173	Ka	1
Gd	3	LIFH	128.537	Lb	1
O	1	LDE1	109.973	Ka	1
Al	4	TAPH	90.851	Ka	1

Table S2: Summary of Raman deconvolutions.

Composition	T_{2g} Pos. (cm^{-1})	T_{2g} FWHM (cm^{-1})	D_1 Pos. (cm^{-1})	D_1 Rel. Intensity (cm^{-1})	D_2 Pos. (cm^{-1})	D_2 Rel. Intensity (cm^{-1})	X^2
CeO_2	465.060±0.015	7.667±0.042	—	—	—	—	8.876E-03
$Ce_{0.95}Gd_{0.05}O_{2-\delta}$	464.317±0.034	15.950±0.097	543.406±0.728	0.0228±0.0002	601.988±1.242	0.0132±0.0005	6.670E-05
$Ce_{0.90}Gd_{0.10}O_{2-\delta}$	464.199±0.091	22.810±0.260	545.094±0.371	0.0354±0.0011	595.812±1.257	0.0274±0.0003	1.390E-04
$Ce_{0.85}Gd_{0.15}O_{2-\delta}$	465.699±0.114	30.529±0.413	555.798±0.335	0.0796±0.0006	600.991±0.540	0.0504±0.0006	4.380E-04

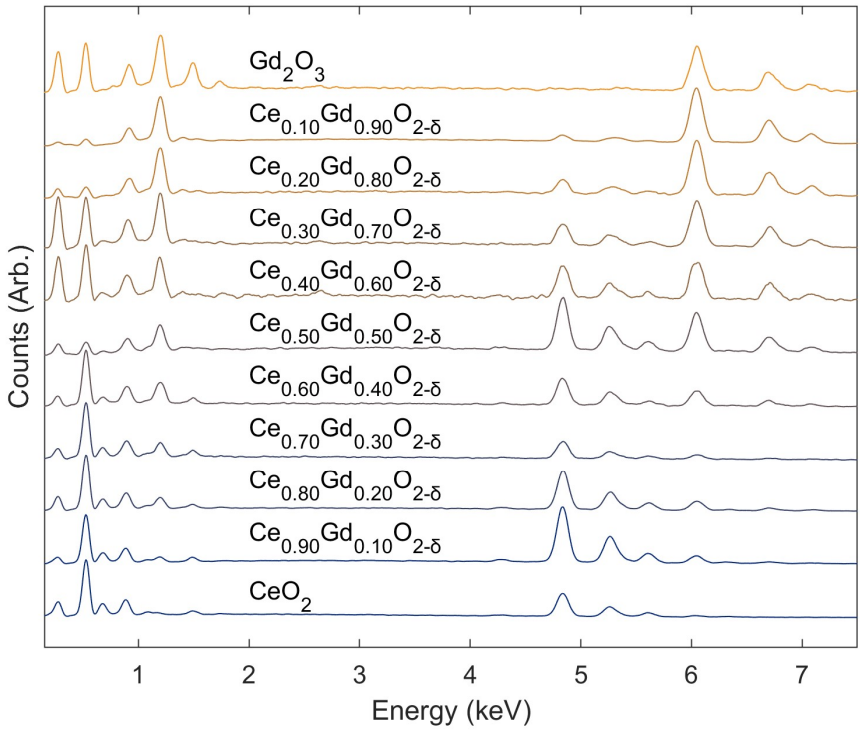

Figure S1: EDS spectra collected on sintered pellets of $Ce_{1-x}Gd_xO_{2-x/2}$

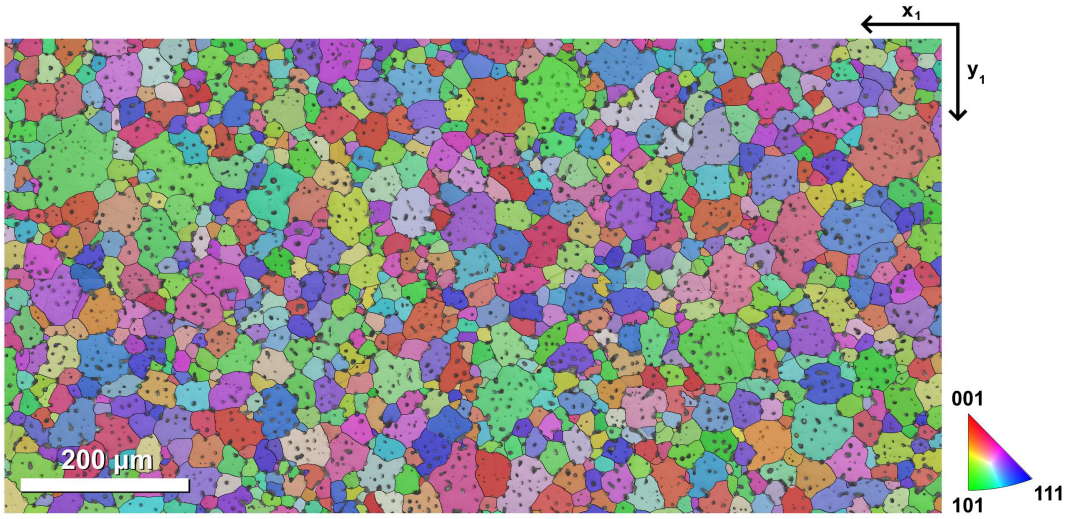

Figure S2a: Montaged EBSD map collected on CeO_2.

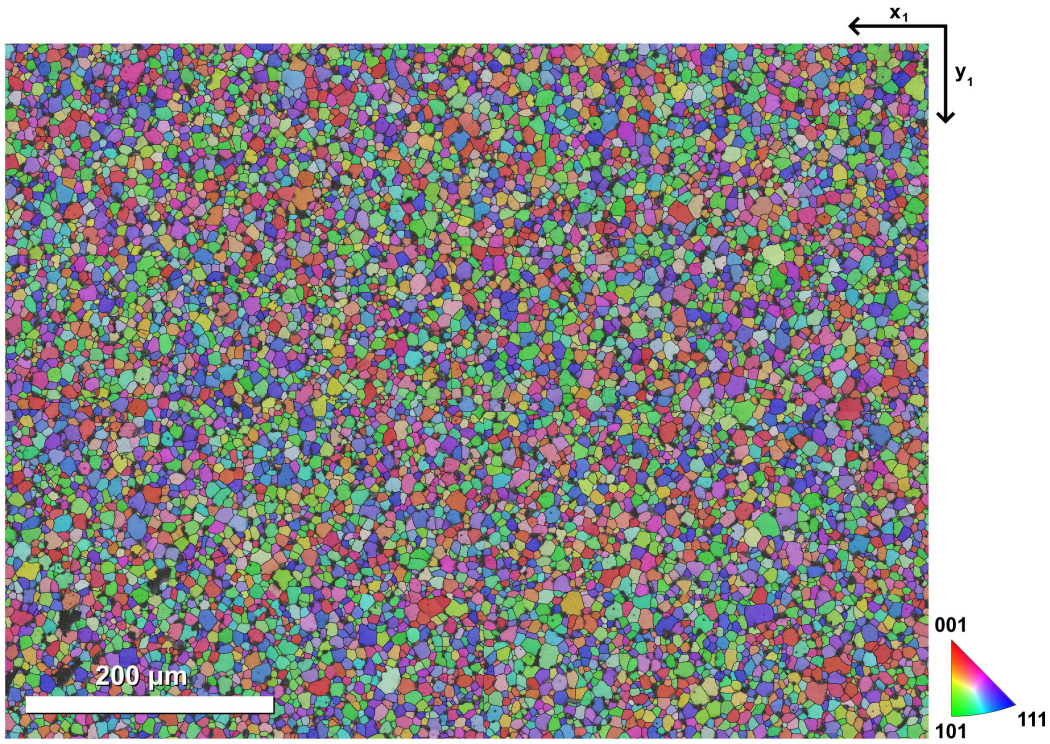

Figure S2b: Montaged EBSD map collected on $Ce_{0.95}Gd_{0.05}O_{2-\delta}$.

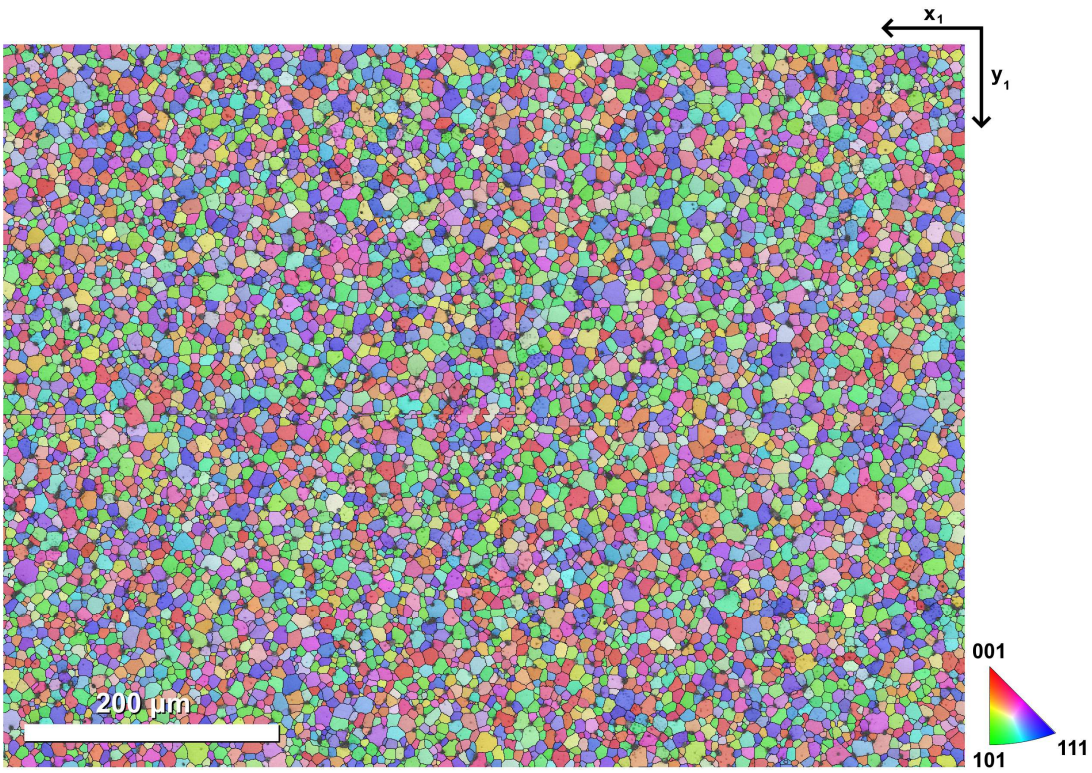

Figure S2c: Montaged EBSD map collected on $Ce_{0.90}Gd_{0.10}O_{2-\delta}$.

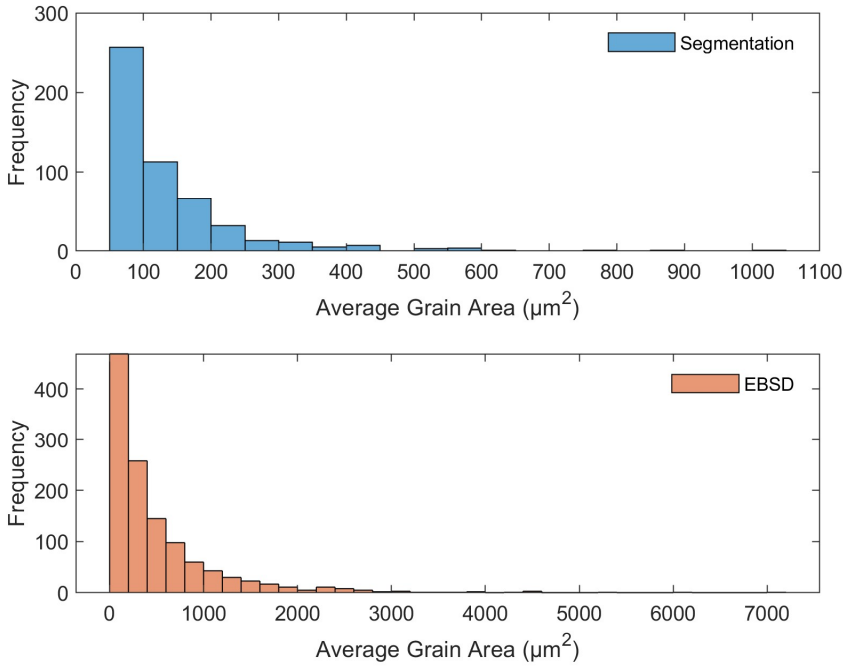

Figure 3a: Histograms of grain areas in x = 0.00 pellets measured through segmentation of SEM image analysis (segmentation) and EBSD analysis.

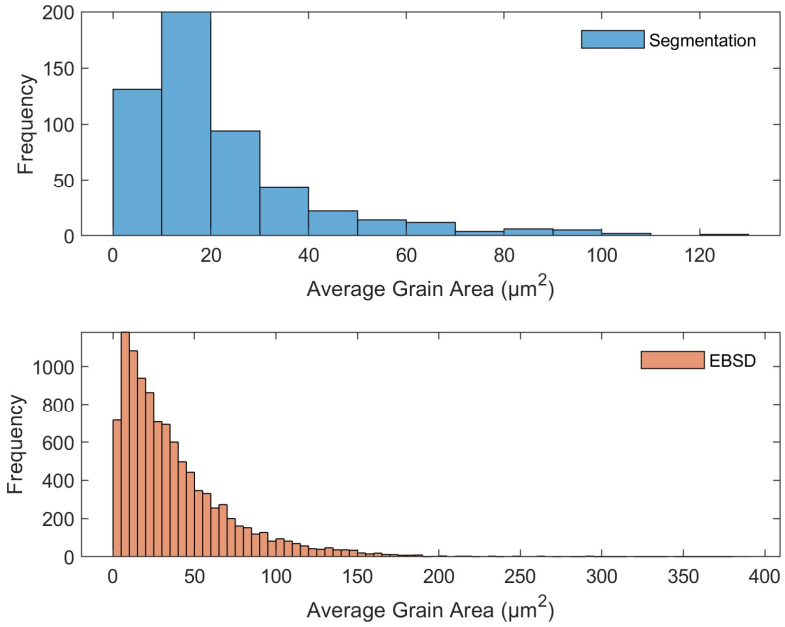

Figure 3b: Histograms of grain areas in x = 0.05 pellets measured through segmentation of SEM image analysis (segmentation) and EBSD analysis.

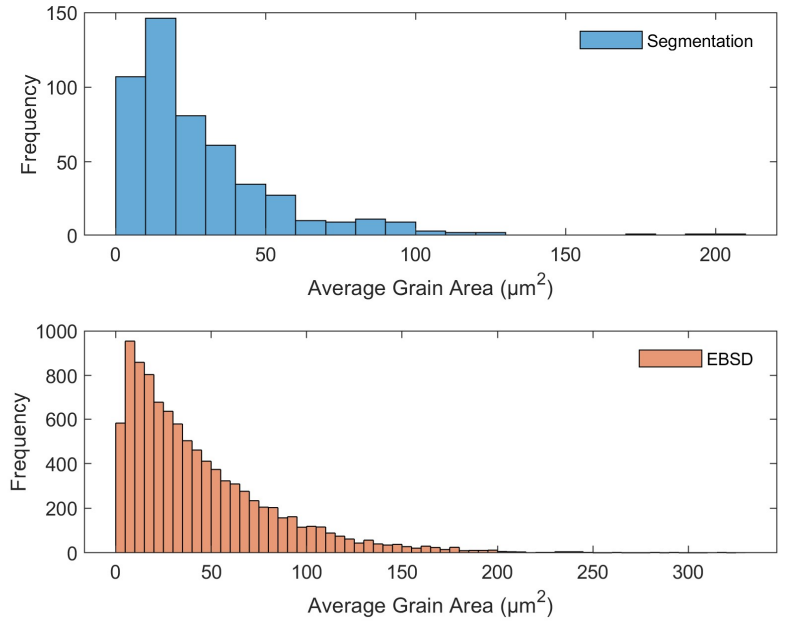

Figure 3c: Histograms of grain areas in x = 0.10 pellets measured through segmentation of SEM image analysis (segmentation) and EBSD analysis.

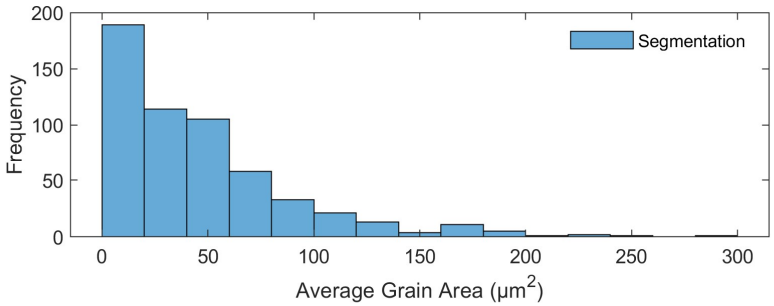

Figure 3d: Histogram of grain areas in x = 0.15 pellets measured through segmentation of SEM image analysis (segmentation).

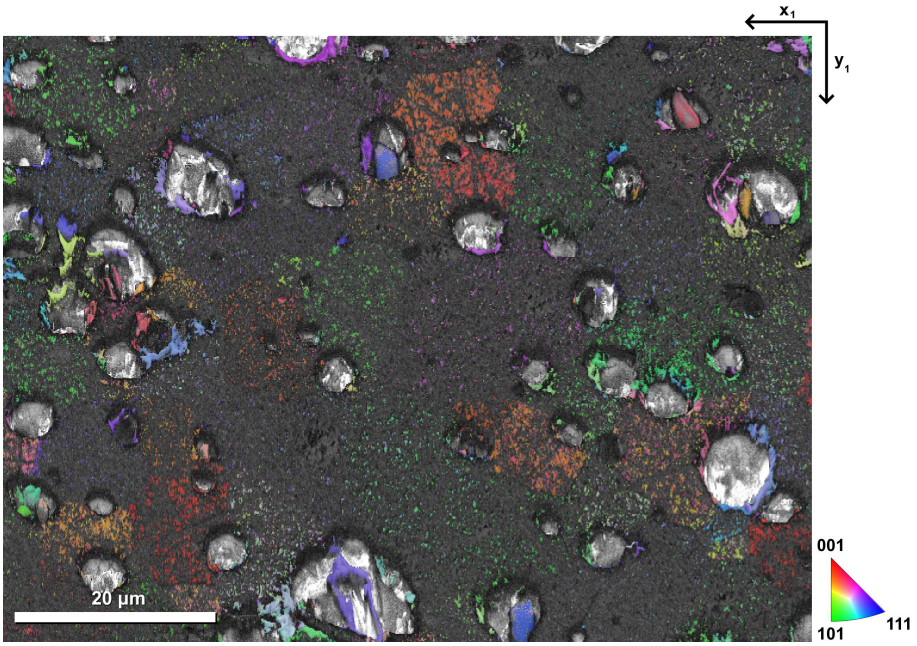

Figure S4a: EBSD map of x = 0.15, poor (< 10%) indexing rates potentially resulted from contributions from C-type nanodomains.

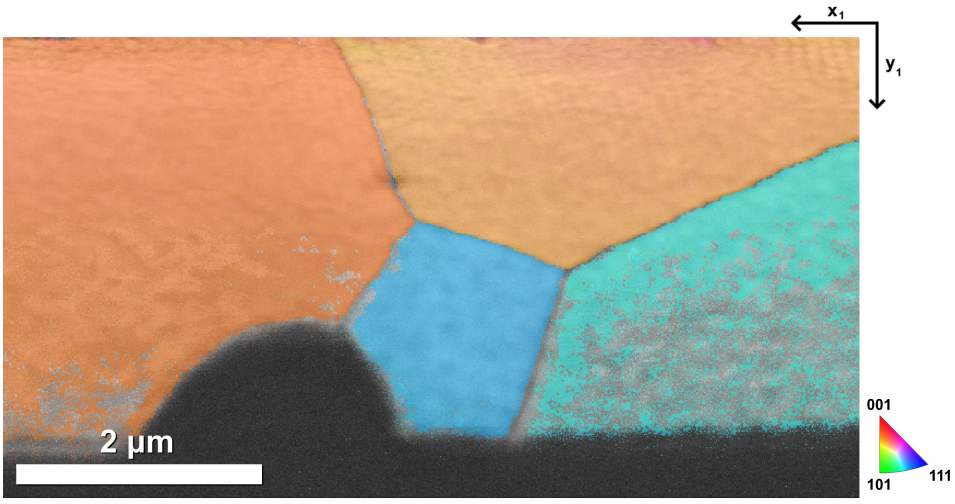

Figure S4b: t-EBSD map of x = 0.15, vastly improved indexing rates result from reduced interaction volume, enabling detector to result fluorite structure with fewer contributions from C-type nanodomains.

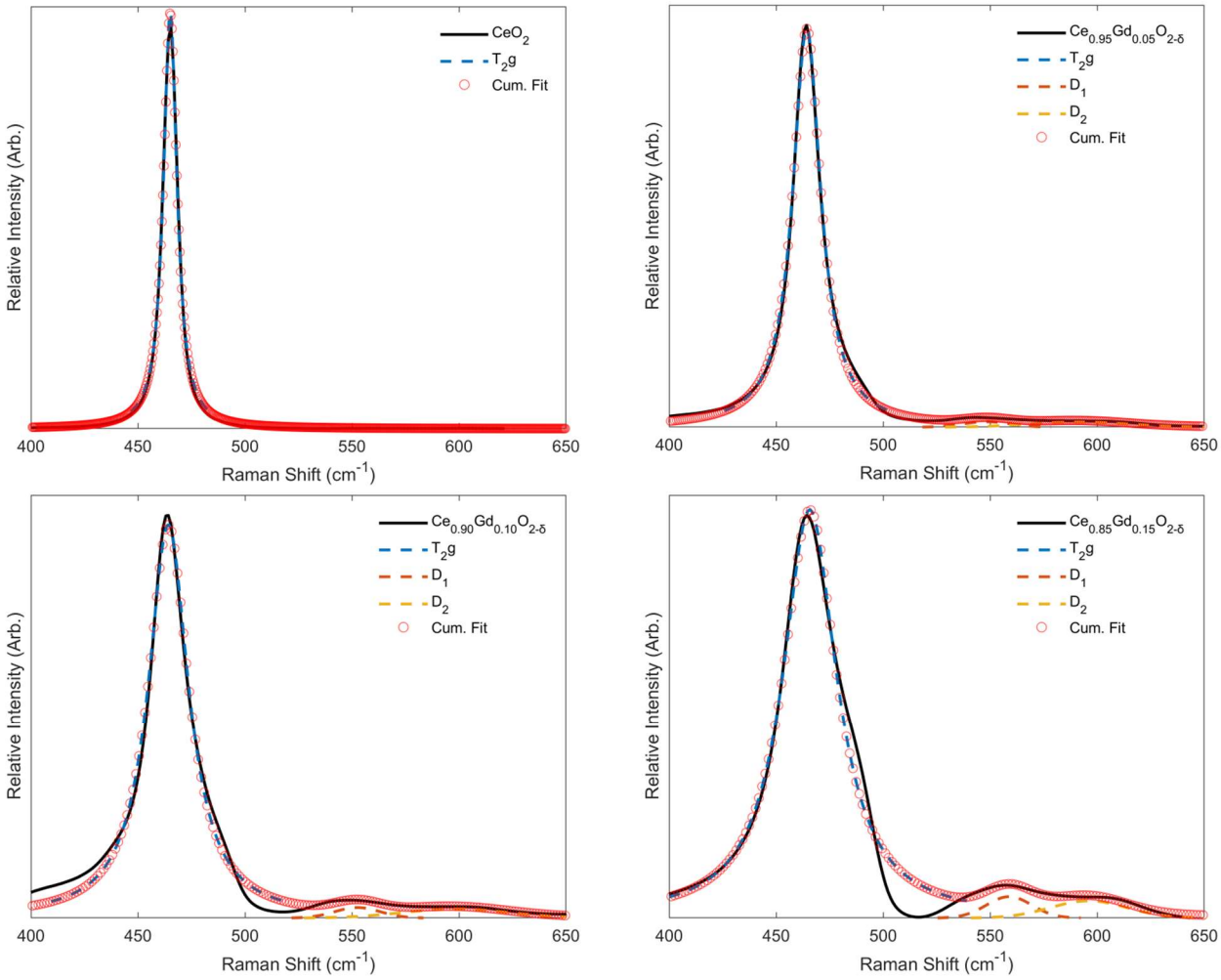

Figure S5: Individual fits for Raman spectra collected on x = 0.00 (a), x = 0.05 (b), x = 0.10 (c), and x = 0.15 (d).

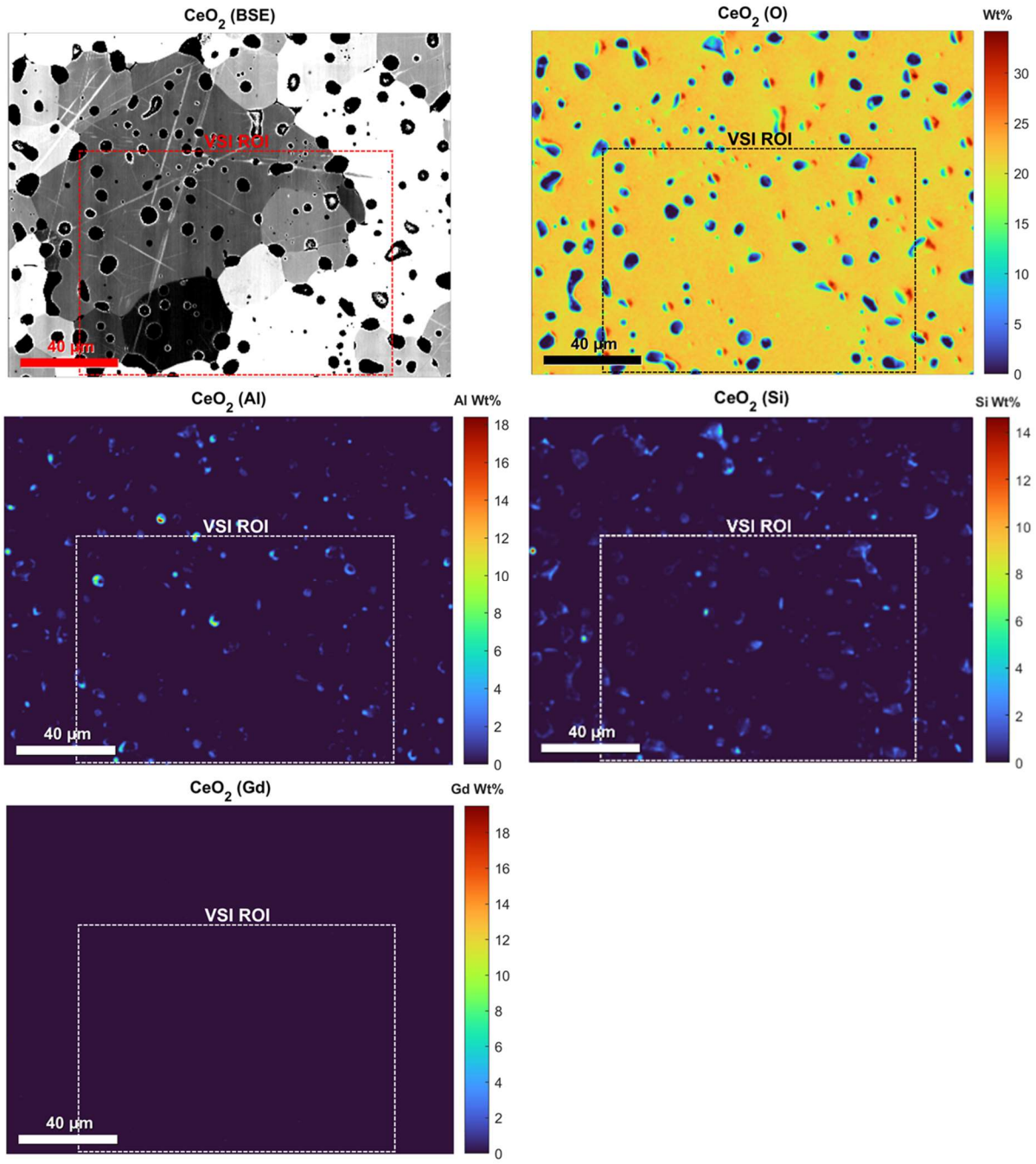

Figure S6a: EPMA maps collected on x = 0.00 not presented in Section 4.7. Al and Si residing in pores resulted from suspension that could not be removed following polishing.

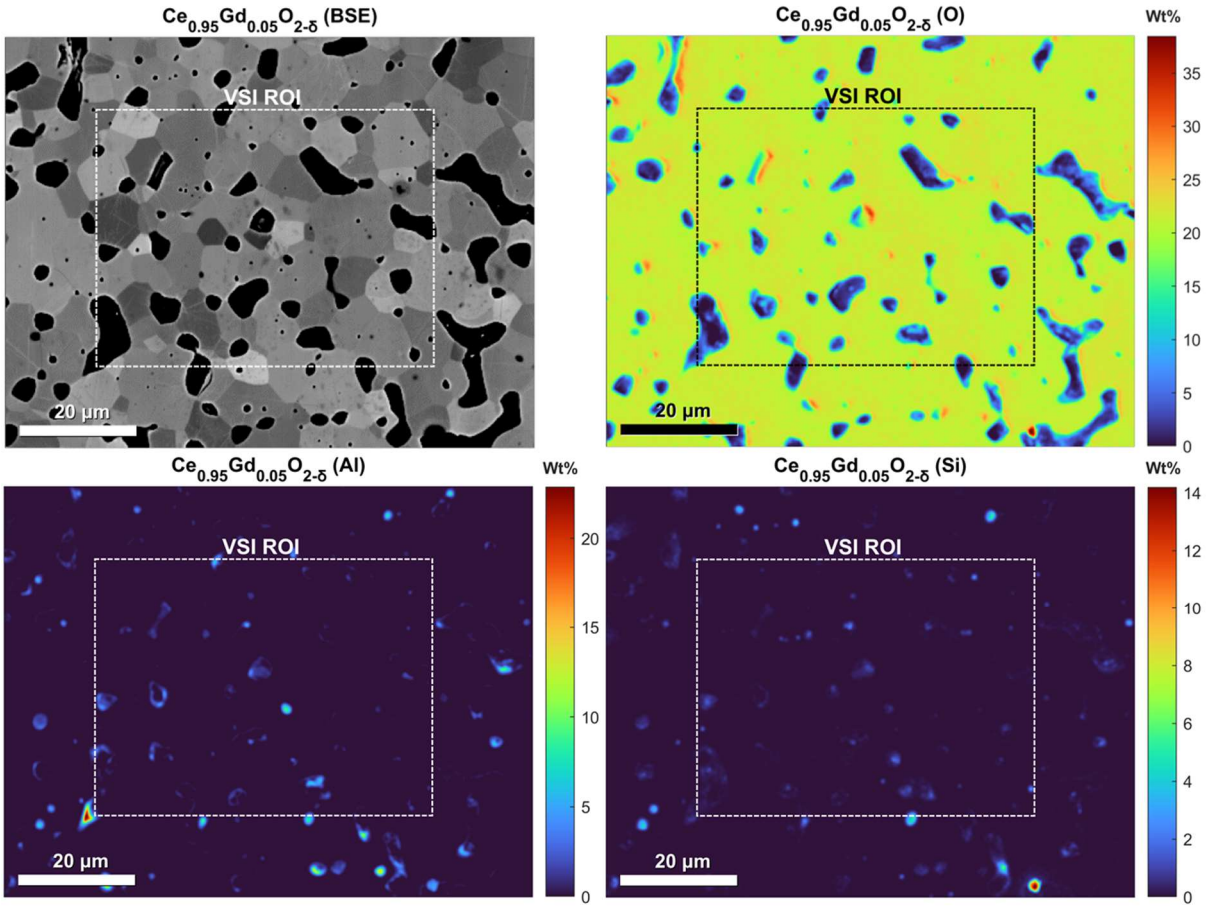

Figure S6b: EPMA maps collected on x = 0.05 not presented in Section 4.7. Al and Si residing in pores resulted from suspension that could not be removed following polishing.

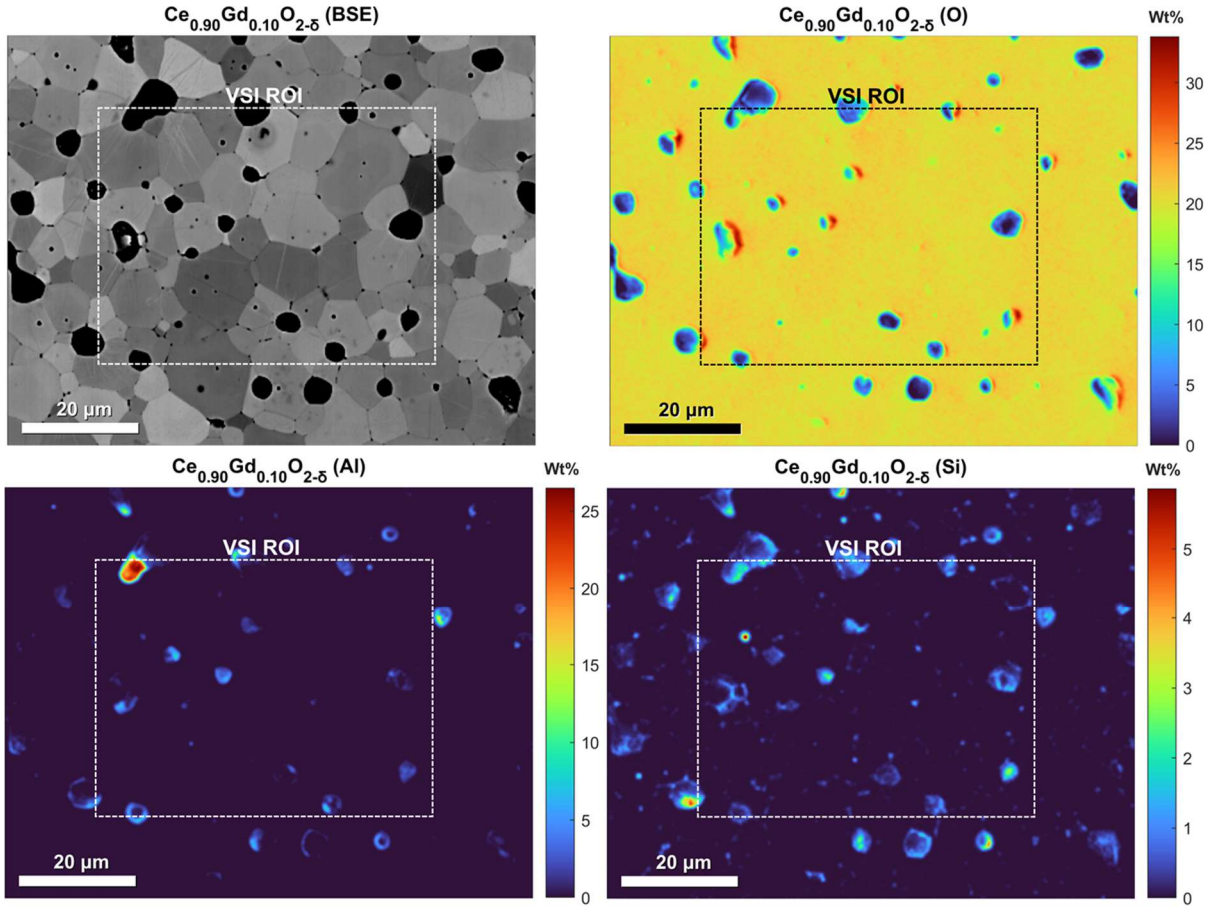

Figure S6c: EPMA maps collected on x = 0.10 not presented in Section 4.7. Al and Si residing in pores resulted from suspension that could not be removed following polishing.

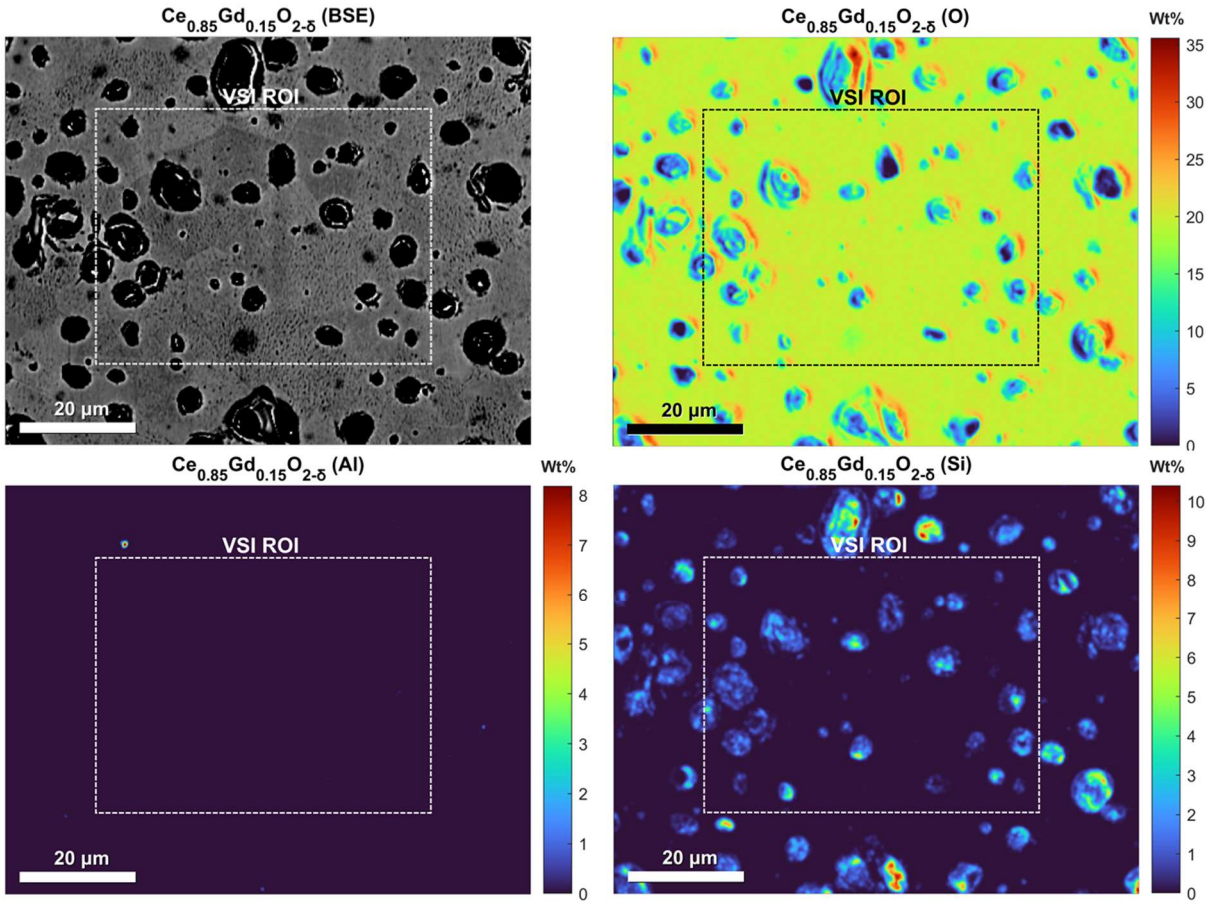

Figure S6d: EPMA maps collected on x = 0.15 not presented in Section 4.7. Al and Si residing in pores resulted from suspension that could not be removed following polishing.

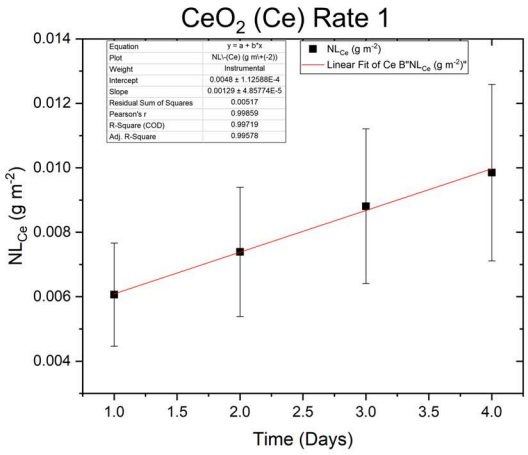
CeO2 (Ce) Rate 1
Equation y = a + b*x
Plot NLi-(Ce) (g m\+(-2))
Weight Instrumental
Intercept 0.0048 ± 1.12588E-4
Slope 0.00129 ± 4.85774E-5
Residual Sum of Squares 0.00517
Pearson's r 0.99859
R-Square (COD) 0.99719
Adj. R-Square 0.99578
NLCe (g m-2)
Linear Fit of Ce B"NLCe (g m-2)"
NLCe (g m-2)
Time (Days)

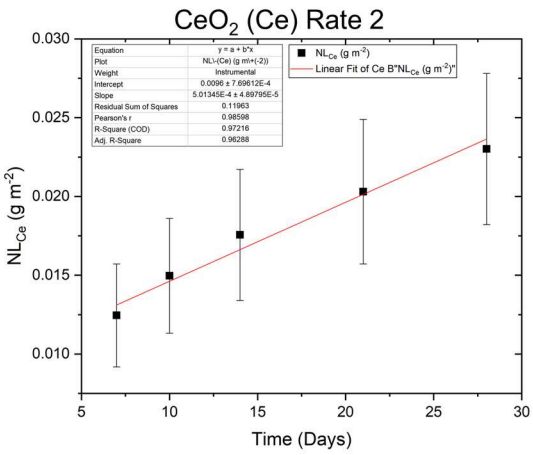
CeO2 (Ce) Rate 2
Equation y = a + b*x
Plot NLi-(Ce) (g m\+(-2))
Weight Instrumental
Intercept 0.0096 ± 7.69612E-4
Slope 5.01345E-4 ± 4.89795E-5
Residual Sum of Squares 0.11963
Pearson's r 0.98598
R-Square (COD) 0.97216
Adj. R-Square 0.96288
NLCe (g m-2)
Linear Fit of Ce B"NLCe (g m-2)"
NLCe (g m-2)
Time (Days)

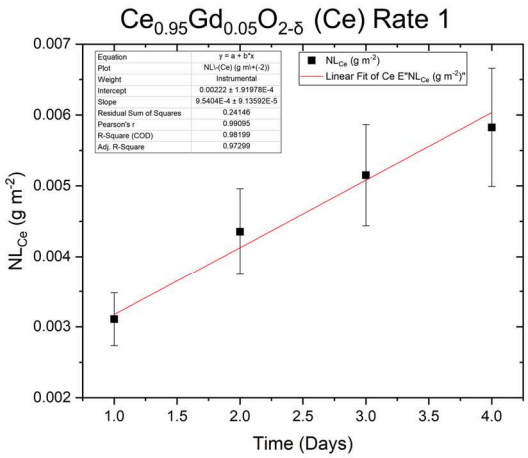
Ce0.95Gd0.05O2-δ (Ce) Rate 1
Equation y = a + b*x
Plot NLi-(Ce) (g m\+(-2))
Weight Instrumental
Intercept 0.00222 ± 1.91978E-4
Slope 9.5404E-4 ± 9.13592E-5
Residual Sum of Squares 0.24146
Pearson's r 0.99095
R-Square (COD) 0.98199
Adj. R-Square 0.97299
NLCe (g m-2)
Linear Fit of Ce E"NLCe (g m-2)"
NLCe (g m-2)
Time (Days)

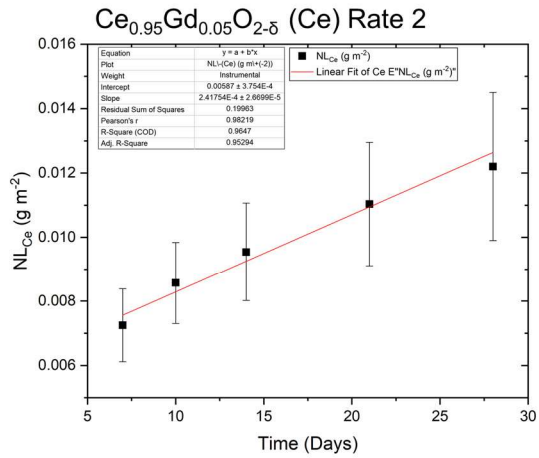
Ce0.95Gd0.05O2-δ (Ce) Rate 2
Equation y = a + b*x
Plot NLi-(Ce) (g m\+(-2))
Weight Instrumental
Intercept 0.00587 ± 3.754E-4
Slope 2.41754E-4 ± 2.8699E-5
Residual Sum of Squares 0.19963
Pearson's r 0.98219
R-Square (COD) 0.9647
Adj. R-Square 0.95294
NLCe (g m-2)
Linear Fit of Ce E"NLCe (g m-2)"
NLCe (g m-2)
Time (Days)

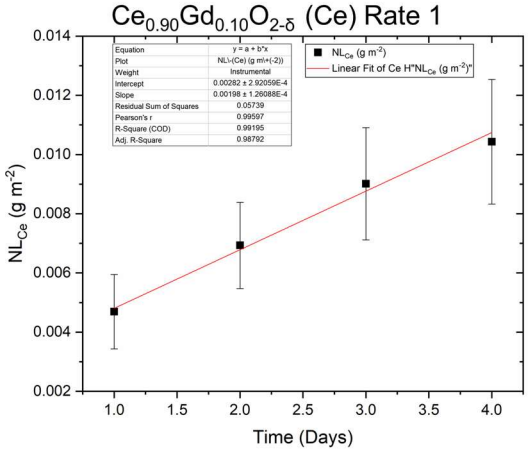
Ce0.90Gd0.10O2-δ (Ce) Rate 1
Equation y = a + b*x
Plot NLi-(Ce) (g m\+(-2))
Weight Instrumental
Intercept 0.00282 ± 2.92059E-4
Slope 0.00198 ± 1.28088E-4
Residual Sum of Squares 0.05739
Pearson's r 0.99597
R-Square (COD) 0.99195
Adj. R-Square 0.98792
NLCe (g m-2)
Linear Fit of Ce H"NLCe (g m-2)"
NLCe (g m-2)
Time (Days)

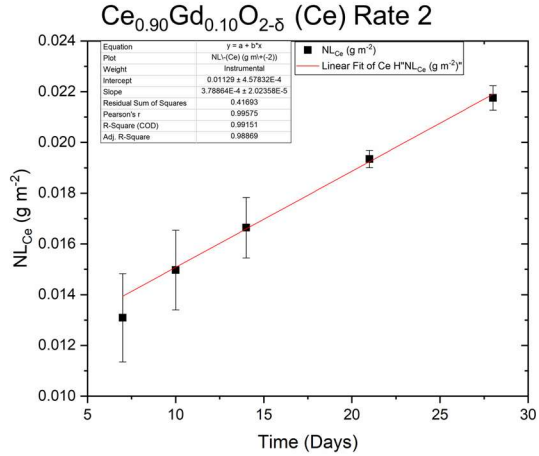
Ce0.90Gd0.10O2-δ (Ce) Rate 2
Equation y = a + b*x
Plot NLi-(Ce) (g m\+(-2))
Weight Instrumental
Intercept 0.01129 ± 4.57832E-4
Slope 3.78864E-4 ± 2.02358E-5
Residual Sum of Squares 0.41693
Pearson's r 0.99575
R-Square (COD) 0.99151
Adj. R-Square 0.98869
NLCe (g m-2)
Linear Fit of Ce H"NLCe (g m-2)"
NLCe (g m-2)
Time (Days)

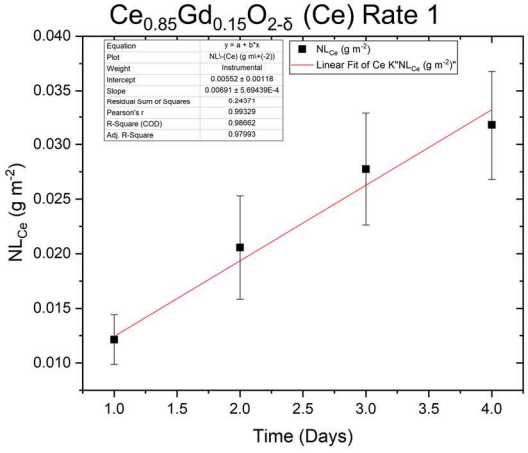
Ce0.85Gd0.15O2-δ (Ce) Rate 1
Equation y = a + b*x
Plot NLi-(Ce) (g m\+(-2))
Weight Instrumental
Intercept 0.00552 ± 0.00118
Slope 0.00691 ± 5.69439E-4
Residual Sum of Squares 0.24971
Pearson's r 0.99329
R-Square (COD) 0.98662
Adj. R-Square 0.97993
NLCe (g m-2)
Linear Fit of Ce K"NLCe (g m-2)"
NLCe (g m-2)
Time (Days)

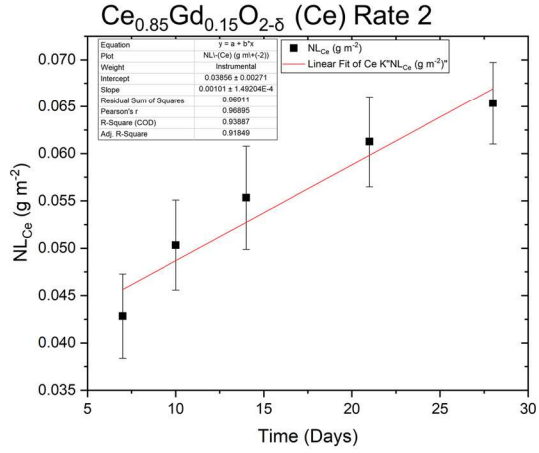
Ce0.85Gd0.15O2-δ (Ce) Rate 2
Equation y = a + b*x
Plot NLi-(Ce) (g m\+(-2))
Weight Instrumental
Intercept 0.03856 ± 0.00271
Slope 0.00101 ± 1.49204E-4
Residual Sum of Squares 0.06011
Pearson's r 0.96895
R-Square (COD) 0.93887
Adj. R-Square 0.91849
NLCe (g m-2)
Linear Fit of Ce K"NLCe (g m-2)"
NLCe (g m-2)
Time (Days)

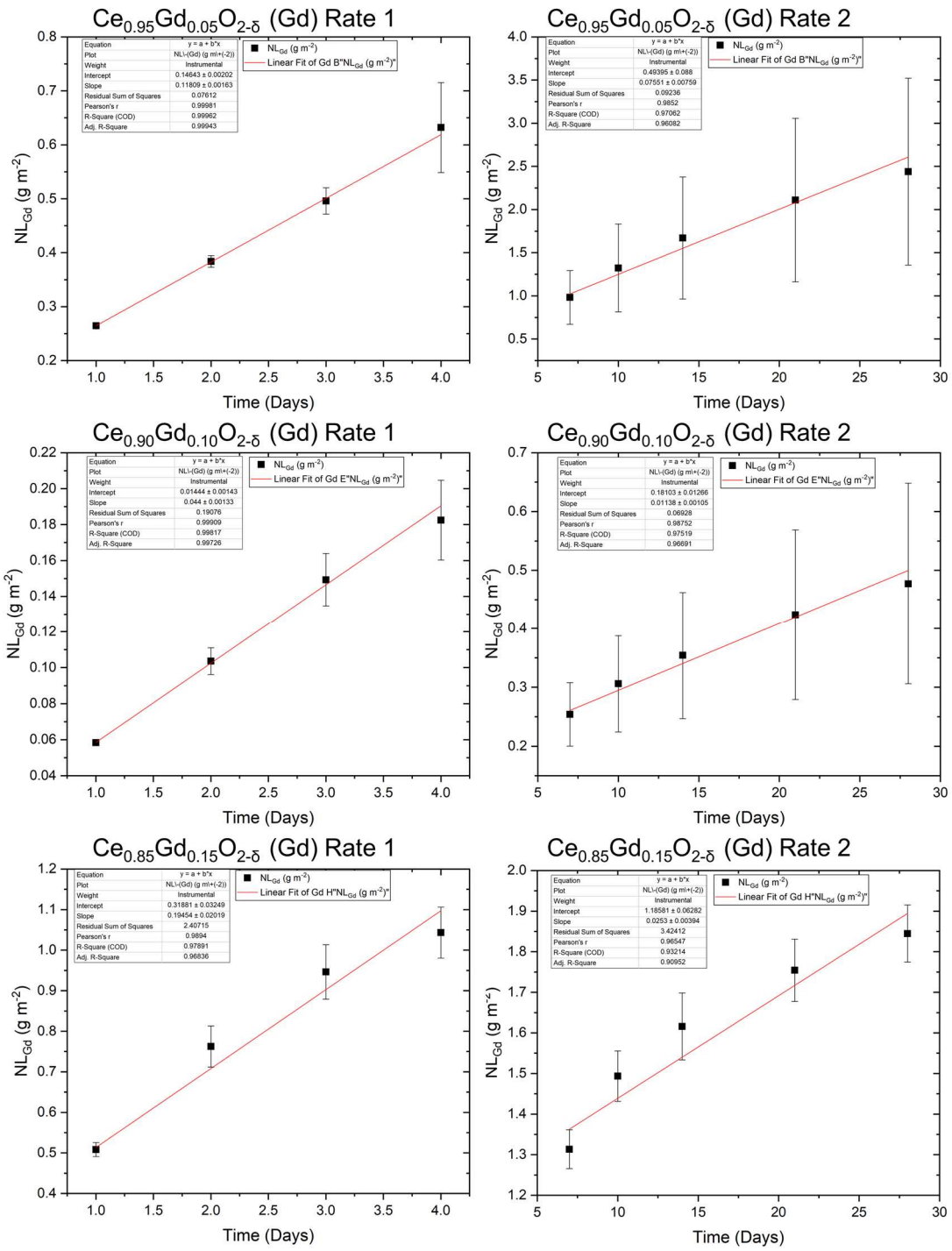

Figure S7: Linear fits used to determine Rate 1 and Rate 2 in C1308 tests on $Ce_{1-x}Gd_xO_{2-x/2}$

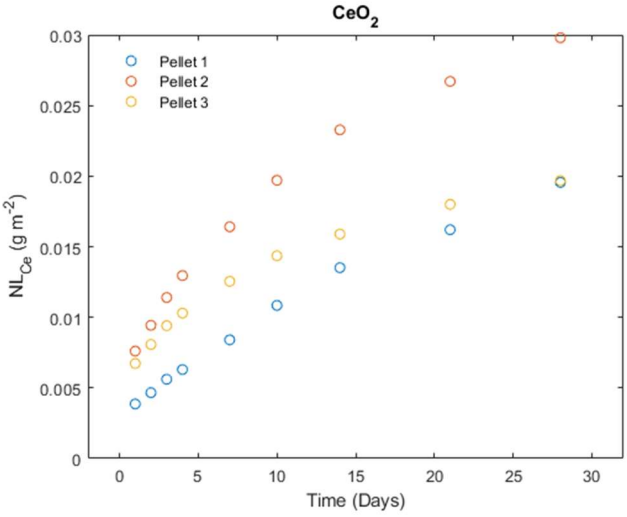
CeO2
Pellet 1
Pellet 2
Pellet 3
NLCe (g m-2)
Time (Days)

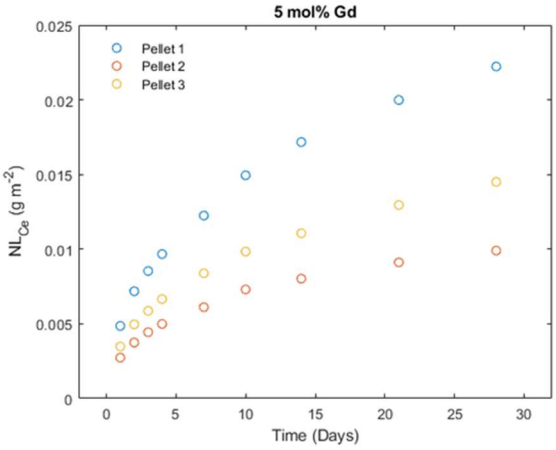
5 mol% Gd
Pellet 1
Pellet 2
Pellet 3
NLCe (g m-2)
Time (Days)

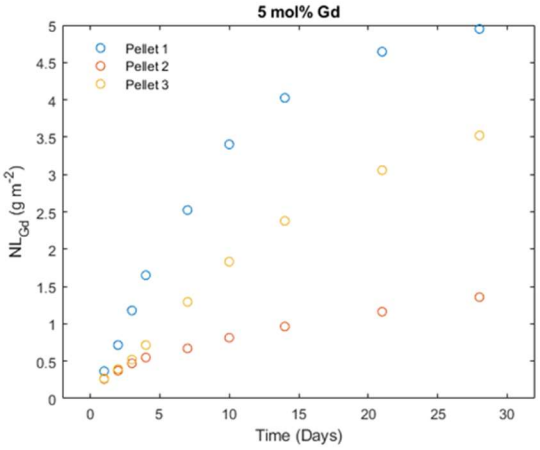
5 mol% Gd
Pellet 1
Pellet 2
Pellet 3
NLGd (g m-2)
Time (Days)

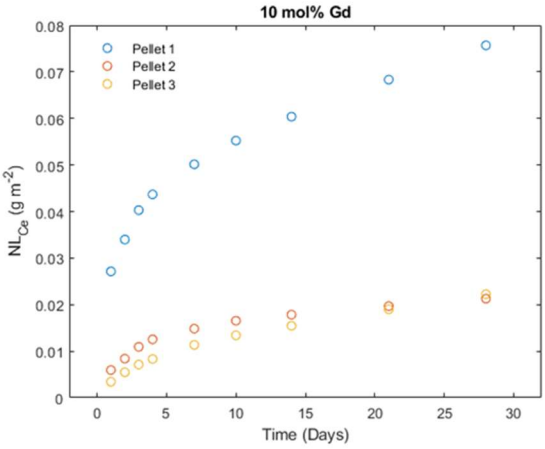
10 mol% Gd
Pellet 1
Pellet 2
Pellet 3
NLCe (g m-2)
Time (Days)

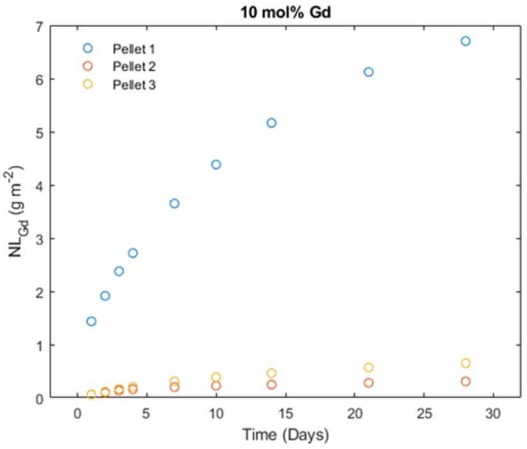
10 mol% Gd
Pellet 1
Pellet 2
Pellet 3
NLGd (g m-2)
Time (Days)

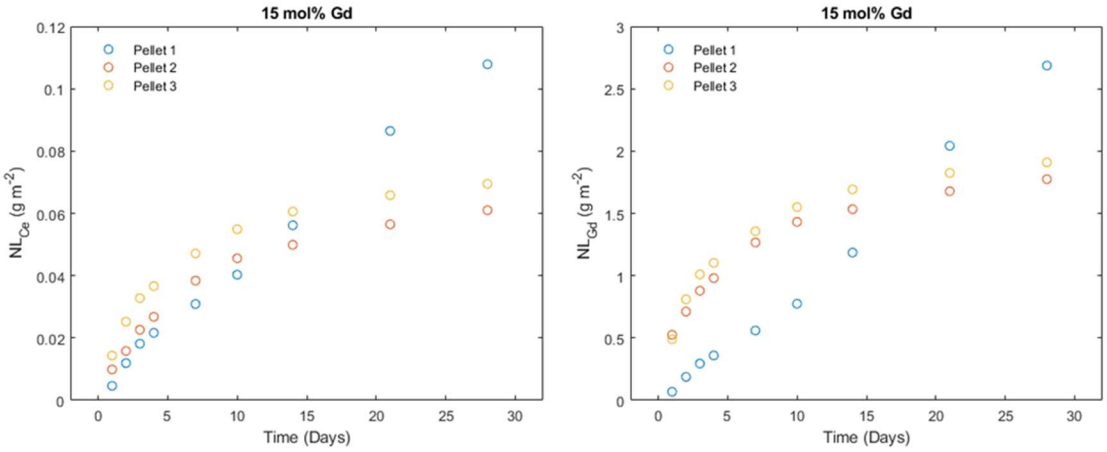

Figure S8: Individual plots of normalised mass loss for each pellet of $Ce_{1-x}Gd_xO_{2-x/2}$ dissolved in triplicate. Note Pellet 1 in x = 0.05, 0.10, and 0.15 exhibit significantly greater dissolution rates compared to Pellets 2 and 3. Pellet 1 in all three compositions was omitted from the averages presented.

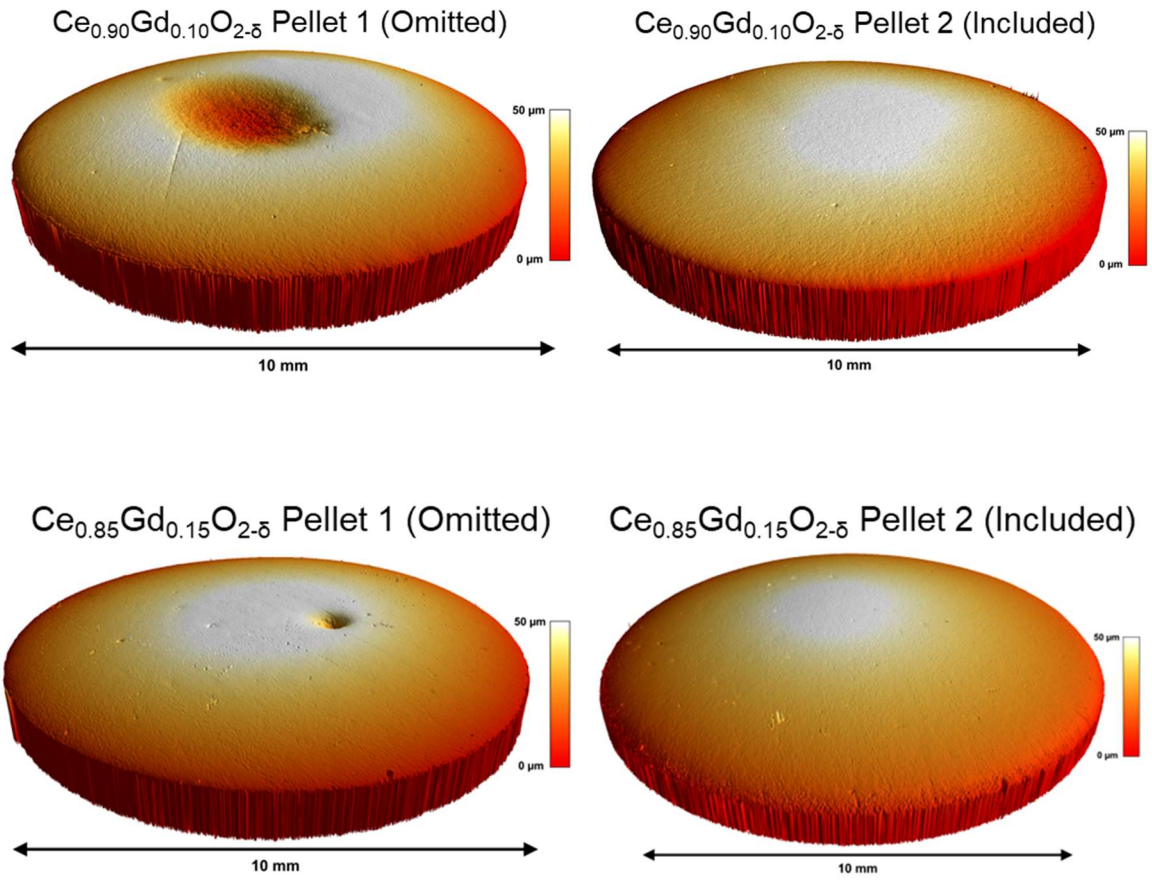

Figure S9: VSI measurements comparing surfaces of anomalous (omitted) pellets with those included in average rate calculations.

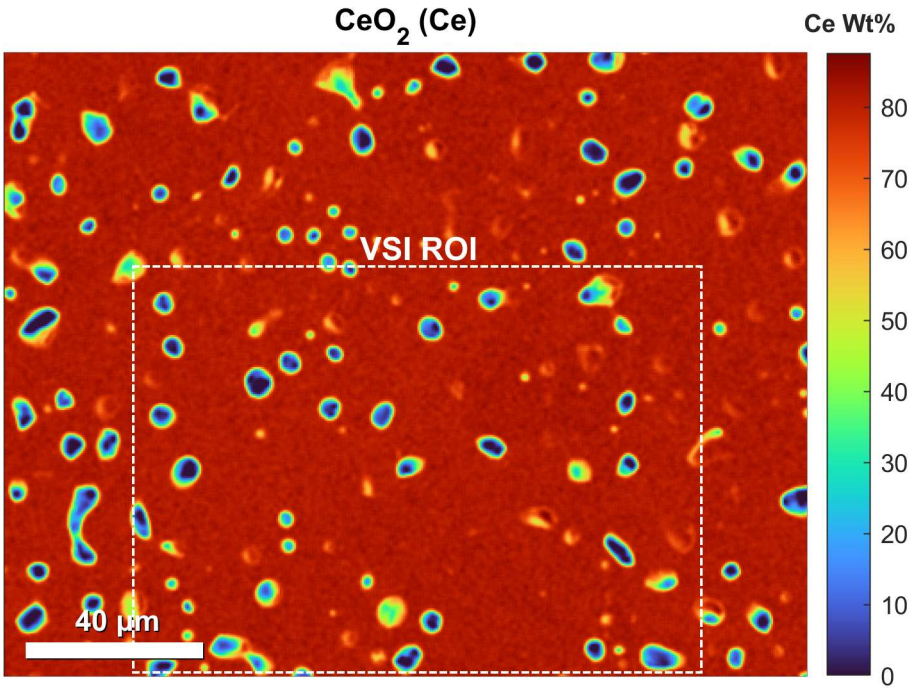

Figure S10a: Ce EPMA map for x = 0.00.

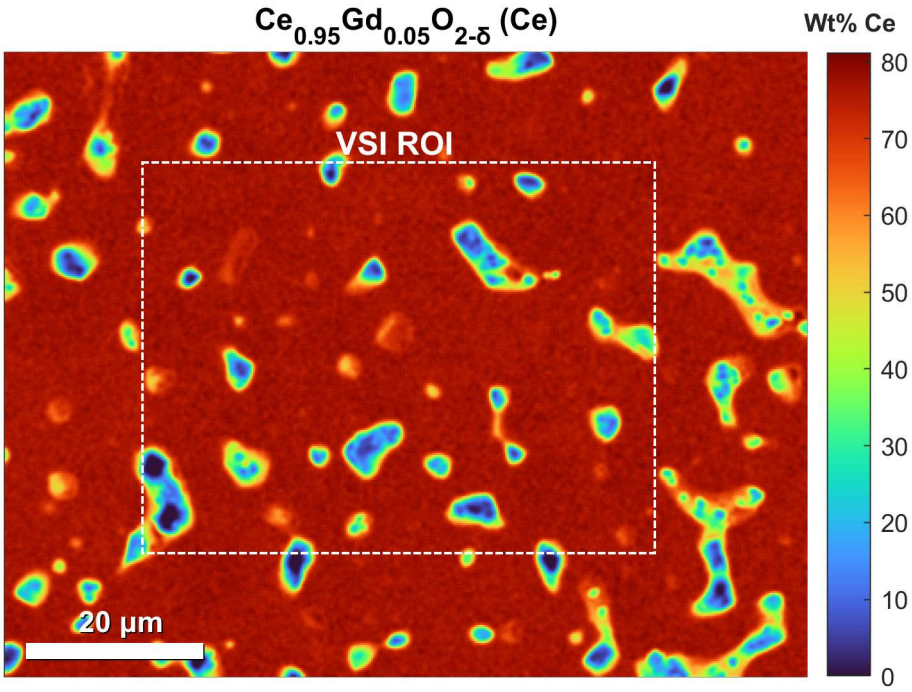

Figure S10b: Ce EPMA map for x = 0.05.

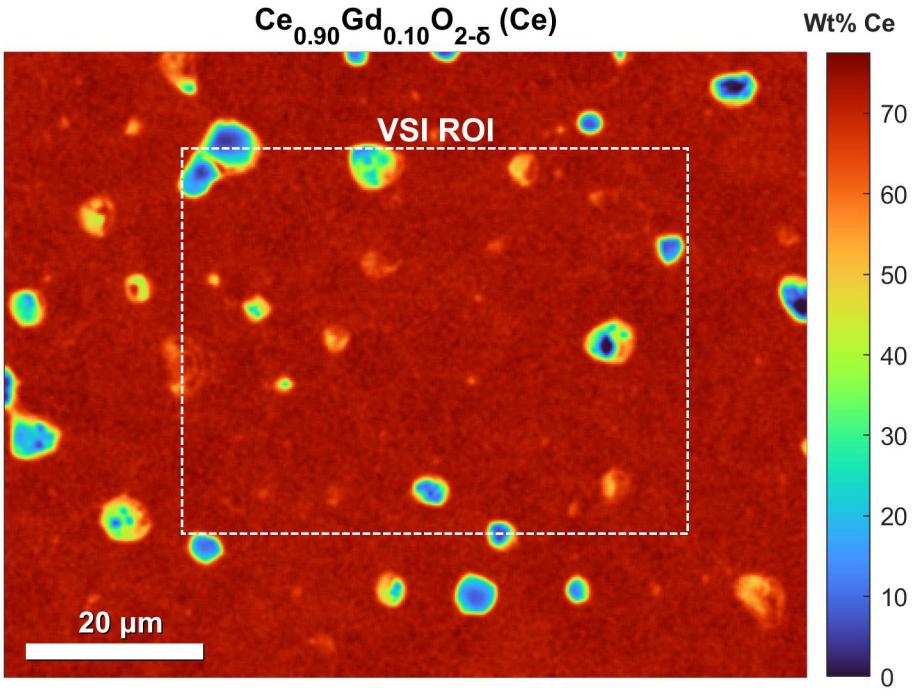

Figure S10c: Ce EPMA map for x = 0.10.

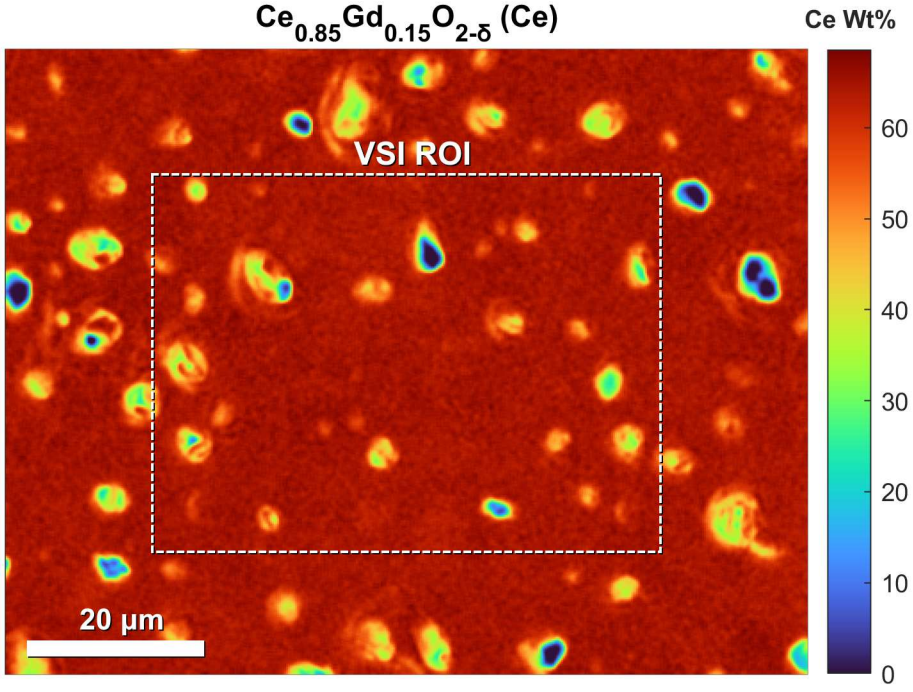

Figure S10d: Ce EPMA map for x = 0.15.

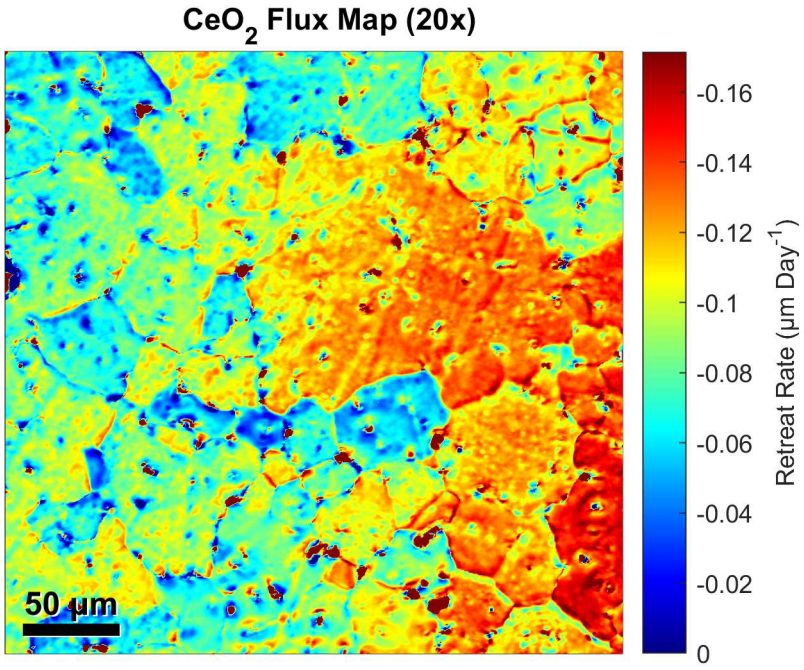

Figure S11a: Low magnification (20x) flux map of x = 0.00 dissolution generated *via* subtraction of VSI measurements taken pre- and post-dissolution.

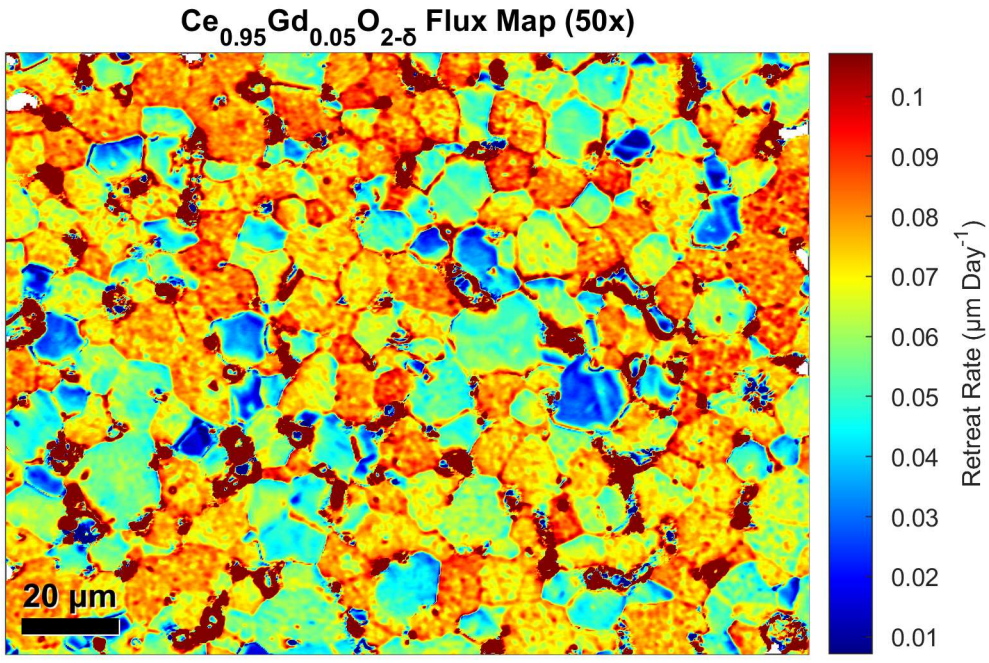

Figure S11b: Low magnification (50x) flux map of x = 0.05 dissolution generated *via* subtraction of VSI measurements taken pre- and post-dissolution.

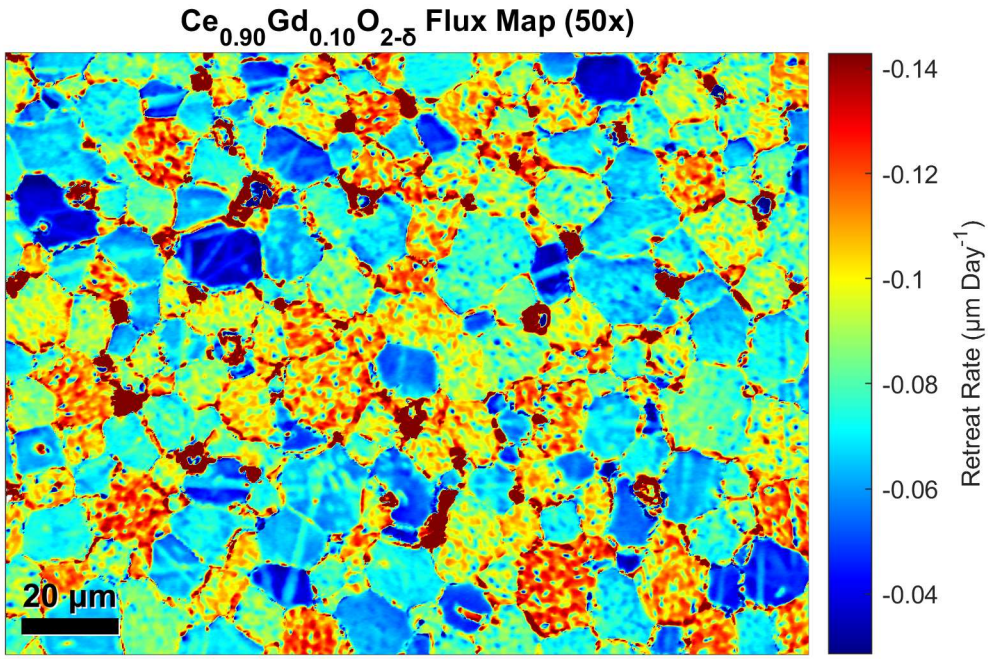

Figure S11c: Low magnification (50x) flux map of x = 0.10 dissolution generated *via* subtraction of VSI measurements taken pre- and post-dissolution.

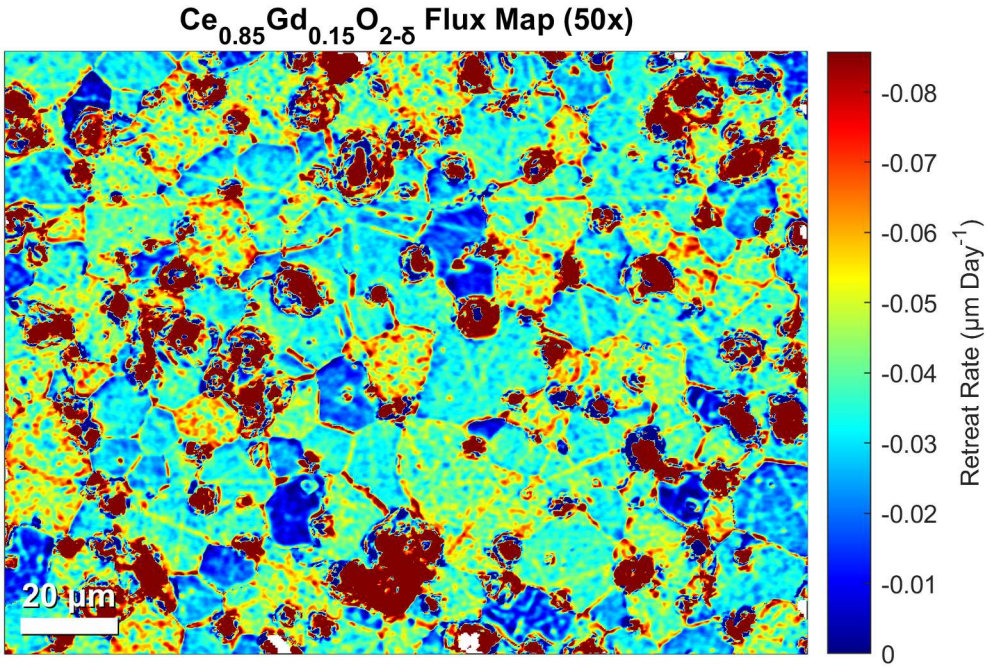

Figure S11d: Low magnification (50x) flux map of x = 0.15 dissolution generated *via* subtraction of VSI measurements taken pre- and post-dissolution.

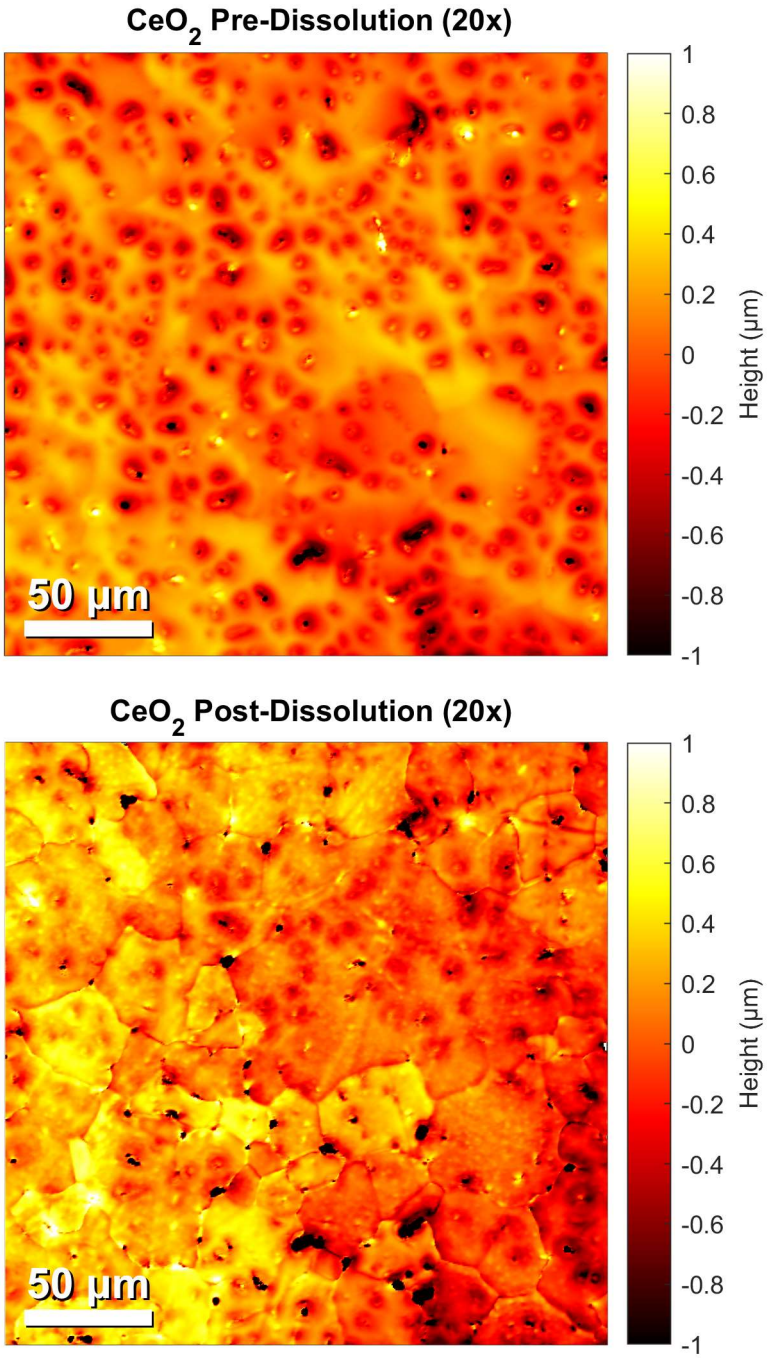

Figure S11e: Low magnification (20x) VSI measurements of x = 0.00 pre- and post-dissolution.

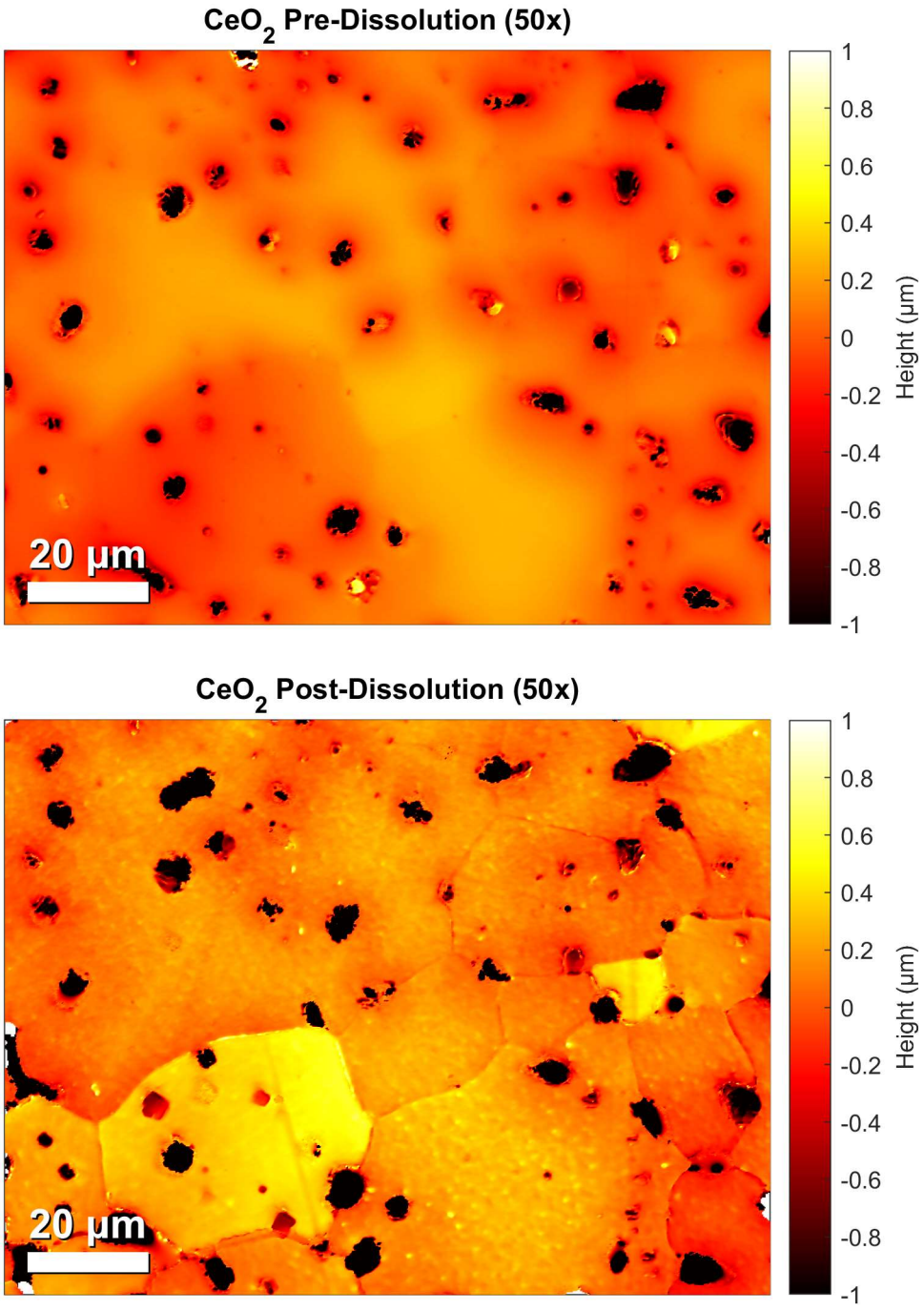

Figure S11f: High magnification (50x) VSI measurements of x = 0.00 pre- and post-dissolution.

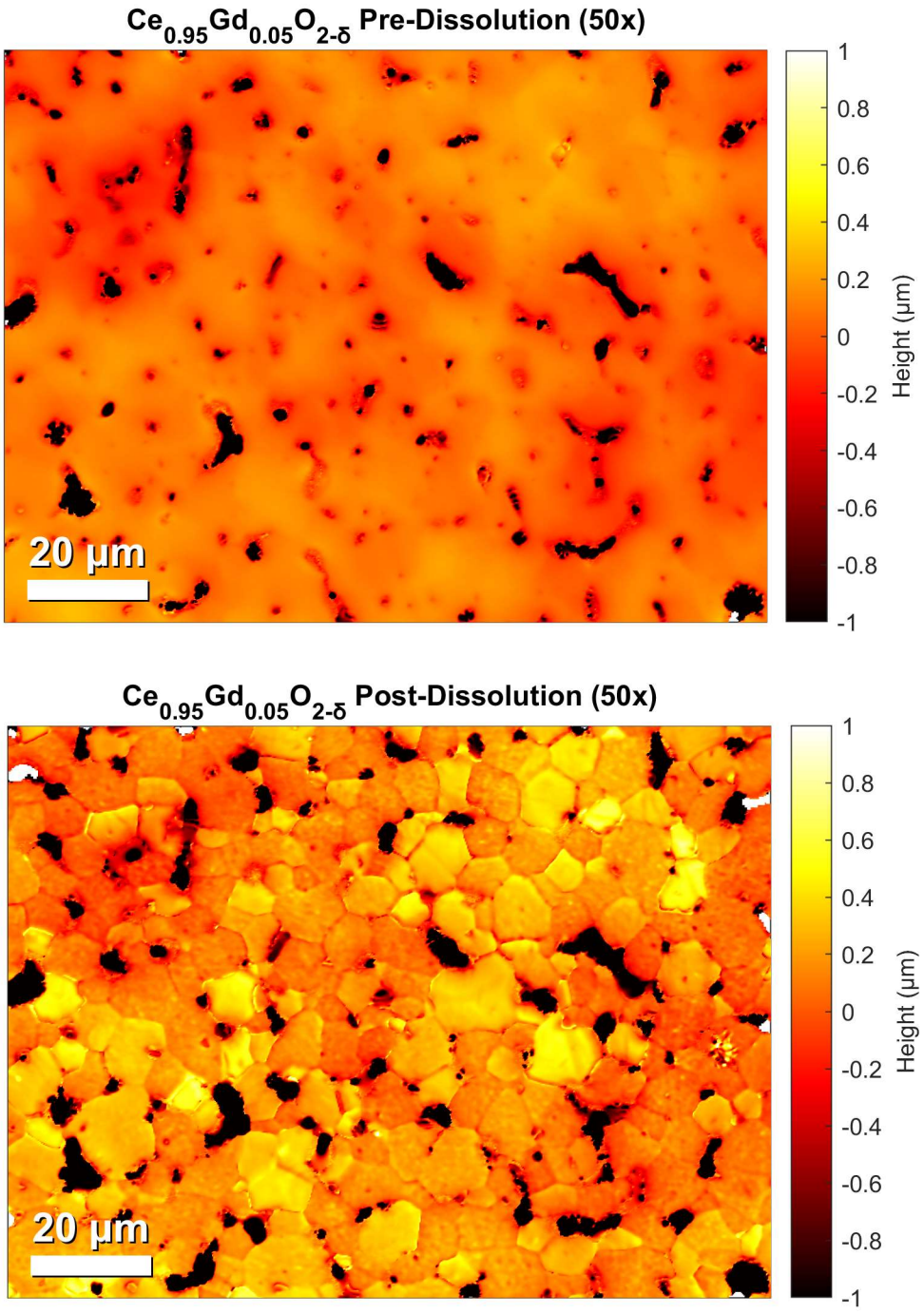

Figure S11g: Low magnification (50x) VSI measurements of x = 0.05 pre- and post-dissolution.

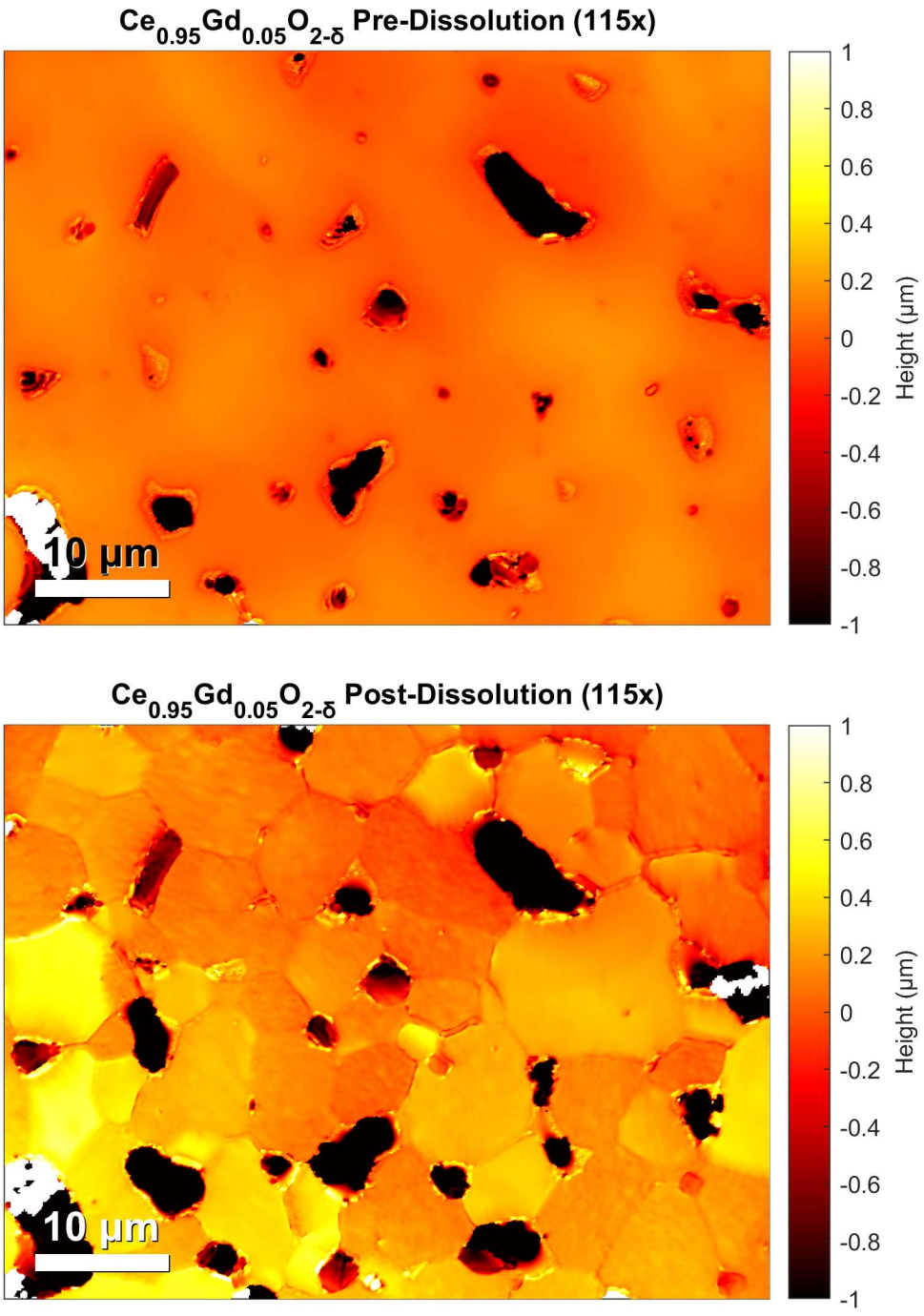

Figure S11h: High magnification (115x) VSI measurements of x = 0.05 pre- and post-dissolution.

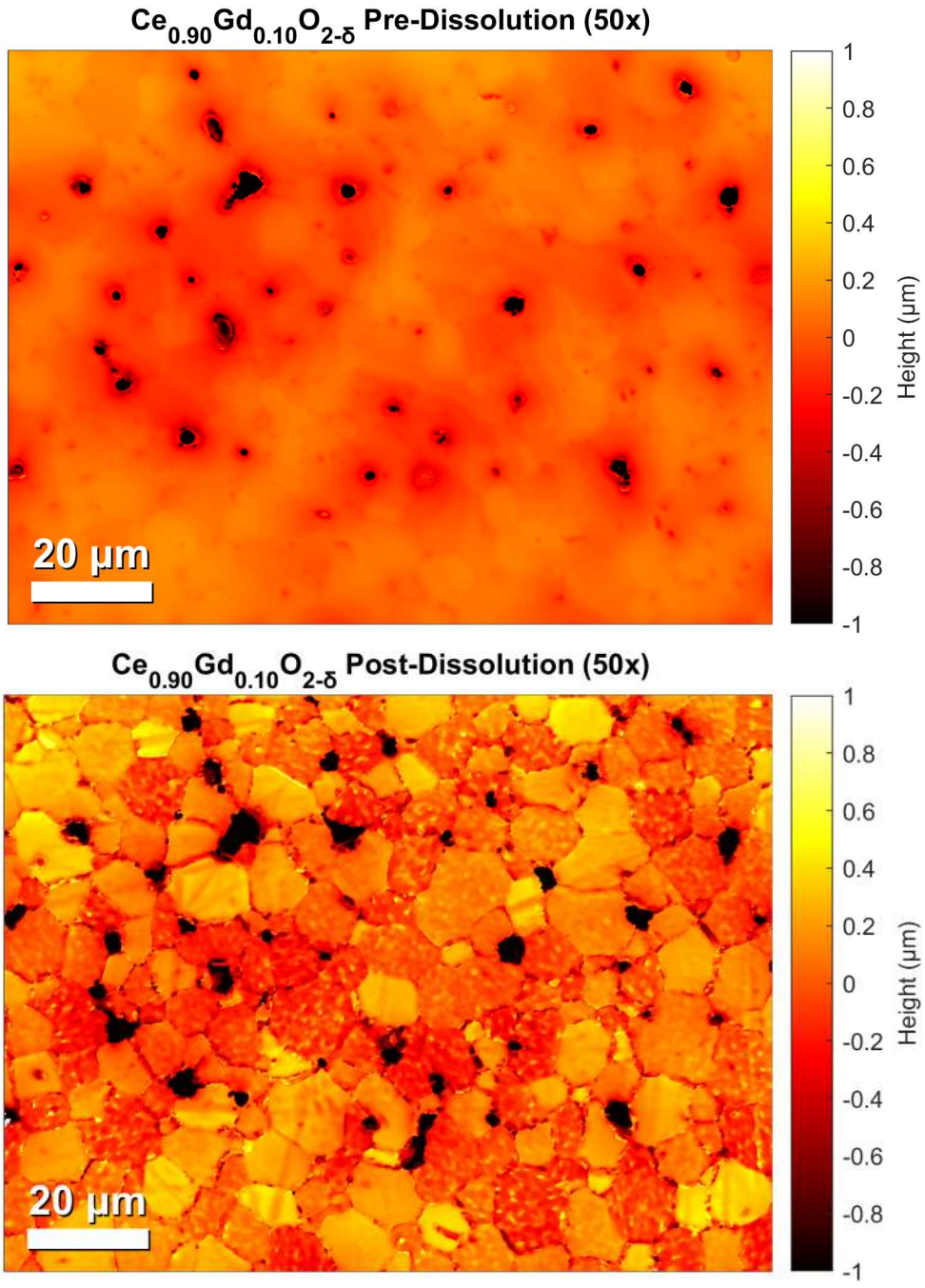

Figure S11i: Low magnification (50x) VSI measurements of x = 0.10 pre- and post-dissolution.

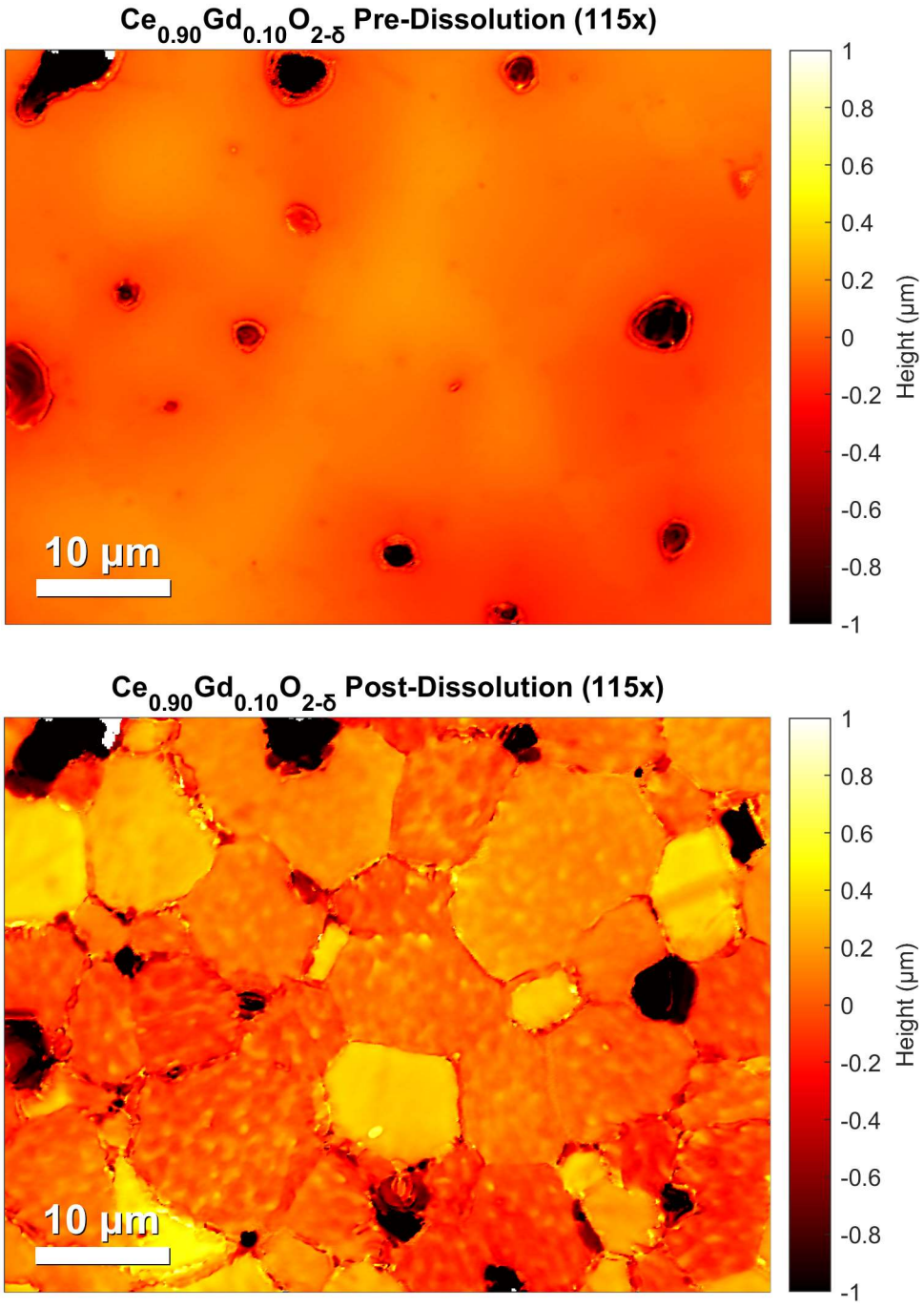

Figure S11j: High magnification (115x) VSI measurements of x = 0.10 pre- and post-dissolution.

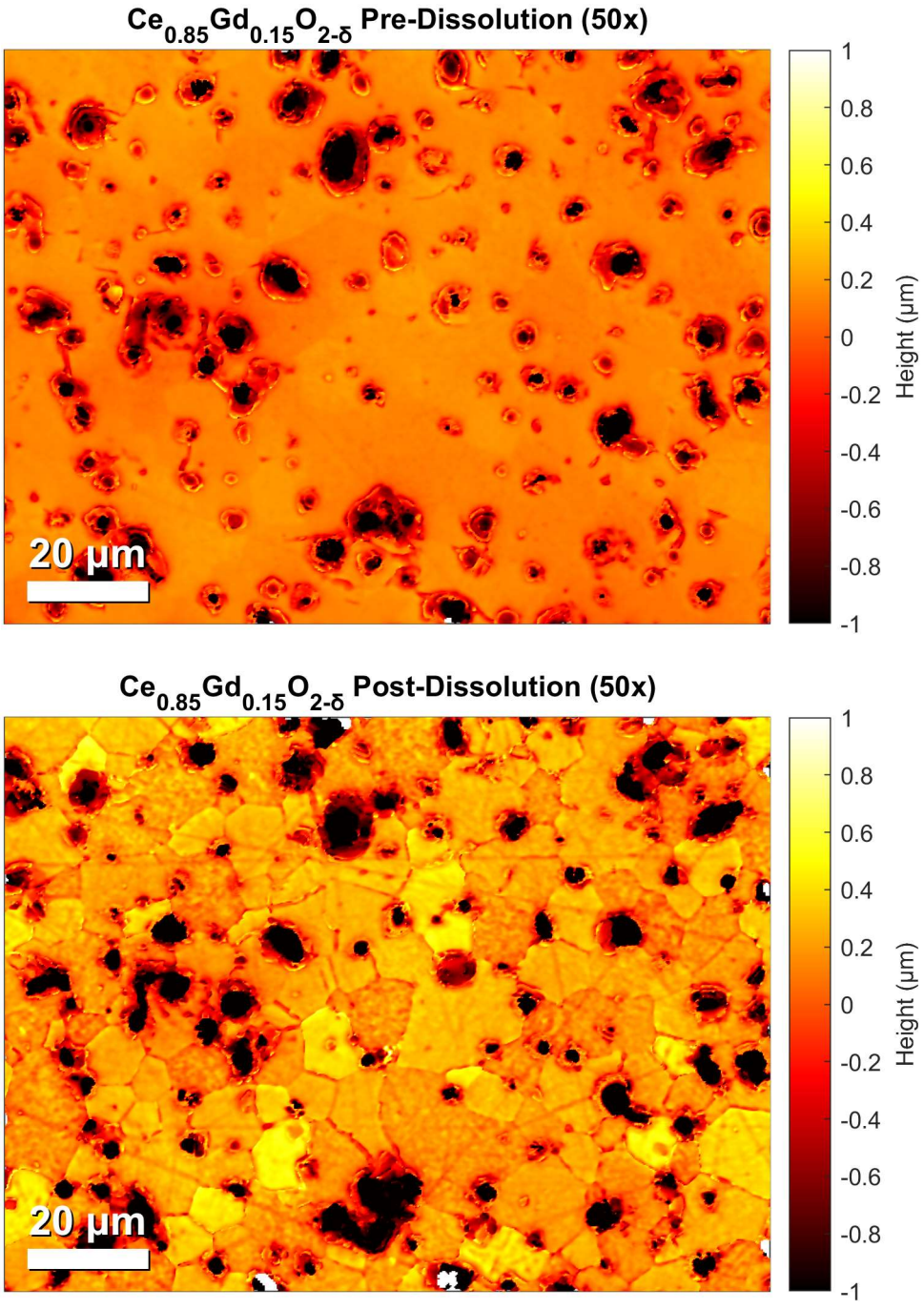

Figure S11k: Low magnification (50x) VSI measurements of x = 0.15 pre- and post-dissolution.

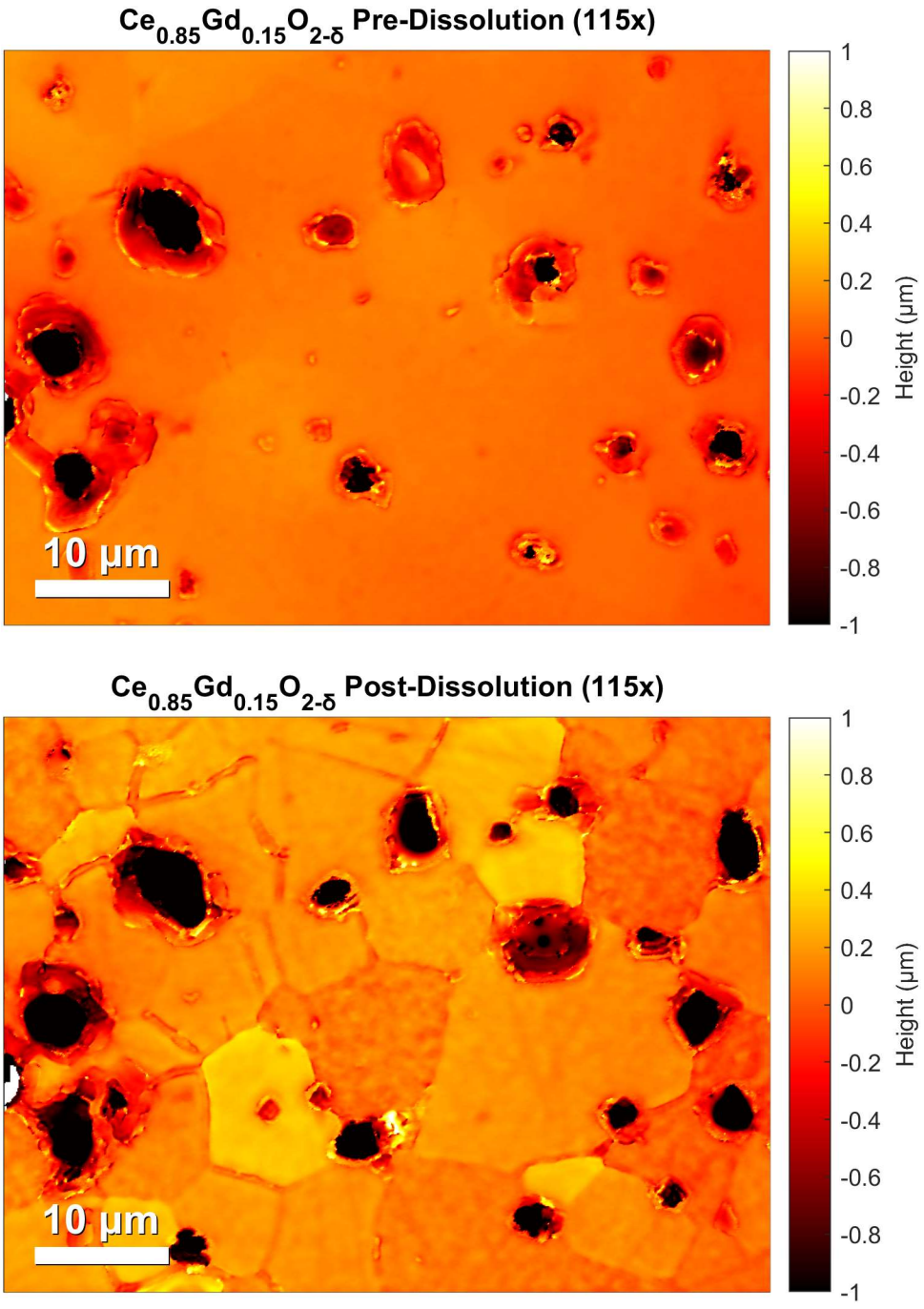

Figure S11l: High magnification (115x) VSI measurements of x = 0.15 pre- and post-dissolution.

6. Summary and conclusions

6.1 Impact of thesis

Research conducted into simulant disposal-MOX compositions of $(U,Th,Gd)O_2$ found single phase cubic fluorite (Fm-3m) materials can be produced *via* both oxalic co-precipitation and solid state synthesis routes. Obtained microstructures, comparable to that of spent fuel, showed slightly increases in grain size and density with increased Gd^{3+} additions, whereas significant incorporation of Th^{4+} had little impact. Fabrication route was found to strongly influence the compositional homogeneity of pellets, with larger Th-rich regions more readily observed in samples prepared through solid state, though Th and Gd-rich regions were present in all samples. Greater asymmetry and peak broadness in XRD patterns of solid state materials suggested these samples, whilst still single phase, comprised a range of $(U,Th,Gd)O_2$ compositions due to poor homogenisation achieved during milling. Interestingly, Th-rich regions were likewise enriched with Gd in co-precipitated samples, but not in solid state materials. Subtle grain boundary segregation of Th resulted in slight enrichment at grain edges, more readily observed in homogenous co-precipitated samples. Th^{4+} additions caused an expansion of the fluorite lattice in accordance with Vegard's law, whereas Gd^{3+} additions contracted the lattice due to oxygen vacancy generation. The dominant charge compensation mechanism used to balance for trivalent Gd^{3+} was determined to be oxygen vacancy generation, with no relationship established between U^{5+} proportion and Gd^{3+} content. These findings show single phase disposal-MOX wasteforms that retain the aqueous durability and radiation tolerance of UO_2 can potentially be produced using heterogenous mixtures of UO_2, PuO_2 and Gd_2O_3, likely to be produced by industrial large-scale dry milling processes.

Research conducted in the $Ce_{1-x}Gd_xO_{2-x/2}$ system revealed the influence of Gd incorporation of phase transformations, secondary phase formation, defect chemistry, and dissolution behaviour. In compositions where $x \leq 0.30$, sintered pellets adopted the fluorite (Fm-3m) structure, for compositions $x > 0.30$, widespread phase transformation to cubic C-type (Ia-3) was observed. Small quantities of Gd-rich secondary phases, believed to have a C-type structure, were observed within the fluorite matrix for $x \geq 0.10$; the size and frequency of these regions increased with Gd addition. Substitution of Ce^{4+} with Gd^{3+} was charge compensated *via* V_O generation. Evidence of V_O ordering to form C-type nanodomains, embedded within the fluorite lattice, was found for $x \geq 0.05$, whilst total lattice disorder was found to increase linearly with Gd incorporation. This increased lattice disorder exerted strong control over dissolution rates, with greatest Ce and Gd normalised release measured in the composition with the highest Gd incorporation ($x = 0.15$) Incongruent release of Ce and Gd is suspected to have

resulted from primarily from preferential dissolution of Gd-rich secondary phases, however accelerated dissolution of Gd-enriched grain boundaries, observed using a novel VSI-based dissolution study, may have contributed to this incongruity. Within regions consisting of a single fluorite phase, heterogenous Gd distribution was found to exert no control over localised dissolution rates. Similarly, the misorientation angle of grain boundaries was also found to have no influence on relative dissolution rates of grain boundaries, regardless of composition.

These conclusions allow a hierarchy of dissolution rate contributors to be established. Firstly, widespread structural alteration of the fluorite lattice represents the most significant impact of Gd^{3+} incorporation in on the dissolution of $Ce_{1-x}Gd_xO_{2-x/2}$. This is followed by secondary phase formation, which can increase the reactive surface area and promote strongly incongruent dissolution. Thirdly, the differing surface energy of exposed planes between grains of differing orientation was shown to exert strong control over localised dissolution rates, however, Gd additions did not alter the grain texture. Grain boundaries also contributed towards accelerated dissolution, but less significantly than high energy exposed planes. Whilst the total grain boundary area increased with the addition of Gd (as grain size decreased), these high energy sites constituted an insignificant fraction of the total surface compared to the grains themselves, limiting their influence on overall dissolution rates. Lastly, both spatial Gd distribution in single-phase fluorite, and grain boundary misorientation angle appeared to have no influence on localised dissolution rates. Whilst high energy surface sites certainly contributed to dissolution, the substitution of Ce^{4+} with Gd^{3+} was not found to influence the relative rate contributions from these regions.

6.2 Future Work

Several further avenues of research could complement the work presented in this thesis.

6.2.1 Further study of simulant disposal-MOX

This thesis demonstrated the successful fabrication of single-phase simulant disposal-MOX materials, sintered at 1700 °C. Sintering pellets at lower temperatures, ranging between 1400 °C - 1700 °C, would permit examination into the role of high-temperature heat treatments in achieving the homogeneity and microstructure of disposal-MOX materials. This further work could validate the feasibility of fabricating disposal-MOX materials at lower temperatures, more attractive to industry. Similarly, additional work could encompass closer emulation of industrial dry ball milling processes, including the incorporation of 'scrap' UO_2 pellet fragments into the wasteform.

Bulk dissolution testing into disposal-MOX is underway within our research group, pairing these results with VSI-based spatially resolved studies could reveal the role of microstructure

and compositional heterogeneity in incongruous elemental release, especially significant in poorly homogenised solid state samples.

Compositions prepared for this work were formulated based on estimated Gd quantities required to ensure $k_{eff} < 1$. Future work could incorporate modelling studies to simulate the influence of spatial Gd distribution on criticality risk, to provide a greater understanding of the degree of required homogenisation.

6.2.2 Further study of $Ce_{1-x}Gd_xO_{2-x/2}$ system

The substitution of Ce^{4+} with Gd^{3+} has been shown to influence the crystal chemistry, phase formation, and microstructure in the $Ce_{1-x}Gd_xO_{2-x/2}$ system. Further investigation into the dissolution behaviour for compositions where $x \geq 0.15$ is necessary to precisely determine the cause of the rapid increase in normalised Ce release beyond this threshold. Whilst some evidence suggested extensive V_O ordering and C-type nanodomain formation may have yielded these greatly increased rates, further characterisation of the crystal structure with HR-TEM is needed to confirm the presence of locally ordered structures and domains. Furthermore, subsequent VSI-based dissolution studies should be conducted on bi-phasic regions in compositions where $x \geq 0.15$ to deconvolute the role of secondary phases in bulk dissolution rates. EBSD of these bi-phasic regions would also be required to confirm the crystal structure of the secondary phases, which were assumed to be C-type in this work.

Whilst the *ex-situ* VSI-based method helped reveal the relative contributions of high-energy surface features during dissolution, the study failed to correlate grain boundary misorientation with retreat rate. This is believed to be largely because of the extensive dissolution that had occurred within the first 7 days. Repeating the study with more frequent sampling during the earliest stages of dissolution may help reveal subtle differences in retreat rate that were concealed by pronounced crystallographic plane retreat after 7 days. Further investigations using *in-situ* AFM measurements would enable more precise measurements of grain boundary depth during the earliest stages of dissolution.

Work conducted in this study suggested sintering temperatures play an important role in secondary phase formation. Oxide precursors were believed to be highly homogenous mixed oxide powder of $Ce_{1-x}Gd_xO_{2-x/2}$, diffusion during sintering is likely to have facilitated significant segregation *via* diffusion at highly elevated temperatures. Systemic characterisation of oxalate and oxide precursors prior to sintering could help confirm the cause of secondary phase formation to be segregation during sintering, not inhomogeneity in the initial green pellets. Further investigation into the role of sintering temperature and partial oxygen pressure could reveal the reason beyond secondary phase formation at low ($x = 0.10$) rates of Gd incorporation, which were previously unreported in the literature.

Expanding the study to encompass the incorporation of different additions, such as Y^{3+} and Th^{4+} in CeO_2 would permit investigation into the influence of crystal radius and valency on heterogenous dissolution. The comparison of trivalent and tetravalent dopants with similar crystal radii could be used to examine the role V_O ordering on dissolution rates and cation segregation.

Finally, repeating the $Ce_{1-x}Gd_xO_{2-x/2}$ study with $U_{1-x}Gd_xO_{2-\delta}$ would assess the relevance of its findings in the context of oxidative dissolution.